ELECTRON SCATTERING FROM A HIGH MOMENTUM NEUTRON IN DEUTERIUM

by

Alexei V. Klimenko
M.S. June 1999, Moscow University of Technology
M.S. May 2001, Old Dominion University

A Dissertation Submitted to the Faculty of
Old Dominion University in Partial Fulfillment of the
Requirement for the Degree of

DOCTOR OF PHILOSOPHY

PHYSICS

OLD DOMINION UNIVERSITY
May 2004

Approved by:

Sebastian Kuhn (Director)

Gary Copeland

William Jones

Rocco Schiavilla

Lawrence Weinstein

ABSTRACT

ELECTRON SCATTERING FROM A HIGH MOMENTUM NEUTRON IN DEUTERIUM

Alexei V. Klimenko
Old Dominion University, 2004
Director: Dr. Sebastian Kuhn

The deuterium nucleus is a system of two nucleons (proton and neutron) bound together. The configuration of the system is described by a quantum-mechanical wave function and the state of the nucleons at a given time is not known a priori. However, by detecting a backward going proton of moderate momentum in coincidence with a reaction taking place on the neutron in deuterium, the initial state of that neutron can be inferred if we assume that the proton was a spectator to the reaction. This method, known as spectator tagging, was used to study the electron scattering from high-momentum neutrons in deuterium. The data were taken with a 5.765 GeV polarized electron beam on a deuterium target in Jefferson Laboratory's Hall B, using the CLAS detector. The accumulated data cover a wide kinematic range, reaching values of the invariant mass of the unobserved final state W^* up to 3 GeV. A data sample of approximately $5 \cdot 10^5$ events, with protons detected at large scattering angles (as high as 136°) in coincidence with the forward electrons, was selected. The product of the neutron structure function with the initial nucleon momentum distribution $F_{2n} \cdot S$ was extracted for different values of W^*, backward proton momenta p_s and momentum transfer Q^2. The data were compared to a calculation based on the spectator approximation and using the free nucleon form factors and structure functions. A strong enhancement in the data, not reproduced by the model, was observed at $\cos(\theta_{pq}) > -0.3$ (where θ_{pq} is the proton scattering angle relative to the direction of the momentum transfer) and can be associated with the contribution of final state interactions (FSI) that were not incorporated into the model. The bound nucleon structure function F_{2n} was studied in the region $\cos(\theta_{pq}) < -0.3$ as a function of W^* and scaling variable x^*. At high spectator proton momenta the struck neutron is far off its mass shell. At $p_s > 400$ MeV/c the model overestimates the value of F_{2n} in the region of x^* between 0.25 and 0.6. A modification of the bound neutron structure is one of possible effects that can cause the observed deviation.

ACKNOWLEDGMENTS

First of all I would like to express my deep gratitude to all of my family members without whose support this dissertation would never have been written. I would like to thank my father, Vasiliy G. Klimenko, who started preparing me for the career of a scientist from the earliest part of my childhood. He taught me the things he knew and without his insights into the most challenging fields of modern science, I would have never achieved the level of understanding I have. My mother, Olga K. Klimenko, whose infinite love, support and strong belief in my abilities were the things that helped me through the most complicated years of graduate school. The discipline and organizational skills, that so many young people lack nowadays, were forced on me by my grandmother Anna G. Yasyuninskaya. Although frequently frustrated and stubborn in adopting these skills in my teens, graduate school made me realize their true value. I cannot underestimate the contribution to this work of my beloved wife, Kathrynne M. Hanlin. We had met only a few months after I arrived to America. She showed me the America she lived in, her values, and her goals and made me believe again in all the good things in this world that started to fade in the struggling Russian society of the 90s. Kathrynne's strong love for me, ability to make sacrifices, be strong, and patient are what brought this dissertation to life. I should also thank the nicest person I have met in a long time, my mother in law, Theresa J. Hanlin, who was always very supportive and essentially became my Western hemisphere mother.

I am very grateful to the faculty and staff of the Old Dominion University Physics Department. My advisor, Sebastian Kuhn, was a moving force behind every single part of the analysis described in this dissertation. His unshakable optimism in the toughest times and unquenchable desire to learn were among the things that helped me through at the times when I felt lost. A major contribution into my development as a researcher was made by probably one of the greatest teachers I've known, Larry Weinstein, whom I worked with throughout most of my graduate school years. Larry's ability to explain the most complicated things in terms of the most basic concepts was one of the things I always tried to learn from him. I also have to thank Andi Klein who taught me a lot about life and prepared me for the entrance into the real academic world. Andi's fearless openness and honesty were among the qualities of character I always admired and tried to adopt. I am especially thankful to David

Richards, Ian Balitskiy, Anatoliy Radyushkin, and Rocco Schiavilla who did their best to teach me the fundamentals of modern physics. A special role was played throughout my graduate school years by Walton Hooks, whose professionalism and great personality makes the ODU Physics Department work.

I would feel bad not to mention a few more names of the people who in one way or another made this dissertation happen: Harut Avakian, Cornel Butuceanu, Vipuli Dharmawardane, Kim Egiyan, Olga Fylatova, Keith Griffioen, David Hayes, Hassan Ibrahim, Rustam Niyazov, Ales Psaker, Stepan Stepanyan, Carlos and Rocio Velasco.

TABLE OF CONTENTS

Page

CHAPTERS

1 Introduction . . . 1
2 Physics overview . . . 5
 2.1 Electron Scattering Formalism . . . 5
 2.2 Nucleon Structure . . . 8
 2.3 Nuclear models of deuterium . . . 12
 2.4 Nucleons in a Nuclear Medium . . . 16
 2.5 Final State Interactions . . . 26
 2.6 Existing Data Overview . . . 29
 2.7 Analysis Objectives . . . 33
3 Experimental Setup . . . 36
 3.1 Accelerator . . . 36
 3.2 Hall B Beamline . . . 36
 3.3 CEBAF Large Acceptance spectrometer . . . 38
  3.3.1 Wire Chambers . . . 39
  3.3.2 Scintillator Counters . . . 41
  3.3.3 Electromagnetic Calorimeter . . . 42
  3.3.4 Cherenkov Counters . . . 44
 3.4 Target . . . 46
4 Data Analysis . . . 48
 4.1 Good Data File Selection . . . 49
 4.2 Detector Calibration . . . 52
 4.3 Electron Identification . . . 54
  4.3.1 Cherenkov Detector Fiducial Cuts . . . 54
  4.3.2 Other Electron Identification Cuts . . . 61
  4.3.3 Electron Identification Efficiency . . . 61
  4.3.4 Electron Spectrum Contamination from e^+e^-- pair Production 70
 4.4 Proton Identification . . . 73
  4.4.1 Proton Timing Correction and Selection . . . 73
  4.4.2 Proton Vertex Cuts . . . 78

4.4.3 Proton Energy Loss Correction 79
4.4.4 Accidental Protons 80
4.5 Additional Corrections and Cuts 83
4.5.1 Momentum and Angle Corrections 83
4.5.2 Vertex Correction 85
4.6 Data Simulation 86
4.6.1 Event Generator 87
4.6.2 Detector Simulation 91
4.6.3 Simulation Results 107
4.6.3.1 Inclusive p(e,e')x and d(e,e')X Reaction Simulation . 107
4.6.3.2 Semi-inclusive d(e,e'p) Reaction Simulation 121
5 Results and Discussion 136
5.1 Applied Corrections and Error Estimation 136
5.2 Extraction of the Results 138
5.3 Results and Discussion 142
5.3.1 Deuterium Momentum Distribution 143
5.3.2 Bound Neutron Structure 159
6 Summary 166

APPENDICES

A Full Set of Final Histograms 172

VITA 213

LIST OF FIGURES

Page

1 Electron scattering from a nucleus. 5
2 Schematic diagram showing different parts of nucleon-nucleon potential. 15
3 The deuteron S- and D-wave function components divided by r [63]. . . 15
4 The ratio σ^{Fe}/σ^{D} plotted as a function of Bjorken x. 21
5 The x dependence of bound to free nucleon structure functions for two different values of α_S. 22
6 The light-cone fraction dependence of the ratio of bound to free structure function of the nucleon calculated using different models [47]. . . 25
7 The ratio R_1 plotted for $\alpha = 1.4$ and $p = 322$ MeV/c. 26
8 The ratio R_1 plotted for $\alpha = 1.4$ and $p = 322$ MeV/c. 26
9 The α_S dependence of the ratio of cross sections calculated with FSI effects within the DWIA, and without FSI effects. 27
10 The debris-nucleon cross section, plotted versus the distance z for a fixed value of x and various values of Q^2. 28
11 The ratio of FSI to undistorted momentum distributions of deuterium in the hadronization model. 30
12 Comparison of the experiment with a pair-correlation model. 31
13 Ratios of Drell-Yan dimuon yield per nucleon, $Y_A/Y_{^2H}$. 32
14 Superratio R/R_{PWIA} as a function of Q^2 [22]. 32
15 Comparison of the backward proton spectrum to calculations using the Bonn wave function. 33
16 Comparison of the backward proton spectrum to calculations using the Paris wave function. 33
17 Diagrammatic representation of a spectator mechanism. 34
18 The CEBAF SRF recirculating electron accelerator. 37
19 CEBAF Large Acceptance spectrometer. 38
20 Vertical cut through the drift chambers transverse to the beam line at the target location showing the geometric relationship of the detectors. 40

21 Schematic representation of a typical drift-chamber sector (R3 in this case) highlighting some of the common hardware pieces used by each. 40

22 Horizontal cut through the CLAS detector at beam line elevation showing two charged particles transversing the drift chambers in opposite sectors. 40

23 Representation of portion of an R3 sector showing the layout of its two superlayers. 40

24 View of the time-of-flight scintillator counters in one sector. 42

25 Exploded view of one of the six CLAS electromagnetic calorimeter modules. 43

26 A schematic diagram of the array of optical modules in one of the six sectors. 44

27 Optical arrangement of one of the 216 optical modules of the CLAS Cherenkov detector, showing the optical and light collection components. 45

28 E6 target cell with plumbing exposed (top) and with heat shields in place (bottom). 47

29 E6 target layout. 47

30 Number of electrons passing all the cuts found in the file vs run and file number. 51

31 Radio-frequency offsets (TOF) - left; drift chamber spatial residuals - right. 53

32 Drift chamber residuals dependence on the run number for all 6 superlayers. 55

33 TOF resolution (left) and mean value of RF offsets (right). 56

34 EC time resolution (left) and mean sampling fraction of EC (right). . 56

35 Momentum of electron vs scattering angle. 58

36 Azimuthal vs. polar angle of scattered electron for the low momentum part of the data (0.0 GeV/c$<P_{el}<$3.0 GeV/c). 59

37 Azimuthal vs. polar angle of scattered electron for the low momentum part of the data (3.0 GeV/c$<P_{el}<$6.0 GeV/c). 60

38 Total energy deposited in EC vs. energy deposited in the inner layer of EC. 62

39 Total energy deposited in EC vs. energy deposited in the inner layer of EC. 63

40 Electron vertex for the full (solid line) and empty (dashed line) target. 64

41 Trigger efficiency. 65

42 Example of the simulated Cherenkov detector response to the electron (solid line) overlayed with the electron measured Cherenkov detector response (black triangles). 67

43 Loss of the electrons due to the cut on Cherenkov detector spectrum of the electron. 67

44 Example of the electron spectrum from Cherenkov detector (solid line) overlayed with the pion spectrum (dashed line) and CC response simulation (dash-dotted line). 68

45 The fit to the estimated electron spectrum contamination with pion after CC cut. 69

46 The fit to the estimated number of pions relative to the number of electrons in the uncut data sample. 69

47 The relative gain in the number of counts after lowering the EC electron threshold by 30% as a function of electron momentum. 70

48 Electron EC spectra for the e+e- background study 71

49 Positron EC spectra for the e+e- background study 71

50 The fit of the momentum dependence of the positron to electron ratio. 72

51 The proton time vertex, calculated using (45), before the correction for TOF paddle #40. 74

52 The particle coordinate on the scintillator plane Z_{sc} [cm] is plotted versus the proton time vertex for TOF paddle #40. 75

53 The proton timing is plotted as a function of the position on the scintillator plane 76

54 The proton timing is plotted as a function of the position on the scintillator plane 77

55 Electron vertex vs proton vertex. 78

56 The vertex difference between proton and electron. 79

57 Fit of function (47) to the energy loss of the proton going at 100^o scattering angle in the lab. 81

58 Fit of function $\frac{B}{\sin(\theta_p)} + C$ to the parameter obtained from the fit of Fig. 57 for different values of proton scattering angle. 81

59 The proton time vertex distribution for 6 different proton momentum bins . . . 82
60 Uncorrected invariant mass of the proton (left); corrected (right). . . 85
61 Uncorrected position along the length of the target cell, where the electron originated from (left); corrected (right). . . 86
62 The spectral function based on Paris potential (dark line) compared with the spectral function from the Argonne v_{18} potential (light points). 89
63 Drift chamber occupancies for Sectors 1 through 3. . . 93
64 Drift chamber occupancies for Sectors 4 through 6. . . 94
65 Sector 1 drift chamber occupancies for 6 different runs throughout the run period. . . 95
66 Sector 2 drift chamber occupancies for 6 different runs throughout the run period. . . 96
67 Sector 3 drift chamber occupancies for 6 different runs throughout the run period. . . 97
68 Sector 4 drift chamber occupancies for 6 different runs throughout the run period. . . 98
69 Sector 5 drift chamber occupancies for 6 different runs throughout the run period. . . 99
70 Sector 6 drift chamber occupancies for 6 different runs throughout the run period. . . 100
71 Electron time vertex plotted versus paddle number for simulation (left) and data (right). . . 101
72 Electron time vertex plot versus scintillator paddle number for simulation (left) and data (right). . . 102
73 Drift Chamber spatial residuals for run # 31974 (left) and simulation (right). . . 104
74 Electron time vertex for data (left) and simulation (right) (bad scintillator paddles were excluded). . . 105
75 Simulated invariant mass. . . 105
76 Energy deposited in the inner layer of the calorimeter . . . 106
77 Total energy deposited in the calorimeter. . . 107
78 Cherenkov detector spectrum for data (left) and simulation (right). . 108
79 Cherenkov detector spectrum for data (left) and simulation (right). . 109

80 Target vertex for the experimental data. 110
81 Target vertex for the data after empty target subtraction (dashed line) and the simulation (solid line). 110
82 Electron scattering angle in data (black points) and simulation (solid line). 111
83 Electron scattering angle (ratio of data to simulation). 112
84 Scattering angle of the electron: the average ratio of data over simulation for sectors 1 through 4. 113
85 Sector 5 normalized to the average of first 4 sectors. 113
86 Sector 6 normalized to the average of first 4 sectors. 113
87 Electron momentum for data (black points) and simulation (solid line). 114
88 Electron momentum (ratio of data divided by simulation). 115
89 Electron momentum distribution for all 6 sector of the spectrometer combined. Ratio of data to simulation. 116
90 Invariant mass W (the "step" in the distribution is a result of the fiducial cut). 117
91 Same as Fig. 90, with an enhancement of the quasi-elastic region. . . 118
92 Ratio of data over simulation for the invariant mass distribution ($d(e,e')X$ reaction). 119
93 Q^2 distribution of $p(e,e')p$ scattering for data (triangles) and simulation (solid line). 120
94 Ratio of Q^2 distribution of $p(e,e')p$ for data over simulation. 120
95 Q^2 distribution for data (triangles) and simulation (solid line) for $d(e,e')X$ reaction. 120
96 Ratio of Q^2 distribution for data over simulation for $d(e,e')X$ reaction. 120
97 Proton vertex: data before the background subtraction (thin line); simulation (thick line); accidentals (dot-dashed line); empty target (dashed line). 121
98 Proton vertex for data after background subtraction (thin line) and simulation (thick line). 121
99 Proton time vertex: data (solid) and simulation (dot-dashed). 123
100 Proton time vertex after background subtraction for data (solid) compared with simulation (dot-dashed line). 124

101 Proton time vertex plotted as a function of proton position on scintillator plane: data for sectors 1 through 3 is presented on the left panels and simulation on the right. 125

102 Proton time vertex plotted as a function of proton position on scintillator plane: data for sectors 4 through 6 is presented on the left panels and simulation on the right. 126

103 Ratio of simulation divided by data plotted as a function of Z_{SC}. . . 128

104 Ratio of simulation divided by data plotted as a function of Z_{SC} after most of the inefficient regions were removed (breaks in the histograms). 129

105 Proton scattering angle distribution after inefficient regions identified from Z_{SC} plot were removed. 130

106 Cosine of proton angle with respect to the momentum transfer direction for data (black triangles) and simulation (blue solid line). 131

107 Ratio of data to simulation for the cosine of the proton angle with respect to the momentum transfer direction. 131

108 The fit (solid line) of accidentals (dashed line) and simulation smeared with Gaussian (with σ shown in the right upper corner of each plot) overlaid with the data (black triangles). 133

109 Same as Fig. 108, except for proton momenta between 360 and 420 MeV/c; vertical lines indicate the ID cut. 134

110 Cosine of the proton scattering angle with respect to the direction of momentum transfer integrated over all electron kinematics. 144

111 Momentum distribution of the scattered proton for different ranges of scattering angles and invariant mass of the unobserved final state. . . 145

112 $F_{2n}(W^*, Q^2)$ times $P(\vec{p_s})$ versus the cosine of the proton scattering angle with respect to the direction of momentum transfer. 147

113 $F_{2n}(x^*, Q^2)$ times $P(\vec{p_s})$ versus the cosine of the proton scattering angle with respect to the direction of momentum transfer. 148

114 Invariant mass of the unobserved final state W^* potted versus scaling variable x^*. 149

115 $F_{2n}(W^*, Q^2)$ times $P(\vec{p_s})$ versus the cosine of the proton scattering angle with respect to θ_{pq} for two different of Q^2. 150

116 $F_{2n}(W^*, Q^2)$ times $P(\vec{p_s})$ versus $\cos(\theta_{pq})$ for four different values of proton momentum, but for the same value of $W^* = 0.94$ GeV and $Q^2 = 1.8$ GeV^2/c^2. 151

117 $F_{2n}(W^*, Q^2)$ times $P(\vec{p_s})$ versus $\cos(\theta_{pq})$ for four different values of proton momentum, but for the same value of $W^* = 1.5$ GeV and $Q^2 = 1.8$ GeV^2/c^2. 152

118 $F_{2n}(W^*, Q^2)$ times $P(\vec{p_s})$ versus $\cos(\theta_{pq})$ for four different values of proton momentum, but for the same value of $W^* = 2.02$ GeV and $Q^2 = 1.8$ GeV^2/c^2. 153

119 $F_{2n}(W^*, Q^2)$ times $S(\alpha_s, p_T)$ versus α_s for different ranges of the invariant mass W^*, for the upper Q^2 bin $(2.1 - 5.0$ GeV^2/c$^2)$ and p_T between 250 and 350 MeV/c. 155

120 $F_{2n}(W^*, Q^2)$ times $S(\alpha_s, p_T)$ versus α_s for four different values of proton momentum, but for the same value of $W^* = 0.94$ GeV and $Q^2 = 1.8$ GeV^2/c^2. 156

121 $F_{2n}(W^*, Q^2)$ times $S(\alpha_s, p_T)$ versus α_s for four different values of proton momentum, but for the same value of $W^* = 1.5$ GeV and $Q^2 = 1.8$ GeV^2/c^2. 157

122 $F_{2n}(x^*, Q^2)$ times $S(\alpha_s, p_T)$ versus α_s for four different values of proton momentum, but for the same value of $x^* = 0.25$ and $Q^2 = 1.8$ GeV^2/c^2 .158

123 Structure function $F_{2n}(W^*, Q^2)$ versus the invariant mass of the unobserved final state W^* for the lower bin in $Q^2 = 1.8$ Gev^2/c^2. 161

124 Structure function $F_{2n}(W^*, Q^2)$ versus the invariant mass of the unobserved final state W^* for the upper bin in $Q^2 = 2.8$ Gev^2/c^2. . . . 162

125 Structure function $F_{2n}(x^*, Q^2)$ versus the scaling variable x^* for the lower bin in $Q^2 = 1.8$ Gev^2/c^2. 163

126 Structure function $F_{2n}(x^*, Q^2)$ versus the scaling variable x^* for the upper bin in $Q^2 = 2.8$ Gev^2/c^2. 164

127 $F_{2n}(W^*, Q^2)$ times $P(\vec{p_s})$ versus $\cos(\theta_{pq})$ for different ranges of the invariant mass W^*, for lower Q^2 bin (1.2-2.1 GeV^2/c^2) and for the lowest proton momentum bin $(280 - 320$ MeV/c). 174

128 The same as Fig. 127, but for the higher momentum transfer Q^2 bin $(2.1 - 5.0$ GeV^2/c$^2)$. 175

129 The same as Fig. 127, but for the higher proton momentum p_s bin $(320 - 360$ MeV/c). 176

130 The same as Fig. 129, but for the higher momentum transfer Q^2 bin $(2.1 - 5.0$ GeV^2/c^2). 177

131 The same as Fig. 127, but for the higher proton momentum p_s bin $(340 - 420$ MeV/c). 178

132 The same as Fig. 131, but for the higher momentum transfer Q^2 bin $(2.1 - 5.0$ GeV^2/c^2). 179

133 The same as Fig. 127, but for the higher proton momentum p_s bin $(420 - 550$ MeV/c). 180

134 The same as Fig. 133, but for the higher momentum transfer Q^2 bin $(2.1 - 5.0$ GeV^2/c^2). 181

135 The same as Fig. 127, but for the higher proton momentum p_s bin $(550 - 700$ MeV/c). 182

136 The same as Fig. 135, but for the higher momentum transfer Q^2 bin $(2.1 - 5.0$ GeV^2/c^2). 183

137 $F_{2n}(x^*, Q^2)$ times $P(\vec{p_s})$ versus $\cos(\theta_{pq})$ for different ranges of the scaling variable x^*, for the lower Q^2 bin (1.2-2.1 GeV^2/c^2) and for the lowest proton momentum bin $(280 - 320$ MeV/c). 184

138 The same as Fig. 137, but for the higher momentum transfer Q^2 bin $(2.1 - 5.0$ GeV^2/c^2). 185

139 The same as Fig. 137, but for the higher proton momentum p_s bin $(320 - 360$ MeV/c). 186

140 The same as Fig. 139, but for the higher momentum transfer Q^2 bin $(2.1 - 5.0$ GeV^2/c^2). 187

141 The same as Fig. 137, but for the higher proton momentum p_s bin $(360 - 420$ MeV/c). 188

142 The same as Fig. 141, but for the higher momentum transfer Q^2 bin $(2.1 - 5.0$ GeV^2/c^2). 189

143 The same as Fig. 137, but for the higher proton momentum p_s bin $(420 - 550$ MeV/c). 190

144 The same as Fig. 143, but for the higher momentum transfer Q^2 bin $(2.1 - 5.0$ GeV^2/c^2). 191

145 The same as Fig. 137, but for the higher proton momentum p_s bin $(550 - 700$ MeV/c). 192

146 The same as Fig. 145, but for the higher momentum transfer Q^2 bin $(2.1 - 5.0$ GeV^2/c^2). 193

147 $F_{2n}(x^*, Q^2)$ times $S(\alpha_s, p_T)$ versus α_s for different ranges of the scaling variable x^*, for the lower Q^2 bin (1.2-2.1 GeV^2/c^2) and for the lowest proton transverse momentum bin $(150 - 250$ MeV/c). 194

148 The same as Fig. 147, but for the higher momentum transfer Q^2 bin $(2.1 - 5.0$ GeV^2/c^2). 195

149 The same as Fig. 147, but for the higher proton transverse momentum p_T bin $(250 - 350$ MeV/c). 196

150 The same as Fig. 149, but for the higher momentum transfer Q^2 bin $(2.1 - 5.0$ GeV^2/c^2). 197

151 The same as Fig. 147, but for the higher proton transverse momentum p_T bin $(350 - 450$ MeV/c). 198

152 The same as Fig. 151, but for the higher momentum transfer Q^2 bin $(2.1 - 5.0$ GeV^2/c^2). 199

153 The same as Fig. 147, but for the higher proton transverse momentum p_T bin $(450 - 550$ MeV/c). 200

154 The same as Fig. 153, but for the higher momentum transfer Q^2 bin $(2.1 - 5.0$ GeV^2/c^2). 201

155 The same as Fig. 147, but for the higher proton transverse momentum p_T bin $(550 - 650$ MeV/c). 202

156 The same as Fig. 155, but for the higher momentum transfer Q^2 bin $(2.1 - 5.0$ GeV^2/c^2). 203

157 $F_{2n}(W^*, Q^2)$ times $S(\alpha_s, p_T)$ versus α_s for different ranges of the invariant mass W^*, for lower Q^2 bin (1.2-2.1 GeV^2/c^2) and for the lowest proton transverse momentum bin $(150 - 250$ MeV/c). 204

158 The same as Fig. 157, but for the higher proton transverse momentum p_T bin $(250 - 350$ MeV/c). 205

159 The same as Fig. 158, but for the higher momentum transfer Q^2 bin $(2.1 - 5.0$ GeV^2/c^2). 206

160 The same as Fig. 157, but for the higher proton transverse momentum p_T bin $(350 - 450$ MeV/c). 207

161 The same as Fig. 160, but for the higher momentum transfer Q^2 bin $(2.1 - 5.0\ \mathrm{GeV^2/c^2})$. 208
162 The same as Fig. 157, but for the higher proton transverse momentum p_T bin $(450 - 550\ \mathrm{MeV/c})$. 209
163 The same as Fig. 162, but for the higher momentum transfer Q^2 bin $(2.1 - 5.0\ \mathrm{GeV^2/c^2})$. 210
164 The same as Fig. 157, but for the higher proton transverse momentum p_T bin $(550 - 650\ \mathrm{MeV/c})$. 211
165 The same as Fig. 164, but for the higher momentum transfer Q^2 bin $(2.1 - 5.0\ \mathrm{GeV^2/c^2})$. 212

LIST OF TABLES

Page

I E6A trigger setup. 48
II E6A accumulated statistics 49
III Accumulated charge of beam electrons over different run ranges for 3 categories of runs, sorted according to their projected quality. 52
IV Ratio of the total events to the events within the proton time quality cut for data and simulation. 122
V Scaling factor for different ranges in momentum introduced for two-step accidentals, defined as an on-time proton with $\Delta Z > 1.4$ cm. . . 132
VI The fraction of events surviving the vertex difference cut in data and simulation. 135
VII Estimated total fraction of accidentals in a given momentum bin. . . 135
VIII Constant correction factors applied to the data and systematic errors associated with various sources of uncertainty. 138
IX Bin division for the first set of histograms. 139
X Bin division for the second set of histograms. 139
XI Bin division for the third set of histograms. 139
XII Bin division for the fourth set of histograms. 140
XIII Bin division for the fifth set of histograms. 140
XIV Bin division for the sixth set of histograms. 140

CHAPTER 1

INTRODUCTION

Any physical process in nature is governed by four fundamental forces known to date: gravitational, electromagnetic, weak and strong. The gravitational force is the weakest and becomes relevant on the scale of celestial objects. The electromagnetic force manifests itself in the interaction of electrically charged stationary or moving objects and is the best understood of the four. Atomic physics is formulated on the foundation of electromagnetic theory. Strong and weak forces act on the subatomic level in the atomic nucleus.

In the standard model of particle physics all of the particles that undergo strong interaction are thought to be composed of several "flavors" of point-like, indivisible building blocks, known as quarks. In addition to an electric charge of $\pm 1/3$ or $\pm 2/3$, quarks carry a color charge that can be red, green or blue. Quarks are postulated to be confined within hadrons (protons, neutrons, pions, etc.) by requiring all observable objects to be colorless. This is based on the fact that free quarks were never observed experimentally.

Decades before the evidence of nucleon (protons and neutrons) substructure was discovered, numerous models were developed that successfully described most nuclear phenomena only in terms of nucleons, their excited states and strong force mediators - mesons. Nucleons and mesons are often called the "conventional" degrees of freedom of nuclear physics. The true theory of strong interactions, quantum chromodynamics (QCD), describes physical processes in terms of quarks (also frequently referred to as partons). The strong force in QCD is carried by another type of parton, called a gluon.

QCD is very successful in describing the interaction of quarks at short distances, where perturbative methods, similar to those of quantum electrodynamics (QED) in atomic physics, are applicable. In QED, due to the effects of charge screening, the electromagnetic force grows weaker as the distance between charged particles increases. For the strong force the opposite is observed - a phenomenon dubbed "color charge antiscreening". The further one quark moves away from the other, the stronger is the attraction it experiences. As a result the same perturbative methods cannot

This Dissertation follows the form of *The Physical Review, C* be applied anymore to solve QCD at the length scales of a nucleus. The present difficulty to make rigorous predictions based on QCD at low energies (corresponding to large distances between the quarks) leaves us no choice but to continue to employ nuclear theories based on “effective” degrees of freedom - nucleons and mesons. In an attempt to resolve this discontinuity of theories, the focus of modern nuclear physics is on the intermediate region where QCD is not yet solvable, but the quark-gluon substructure of the nucleons cannot be ignored anymore and has to be taken into account in the nuclear models.

Protons and neutrons bound inside a nucleus are in constant motion. Quantum mechanically this can be described in terms of a momentum wave function $\psi(\vec{p})$, from which a probability $|\psi(\vec{p})|^2$ of finding a nucleon (within a nucleus) with a certain momentum $\vec{p}$ can be calculated. In the simplest models of the lightest two-nucleon bound state (deuterium), the wave function is obtained from the solution of the non-relativistic Schrodinger equation. A nucleon-nucleon potential needs to be constructed to calculate the nuclear wave function. Through Fourier transformation one can translate the spatial wave function into a momentum one. Due to the Heisenberg uncertainty principle, large momenta of the nucleons inside of the nucleus can be associated with small internucleon spatial separation. The root-mean-square charge radius of the deuterium nucleus is 2.130 fm, while the radius of the unbound proton is 0.862 fm. In all of the models of the deuterium nucleus, the nucleons have mostly low momenta and therefore are relatively far apart.

However, even in the wave functions obtained from conservative models of the nucleon-nucleon potential there is a probability for the nucleons to have momentum high enough so that proton and neutron can come very close together or even overlap. In such high density configurations the shape and size of the nucleons as well as the quark distribution within a nucleon can become modified. It is also possible that under these conditions the nucleons start to exchange quarks with each other or even merge into a single “six-quark bag”. The quark-gluon degrees of freedom thus might play a direct role in modification of the nucleon structure in high density nuclear configurations. The analysis presented here is aimed at advancing the understanding of high density, high momentum nuclear matter.

To study high density configurations, we can use electron scattering. Electrons have been used as probes of matter by scientists in different fields for many decades. The interaction of the electron with matter is well understood in the framework of

QED. In nuclear physics, accelerated electrons are used to study the response of the nuclei to the transfered energy and momentum, that can be deduced if the scattered electron is measured. At relatively low energy transfer (elastic scattering) the shape and size of the nucleus can be studied. At higher transfered energies and momenta, information about the internal structure of the nucleus (resonance excitations) and quark distribution (deep inelastic scattering) can be obtained. To study high density nuclear configurations, the electron has to scatter from a high-momentum nucleon within a nucleus. In the case of scattering from a deuteron this can be easily verified by taking advantage of the inherently simple structure of the two-nucleon system. If all the momentum and energy is transfered to the neutron, the proton is a spectator to the reaction and recoils with its initial momentum. Assuming that the detected proton was indeed a spectator to the reaction, the initial momentum of the struck neutron can be obtained using momentum conservation law. Thus the neutron is "tagged" by the backward going spectator proton. Measurement of a high-momentum recoiling backward proton allows us to infer that the electron interacted with a high-momentum neutron in deuterium.

The scattered electron was detected in coincidence with the backward proton in the CEBAF Large Acceptance Spectrometer (CLAS), installed in Jefferson Laboratory's Hall B. The spectrometer detects almost all of the charged particles produced by the electron interaction with the target nucleus. The detector has almost full angular coverage; however there are certain limitations on the particle momentum and scattering angle. If at the time of interaction the deuterium wave function is in its high-momentum configuration, the recoiling spectator has a high enough momentum and can be detected by the spectrometer. The protons detected in the forward region can be produced in a number of processes such as direct proton knock-out or target fragmentation. The protons detected in the backward region of the detector are mostly recoiling spectators. Therefore, a data sample where a backward proton is detected in coincidence with the forward electron, was selected and analyzed.

In Chapter 1 a basic formalism of electron scattering is given, followed by the discussion of the deuterium nucleus models and theories describing the electron scattering from the bound nucleon. The theoretical models of final state interactions are presented. The overview of the existing experimental data, relevant for the discussion, and statement of the present analysis goals is followed by Chapter 2 and the overview of the experimental setup. In Chapter 3 all steps of the data analysis and related issues are discussed in fine details. The final analysis results and their discussion are presented in Chapter 4. The complete set of distributions that contain analysis results, can be found in Appendix A.

CHAPTER 2

PHYSICS OVERVIEW

2.1 ELECTRON SCATTERING FORMALISM

The electron, an elementary point particle of spin 1/2 and negative charge, is a perfect probe to study the properties of the nucleus. Its interaction with matter is well studied and understood. The theory of electromagnetic interactions of particles is called quantum electrodynamics (QED). The interaction is also weak enough to treat it using the perturbation theory. In QED, the scattering of an electron from a nucleus, in the first order (Born approximation), is described in terms of an exchange of a single virtual photon. A virtual photon, just like a real one, has spin 1 and both leptonic and baryonic numbers equal to 0. However, unlike a real photon, it can have mass and longitudinal polarization – that is what makes it virtual. A virtual photon can be thought of as a quantum of the electromagnetic field. Diagrammatically the process is usually written as it is shown in Fig. 1. As the wavelength of the virtual photon decreases (corresponding to the increasing energy of the incident electron) more fine details of the target nucleus can be resolved. In the case of relatively low energy transfer, the virtual photon simply knocks out a nucleon as a whole. This mechanism is known as quasi-elastic scattering. Inelastic scattering occurs at energies high enough for the virtual photon to excite the nucleon into higher energy state resonances or completely disintegrate it. The momentum of the virtual photon in case of deep inelastic scattering (DIS) is high enough that it can now resolve quarks in the interior of the nucleon.

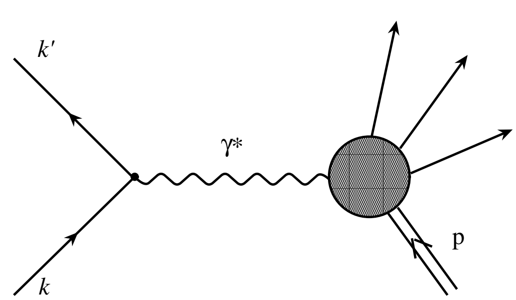

FIG. 1: Electron scattering from a nucleus.

One of the most important quantities extracted in a scattering experiments is the cross section σ, which is a measure of the probability of interaction between the incident electron and the target nucleon. The total cross section is defined as:

$$\sigma_{tot} = \frac{number\, of\, reactions\, per\, unit\, time}{number\, of\, beam\, electrons\, per\, unit\, time\, \times\, number\, of\, target\, nucleons\, per\, unit\, area} \quad (1)$$

When the measurement is limited to a certain kinematic bin, the cross section is called partial and a phase space $\Delta\Phi$ factor appears on the right hand side of the expression (1). When the kinematic bin becomes very small, the ratio $\Delta\sigma/\Delta\Phi$ approaches a finite value and is called a differential cross section.

Theoretically, the number of reactions per unit time in the formula (1) can be calculated if one knows the interaction potential and therefore can write down a Hamiltonian for the interaction $\mathcal{H}_{int}$. The rate of interaction is proportional to the absolute square of the matrix element:

$$\mathcal{M}_{fi} =< \psi_i|\mathcal{H}_{int}|\psi_f >$$

where ψ_i and ψ_f are wave functions of the initial and final state of the system. Then, according to Fermi's Golden Rule, the partial cross section for inclusive lepton scattering can be written as:

$$\Delta\sigma = \frac{2\pi}{j_{in}}|\mathcal{M}_{fi}|^2\Delta\Phi \quad (2)$$

where j_{in} is the beam current density.

For electron scattering from another point particle (for example, a muon) the interaction potential is well known and can be found from the solution of Maxwell's equation:

$$\bigtriangledown^2 A^\mu = j^\mu \quad \rightarrow \quad A^\mu = \frac{1}{Q^2}j^\mu$$

where $Q^2 = -q^\mu q_\mu = 4EE'\mathrm{sin}(\theta_{el}/2)$ and $q^\mu = (E-E', \vec{k}-\vec{k'})$ is the momentum transfer 4-vector $k^\mu = (E, \vec{k})$ and $k'^\mu = (E', \vec{k'})$ are the 4-vectors of the incident and scattered electron and j^μ is the electron (4-vector) current density that in terms of Dirac spinors u, Dirac γ-matrices and electron charge e can be expressed as: $j^\mu = -e\bar{u}\gamma^\mu u$. The transition matrix element can be rewritten as:

$$\mathcal{M}_{fi} = j^{\mu}_{(1)} \frac{1}{Q^2} j^{(2)}_{\mu} \tag{3}$$

where $j^{\mu}_{(1)}$ is the current density of the incident electron beam and $j^{\mu}_{(2)}$ is the current density of the target point particle.

For the scattering of a hypothetical spinless electron on a spinless and infinitely heavy point particle, the transition matrix can be calculated and the differential cross section takes the form:

$$\frac{\mathrm{d}\sigma}{\mathrm{d}\Omega} = \frac{4e^2\alpha^2_{EM}E'^2}{Q^4}$$

where $\alpha_{EM} = \frac{1}{137}$ is the coupling constant of the electromagnetic interaction (also known as the fine structure constant) and e is the electron charge.

For the scattering of a spin-1/2 unpolarized electron on an unpolarized point particle with non-zero spin, the transition matrix element has to be averaged over all spin states of the beam and the target:

$$< |\mathcal{M}_{fi}|^2 >= \frac{1}{(2s_{el}+1)(2s_{tgt}+1)} \sum_{\substack{all\ spin \\ states}} |\mathcal{M}_{fi}|^2$$

The factor in front of the sum accounts for the degeneracy of the spin states; here s_{el} is the spin of the beam particle (in our case an electron) and s_{tgt} is the spin of the target particle. As a result of the averaging over spin of the beam particle an extra factor of $[1 - \beta^2 \sin^2(\theta_{el}/2)]$ appears in the expression for the cross section ($\beta = v_{el}/c$ with c being the speed of light), another factor of $(1 + 2\nu^2/Q^2 \tan^2(\theta_{\mathrm{el}}/2))$ comes from averaging over spins of the target particle (where $\nu = E - E'$ is the energy transfer). The recoil of the target results in an extra factor of E'/E and the final differential cross section for lepton-lepton scattering takes the form (see S.E. Kuhn HUGS lecture [5]):

$$\frac{\mathrm{d}\sigma}{\mathrm{d}\Omega} = \frac{4e^2\alpha^2_{EM}E'^2}{Q^4}\frac{E'}{E}\left(1 - \beta^2\sin^2(\theta_{el}/2)\right)\left(1 + \frac{2\nu^2}{Q^2}\tan^2(\theta_{\mathrm{el}}/2)\right) \tag{4}$$

For high energy electrons the factor $[1 - \beta^2 \sin^2(\theta_{el}/2)]$ can be approximated with $\cos^2(\theta_{\mathrm{el}}/2)$ and the cross section (4) can be rewritten as:

$$\frac{\mathrm{d}\sigma}{\mathrm{d}\Omega}=\frac{e^2\alpha_{EM}^2}{4E^2\sin^4(\theta_{\mathrm{el}}/2)}\frac{E'}{E}\left(\cos^2(\theta_{el}/2)+\frac{Q^2}{2M^2}\sin^2(\theta_{\mathrm{el}}/2)\right) \tag{5}$$

2.2 NUCLEON STRUCTURE

The above formalism was derived using the assumption of structureless target particle. For the electron scattering from the proton, the target cannot be assumed to be structureless and therefore the target current density $j^{\mu}_{(2)}$ appearing in equation (3) cannot be exactly evaluated. However, one can guess the general form of the hadronic current density (J^{μ}) using the consideration that J^{μ} has to be a Lorentz 4-vector. The form of J^{μ} should be the most general that is possible to construct out of 4-vectors p, $p'$and q (as it was shown by Halzen and Martin [3]):

$$J^{\mu}=e\bar{u}\left[F_1(Q^2)\gamma^{\mu}+\frac{\kappa}{2M}F_2(Q^2)i\sigma^{\mu\nu}q_{\nu}\right]u \tag{6}$$

where F_1 and F_2 are independent form factors and κ is anomalous magnetic moment. At low momentum transfer ($Q^2\to 0$), when the virtual photon does not resolve the target nucleon structure, the cross-section should be that of a particle with charge e and magnetic moment $(1+\kappa)e/2M$. Hence in this limit $F_1(0)=1$ and $F_2(0)=1$ for the proton and for the neutron $F_1(0)=0$ and $F_2(0)=1$.

Using this form of hadronic current the electron-proton cross section can be calculated to give:

$$\frac{\mathrm{d}\sigma}{\mathrm{d}\Omega}=\frac{e^2\alpha_{EM}^2}{4E^2\sin^4(\theta_{\mathrm{el}}/2)}\frac{E'}{E}\left(\left[F_1^2+\frac{\kappa^2Q^2}{4M^2}F_2^2\right]\cos^2(\theta_{el}/2)+\frac{Q^2}{2M^2}\left[F_1+\kappa F_2\right]^2\sin^2(\theta_{\mathrm{el}}/2)\right) \tag{7}$$

For convenience the linear combination of form factors is commonly used:

$$\begin{aligned} G_E &= F_1-\tfrac{\kappa Q^2}{4M^2}F_2 \\ G_M &= F_1+\kappa F_2 \end{aligned} \tag{8}$$

The cross section (9) can be expressed using the change of variables (8) as:

$$\frac{\mathrm{d}\sigma}{\mathrm{d}\Omega}=\frac{e^2\alpha_{EM}^2}{4E^2\sin^4(\theta_{\mathrm{el}}/2)}\frac{E'}{E}\left(\left[\frac{G_E^2+\tau G_M^2}{1+\tau}\right]\cos^2(\theta_{el}/2)+2\tau G_M^2\sin^2(\theta_{\mathrm{el}}/2)\right) \tag{9}$$

where $\tau = Q^2/4M^2$.

With an increase in momentum and energy transfer, the nucleon can be excited into one of its resonances. Since the final state cannot be described with the same Dirac spinor u as the initial one anymore, the expression for the hadronic current (6) ceases to work. Instead, a hadronic tensor $W^{\mu\nu}$ is introduced and the cross section for electron-nucleon scattering becomes:

$$\mathrm{d}\sigma \sim L^e_{\mu\nu} W^{\mu\nu} \tag{10}$$

where $L^e_{\mu\nu}$ is the well-known leptonic tensor:

$$L_e^{\mu\nu} = \frac{1}{2}\sum_{spins}[\bar{u}\gamma^\mu u][\bar{u}\gamma^\nu u]^* = \frac{1}{2}\mathrm{Tr}((\not{k}' + m)\gamma^\mu(\not{k} + m)\gamma^\nu) \tag{11}$$

where m is the mass of the electron.

The most general form of the hadronic tensor can be expressed in terms of the initial momentum 4-vectors of the system:

$$W^{\mu\nu} = -W_1 g^{\mu\nu} + \frac{W_2}{M^2}p^\mu p^\nu + \frac{W_4}{M^2}q^\mu q^\nu + \frac{W_5}{M^2}(p^\mu q^\nu + q^\mu p^\nu) \tag{12}$$

where $p^\mu = (M, 0, 0, 0)$ is a momentum 4-vector of a free nucleon. This can be further simplified by use of current conservation law to give:

Here W_1 and W_2 are now inelastic structure functions, that depend both on Q^2 and energy transfer $\nu = E - E'$. The cross section then becomes:

$$\frac{\mathrm{d}^2\sigma}{\mathrm{d}\Omega dE'} = \frac{4E'^2\alpha^2_{EM}}{Q^4}\left(W_2(Q^2,\nu)\mathrm{cos}^2(\theta_{el}/2) + 2W_1(Q^2,\nu)\mathrm{sin}^2(\theta_{\mathrm{el}}/2)\right) \tag{13}$$

It is also convenient to introduce a new kinematic variable, the invariant mass of the final hadronic state, defined as:

$$W^2 = (p^\mu + q^\mu)^2 \tag{14}$$

For the simple case of electron scattering from a free nucleon, the invariant mass is $W^2 = M^2 + 2M\nu - Q^2$. In the case of elastic scattering, the invariant mass is equal to the mass of the nucleon, $W^2 = M^2$, therefore $Q^2 = 2M\nu$. In the resonance region W is the mass of the excited resonance, with resonances appearing in the cross section as peaks with finite width at a given W (for example, the Δ_{1232} resonance centered at 1232 MeV, the S_{11}/D_{13} resonances around 1500 MeV, the F_{15}/D_{13} resonances around 1700 MeV).

As the invariant mass W increases, the nucleon completely breaks up into numerous debris. A series of experiments at the Stanford Linear Accelerator (SLAC) at large momentum and energy transfer showed that the nucleon is made of hard point-like objects [4]. The cross section for the electron scattering from the proton target at large angles was found by Panovsky [6] to be much greater than expected. The scaling of the structure functions W_1 and νW_2 was also observed by Bloom and Breidenbach [9, 10]. Starting from current algebra, Bjorken [7] showed that in the limit of $\nu, Q^2 \to \infty$ (known as Bjorken limit) and fixed Q^2/ν the structure functions should exhibit a scaling behavior.

To understand Bjorken scaling the intuitive picture of the quark parton model (QPM) was develop by Feynman [8]. In QPM, the nucleon is viewed as a dynamic system of point-like particles, each carrying a different fraction of the nucleon momentum x. Since in this picture an electron is interacting with a Dirac particle, the cross section should have the form of equation (5), which describes the scattering of a point particle from another point particle. For the inelastic cross section (13) to take this form, the inelastic structure functions should be:

$$\begin{aligned} 2W_1 &= \tfrac{Q^2}{2m^2}\delta\left(\nu - \tfrac{Q^2}{2m}\right) \\ W_2 &= \delta\left(\nu - \tfrac{Q^2}{2m}\right) \end{aligned} \tag{15}$$

where m is the mass of the point object within the nucleon with which the virtual photon interacts, and the δ-function ensures energy conservation ($W^2 = m^2 \quad \rightarrow Q^2 = 2m\nu$). However, since the quarks are not at rest within the nucleon, there is a smearing of the δ-function.

An intuitive picture emerges in the frame where the virtual photon, interacting with a quark, transfers no energy (Breit frame) and its momentum 4-vector is $q^\mu = (0, 0, 0, Q)$. Using a Lorentz boost with $\gamma = |\mathbf{q}|/Q$ and $\gamma\beta = \nu/Q$ the momentum 4-vector of the nucleon, at rest in the lab frame, can be transformed into the Breit frame as $p^\mu = (\frac{M|\mathbf{q}|}{Q}, 0, 0, -\frac{M\nu}{Q})$. In the Bjorken limit, the nucleon does not have transverse momentum ($p_\perp = 0$) and its longitudinal momentum is infinitely large $p_{||} \to \infty$. The frame of reference in which $p_{||} \to \infty$ is called the "infinite momentum frame" (IMF) and in the Bjorken limit it coincides with the Breit frame. In IMF, due to the effects of time dilation, the quarks within a nucleon can be approximated to be quasi-free on the scale of interaction time. If the quark on which the scattering takes place, has initial longitudinal momentum p_i^q in the Breit frame, then after the interaction its momentum is $p_f^q = p_i^q + Q = -p_i^q$ (since no energy is transfered, the absolute value of the momentum must stay unchanged). The initial longitudinal momentum of the quark can thus be expressed as $p_i^q = \frac{Q}{2}$. Therefore the virtual photon can only couple to the quark that has just the right longitudinal momentum [5]. The fraction of the nucleon momentum carried by the quark can now be evaluated:

$$x = \frac{-p_i^q}{p_{||}} = \frac{Q}{2} \cdot \frac{Q}{M\nu} = \frac{Q^2}{2M\nu} \tag{16}$$

which is the Bjorken scaling variable.

In analogy with a nuclear spectral function, a momentum distribution of quarks and gluons (parton distribution) within a nucleon can be introduced: $f_i(x)$. This function gives a probability of finding a parton of type "i" within a nucleon with momentum fraction x. The momenta of all the partons should add up to give the momentum of a nucleon, therefore the following normalization condition should stand:

$$\sum_i \int dx\, x\, f_i(x) = 1$$

here i runs over all possible partons.

Using $f_i(x)$, the cross section for deep inelastic scattering can be written as:

$$\frac{\mathrm{d}^2\sigma}{\mathrm{d}\Omega dE'} = \frac{4E'^2\alpha_{EM}^2}{Q^4}\left(\frac{x}{\nu}e_i^2 f_i(x)\cos^2(\theta_{el}/2) + \frac{1}{M}e_i^2 f_i(x)\sin^2(\theta_{\mathrm{el}}/2)\right)$$

The cross section should also be summed over all quark flavors i:

$$\frac{\mathrm{d}^2\sigma}{\mathrm{d}\Omega \mathrm{d}E'} = \frac{4E'^2\alpha_{EM}^2}{Q^4}\left(\frac{F_2(x)}{\nu}\cos^2(\theta_{el}/2) + \frac{F_1(x)}{M}\sin^2(\theta_{\mathrm{el}}/2)\right) \tag{17}$$

where the structure functions F_1 and F_2 are given (in the QPM picture) by:

$$F_2(x) = x \sum_i e_i^2 f_i(x) \tag{18}$$

$$F_1(x) = \frac{1}{2} \sum_i e_i^2 f_i(x) \tag{19}$$

These structure functions are related to the previously introduced structure functions

W_1 and W_2 through the expressions:

$$MW_1(x, Q^2) = F_1(x)$$
$$\nu W_2(x, Q^2) = F_2(x)$$

The two DIS structure function are connected by Callan-Gross relation [11]:

$$F_2(x) = 2xF_1(x) \tag{20}$$

The cross section (17) can be rewritten in relativistically invariant form:

$$\frac{d^2\sigma}{dxdQ^2} = \frac{4\pi\alpha_{EM}^2}{Q^4}\left[y^2F_1(x) + \frac{1}{x}\left(1 - y - \frac{M^2x^2y^2}{Q^2}\right)F_2(x)\right] \tag{21}$$

where $y = \frac{q^\mu p_\mu}{k^\mu p_\mu}$ (p_μ is nucleon momentum 4-vector) with $y = \frac{\nu}{E}$ in the laboratory frame. The scaling variable x, used in (54), can be written down in a manifestly covariant form as $x = \frac{Q^2}{2p^\mu q_\mu}$.

2.3 NUCLEAR MODELS OF DEUTERIUM

The deuteron is a very loosely bound nucleus, compared to the heavier nuclei. Due to a low binding energy of only 2.2246 MeV, the deuteron has no excited states. The parity of the deuteron is positive. In a picture that includes only nucleon degrees of freedom, the deuteron wave function can be written as a product of the wave function of the neutron, the wave function of the proton and the wave function for the relative motion between the neutron and the proton. Independently of the parity of the intrinsic wave functions of the nucleons, their product will always give the same result under reflection of the coordinate system through the origin. Therefore, for the deuteron wave function to have a positive parity, the orbital wave function of the relative motion of the two bound nucleons has to have a positive parity. The spin of the ground state of the deuteron is $J = 1$, where $\mathbf{J} = \mathbf{L} + \mathbf{S}$. The sum of the intrinsic spins of the nucleons, $\mathbf{S}$, can take values of 0 or 1. For the orbital part of the wave function to have positive parity, the orbital angular momentum L should have an even value. The states with $S = 0$ and L greater then 2 are therefore excluded. Remaining are two existing parts of the deuterium wave function with angular momenta $L = 0$ and $L = 2$, that are usually referred to as S- and D-wave. Using formalism of quantum mechanics the deuterium wave function can be written as:

$$|\psi_d >= a|S > +b|D >$$

In a basic non-relativistic nuclear model, the wave function of the deuteron is calculated using the Hamiltonian (see Van Orden and Garcon [37]):

$$H = T_1 + T_2 + V$$

where T_i is the kinetic energy operator of nucleon i (proton or neutron) and V is the nucleon-nucleon potential. The mixing of S and D states in deuterium wave function implies that off-diagonal elements of the Hamiltonian are non-vanishing:

$$H_{12} = H_{21} =< S|H|D >\neq 0$$

Since the nucleon kinetic energy operators T_1 and T_2 give only diagonal matrix elements (H_{11} and H_{22}), the mixing should be included in a nucleon-nucleon potential. An appropriate choice is an operator formed by the scalar product of a second-rank operator in intrinsic spin space (σ) and a similar one in coordinate space ($\mathbf{r}$):

$$S_{12} = \frac{3}{r^2}(\sigma_\mathbf{1} \cdot \mathbf{r})(\sigma_\mathbf{2} \cdot \mathbf{r}) - \sigma_\mathbf{1} \cdot \sigma_\mathbf{2}$$

where indices refer to one of the two nucleons (see Wong [25]). This operator is know as a tensor operator.

Using symmetry arguments, the general form of the nucleon-nucleon potential can be derived. The nuclear potential has to possess isospin, translational and Galilean invariances. It should also remain unchanged under time reversal, permutation between the two nucleons, space rotation and reflection. In terms of independent variables, the potential can only be a function of spin ($\sigma_1$and σ_2), isospin ($\tau_1$and τ_2), momentum (p) and space (r) operators. From the considerations above, the following form was obtained by Okubo and Marshak [26]:

$$
\begin{aligned}
V(r, \sigma_1, \sigma_2, \tau_1, \tau_2) = V_0(r) + V_\sigma(r)\sigma_1 \cdot \sigma_2 + V_\tau(r)\tau_1 \cdot \tau_2 + V_{\sigma\tau}(r)(\sigma_1 \cdot \sigma_2)(\tau_1 \cdot \tau_2) \\
+V_{LS}(r) L \cdot S + V_{LS\tau}(r)(L \cdot S)(\tau_1 \cdot \tau_2) \\
+V_T(r) S_{12} + V_{T\tau}(r) S_{12}\tau_1 \cdot \tau_2 \\
+V_Q(r) Q_{12} + V_{Q\tau}(r) Q_{12}\tau_1 \cdot \tau_2 \\
+V_{PP}(r)(\sigma_1 \cdot p)(\sigma_2 \cdot p) + V_{PP\tau}(r)(\sigma_1 \cdot p)(\sigma_2 \cdot p)(\tau_1 \cdot \tau_2)
\end{aligned}
\tag{22}
$$

where quadratic spin-orbit operator was introduced:

$$
Q_{12} = \frac{1}{2}\left\{(\sigma_1 \cdot L)(\sigma_2 \cdot L) + (\sigma_2 \cdot L)(\sigma_1 \cdot L)\right\}
$$

The nuclear potential ideally should be derived in QCD from first principles, however, at present time, due to inability of QCD to describe a long-range quark interaction, it can only be determined from the fit to the experimental data.

In 1934, it was proposed by Yukawa that the nucleon-nucleon strong interaction can be described in terms of the exchange of mesons, in analogy with electromagnetic interaction where the photon is exchanged. The solution of the Klein-Gordon equation gives the following radial dependence for the potential in the one-meson exchange approximation:

$$
\phi(\mathbf{r}) = \frac{g}{4\pi r} e^{-mr} \tag{23}
$$

where g is the strength of the source and m is the mass of the exchanged boson.

The strength of the nucleon-nucleon potential at different distances was tested experimentally using phase-shift analysis of the nucleon-nucleon scattering data (Fig. 2). The potential was found to have a very strong repulsive region at distances less than 1 fm, commonly called the “hard core”. The Yukawa one-meson exchange potential (23) describes the experimental data well in the region of $r > 2$ fm when the exchange particle is a pion ($m_\pi \approx 140$ MeV). In the intermediate region (1 fm $< r <$ 2 fm), the nuclear forces can be modeled by two-pion plus heavier meson exchange. The hard core region of $r < 1$ fm is thought to be due to a combination of multipion exchanges, heavy meson exchanges, and QCD effects.

Many parameterizations of the nucleon-nucleon potential have been developed over the years and successfully used to get an exact wave function for a number of few-body nuclei [27]. The most common potentials used include Reid-SC [29], Paris

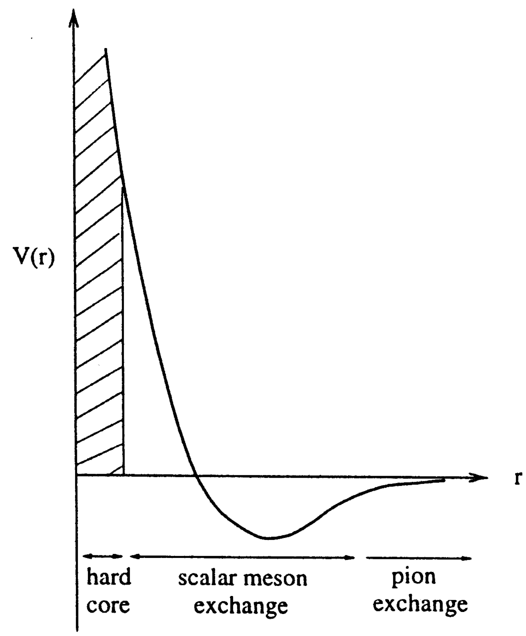

FIG. 2: Schematic diagram showing different parts of nucleon-nucleon potential. The shaded area is the hard core with a radius of about 0.4 fm [25].

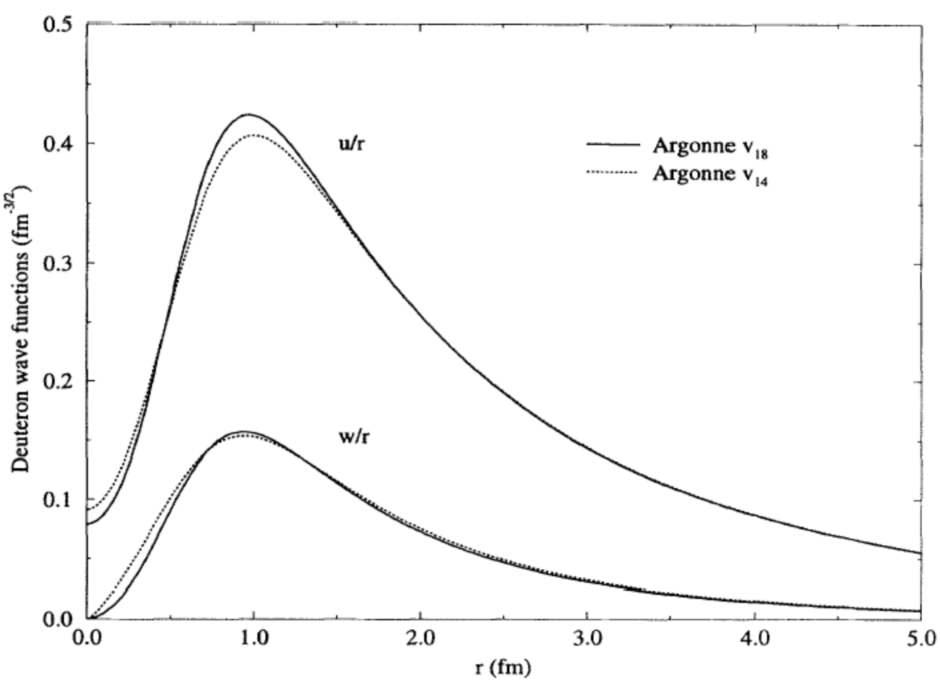

FIG. 3: The deuteron S- and D-wave function components divided by r [63].

[57], Bonn [30], CD-Bonn [31], Nijmegen, Reid93 [31], and Argonne v_{18} [63]. So far reliable calculations have been performed for the nuclei with the maximum number of nucleons up to $A = 12$. The long range of the nucleon-nucleon interaction is well fitted with a one-pion exchange. Hence, the models of the nucleon-nucleon potential are in good agreement with each other at long distances, corresponding to the low momentum part of the wave function ($p < 250$ MeV/c). The nuclear potential at short and intermediate distances, that correspond to the high-momentum part of the wave function, is not understood as well as the long-range part. Depending on the model, one-meson, two-meson as well as a number of phenomenological approaches are employed here. For example, the Paris potential uses single ω exchange with two-pion exchange contributions at the intermediate nucleon-nucleon separations. At short range, phenomenological terms are introduced that are determined by fitting to the data. The Bonn group included one-boson exchange terms, several types of two-meson exchanges (2π, $\pi\rho$, $\pi\omega$), exchange of the effective scalar σ meson and three-pion exchange. A number of interactions where the meson couples to an excited nucleon state (Δ) were also considered. The Argonne potential is parameterized as a sum of two-pion exchange functions at intermediate range plus Woods-Saxon functions (24) at short range:

$$\phi(r) = S^P \left\{ 1 + \exp\left(\frac{r - R}{a} \right) \right\}^{-1} \tag{24}$$

where $R = 0.5$ fm, $a = 0.2$ fm and S^P is a fit parameter. The magnitude of the two-pion exchange terms as well as the radial dependence of Woods-Saxon terms are adjusted to fit the data. The Nijmegen, Argonne, and Bonn potentials were recently fitted separately to np and pp scattering data, which required them to contain charge-symmetry-breaking terms. An example of the deuterium wave function calculated using the Argonne potential is shown in Fig. 3.

2.4 NUCLEONS IN A NUCLEAR MEDIUM

Energy conservation, applied to the deuterium nucleus, requires that the total energy of the proton and neutron, bound within a deuteron, equals the mass of the deuterium nucleus:

$$E_p + E_n = M_d$$

At the same time, the mass of the deuteron is less than the mass of a free proton plus the mass of a free neutron $M_d = M_p + M_n - 2.2246$ MeV. Therefore, both bound neutron and proton can not be on the mass shell at the same time. In the "instant form" dynamics, one of the nucleons is assumed to be on-shell, while the other one is off-shell and its off-shell energy is $E_n^* = M_d - \sqrt{M_p^2 + p_p^2}$. The interaction of the off-shell nucleons is usually built into the nuclear potentials. The determination of free parameters, in these potentials, is done by fitting to free nucleon-nucleon scattering data. Therefore, uncertainty remains in whether the off-shell effects are properly reflected in these models.

The description of electron scattering from an off-shell bound nucleon is another controversial area of modern nuclear physics. One of the possible approaches here is to adopt the light-front (or light-cone) quantization method that became a standard tool in quantum field and string theories [60]. In these dynamics, $x_- = (x_0 - x_3)/\sqrt{2}$ plays the role of time and $x_+ = (x_0 + x_3)/\sqrt{2}$ is a coordinate (here x_3 is in the direction of quantization). The momenta of the particles take the form $p_\pm = (p_0 \pm p_3)/\sqrt{2}$. The most important consequence of light-front quantization is that the relation between energy and momentum of a free particle is given by:

$$p_\mu p^\mu = M^2 = p_+ p_- - p_T^2 \quad \rightarrow \quad p_- = \frac{p_T^2 + M^2}{p_+} \tag{25}$$

a relativistic formula for the kinetic energy which does not contain a square root operator [61]. This feature allows the separation of center of mass and relative coordinates, so that computed wave functions are frame independent. Another variable introduced in light-cone dynamics is the light-cone fraction of the nucleon, defined as:

$$\alpha = A \cdot \frac{p_+}{P_+}$$

where A is the number of the nucleons within a nucleus, p_+ is the light-cone momentum of the nucleon and P_+ is the light-cone momentum of the nucleus. In a specific case of interest, where the proton is a spectator and recoils in a backward direction (relative to the virtual photon $\hat{q}$), the quantization is chosen to be opposite to the direction of the momentum transfer $-\hat{q}$ and the light-cone fraction of the spectator proton takes the form:

$$\alpha_S = \frac{E_S - p_S^{||}}{M}$$

where $p_S^\mu = (E_S, \mathbf{p_S^T}, p_S^{||})$ is the spectator proton momentum 4-vector. The component $p_S^{||}$ of the proton momentum is in the direction of the momentum transfer $\hat{q}$. The components of the proton momentum $\mathbf{p_S^T}$ is transverse to the q vector.

In the light-cone dynamics framework, a non-relativistic deuterium wave function can be rescaled to account for relativistic effects at high momenta [62]:

$$|\psi_{LC}(\alpha_N, \mathbf{p_T})|^2 d\alpha_N d^2p_T = |\psi_{NR}(|\mathbf{k}|^2)|^2 d^3k$$

$$\alpha_N = 1 - \frac{k_{||}}{\sqrt{M^2+k^2}} = 2 - \alpha_S \qquad \mathbf{p_T} = \mathbf{k_T} \qquad k = \sqrt{\frac{M^2+p_T^2}{\alpha_S(2-\alpha_S)} - M^2}$$

where α_N is the light-cone fraction of the nucleus carried by an interacting nucleon and $k^\mu = (k_0, \mathbf{k_T}, k_{||})$ is the internal momentum of the nucleon within a nucleus in a center of mass frame, with $k_0 = \sqrt{M^2+k^2}$. The relativistic effect, in this picture, manifests itself in that the measured momentum of the nucleon $p_{||}$ is rescaled in the lab frame, from the internal momentum $k_{||}$. The resulting deuterium momentum distribution is given by the spectral function:

$$S^{LC}(\alpha_s, \mathbf{p_T}) = \frac{\sqrt{M^2+\mathbf{k}^2}}{2-\alpha_s}|\psi_{NR}(\mathbf{k})|^2 \tag{26}$$

The spectral function is normalized to satisfy the relation:

$$\int\int\int S^{LC}(\alpha_s, p_T)\frac{d\alpha_s}{\alpha_s}d^2p_T = 1$$

In the spectator approximation, the recoiling proton is on-shell at the moment of interaction and receives no energy or momentum transfer, so that its internal momentum and momentum in the lab are the same. The cross-section can then be calculated using an invariant form (54) which can be rewritten in even more general form for the moving nucleon as:

$$\begin{aligned}\frac{d\sigma}{dx^* dQ^2} = \frac{4\pi\alpha_{EM}^2}{x^* Q^4}\left[\frac{y^{*2}}{2(1+R)} + (1-y^*) + \frac{M^{*2}x^{*2}y^{*2}}{Q^2}\frac{1-R}{1+R}\right] F_2(x^*, \alpha_s, p_T, Q^2) \\ \times S^{LC}(\alpha_s, p_T)\frac{d\alpha_s}{\alpha_s}d^2p_T\end{aligned} \tag{27}$$

In this expression the asterisk is used for the variables that were defined in a manifestly covariant way and $R = \frac{\sigma_L}{\sigma_T}$ is the ratio between the longitudinal and transverse cross sections. For instance, the Bjorken scaling variable $x = \frac{Q^2}{2M\nu}$ and variable

$y = \frac{\nu}{E}$, that are valid for the scattering from a free nucleon, are replaced with their counterparts for the scattering on a moving neutron inside of the deuteron:

$$x^* = \frac{Q^2}{2p_N^\mu q^\mu} \approx \frac{Q^2}{2M\nu(2-\alpha_S)} = \frac{x}{2-\alpha_S} \tag{28}$$

$$y^* = \frac{p_N^\mu q_\mu}{p_N^\mu k_\mu} \approx y$$

where $q^\mu = (\nu, \mathbf{q})$ is the momentum transfer 4-vector, $k^\mu = (E, 0, 0, E)$ is the momentum 4-vector of the incident electron, $p_N^\mu = (M_d - E_S, -\mathbf{p_s})$ is the momentum 4-vector of an off-shell neutron and M_s is the mass of the deuterium nucleus . The light-cone fraction of the deuteron carried by the struck neutron α_N and the light-cone fraction carried by the spectator proton α_S satisfy the relation $\alpha_N + \alpha_S = 2$. In this approximation the struck nucleon is assumed to be on the energy shell, but off its mass shell. The mass of the free nucleon M is therefore replaced with the off-shell mass of the bound nucleon:

$$M^{*2} = (M_d - E_S)^2 - p_S^2 \tag{29}$$

The invariant mass of the final hadronic state in $d(e, e'p_s)X$ scattering can be expressed as:

$$\begin{aligned} W^{*2} = (p_n^\mu + q^\mu)^2 &= M^{*2} - Q^2 + (2M - E_s)\nu - p_s^{||} q \\ &= M^{*2} - Q^2 + M\nu\left(2 - \tfrac{E_s + p_s^{||}(q/\nu)}{M}\right) \end{aligned} \tag{30}$$

where it was assumed that $M_d \approx 2M$. In the limit of $q/\nu \to 1$ the fraction in the brackets of the last term in equation (30) takes the familiar form of the light-cone fraction of the nucleus carried by the spectator proton $\alpha_S = \frac{E_S - p_S^{||}}{M}$. Then in the case of scattering from a bound nucleon the invariant mass W takes the form:

$$W^{*2} \approx M^{*2} - Q^2 + M\nu\,(2 - \alpha_S) \tag{31}$$

In the impulse approximation employing the light-cone approach, the inclusive DIS structure function of the nucleus can be approximated in terms of the nucleon structure function and the nuclear light-cone density matrix:

$$F_{2A}(x,Q^2) = \int_x^A \rho_A^N(\alpha_N, p_T) F_{2N}\left(x^*, Q^2\right) \frac{d\alpha_N d^2 p_T}{\alpha_N} \tag{32}$$

In this way the nucleus is built out of a set of free nucleons, i.e. it is assumed that the bound nucleon has the same quark distribution as a free nucleon.

An alternative method of treating the electron scattering from an off-shell nucleon was originally developed for quasi-elastic scattering by deForest [33] and then applied to the nuclear DIS by Meier-Hajduk [34] and infinite nuclear matter by Benhar [35]. The nucleon on which scattering takes place is assumed to be off-shell. The physical 4-momentum transfer $q^\mu = (\nu, \mathbf{q})$ is replaced with $\tilde{q}^\mu = (\tilde{\nu}, \mathbf{q})$, where:

$$\tilde{\nu} = \nu + p_{n0} - \sqrt{|\mathbf{p_n}|^2 + M^2}$$

with $p_n^\mu = (p_{n0}, \mathbf{p_n})$ being the 4-momentum of the struck nucleon. Using this new kinematics the scattering is then treated as taking place on a free nucleon. Essentially, in this method the fraction of the transfered energy $(\nu - \tilde{\nu})/\nu$ is spent to put the struck nucleon on the mass shell. The new 4-vector $\tilde{q}^\mu$ together with the 4-vector of the free nucleon $\widetilde{p_n}^\mu = (\widetilde{p_{n0}}, \mathbf{p_n})$, where $\widetilde{p_{n0}} = \sqrt{M^2 + |p_n|^2}$, are now used to calculate the hadronic tensor (12). Additional factors are introduced into the tensor $W_{\mu\nu}$ in the new quasi-free kinematic variables so that current is conserved.

However, the difference in the x dependence of the inclusive deep inelastic cross section for free and bound nucleons (Fig. 4) observed by the European Muon Collaboration (known as the EMC-effect), cannot be interpreted only in terms of the kinematic shift due to the Fermi motion. A number of models were proposed trying to explain the EMC-effect. A good outline of the state of theory on that issue was given by Sargsian in Ref. [14].

The first kind of models, known as binding models, attempt to describe the effect in terms of conventional nuclear physics degrees of freedom - nucleons and pions. The structure of the nucleon is assumed to remain the same as that of a free nucleon and the nuclear structure function is expressed using (32). In the random-phase approximation (RPA) the deviation from unity in the ratio of cross-sections for a heavier nuclei to deuterium (EMC-effect) is thought to be due to the pion cloud excess. That leads to the reduction of DIS nuclear cross-section per nucleon in the region where the cross-section is thought to be dominated by valence quarks. The pion contribution is simply added to the expression (32). RPA kind of theories, where

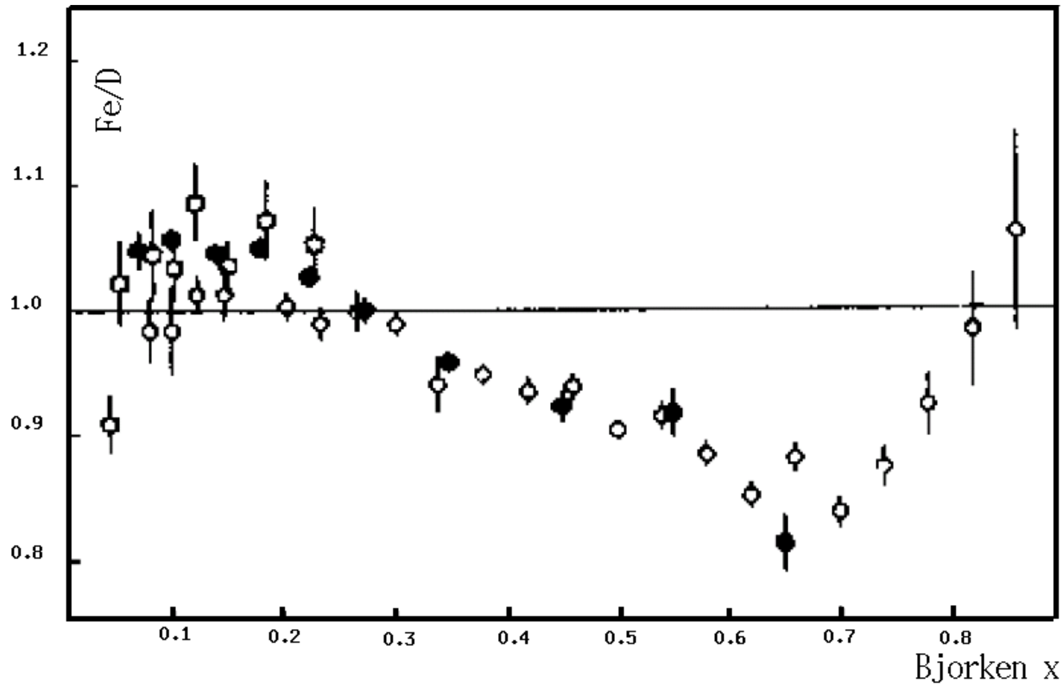

FIG. 4: The ratio σ^{Fe}/σ^{D} plotted as a function of Bjorken x. Black circles are from Ref. [18] and white circles are from [17].

there are strong collective pion modes, are not capable of explaining both EMC [15] and Drell-Yan data [19]. Drell-Yan data restricts the fraction of the momentum that can be carried by the pion cloud in the direction of quantization ($P^+ = P_0 + P_3$), so that the necessary reduction in the nuclear structure function cannot be achieved as shown by Miller [38]. An alternative approach, proposed by Koltun [39], associates a pion excess with the strong short range and tensor correlations, in the structure of a nuclear ground state . It is claimed that in that case the pion excess is simply kinematically inaccessible by the Drell-Yan data and thus the theory is consistent with both EMC and Drell-Yan measurements. The ratio of a tagged neutron structure function to the free neutron structure function for that group of models should be unity at all x.

Another kind of model modifies the quark distribution within the bound nucleon, and uses a new, off-mass-shell structure function to compute the cross section (27). The structure functions here are defined by taking non-relativistic or on-shell limits of the $\gamma^* N$-interaction off-mass-shell amplitude. Melnitchouk and Thomas

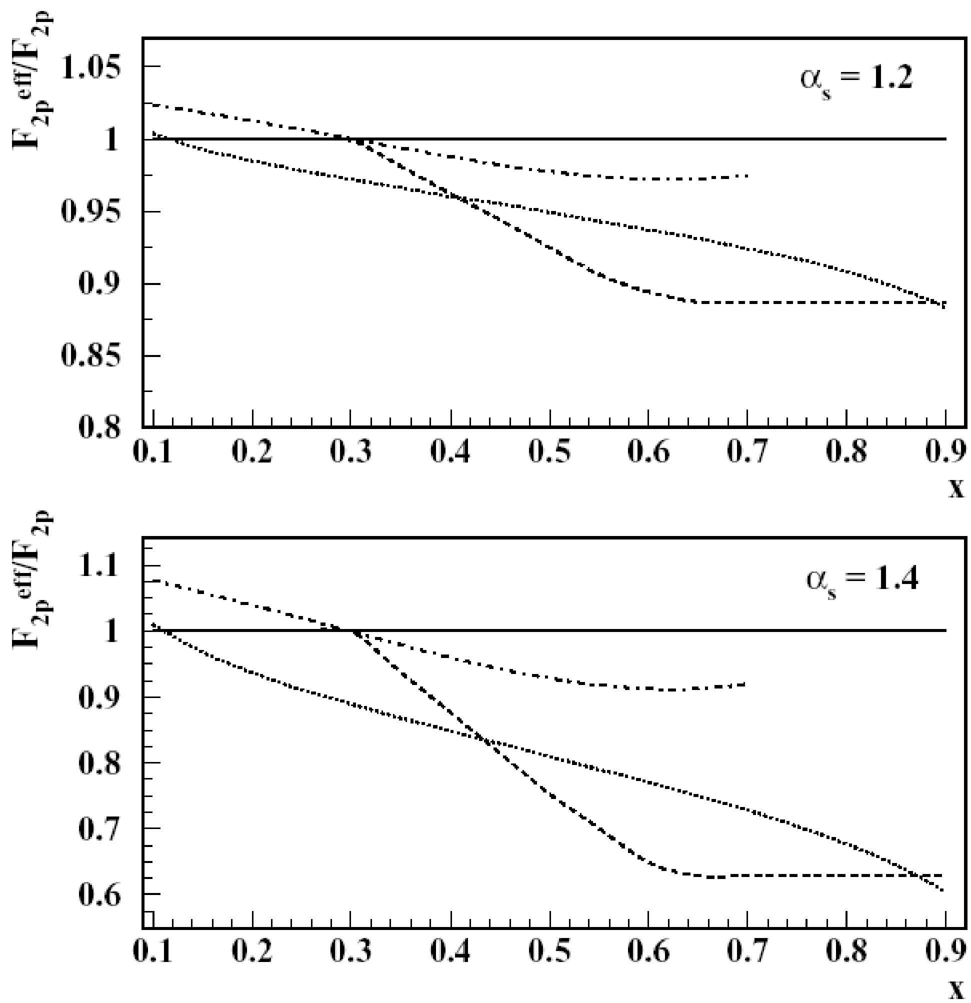

FIG. 5: The x dependence of bound to free nucleon structure functions for two different values of α_S. Calculations are done at $Q^2 = 5$ GeV^2 and for $p_T = 0$ [47]. The dashed line is the PLC suppression model, the dotted is the rescaling model, and the dot-dashed is the binding/off-shell model.

[40, 41] construct the truncated photon-nucleon amplitude from 14 general, independent functions, and then use a parton model to show that only 3 of these are relevant in describing the DIS structure functions of the off-shell nucleon in the Bjorken limit ($Q^2 \to \infty, \nu \to \infty$). Their calculation explicitely satisfies current conservation and the Callan-Gross relation (20). The same method was used to calculate the complete relativistic deuteron structure function, including binding effects, Fermi motion and nucleon off-shell effects [41]. This approach gives less than 10% reduction in the nucleon structure function at $x > 0.4$, compared with the on-shell structure function (Fig. 5, dot-dashed curve). In quark-meson coupling models (QMC) of Blunder, Miller, Lu and Thomas [42, 43] the quarks are bound in non-overlapping nucleon bags. The interaction between the nucleons arises from vector and scalar mesons coupling to the quarks. In spite of the assumption that quarks in this model are localized, the resulting wave function of a bound nucleon is different from that of a free nucleons.

In the model of Frankfurt and Strickman [44] the suppression of compressed (point-like) quark-gluon components of a bound nucleon wave function gives an even steeper drop for the bound nucleon structure function. The attraction is smaller for the nucleon in a point-like configuration (PLC), therefore the wave function of a bound nucleon should be deformed to suppress the probability of PLC, thus increasing the binding energy. At the same time, PLC is expected to be the dominant part of the free nucleon wave function at $x > 0.6$, thus giving rise to the observed EMC-effect. The degree of suppression is proportional to the virtuality of the nucleon. However, the suppression does not lead to a noticeable difference in the average characteristics of a nucleon. For instance, the model predicts only a 2% effect for the quasi-elastic cross section at high Q^2. However, for the far off-shell nucleons that correspond to large values of α_S, the model predicts a strong reduction in the ratio of bound to free nucleon structure functions (Fig. 5). In rescaling models of Close [45], the EMC-effect originates from the confinement scale increase as one goes from the free nucleon to a nucleus. The change of confinement size is attributed to the overlap of nucleons in nuclei that increases with nuclear density. The change in confinement modifies quark and gluon distribution functions. However, the authors show that nucleon and nuclear structure function can be related by rescaling, i.e. there exists a parameter $\xi_A(Q^2)$ such that for nucleus A it can be written:

$$\frac{1}{A}F_{2A}(x,Q^2) = F_{2N}(x,Q^2\xi_A(Q^2)) \tag{33}$$

where $\xi_A(Q^2)$ can also depend on the virtuality of a bound nucleon and is usually determined from the observed EMC-effect. The Q^2 dependence of the rescaling parameter is taken from the general form of the QCD evolution equation. The prediction of this model is compared with the off-shell and PLC models in Fig. 5.

The ratio of the bound to free structure function of a nucleon, plotted as a function of the light-cone fraction of the nucleus carried by the spectator nucleon $\alpha_s = \frac{E_S - p_S^{||}}{M}$ is shown in Fig. 6. As it can be seen from the definition of α_S, large values of this variable correspond to high-momentum spectator nucleons emerging from high density short range nuclear configurations at large backward scattering angles. The light-cone fraction decreases as the component of the momentum of the backward going spectator proton parallel to the direction of the momentum transfer decreases. Fig. 6 indicates that in all models shown, the effect of bound nucleon structure modification increases with increasing $p_S^{||}$.

The most unconventional attempt to explain one of the possible contributions to the EMC-effect is made by model of Carlson and Lassila [23, 46] where nucleons inside of a nucleus in its high density configuration are thought to merge and form multiquark states. For the case of deuterium a 6-quark state would be a part of the deuterium wave function. The cross section for backward proton production is then expressed as a convolution of the distribution function for a valence quark in a 6-quark cluster $V_i^{(6)}$ and the fragmentation function for the 5-quark residuum $D_{p/5q}(z) \propto (1-z)^3$, with $z = \alpha/(2-x)$:

$$\frac{d\sigma}{d\phi dx dQ^2 d(\log\,\alpha) d^2p_T} \simeq \frac{2\alpha_{EM}^2}{xQ^4}(1-y)\sum_i x e_i^2 V_i^{(6)} \frac{\alpha}{2-x} D_{p/5q}(z,p_T) \tag{34}$$

Figs. 7 and 8 show the ratio $R_1 = \frac{F_2^{(6)}(x)\,D_{p/5q}(z,p_T)}{(2-x)(2-\alpha)F_{2n}(\xi)}$, where $F_2^{(6)}$ was estimated in a model where nuclei are treated as containing some fraction of 6-quark clusters and the simple quark distributions of Carlson and Havens were used to get F_{2n} [46]. The ratio is presented in arbitrary units, since the fragmentation function is not normalized. The model suggest a factor of two difference from maximum to minimum of the ratio.

It was estimated that about 5% of the deuterium wave function can be due to 6-quark bag configurations. This is a small contribution to the EMC-effect data that is integrated over the whole momentum range. When only the high-momentum

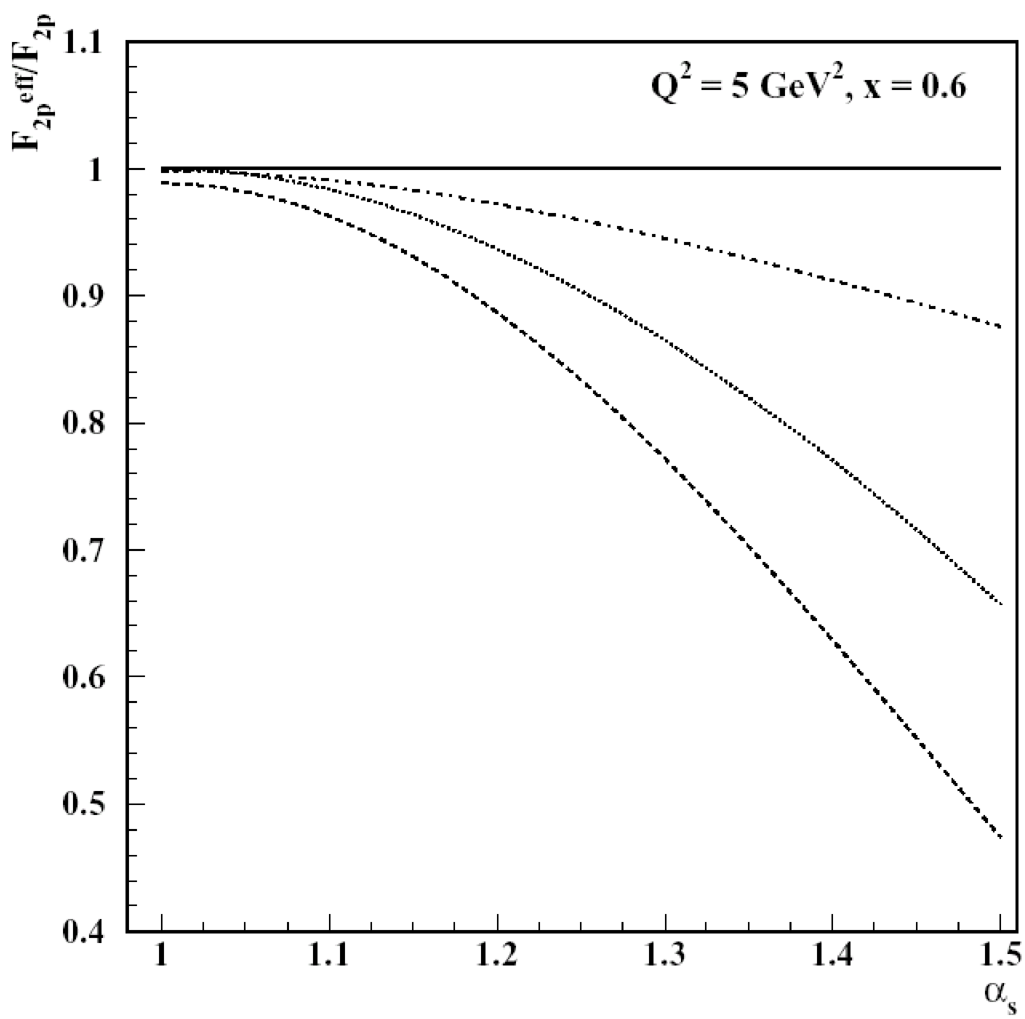

FIG. 6: The light-cone fraction dependence of the ratio of bound to free structure function of the nucleon calculated using different models [47]. The dashed line is the PLC suppression model, the dotted is the rescaling model, and the dot-dashed is the binding/off-shell model.

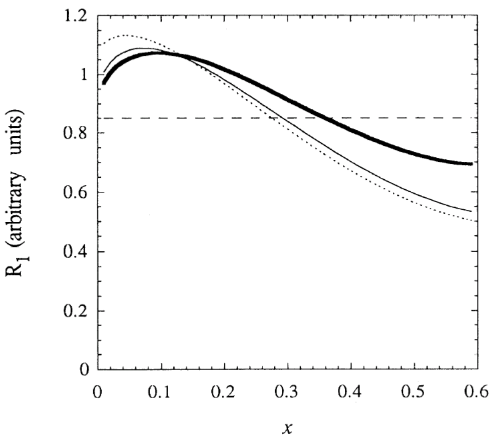

FIG. 7: The ratio R_1 plotted for $\alpha = 1.4$ and $p = 322$ MeV/c. Different curves correspond to different parametrizations of $F_2^{(6)}$ [46]. F_{2n} is obtained from Carlson and Havens quark distribution.

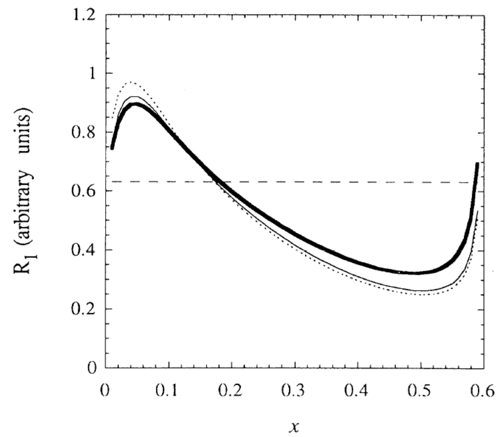

FIG. 8: The ratio R_1 plotted for $\alpha = 1.4$ and $p = 322$ MeV/c. Different curves correspond to different parametrizations of $F_2^{(6)}$ [46]. F_{2n} is obtained from CTEQ distribution functions at $Q^2 = 4$ GeV^2

part of the wave function is tested by proton tagging, the effects of the 6-quark configurations, if they do indeed exist, would become much more pronounced.

2.5 FINAL STATE INTERACTIONS

Final state interactions (FSI) are inevitable in any nuclear scattering experiment; however, there are kinematic regions where FSI are thought to be small, and there are regions where FSI are enhanced. Reliable models of FSI exist for nucleon-nucleon rescattering. In the resonant and deep inelastic region, the estimation of FSI is a lot more challenging. FSI can be modeled by replacing the spectral function (in expression (27)) with a distorted one: $S^{FSI}(\alpha_{s,}p_T)$.

In calculation of Melnitchouk, Sargisian and Strikman [47] the $eD \rightarrow e\,p\,n$ process is used as a first estimate of FSI in electron scattering from the deuteron. This calculation shows that at $\alpha_s > 2 - x$ and $\mathbf{p_T}$ close to zero, the FSI are small (Fig. 9). In this model S^{FSI} is evaluated using a distorted wave impulse approximation (DWIA). It is also shown that FSI effects should not strongly depend on x, thus the ratios of the cross section for different ranges in x is a good tool to look for the EMC-effect in the semi-inclusive $eD \rightarrow e\,p\,X$ process. In the limit of large x, FSI become much more important for heavier nuclei, where rescattering hadrons produced in the

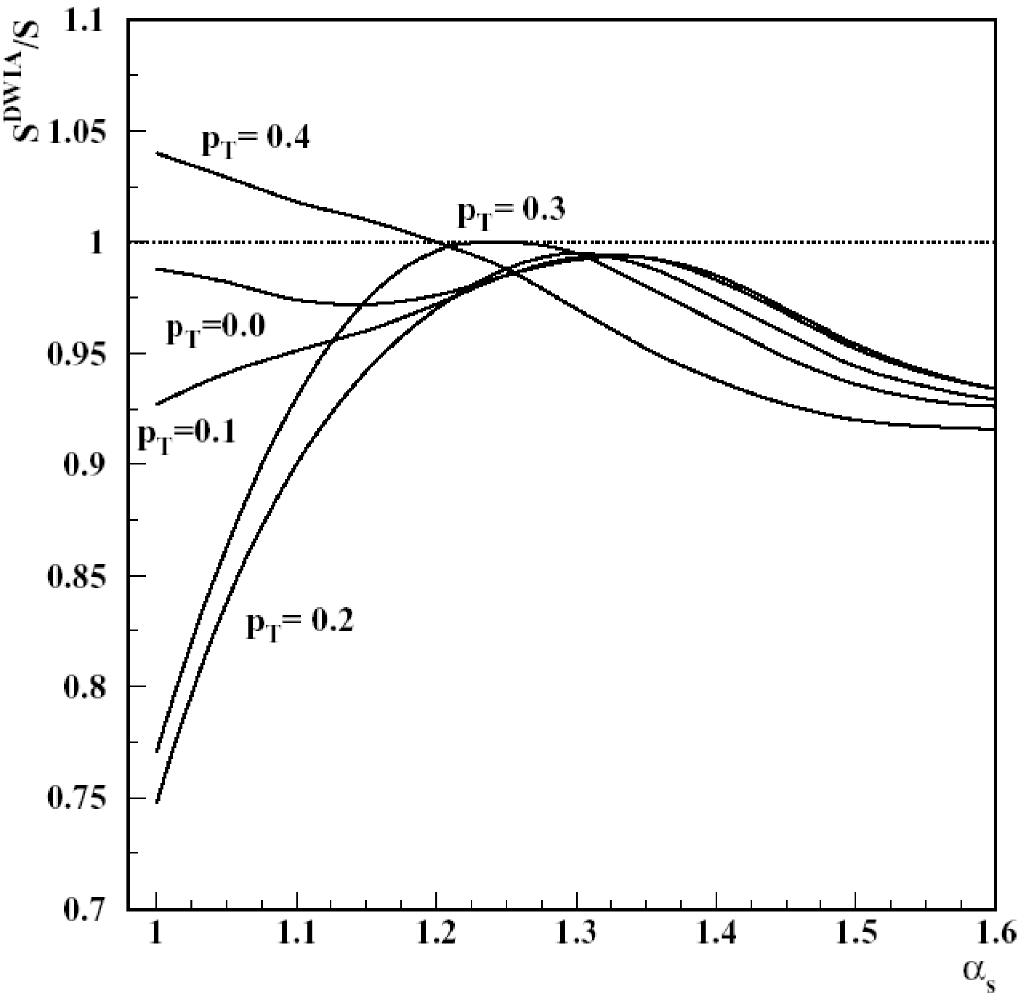

FIG. 9: The α_S dependence of the ratio of cross sections calculated with FSI effects within the DWIA, and without FSI effects. The curves correspond to different values of the spectator nucleon transverse momentum p_T (in GeV/c).

elementary DIS off the short-range correlation are dynamically enhanced. Therefore deuterium targets, in the authors' opinion, provide the best way of looking for the EMC effect for bound nucleons.

A more recent publication by Cioffi and Kaptari [48] discusses backward proton production and FSI associated with DIS, evaluating S^{FSI} within a hadronization framework. The reinteraction of the backward going spectator protons with the debris formed in a hadronization process is modeled using an effective cross section:

$$\sigma^{eff} = \sigma^{NN} + \sigma^{\pi N}(n_M + n_G) \tag{35}$$

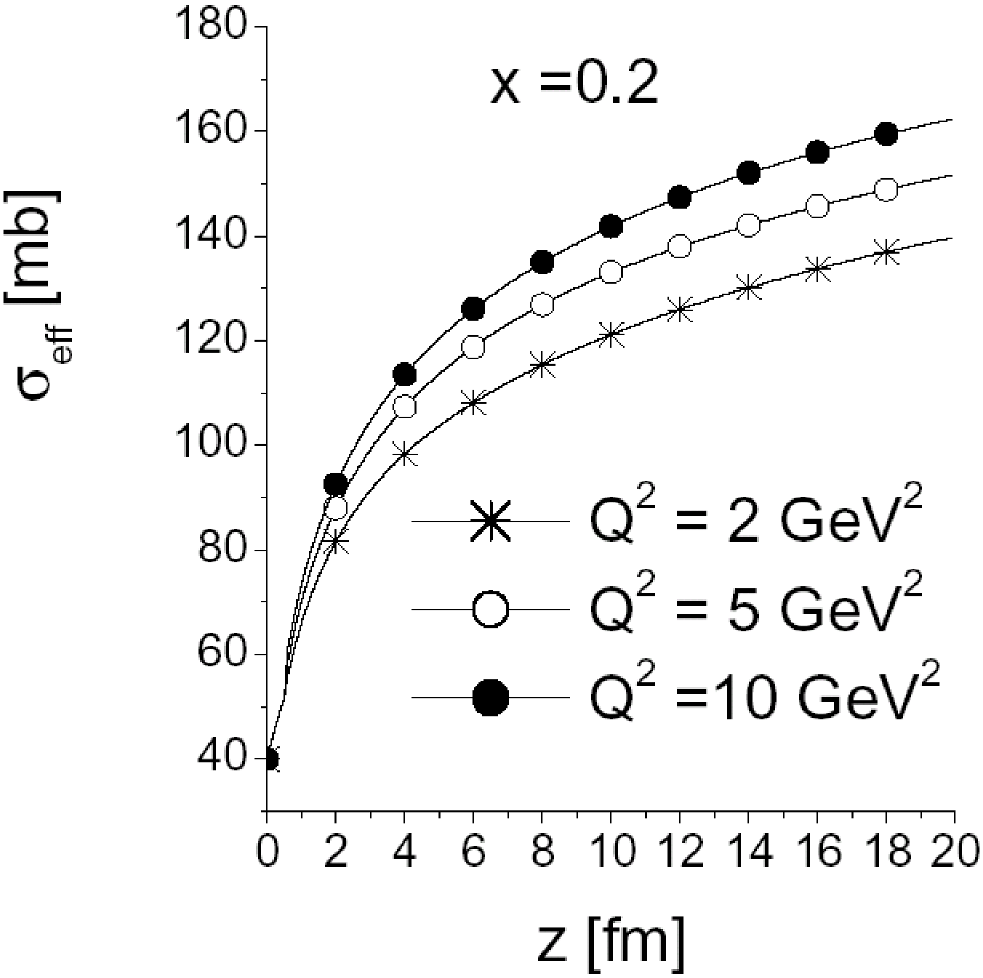

FIG. 10: The debris-nucleon cross section, plotted versus the distance z for a fixed value of x and various values of Q^2.

where σ^{NN} and $\sigma^{\pi N}$ are the total cross sections of the nucleon-nucleon and meson-nucleon interaction, and n_M and n_G are the effective numbers of created mesons and radiated gluons. The cross section (35) asymptotically tends to exhibit a simple logarithmic behavior (Fig. 10). The magnitude of the effective reinteraction cross section differs significantly for different models, especially at angles of proton emission $\theta \sim 90^o$. This kinematic region is proposed by the authors as the best place to test various models of hadronization. In contrast with the calculation discussed in the beginning of the section, the model of [48] predicts a significant effect of FSI for proton momenta $|\mathbf{p}_s| > 250$ MeV/c even for extreme backward kinematics (Fig. 11).

Using experimental data analyzed here, it will be possible to test both models discussed above in a wide range of spectator proton emission angles, momenta and consequently a wide range of α_s. Both models predict strong distortion due to FSI in the region of transverse kinematics when a spectator proton is emitted perpendicular to the direction of momentum transfer. Focusing on a kinematic region of large backward scattering angles of a spectator proton (relative to the direction of the momentum transfer) is expected to reduce the FSI interference.

2.6 EXISTING DATA OVERVIEW

Little data exists on the semi-inclusive scattering of a lepton from deuterium with a recoiling nucleon in a backward direction with respect to the momentum transfer. The data published so far was taken using either neutrino or antineutrino beams and had very low statistics that do not allow detailed investigation of the cross sections of interest. These experiments (see Berge and Efremenko [12, 13]) focused on measuring the momentum, energy, and angular distributions of protons in the backward hemisphere relative to the beam line. Despite the low statistics, a notable difference in the distributions for backward and forward protons was observed. The data were shown to agree well with a pair-correlation model in which the detected backward proton is assumed to be a spectator to the reaction (Fig. 12).

The cross section ratio σ^{Fe}/σ^{D} measured by the European Muon Collaboration [15] (where σ^{Fe} and σ^{D} are cross sections per nucleon for iron and deuterium respectively) showed deviations from unity (now known as the EMC-effect) that could not be explained only in terms of nucleon Fermi motion (Fig. 4). That was the first evidence that the nuclear medium influences DIS processes. It provided an indication that nuclear matter is getting modified as its density increases. The effect was later

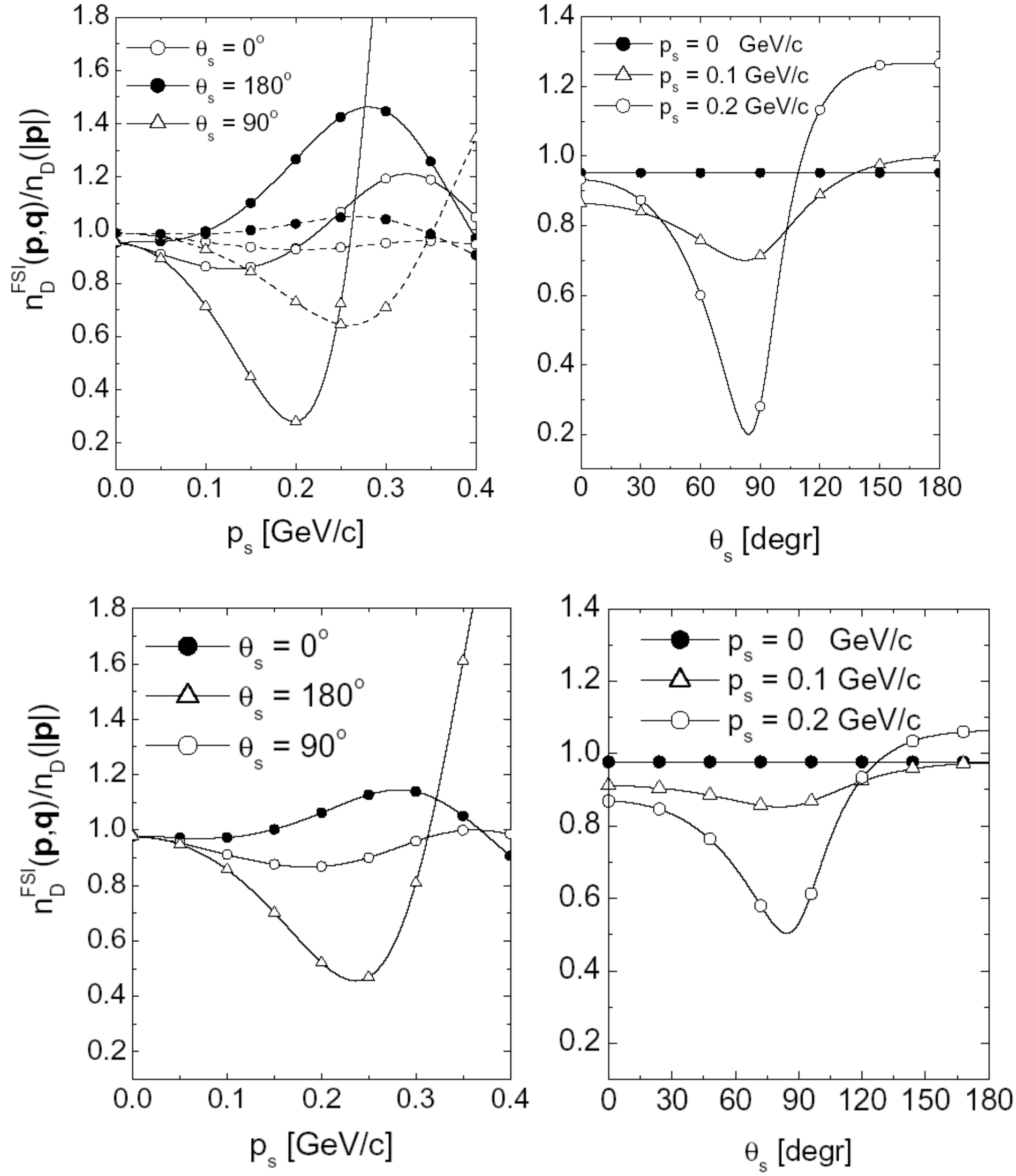

FIG. 11: The ratio of FSI to undistorted momentum distributions of deuterium in the hadronization model. Solid curves are obtained using functional form (35) for the effective cross section, dashed curves were obtained using constant value of $\sigma_{eff} = 20$ mb. Top distributions are for deep inelastic scattering at $Q^2 = 5$ GeV^2 and $x = 0.2$. The bottom distributions are for quasi-elastic scattering at $Q^2 = 5$ GeV^2. On the left side the ratio is plotted as a function of spectator momentum and on the right side the dependence on the spectator emission angle is shown.

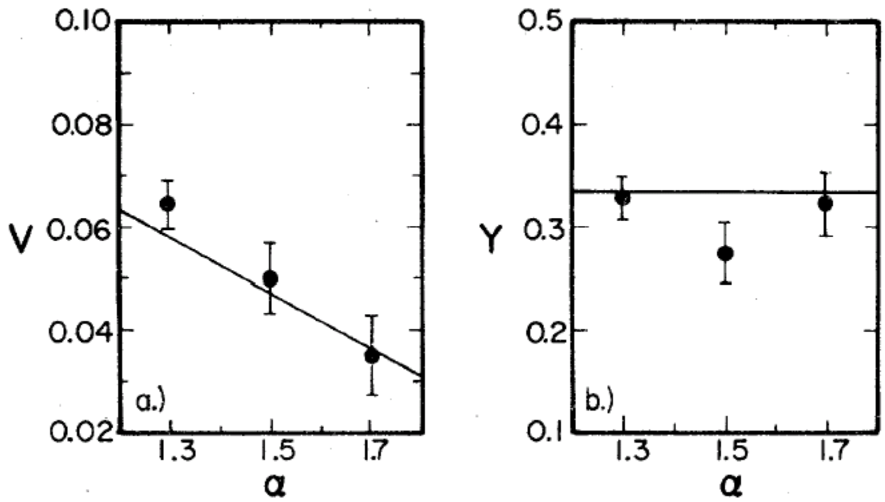

FIG. 12: Comparison of the experiment with a pair-correlation model. α dependence of the scaling variable $\mathrm{v} = E_\mu(1-\cos\theta_\mu)/m$ (E_μ and θ_μ are muon energy and angle) and y.

confirmed by data from SLAC [16, 17] and CERN [18].

An independent measurement of the modification of the quark structure of nuclei was later done at Fermilab [19] using continuum dimuon production in high-energy hadron collisions, known as the Drell-Yan process [20]. The measurement has shown no nuclear dependence in the production of the dimuon pairs in the region $0.1 < x < 0.3$, and therefore, no modification of the antiquark sea in this range. A number of models developed to explain the EMC-effect in terms of strong enhancement of the pion cloud were ruled out by this experiment (Fig. 13).

A recent polarization transfer measurement by Dieterich and Strauch [21, 22] in the $^4\mathrm{He}(\vec{e}, e'\vec{p})^3\mathrm{H}$ reaction suggested medium modification of the electromagnetic form factors of the nucleon. The observed 10% deviation from unity (Fig. 14) could only be explained by supplementing the conventional nuclear description with effects due to medium modification of the nucleon as calculated by the QMC model [43, 42].

A model in which the neutron and proton form a single 6-quark cluster was recently tested [23] against old backward proton production data from neutrino scattering on deuterium collected at Fermilab [24]. These data had sufficient acceptance for backward protons but were not previously analyzed for this signal. The proton

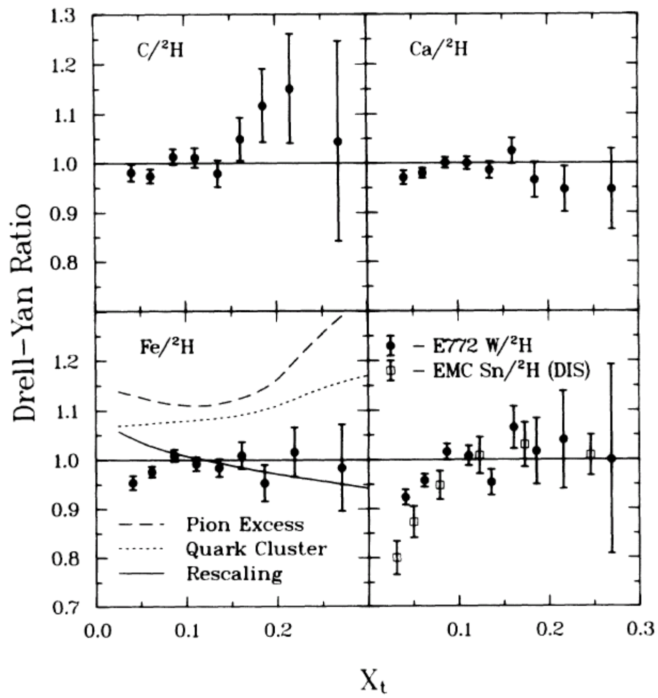

FIG. 13: Ratios of Drell-Yan dimuon yield per nucleon, $Y_A/Y_{^2H}$. The curves shown for $Fe/^2H$ are predictions of various models of the EMC-effect [19]. Also shown the DIS data for $Sn/^2H$ from the EMC.

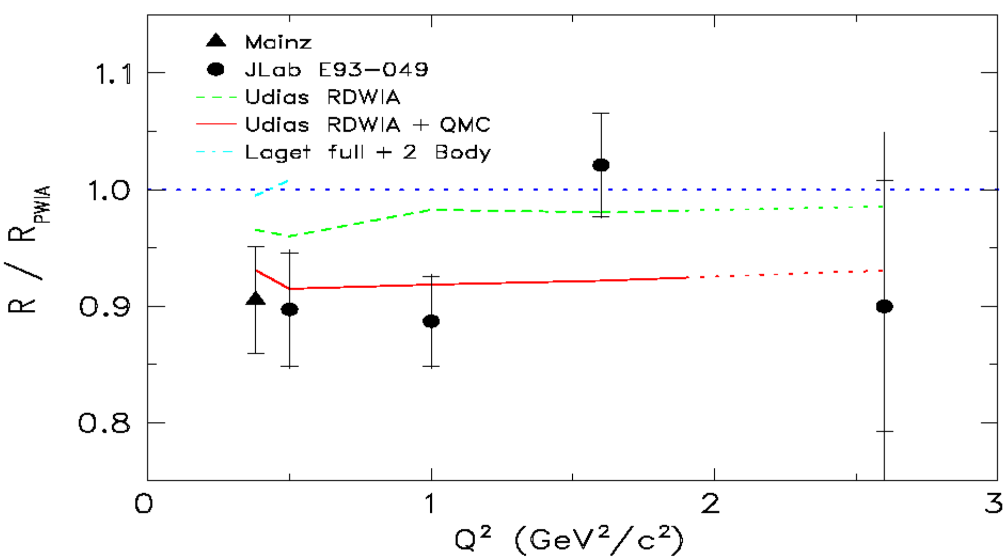

FIG. 14: Superratio R/R_{PWIA} as a function of Q^2 [22]. R is defined as a double ratio $(P'_x/P'_z)_{He})/((P'_x/P'_z)_H)$ where P'_x and P'_z are longitudinal and transverse transferred polarizations. Points with with error bars show data from two different sources. Lines indicate the prediction of various theoretical calculations.

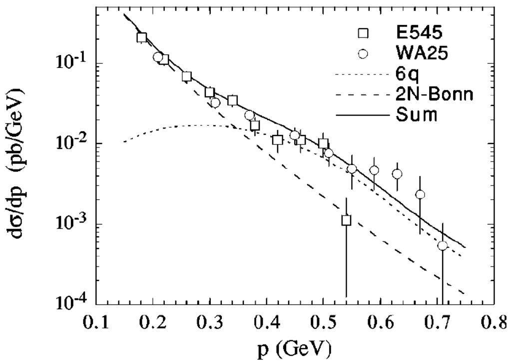

FIG. 15: Comparison of the backward proton spectrum to calculations using the Bonn wave function.

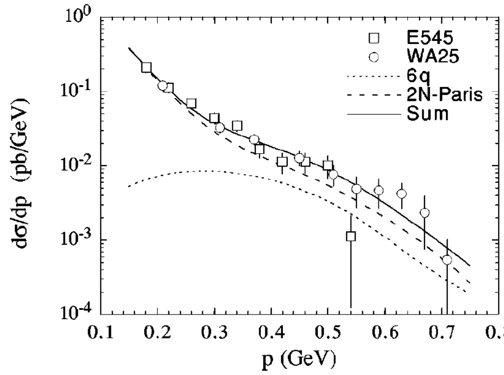

FIG. 16: Comparison of the backward proton spectrum to calculations using the Paris wave function.

spectrum from neutrino and antineutrino scattering from deuterium, taken at CERN [36], was also discussed. The authors compared the momentum distribution of backward protons with the prediction of a 6-quark cluster model. Predictions of the model were shown to be in a good agreement with the data, however, the statistics of the data were not sufficient to study the dependence on any other kinematic variables (Fig. 15,16).

2.7 ANALYSIS OBJECTIVES

The atomic nucleus is thought to be a highly dynamic system. Even in its ground state the momentum density distribution of the deuteron goes far beyond its average value of 100 MeV/c, reaching momenta of up to 600 MeV/c even in the most conservative models. When an electron scatters from a free nucleon, the initial state of the system is fully defined. In case of scattering from a bound nucleon, the momentum of the nucleon to which the virtual photon couples is not known a priori and without additional information only probability statements can be made regarding it (nuclear spectral function). This purely kinematical obstacle in the way of an exact measurement, can be easily dealt with in the way described below. However, a conventional approach in this situation is to introduce a phenomenological correction to the final result of the measurement or simply to ignore the uncertainty and add it to the systematic error. In the spectator approximation, the electron scatters from one of the nucleons within a nucleus (that is off its mass shell), while no energy

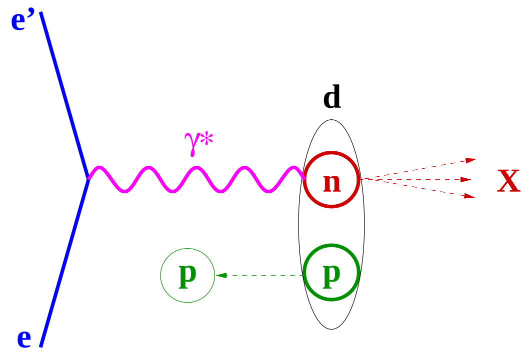

FIG. 17: Diagrammatic representation of a spectator mechanism.

or momentum is transfered to the other, on-shell nucleons, that simply recoil with their initial internal momentum (Fig. 17). In the case when the spectator nucleon is the proton, and the deuteron wave function (at the moment of interaction) was in its high-momentum configuration, the spectator proton has high enough momentum and can be easily detected. The initial kinematic state of the struck neutron can then be deduced using the momentum 4-vector of the detected spectator proton based on the momentum and energy conservation laws.

A test of the nuclear spectator model and its limitations is the first goal of the present analysis. In the kinematic region where the model approximately works, it can be used to study the properties of the bound neutron on which the interaction takes place. As it was shown in section 2.4, different theories have very different predictions for the magnitude of the bound nucleon cross section depending. First of all, the quality of two prescriptions (cited above) to treat the relativistic effects will be tested. With the statistics available in the collected data described here, it will be possible to test extracted experimental cross sections against numerous approaches to electron scattering from a bound nucleon, using the detected backward going proton to control the degree of off-shellness of the interacting bound neutron. Our experimental data also have wide coverage in different kinematic variables that will allow us to study the high-momentum part of the deuterium wave function. Final state interactions (FSI) and target fragmentation can distort even the proton moving in a backward direction. The inelastic and deep inelastic regions of electron scattering from nuclei remain the least studied, when it comes to final state interactions. Existing models of FSI (section 2.5) give sharply different predictions for the degree of distortion of the outgoing spectator proton. The data presented here cover a wide range of backward proton momenta and emission angles that will be employed to test existing FSI models.

CHAPTER 3

EXPERIMENTAL SETUP

3.1 ACCELERATOR

The Continuous Electron Beam Accelerator Facility (CEBAF) operating at the Thomas Jefferson National Accelerator Facility (Jefferson Laboratory) is designed based on superconducting radio-frequency (RF) technology (Fig. 18). The injector linac delivers 67 MeV unpolarized or polarized electrons. Polarized electrons are produced at the laser-driven photocathode source and unpolarized ones are emitted from a conventional thermionic gun. Electrons are injected with a frequency of 1.497 GHz in synchronicity with the accelerating electromagnetic wave of 1.497 GHz into the superconducting cryomodules of the first linac. Electrons are accelerated through 20 cryomodules to an energy of up to approximately 0.6 GeV and then delivered to the second identical linac through a recirculating arc. Cryomodule cavities operate at a temperature of 2 K with an average field gradient of 7.5 MeV/m. The second linac accelerates the electron bunch by another 0.6 GeV. The beam can then be extracted and delivered to experimental halls with an energy of up to 1.2 GeV or delivered to the first linac through the recirculation arc for another acceleration cycle. The RF separator of the extraction elements is designed to deliver beams of 499 MHz frequency to three experimental halls simultaneously. The accelerator is capable of up to 5 laps of acceleration, producing an electron beam of almost 6 GeV maximum energy. The spread of the beam energy is within 0.01%.

3.2 HALL B BEAMLINE

The electron beam delivered to Hall B is monitored by a number of devices that provide complete information on the beam quality and its important characteristics (position, shape and current). Three nanoamp (nA) beam position monitors located in the hall measure the position of the beam in real-time with a resolution of better than 100 μm. They also measure the magnitude of the beam current. Approximately 22 m upstream from the center of the CLAS detector is the tagger “harp” and radiator assembly. The harp measures the beam profile by passing a pair of 50 μm tungsten wires through the beam. The response of the beam halo monitor photomultiplier

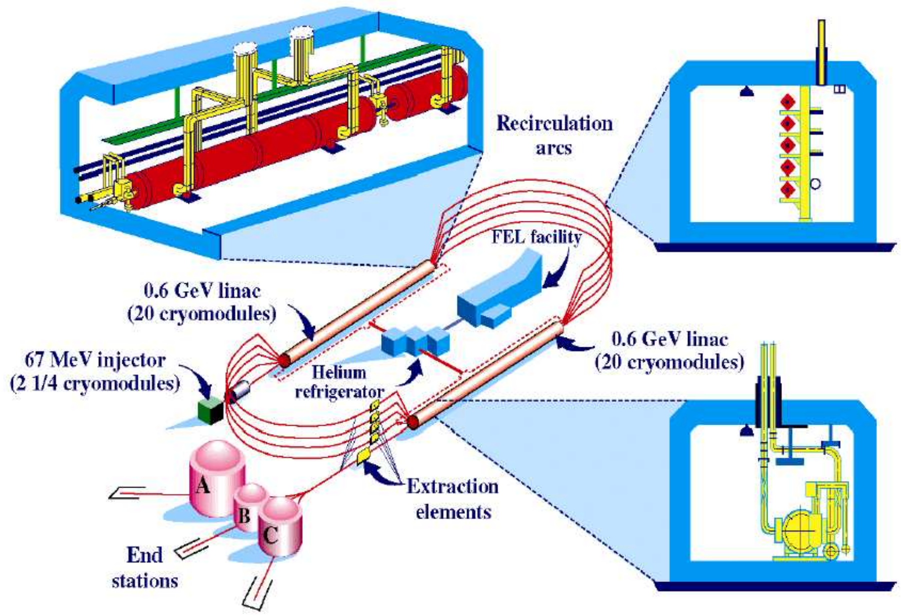

FIG. 18: The CEBAF SRF recirculating electron accelerator.

tubes is recorded as a function of harp position. Such a "harp scan" measures the beam position and shape. The width of the beam is typically less than 200 μm.

The integrated electron beam charge is directly collected with a Faraday cup (FC) located at the very end of the beam line, 20 m downstream from the center of the Hall B detector. The FC accurately measures the integrated beam current, which is needed to extract absolute cross sections. The Faraday cup is made out of 4 tons of lead and is 70 radiations lengths deep. High-energy beam electrons deposit all of their energy within the volume of the Faraday cup and the accumulated charge is measured. The signal from the FC is split and recorded (gated by the state of the data acquisition system) so that the total charge incident on the target as well as the charge incident during the time the data acquisition is running (live-gated) are accumulated. During the period of the experiment discussed here, the Faraday cup operated at 9264 counts per 1 nC.

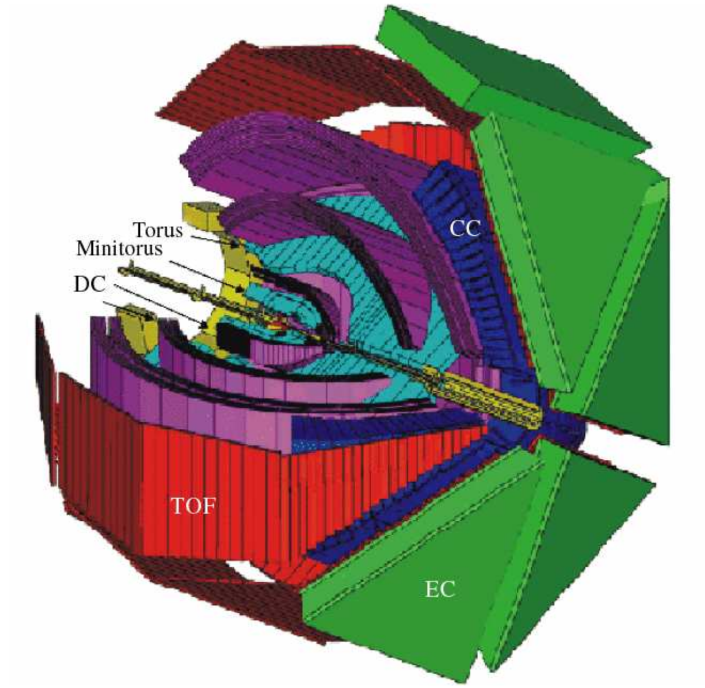

FIG. 19: CEBAF Large Acceptance spectrometer.

3.3 CEBAF LARGE ACCEPTANCE SPECTROMETER

There are three experimental halls at Jefferson Laboratory at the moment: Halls A, B and C. There are also plans to build a fourth hall, Hall D when the accelerator is upgraded to 12 GeV. Hall A houses two High Resolution Spectrometers (HRS), each covering about a 6 msr solid angle. Hall C has two spectrometers: the High Momentum Spectrometer (HMS) with a 6 msr solid angle acceptance and Short Orbit Spectrometer (SOS) that has a 9 msr acceptance.

Installed in experimental Hall B is the CEBAF Large Acceptance Spectrometer (CLAS). CLAS has almost 4π acceptance in solid angle and covers angles with respect to the direction of the beam from 8 to 142^{o} and almost 360^{o} around the beam line (Fig. 19). The detector is divided in 6 identical sectors of spectrometers, with 5 meter long superconducting coils located in between the sectors. The main magnetic torus creates a toroidal magnetic field within the detector volume with $\int B \times dl$ varying from 2 T m at the most forward angles to about 0.5 T m for back angles. Depending on the direction of the field, negatively charge particles are bent towards (inbending) or outwards the beam line. Inbending field configuration is standard in CLAS experiments, however additional running with outbending setup allows wider coverage in kinematics of scattered electron as well as other charged particles. In order to shield the detectors from the charged electromagnetic background emerging from the target, the detector is equipped with a small normal-conducting secondary torus ("mini-torus") that surrounds the target in the center of CLAS. The strength of the "mini-torus" magnetic field is only $1-5\%$ of the main torus and has little effect on high-momentum charged particles. Each sector has three layers of drift chambers (DC) and one layer of scintillator counters (SC) that cover full detector acceptance. The Cherenkov counters (CC) and electromagnetic calorimeter (EC) are installed in the forward region. These detectors, covering the region from 8 to 45°, are responsible for electron identification and pion rejection.

3.3.1 Wire Chambers

To track charged particles emitted from the target, CLAS is equipped with 18 wire chambers - a set of 3 chambers ("regions") in each of the 6 sectors of the detector. Based on the curvature of the track, the momentum of the particle can be deduced. The chambers were designed to track particles with a momentum greater then 200 MeV/c over a range of angles from 8° to 142°. The goals for track resolution at the time of drift chamber design were 0.5% for particle momentum and 2 mrad for particle angle reconstruction. That was achieved by measuring the track in three regions along the particle path with a spatial resolution of 100 μm for each point. The three radial locations in each sector (where the three chambers are located) are referred to as "Region 1", where the chambers surround the target in an area of low magnetic field, "Region 2", that is larger and situated between the magnetic coils where the field is maximum, and "Region 3", with the largest chambers located outside of the magnetic coils (Fig. 20, 22). To fill the available space between the magnetic coils, the chambers are wedge shaped, with the end plates making 60° angle with respect to each other (Fig. 21). The unconventional geometry of CLAS required special design considerations [51]. The drift chambers have thin endplates and low-profile wire connections and on-board preamplifiers to conceal inactive areas of the detector within the shadow regions of the torus cryostat. In order to reduce multiple scattering, the total amount of material in the tracking region of CLAS was required to be less than 1% of a radiation length.

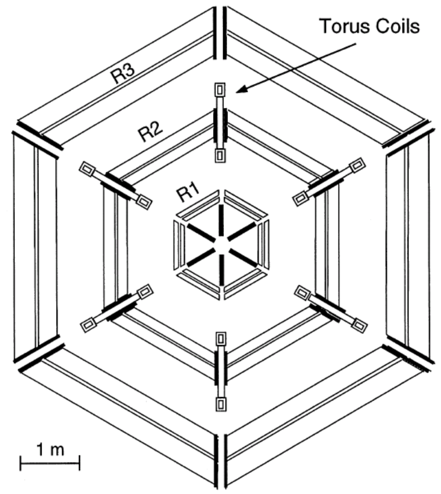

FIG. 20: Vertical cut through the drift chambers transverse to the beam line at the target location showing the geometric relationship of the detectors.

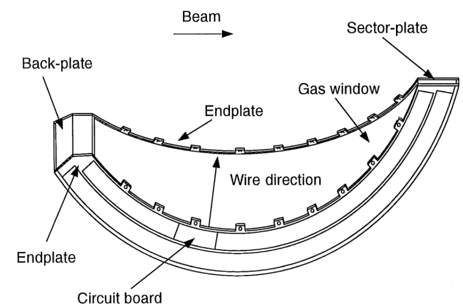

FIG. 21: Schematic representation of a typical drift-chamber sector (R3 in this case) highlighting some of the common hardware pieces used by each.

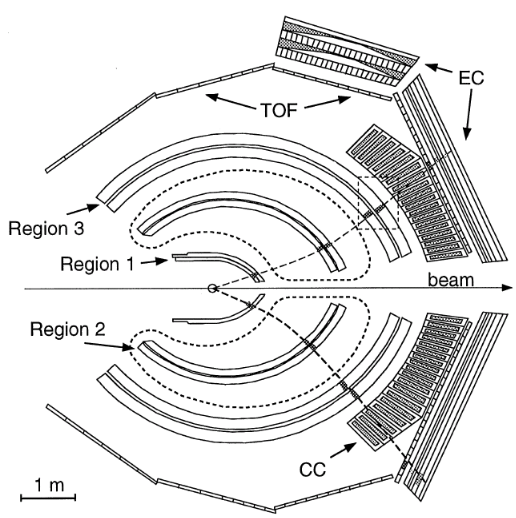

FIG. 22: Horizontal cut through the CLAS detector at beam line elevation showing two charged particles transversing the drift chambers in opposite sectors. The dotted lines show the projection of the torus coils on the sector mid-plane. Fig. 23 shows an enlargement of the boxed area.

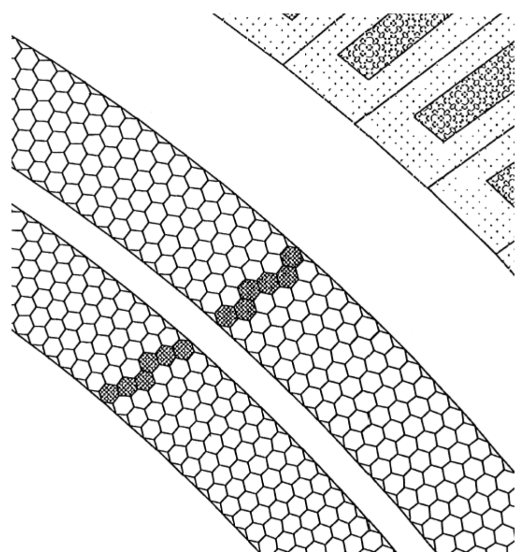

FIG. 23: Representation of portion of an R3 sector showing the layout of its two superlayers. The sense wires are at the center of each hexagons and the field wires are at the vertices.

The CLAS drift chambers contain almost 130,000 wires. To reduce wire aging it uses 20 μm tungsten gold-plated wires. Wires in each chamber are arranged in groups of two superlayers, one axial to the magnetic field and the other tilted at a 6° stereo angle around the radius of each layer to provide azimuthal tracking information (Fig. 23). Such a configuration serves the purpose of pattern recognition and also provides tracking information redundancy. Each superlayer consists of six layers of drift cells (with the exception of the first superlayer of Region 1 which has only four), arranged in a "brick-wall" pattern. Each drift cell has a sense-wire in the center with six field-wires around it forming a quasi-hexagonal pattern.

The principle of drift chamber detectors is based on the ability of high-energy charged particles to ionize matter. The volume of each drift chamber region is filled with a 90% argon - 10% CO_2 mixture that was chosen for its fairly high saturated drift velocity (4 cm/μs) and rather low operational voltage plateau with respect to the values of high voltage where breakdown occurs. A charged particle that passes through a chamber drift cell ionizes the gas atoms. The ionization avalanche of electrons produced drifts towards the sense wire and the signal is recorded by the chamber electronics. Drift chambers have to be frequently recalibrated since the track reconstruction depends on the knowledge of the drift time-to-distance function that is strongly dependent on a number of varying characteristics of the state of the gas mixtures (pressure, humidity).

3.3.2 Scintillator Counters

The CLAS Time-Of-Flight (TOF) system, covering an area of 206 m^2, is composed of scintillation counters 5.08 cm thick, 15 and 22 cm wide, and 32 to 450 cm long (Fig. 24). The system serves as the main means of particle identification, by measuring the time a particle travels from the point of interaction inside of the target to the outer boundary of the CLAS detector, where the TOF system is located. In conjunction with the information obtained from the DC about the length of the particle trajectory, the velocity of the particle can be determined as $\beta = r_{sc}/(t{\cdot}c)$, where r_{sc} is the particle pathlength, t is the particle time of flight and $c = 29.97$ cm/ns is the speed of light. CLAS drift chambers also measure the momentum of the charged particles from the track curvature. The mass of the particle can then be reconstructed as $m = \frac{p\sqrt{1-\beta^2}}{\beta}$.

The TOF system was designed with excellent timing resolution for particle identification and good system segmentation for flexible triggering and prescaling. The

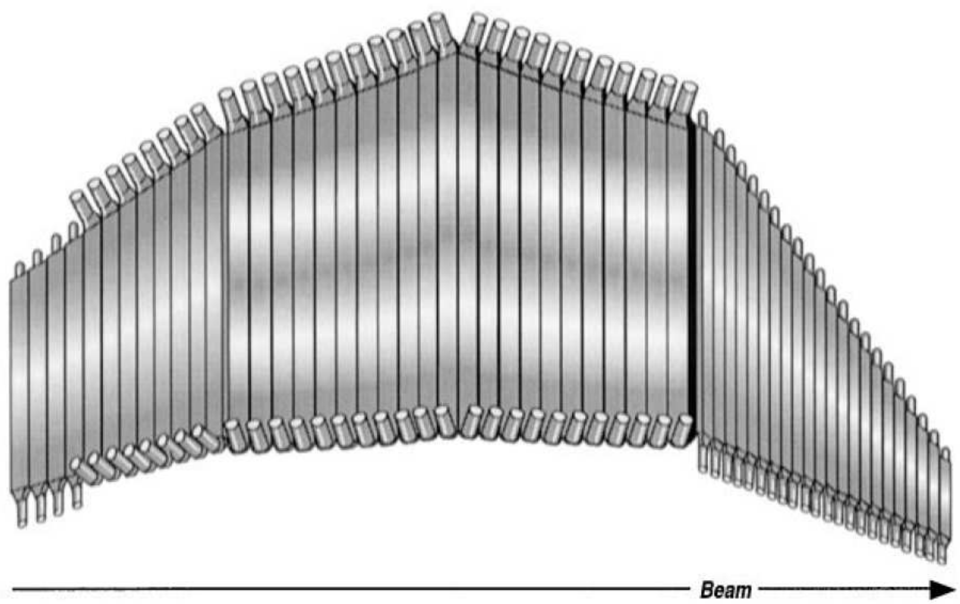

FIG. 24: View of the time-of-flight scintillator counters in one sector.

design time resolution of 120 ps at small angles and 250 ps at angles above 90° allows separation of pions and kaons up to 2 GeV/c. The actual intrinsic time resolution of the detector varies from 80 ps for the short counters to 160 ps for the longer counters [49].

3.3.3 Electromagnetic Calorimeter

The forward region of each sector of the detector is equipped with a lead-scintillator electromagnetic sampling calorimeter (EC). The primary purpose of the EC is detection of and triggering on electrons at energies above a given threshold. The deposited energy information is available at the trigger level to reject minimum ionizing particles [50]. The calorimeter can also detect neutral particles (photons and neutrons). The detector is made of alternating layers of scintillator strips and lead sheets with a total thickness of 16 radiation lengths. The thickness ratio of lead to scintillator is 0.2. In such a configuration about 1/3 of the shower energy is deposited in the scintillator. The EC modules are equilateral triangles and match the hexagonal geometry of CLAS. Each of the 6 modules contains a sandwich of 39 layers of 10 mm thick scintillator followed by 2.2 mm thick lead sheet (Fig. 25). The area of the

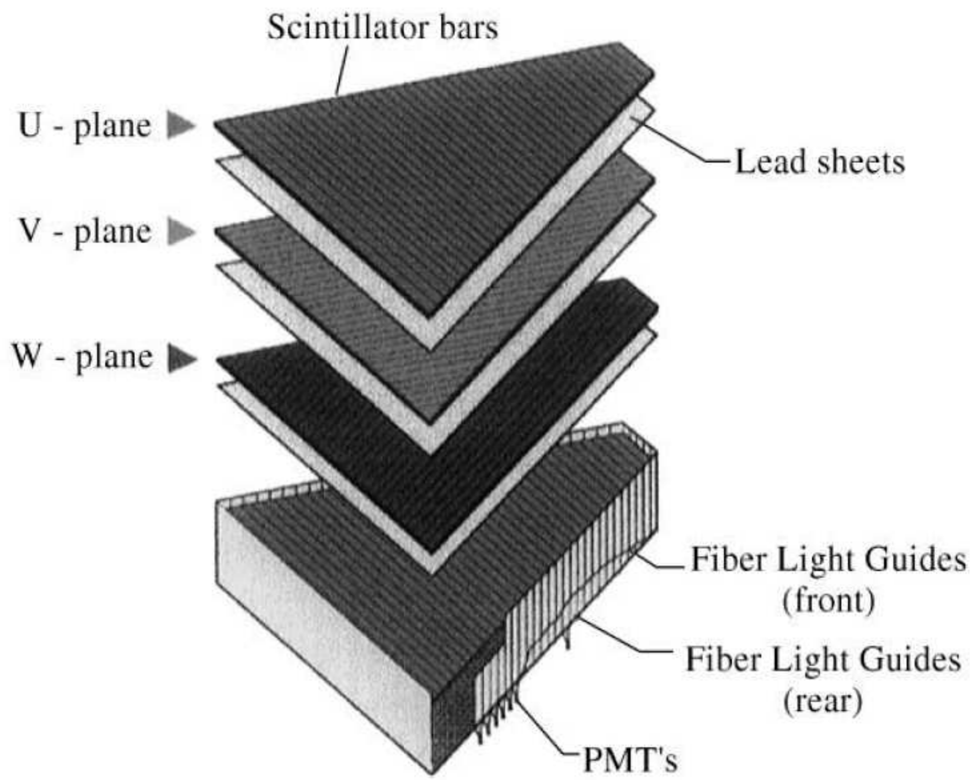

FIG. 25: Exploded view of one of the six CLAS electromagnetic calorimeter modules.

layers progressively increases to minimize shower leakage at the edges and reduce the dispersion in the signal arrival time from different layers of scintillators. For the purpose of readout, each scintillator layer is made of 36 strips parallel to one side of the triangle, with the orientation of the strips rotated by 120° in each successive layer (Fig. 25). Different strip orientations are labeled U, V and W, each one having 13 layers, which provide stereo information on the location of energy deposition. Each view (U, V or W) is also subdivided into 5 inner and 8 outer layers. The calorimeter electronics were designed to sum 36 photomultiplier anode signals belonging to the same U, V or W view. Two other electronics modules also provide summation in various combinations, including U+V+W separately for inner and outer layers as well as the total energy sum.

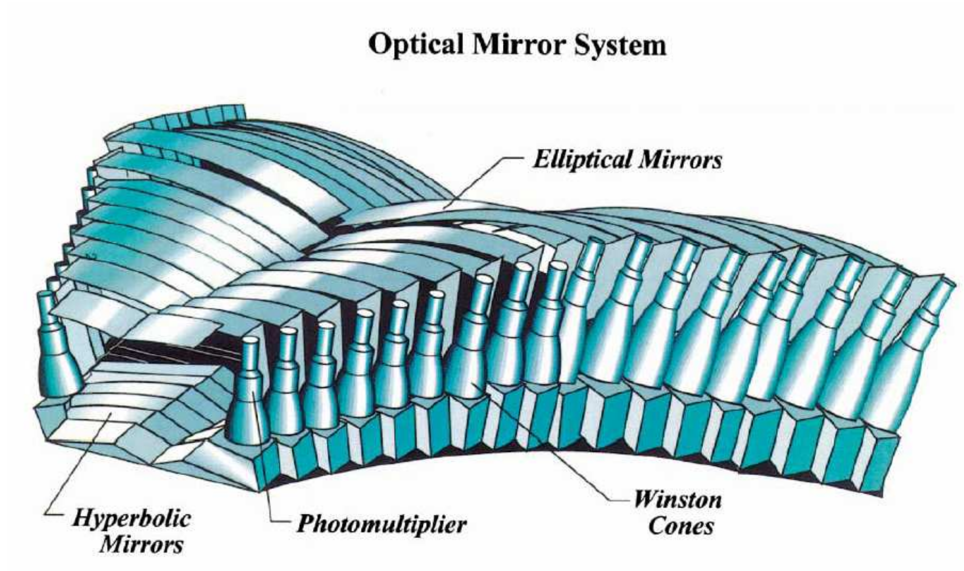

FIG. 26: A schematic diagram of the array of optical modules in one of the six sectors.

3.3.4 Cherenkov Counters

The Cherenkov Counter (CC) serves the functions of triggering on electrons and separating electrons from pions. The CC operates based on the physical effect discovered by Cherenkov: a particle traveling through a medium with a speed exceeding the speed of light in this medium emits electromagnetic radiation. The speed of light in a medium is related to the index of refraction in this medium, $v = c/n$, where c is the speed of light in vacuum and n is the index of refraction of the medium. The threshold for Cherenkov light emission is then:

$$\beta = \frac{v}{c} = \frac{1}{n} \tag{36}$$

The CLAS Cherenkov detector uses perfluorebutane gas (C_4F_{10}) as its medium. The index of refraction of perfluorbutane is 1.00153 which corresponds to a threshold in the particle's energy of:

$$E = \frac{m}{\sqrt{1-\beta^2}} = \sqrt{\frac{n}{n-1}}m = 18.09 \cdot m \tag{37}$$

with m being the mass of a particle. For pions the threshold is $p_\pi \approx 2.5$ GeV/c.

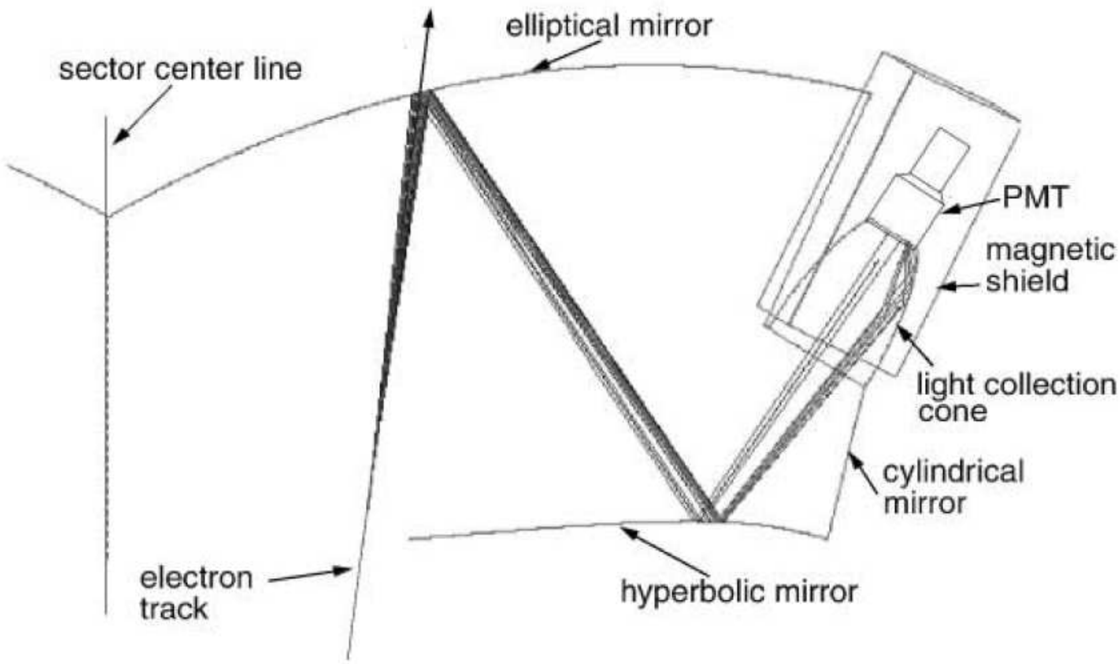

FIG. 27: Optical arrangement of one of the 216 optical modules of the CLAS Cherenkov detector, showing the optical and light collection components.

Due to the toroidal configuration of the magnetic field within a detector the trajectories of particles incident on the CC plane lie approximately in planes of a constant azimuthal angle ϕ, thus the light collection optics is designed to focus light in $\phi-$ direction [53]. The CC detectors in each sector is subdivided into 2 identical subsectors that each contain 18 collections modules (Fig. 26). The optics focuses the light onto a PMT located in the region obscured by the coils. The optical elements of each module consist of two focusing mirrors, a "Winston" light collection cone and cylindrical mirror at the base of the cone (Fig. 27). PMTs are mounted at the base of each "Winston" cone for Cherenkov light detection, which is mostly ultraviolet.

The Cherenkov detector is known to have variations in the optical collection efficiency associated with the individual mirror segments. Except for isolated spots at the midplane, where gaps between the mirrors are largest, the electron efficiency within a fiducial region should exceed 99%. Outside of the region of high optical collection efficiency, the photo-electron efficiency decreases rapidly and this region has to be excluded from the analysis using fiducial cuts.

3.4 TARGET

The scattering chamber (Fig. 29) was installed in the center of CLAS to allow for the detection of the most backward going particles. The target cell was also manufactured with the target cryogenics and support structures appearing only at $\theta > 140^o$ with respect to the beam line to allow free passage for the most backward going particles. It was also the first time that a target cell of such a small diameter was used in CLAS. Smaller target size minimizes the energy loss and allows lower momentum particles to reach the detector systems and be reconstructed. The kapton (7.2 mg/cm^2) target cell diameter is 1.2 cm upstream and 0.7 cm downstream. The shape of the cell allows target material bubbles (hydrogen or deuterium) produced by the incident electron beam to escape the cell easily. Aluminum entrance and exit windows are 4 mm in diameter and have a thickness of 15 μm. The target cell is thermally insulated with 5 layers of aluminized mylar (0.88 mg/cm^2 per layer), each layer of which is combined with a layer of cerex (1.0 mg/cm^2 per layer). The physical length of the target cell is 5 cm (Fig. 28). The target cell is contained within the vacuum of the scattering chamber. The scattering chamber walls are built out of foam with 64 mg/cm^2 density and the chamber is covered with a nylon (4.0 mg/cm^2) safety sock. Connected to the scattering chamber is the exit tube, which is made out of carbon fiber and epoxy. Particles coming from electron scattering within the target cell volume and detected within the CLAS acceptance do not pass through the scattering chamber exit tube. The scattering chamber exit window is a 71 μm thick aluminum foil.

Two different materials were used to fill the target cell over the course of the experiment: liquid deuterium and liquid hydrogen. At the nominal temperature of 22 K and pressure of 1315 mbar, liquid deuterium has a density of 0.162 g/cm^3 [54]. The liquid hydrogen target was kept at 20 K and 1100 mbar that corresponds to a density of 0.0711 g/cm^3 [55].

FIG. 28: E6 target cell with plumbing exposed (top) and with heat shields in place (bottom).

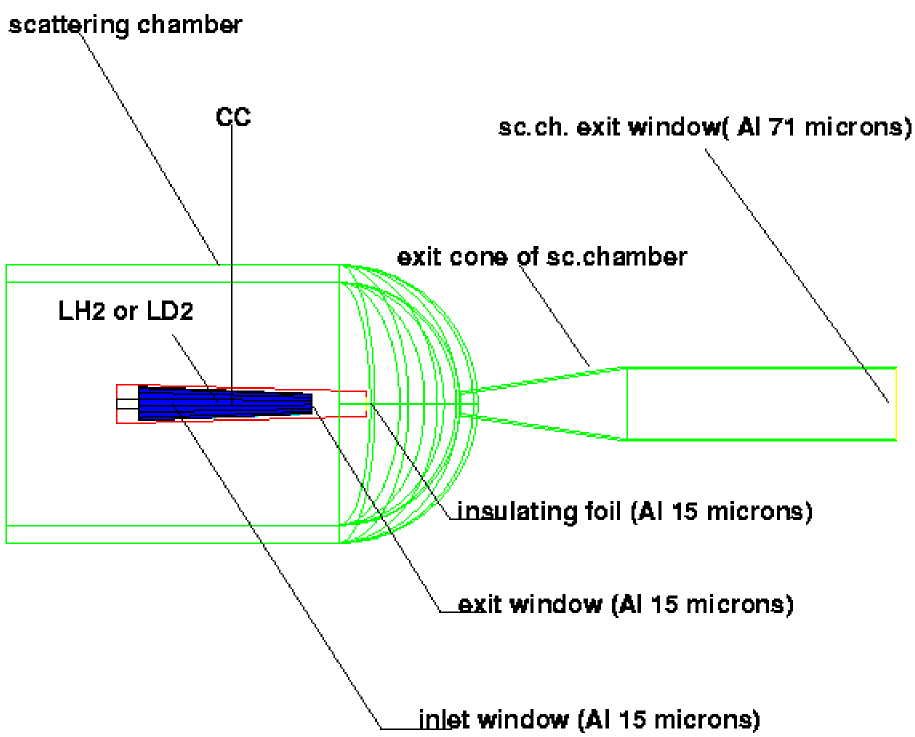

FIG. 29: E6 target layout.

CHAPTER 4

DATA ANALYSIS

This experiment, E94-102, and its analysis, presented here, were proposed in 1994. The experiment ran as a part of the E6 run group from January 30th till March 16th, 2002 in Hall B of the Jefferson Laboratory. A polarized electron beam with 5.75 GeV energy and an average current of 8 nA was used. The achieved luminosity on the liquid deuterium target was 1.1×10^{34} cm$^{-2} \cdot$ s^{-1}. The data were collected at two different configurations of the magnetic field: inbending and outbending. This dissertation covers only the data taken with the standard, inbending, magnetic field setting. The trigger was defined by a coincidence between the Cherenkov counter (a signal of at least 1 photo-electron corresponding to 100 mV) and the electromagnetic calorimeter (a total deposited energy of at least 0.5 GeV was required corresponding to 172 mV). The level 2 trigger that requires a track candidate in the sector of the calorimeter hit was also used. With such a trigger configuration the data rate was about 3 kHz and the dead time was usually less then 13%. Two more trigger configurations, prescaled by a factor of 10 (trigger 7) and 100 (trigger 8), were used to collect a data sample for trigger efficiency studies. Trigger 7 had the Cherenkov threshold lowered to 0.2 photo-electrons and the threshold for the total deposited energy in the calorimeter reduced to 240 MeV. Trigger 8 did not require a signal in the Cherenkov counter. The complete information on trigger setup is presented in Table I. The amount of data collected during the 40 days of the experimental run is summarized in Table II.

Trigger Bit	Prescaled	CC, mV	EC_{inner}, mV	EC_{tot}, mV	Level 2
1-6	1	100	72	172	yes
7	10	20	72	80	no
8	100	0	0	80	no

TABLE I: E6A trigger setup. The Cherenkov detector thresholds are given in column "CC, mV". 100 mV trigger setup corresponds to the requirement of 1 photo-electron. The threshold of the energy deposited by the electron in the inner layers of the calorimeter is given in column EC_{inner} and column EC_{tot} contains the thresholds of the total deposited energy. A calorimeter trigger setting of 1 mV corresponds approximately to a 3 MeV threshold.

Target	Magnet Setup	Data Collected (mC)	Data Collected (triggers $\times 10^6$)
Liquid Deuterium (LD_2)	2250 A	9.4855	4055.43
LD_2	-2250 A	0.7793	452.87
Liquid Hydrogen (LH_2)	2250 A	0.6622	209.31
LH_2	-2250 A	0.2436	66.14
Empty (E)	2250 A	2.9387	77.83
E	-2250 A	0.4703	78.51
Total LD_2	-	10.2448	4508.3
Total LH_2	-	0.9058	275.45

TABLE II: E6A accumulated statistics

This chapter contains a comprehensive, detailed description of all the undertaken steps of the data analysis. The data quality checks together with detector calibrations are first presented. Electron identification cuts and their efficiency are discussed next followed by the description of several studies of the electron spectrum backgrounds. Proton identification cuts are then developed and the question of accidental *ep* coincidences is investigated. The discussion of applied particle kinematic corrections is followed by a complete description of the data simulation and the study of the detector acceptance.

4.1 GOOD DATA FILE SELECTION

Many things can go wrong during the data acquisition process in such a complicated detector as CLAS. Hardware problems can be classified in two general groups: 1) time independent dead parts of the detector present over the whole run period; 2) random small problems appearing and disappearing unpredictably over the course of data acquisition. The first kind of problem can be easily taken into account in the simulation when calculating detector acceptance or simply excluded from the analysis by setting geometrical cuts on the parts of the detector where the problem is known to be present. The second type takes place if some part of the software or hardware system goes down and is brought back up shortly by the shift operator. Unfortunately, it is much more complicated to deal with the second type. The most efficient solution for the second case is to exclude the runs (or parts of the run) where the problem occurs.

The stability of the electron detection efficiency can be monitored using the number of the electrons per accumulated beam charge (38):

$$C = \frac{N_{electron}}{Q_{Faraday\,Cup}} \tag{38}$$

In Fig. 30 this quantity is plotted as a function of run number separately for each sector. A large variation of about 10% on C comes from the fact that the integrated Faraday cup charge is recorded in the data stream every 10 s (for run conditions of this experiment typical charge accumulated on the FC in 10 s is 0.114 μC), while the average total charge accumulated in one data file is approximately $1\mu C$. This is however not an issue when calculating the charge for the whole run (the group of 30 data files), since in that case the uncertainty in the charge remains the same (0.114 μC), but the total charge for the whole run is on the order of 30 μC, i.e. the charge for the whole run period has only 0.4% uncertainty.

Most of the run period in Fig. 30 appears stable with the exception of runs after run #31970, where a significant part of the sector 6 drift chamber in region 1 lost a large section of wires. The inefficient region was then progressively increasing all the way until the end of the experiment. Sector 6 was excluded from the analysis for these runs and the appropriate correction was made to the cross section normalization. In general all the runs with C less then 2000 were not analyzed. An exception was made for sector 5 that had a time independent drift chamber inefficiency. For sector 5 good runs were defined to have $C > 1800$. The files with C above the main band in Fig. 30 were not excluded. Those are usually the very last files in the run with a few events on only a few readings of the Faraday cup charge. That results in a larger then 10% error in the estimation of C. However, only overestimation of electron detection efficiency occurs here, since the FC charge can be only underestimated.

For the purpose of simulation normalization and comparison with data, the total accumulated charge was calculated for different groups of runs. The summary is presented in Table III. Here "golden" runs were defined to have no negative comments in experiment log books. The runs in this group were also required to have at least 10^6 events (20 files). The run was labeled as "silver" if it had no negative records associated with it in the logs, but it had less then 10^6 events. "Poor" runs had some problem noted in the log entry. The problems included drift chamber low and high voltage trips as well as calorimeter and TOF trips. Poor runs were not used for

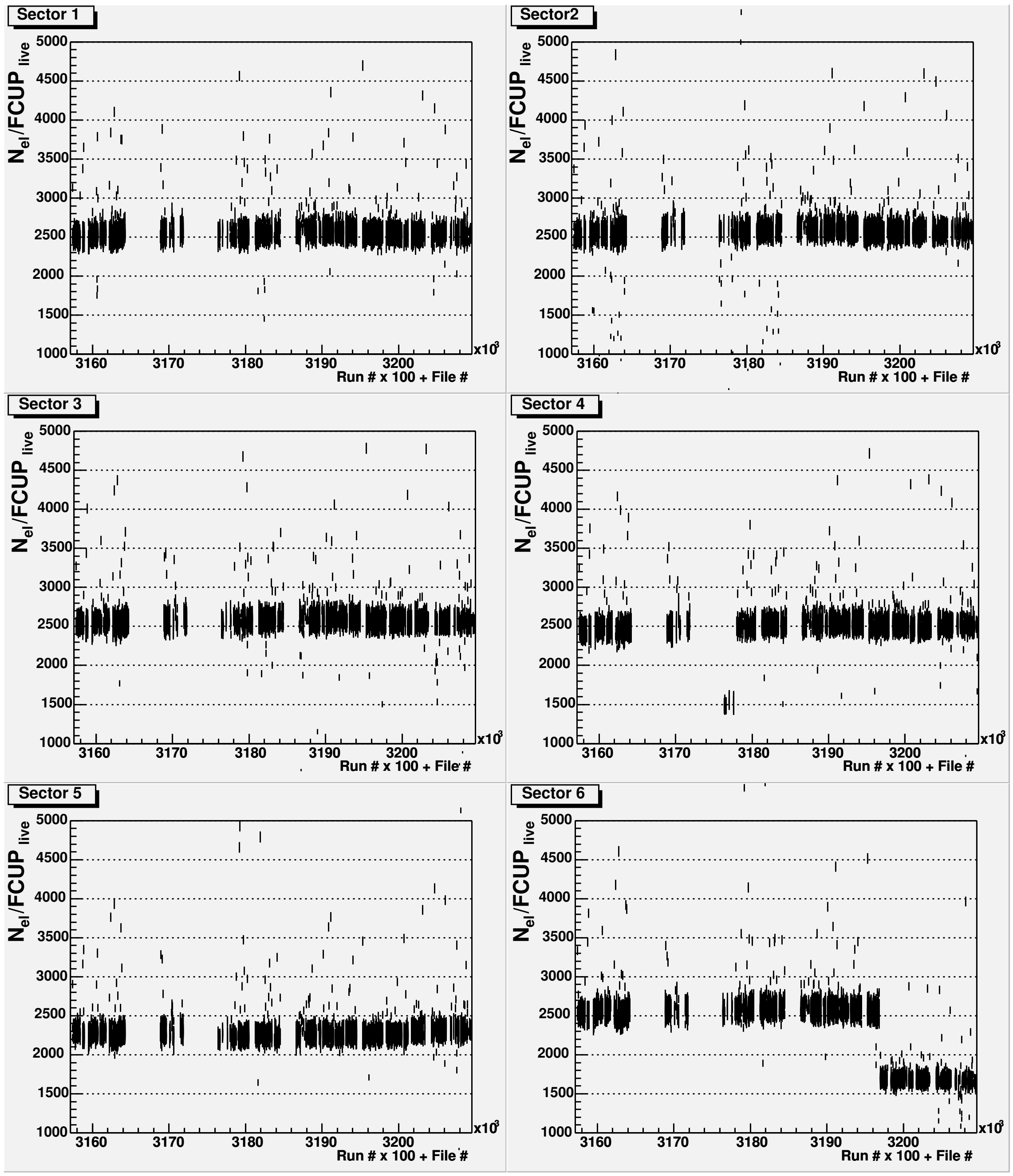

FIG. 30: Number of electrons passing all the cuts found in the file vs run and file number.

Range of Runs	Golden Runs	Silver Runs	Poor Runs
31575-31969	3761.56 μC	256.739 μC	2059.93 μC
31970-32095	2626.96 μC	82.7461 μC	366.835 μC

TABLE III: Accumulated charge of beam electrons over different run ranges for 3 categories of runs, sorted according to their projected quality.

calibration, but were considered for data analysis if they pass the quality reevaluation described above.

4.2 DETECTOR CALIBRATION

Since the detector began its operation in 1998, the CLAS collaboration put great effort in the development of a calibration code for all of the detector systems. Drift chambers and the time-of-flight detectors have an established calibration procedure which is commonly done by each run group individually [73, 74]. Cherenkov detectors and electromagnetic calorimeters are not as time consuming to calibrate and the calibration is usually done by the detector experts [75].

Depending on different conditions (atmospheric pressure, humidity, etc.) the ionization properties of the drift chamber gas mixture can change, thus changing the drift time recorded by the chamber electronics. The drift time also depends on the entrance angle of the particle into the DC cell, the velocity of the particle, and the strength of the magnetic field in the region. To take all these factors into account, the dependence of the drift distance on time can be parameterized in terms of a power law (39):

$$x(t) = v_0 t + \eta \left(\frac{t}{t_{max}}\right)^q + \kappa \left(\frac{t}{t_{max}}\right)^p \tag{39}$$

where t_{max} is the drift time of the electron along the longest path from the far-most corner of the cell, v_0 the value of the saturated drift velocity near t=0, η and κ , q and p are parameters determined from a fit [51, 52].

Each sector has 3 independent wire chambers, called Regions 1, 2 and 3. Within each region there are 2 superlayers of wires. Each superlayer contains 6 layers of sense wires (the first superlayer of Region 1 has only four). The track of the particle

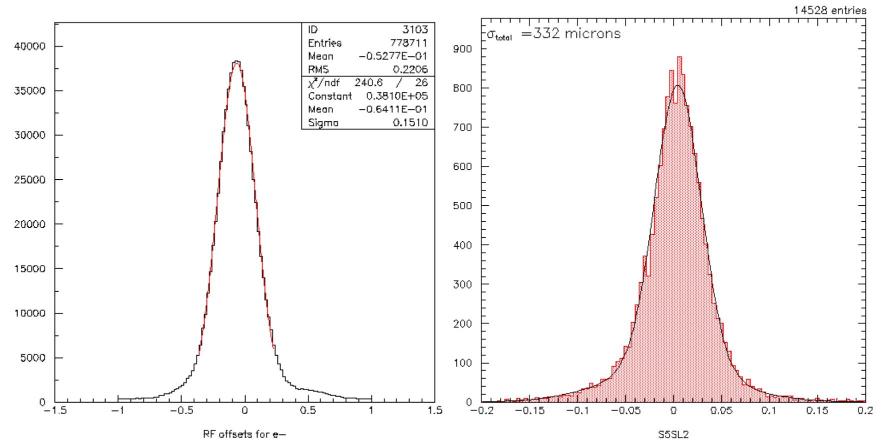

FIG. 31: Radio-frequency offsets (TOF) - left; drift chamber spatial residuals - right.

is reconstructed by fitting it to the wires in all 6 superlayers that have a drift time information for a given event. Each set of parameters is found separately for each superlayer in each region of each sector, that totals to 36 sets of parameters.

A good resolution in DC and TOF timing was achieved for the run conditions of the experiment as compared with other run groups. The TOF resolution is defined as the width of the distribution of the difference between the expected time of arrival of the trigger particle (electron) to the SC detector and the one recorded by the SC. The expected arrival time is obtained by back-tracking the electron to the target and associating it with a certain beam bunch using a time stamp generated by the accelerator in sync with the beam bucket (RF signal). According to the Gaussian fit (Fig. 31), the TOF resolution for this experiment is approximately 150 ps. The resolution of the drift chambers is evaluated using the so-called spatial residual that is calculated from the formula $Residual = FitDOCA - CalcDOCA$. DOCA stands for "the distance of the closest approach". $CalcDOCA$ is the distance from the wire to the track as it is calculated from the drift to distance function (39) using the parameters obtained from the calibration fit. $FitDOCA$ is the distance from the wire to the actual fitted track. Drift chamber resolutions are in general very sensitive to the run conditions. We observed a dependence of the width and mean of the distribution (Fig. 31) on such variables as the occupancies of the DC, energy of the beam, etc. The width of the residuals distribution also usually increases with the increase in the number of the superlayer. Our spatial resolution for track reconstruction was found to be $\sim$400 μm for Region 1, $\sim$425 μm for Region 2 and $\sim$500μm for Region 3. The E1-6 experiment, that collected data with hydrogen target at the same beam energy of 5.75 GeV, achieved comparable DC resolutions of $\sim$390 μm for Region 1, $\sim$475 μm for Region 2 and $\sim$550μm for Region 3. Time resolution of the TOF for E1-6 is 142 ps.

Calibration constants can also have a time dependence. The only way to deal with it is to check the stability of the constants over the whole run period, and if necessary, select a new set of constants. The most sensitive to environmental conditions are drift chamber constants. DCs had to be recalibrated twice for the analyzed data set. The time dependence of the DC residuals after the final calibration iteration is shown in Fig. 32. There are no major fluctuations over the experimental run in the drift chamber residuals with an exception of sector 6 closer to the end of the run. That is a result of DC inefficiency discussed earlier in section 4.1.

Calibration of the scintillator counters and electromagnetic calorimeter were also tested against time deviations. Fig. 33 shows the time-of-flight resolution plotted as a function of the run number and the average value of RF offsets also plotted versus run number. No drastic changes can be seen throughout the experimental run. At the end of the run, data were collected using the inverted magnetic field setup. That explains a step in TOF resolution around run 32095. It can be seen that better TOF resolution was achieved for the outbending part of the run than for the inbending.

Fig. 34 shows the sampling fraction of the calorimeter as a function of run number and the calorimeter time resolution. The sampling fraction of the calorimeter is lower for runs 31764−31776 due to the known malfunction of the EC during this period of time. These runs were excluded from the data analysis. The sampling fraction increased slightly around run 31780 when a different set of pedestal constants was entered in a calibration database. This is a minor change and does not affect particle identification efficiency.

4.3 ELECTRON IDENTIFICATION

4.3.1 Cherenkov Detector Fiducial Cuts

Electron fiducial cuts are set to eliminate the region of the detector where the Cherenkov counters are inefficient. The Cherenkov detector was part of the hardware

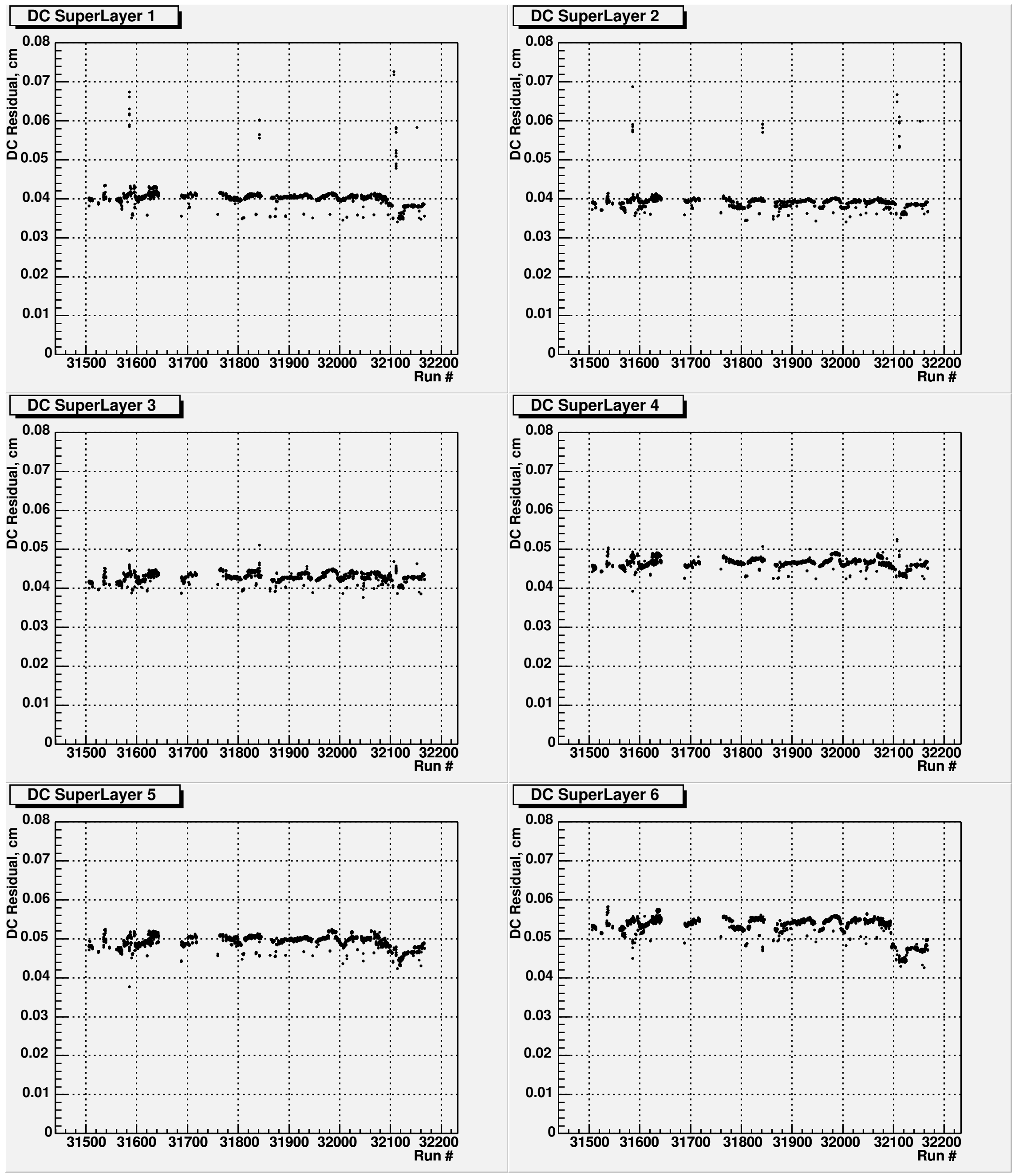

FIG. 32: Drift chamber residuals dependence on the run number for all 6 superlayers.

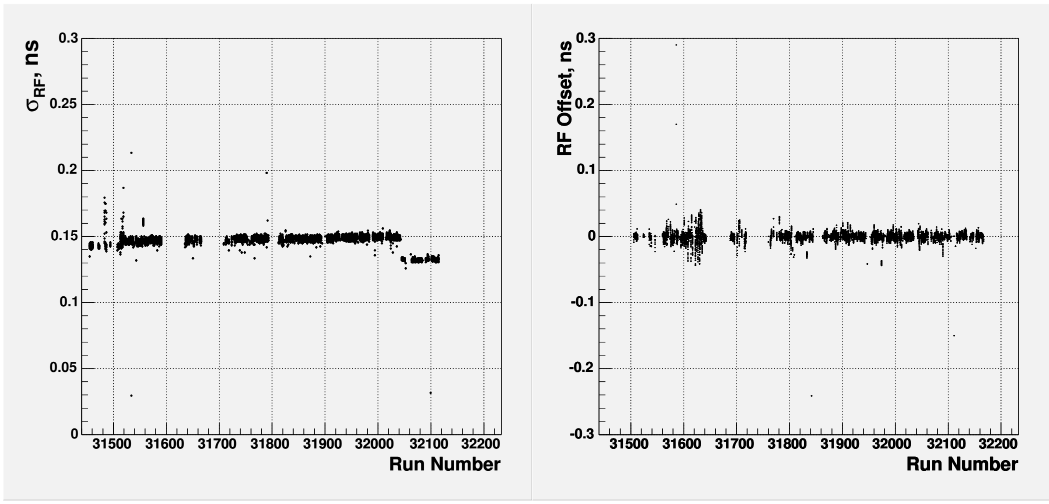

FIG. 33: TOF resolution (left) and mean value of RF offsets (right).

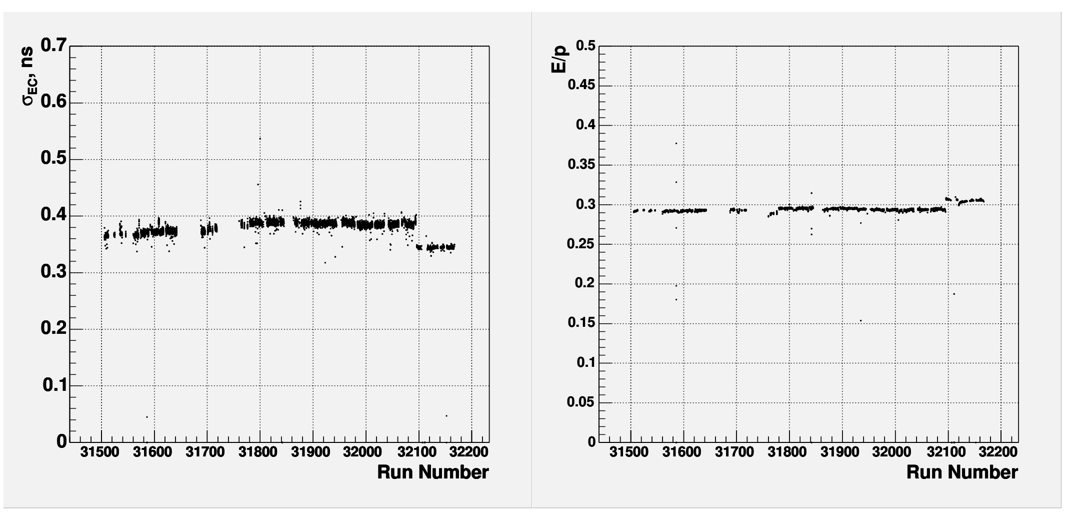

FIG. 34: EC time resolution (left) and mean sampling fraction of EC (right).

trigger during the experiment to reduce the pion contamination of the recorded, raw data set. The trigger was set to 100 mV, which corresponds on average to 1 photo-electron registered by the PMT (see Table I). Therefore, it is very important to use only the part of the data set where an electron is detected in a region of CC efficiency not less than 90%. This requirement gives a guarantee of comparably small systematic error related to Cherenkov counter efficiency.

CC efficiency estimation is a highly non-trivial task. The CLAS Cherenkov counter expert, Alexander Vlassov, came up with a method to calculate the expected number of photo-electrons as function of position on the CC plane, entrance angle, and momentum of a particle. The method was implemented in the form of a C (programming language) function and was used here to estimate the efficiency of a detector. The Cherenkov Counters are very efficient in pion rejection up to $P \approx 2.5$ GeV/c, where pions start to emit Cherenkov light. At momenta $P > 3.0$ GeV/c the CC completely loses efficiency in pion rejection. For lower momenta of the particle $P < 3.0$ GeV/c a software cut of 2.5 photo-electrons to identify an electron was required. At this threshold, Poisson statistics show that 90% efficiency requires an expected average signal of 5.4 photo-electrons. For the part of the data with electron momentum $P_{el} > 3.0$ GeV/c, a software cut of 1 photo-electron was used (that coincides with trigger bits 1-6 settings). According to Poisson statistics, it takes on average 3.3 photo-electrons to reach 90% efficiency above a 1 photo-electron threshold.

CC fiducial cuts were previously applied by other run groups. One of them (Volker Burket, E1) came up with a parameterization function of particle momentum, scattering angle, and magnetic field within the detector volume, to cut the inefficient edges of CC. Parameters of the acceptance cut function need to be adjusted to fit the specific overall detector setup and physical condition of the Cherenkov detector at the time of this experiment. The momentum dependence of the θ cut-off of the acceptance is determined using a two-dimensional histogram of the electron scattering angle vs momentum (Fig. 35). The histogram contains only the events with the average expected number of photo-electrons $N_{phe} > 5.4$. The parameters of the acceptance cut $\theta_{cut}(P_{el})$ were then adjusted for the function to go through the minimum θ with $N_{phe} > 5.4$ for a given value of momentum:

$$\theta_{cut}(P_{el}) = 12.0 + \frac{25.0 \cdot I_{torus}}{3375 \cdot (P_{el} + 0.22)} \tag{40}$$

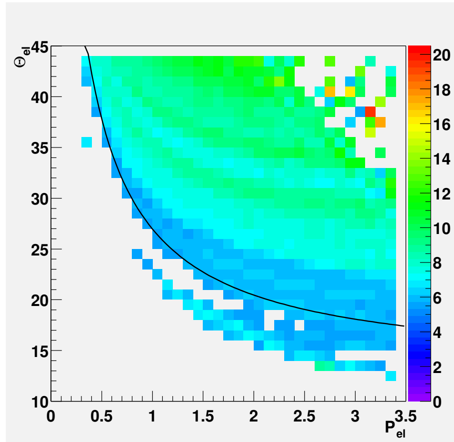

FIG. 35: Momentum of electron vs scattering angle. Colors (shades of grey) represent the average number of photo-electrons as calculated by Vlassov's function. The black line is the $\theta_{cut}(P_{el})$ fiducial cut function. Colorless areas have on average less than 5.4 photo-electrons.

with I_{torus} - torus current [A] and P_{el} - electron momentum [GeV/c].

Then using the distribution of the average number of photo-electrons in the $\theta - \phi$ plane for each of 6 momentum bins in the region of $P_{el} < 3.0$ GeV/c (Fig. 36), the parameters of the azimuthal acceptance $\Delta\phi(\theta, p)$ were fixed:

$$\Delta\phi = 35 \cdot \sin\left((\theta_{el} - \theta_{cut}(P_{el}))\frac{\pi}{180^o}\right)^{\xi} \tag{41}$$

where θ_{el} - polar angle of the detected electron, θ_{cut} - boundary of the cut on polar angle of the electron and ξ is defined with (42):

$$\xi{=}0.33 \cdot \left(P_{el}\frac{3375}{I_{torus}}\right)^{0.33} \tag{42}$$

The same technique was used to define the fiducial cut for $P_{el} > 3.0$ GeV/c to obtain the following functional form (Fig. 37):

$$\theta_{cut}(P_{el}) = 11.5 + \frac{22.5 \cdot I_{torus}}{3375 \cdot (P_{el} + 0.17)} \tag{43}$$

$$\Delta\phi = 42 \cdot \sin\left((\theta_{el} - \theta_{cut}(P_{el}))\frac{\pi}{180^o}\right)^{\xi} \tag{44}$$

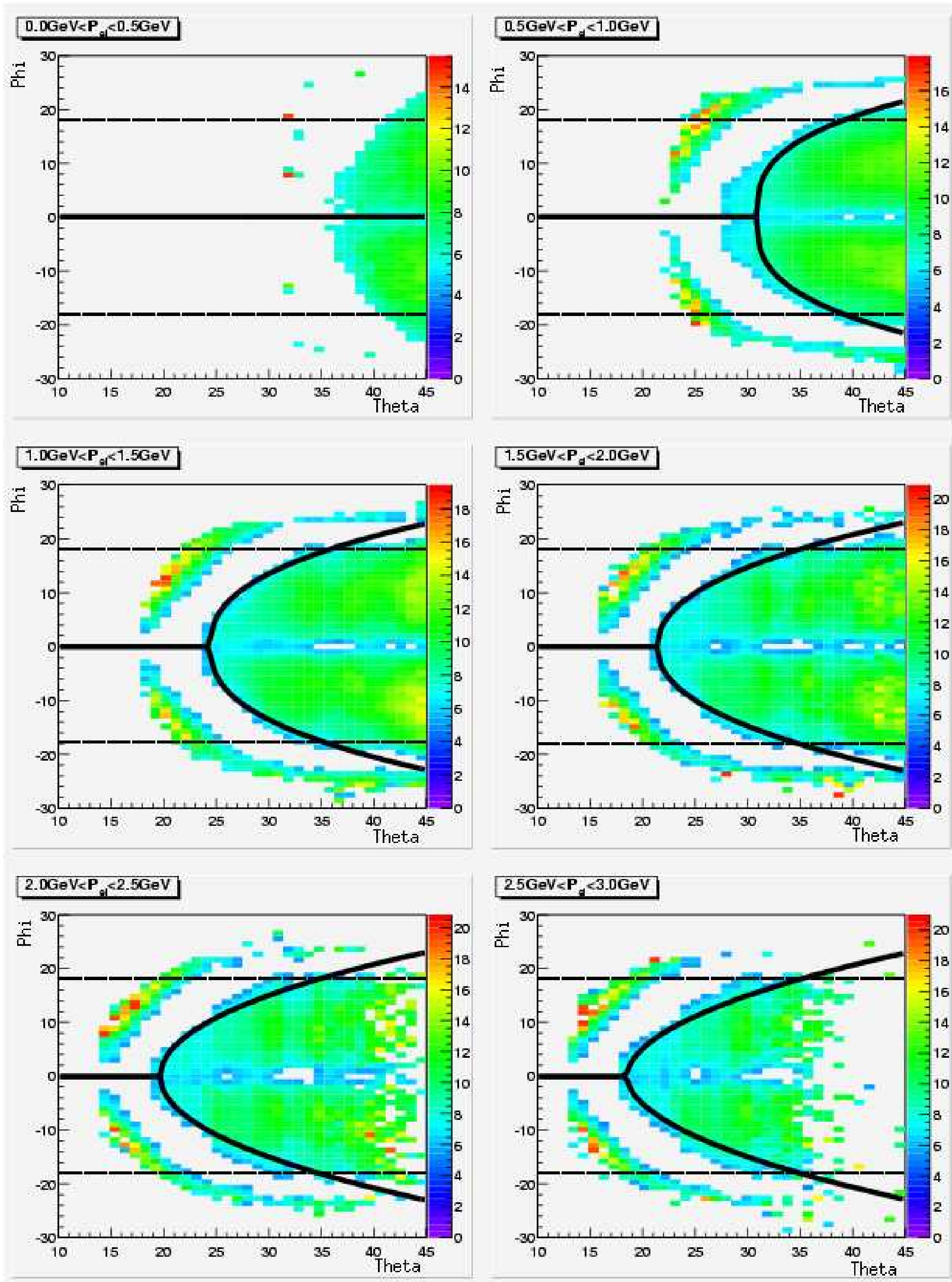

FIG. 36: Azimuthal vs. polar angle of scattered electron for the low momentum part of the data (0.0 GeV/c$<P_{el}<$3.0 GeV/c). Colors (shades of grey) represent the average number of photo-electrons registered by CC as calculated by Vlassov's function. The black solid line represents $\Delta\phi_{el}$ fiducial limits for a range of θ_{el} as defined by function (41). The black dashed line indicates a fixed limit on the maximum and minimum ϕ in a sector. Colorless areas have on average of less then 5.4 photo-electrons.

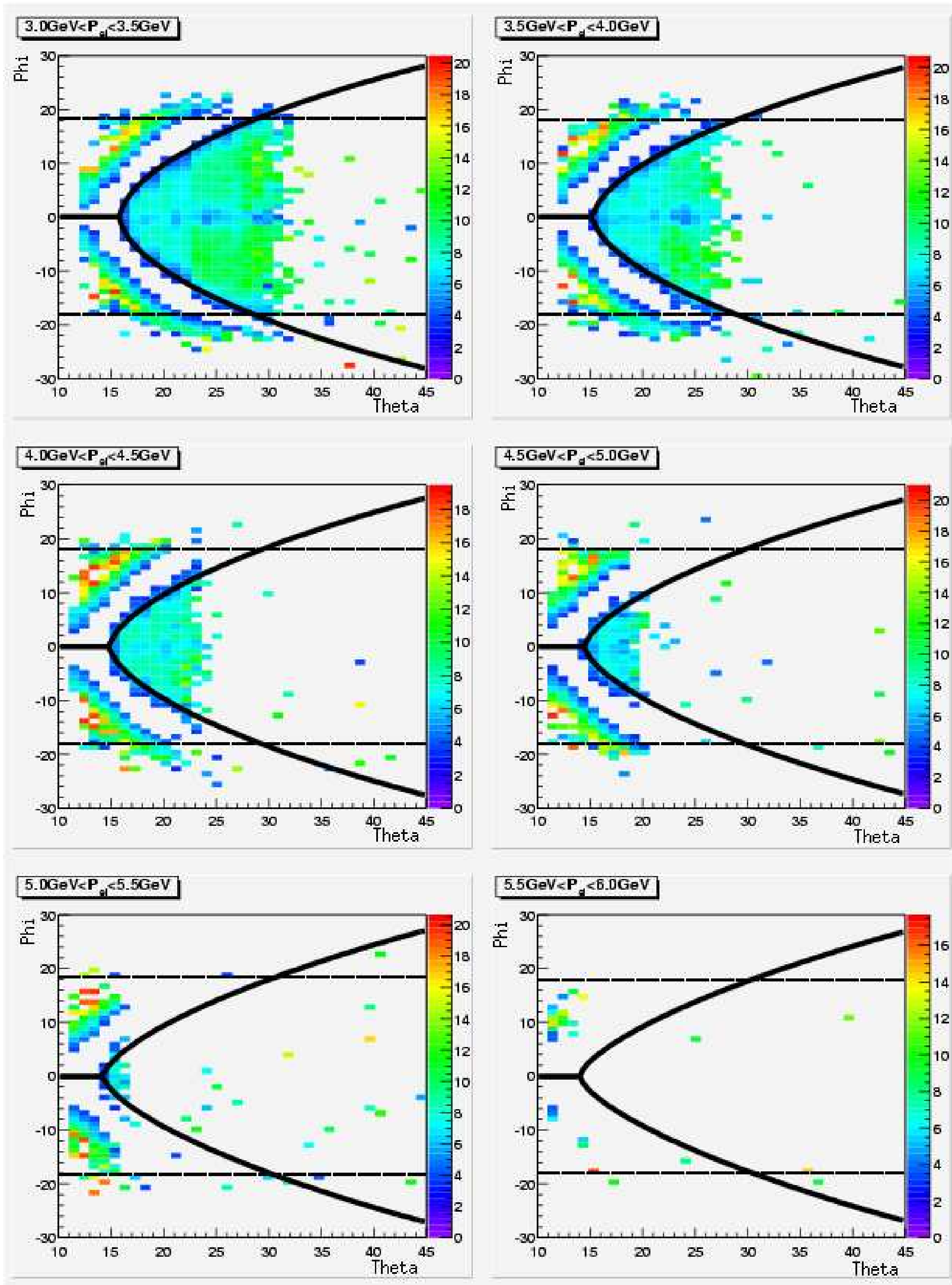

FIG. 37: Azimuthal vs. polar angle of scattered electron for the low momentum part of the data (3.0 GeV/c$<P_{el}<$6.0 GeV/c). Colors (shades of grey) represent the average number of photo-electrons registered by CC as calculated by Vlassov's function. The black solid line represents $\Delta\phi_{el}$ fiducial limits for a range of θ_{el} as defined by function (44). The black dashed line indicates a fixed limit on the maximum and minimum ϕ in a sector. Colorless areas have on average of less then 3.3 photo-electrons.

To eliminate an inefficient region on the very edge of the detector, where the above functions cease to work, the condition was also set for the good electron to be within the angular range: $18^o < \phi_{el} < -18^o$ (dashed lines on Fig. 36 and 37).

4.3.2 Other Electron Identification Cuts

The main contaminant of the trigger particle (electron) spectrum are negatively charged pions (π^-). They can produce more than 2.5 photo-electrons in a highly efficient region of a Cherenkov, by electron knock-out at $P < 2.5$ GeV/c or by Cherenkov radiation at $P > 2.5$ GeV/c. The pion contamination in the electron spectrum was reduced by setting cuts on energy deposition in the electromagnetic calorimeter. In Figs. 38 and 39, the total energy deposited by the first particle in the event in the calorimeter (EC_{total}) is plotted versus energy deposited in the inner layer of calorimeter (EC_{inner}). Both quantities are normalized to the total momentum of the particle. The plots were produced for 12 different ranges of momentum of the electron. The electron produces an electromagnetic shower immediately after it enters the calorimeter, which can be seen in Figs. 38 and 39 as a large sampling fractions signal ($E/p > 0.2$), both in the inner layers of the EC and all of the EC layers together. At the same time, pions make mostly a minimum ionizing signal with a small sampling fraction. It is clearly seen (especially at low momenta), that the minimum ionizing particles band can be easily rejected by requiring $EC_{inner} > 0.08 \cdot P$ and $EC_{total} > 0.22 \cdot P$. The solid line in Figs. 38 and 39 indicate the cut applied in the data analysis to select good electrons.

A vertex cut of $-2.0 < Z_{el} < 1.5$ cm was applied to the data in order to reject electron scattered from the target cell walls (Fig. 40). The scattered electron was also required to have a minimum momentum of 1 GeV/c, to reject the part of a data sample with high levels of pion and e^+e^- contamination (see Sec. 4.3.3, 4.3.4).

4.3.3 Electron Identification Efficiency

To estimate the efficiency of the hardware trigger and data quality cuts, a sample of data with loose hardware and no software cuts in it (trigger bit 8, see Table I), collected over the course of the experiment was used. Due to the loose EC trigger setting and no CC threshold (as well as the absence of the Level 2 trigger requirement), the "trigger 8" prescaled data sample contains almost unbiased pion and electron samples. Electron identification (ID) cuts were applied both to the data

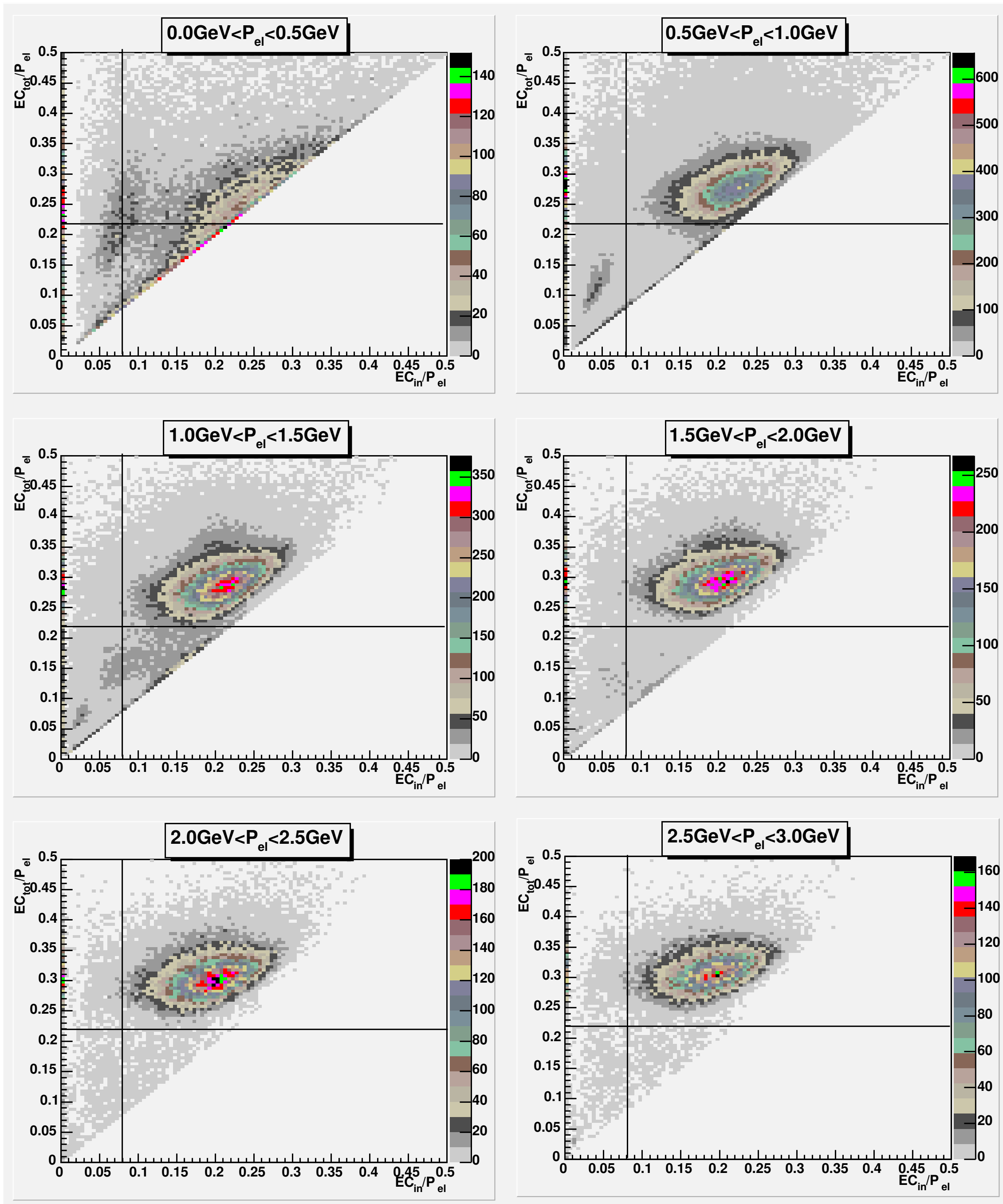

FIG. 38: Total energy deposited in EC vs. energy deposited in the inner layer of EC. Color (shades of grey) represents the number of events in each bin. Solid line indicates an electron ID cut.

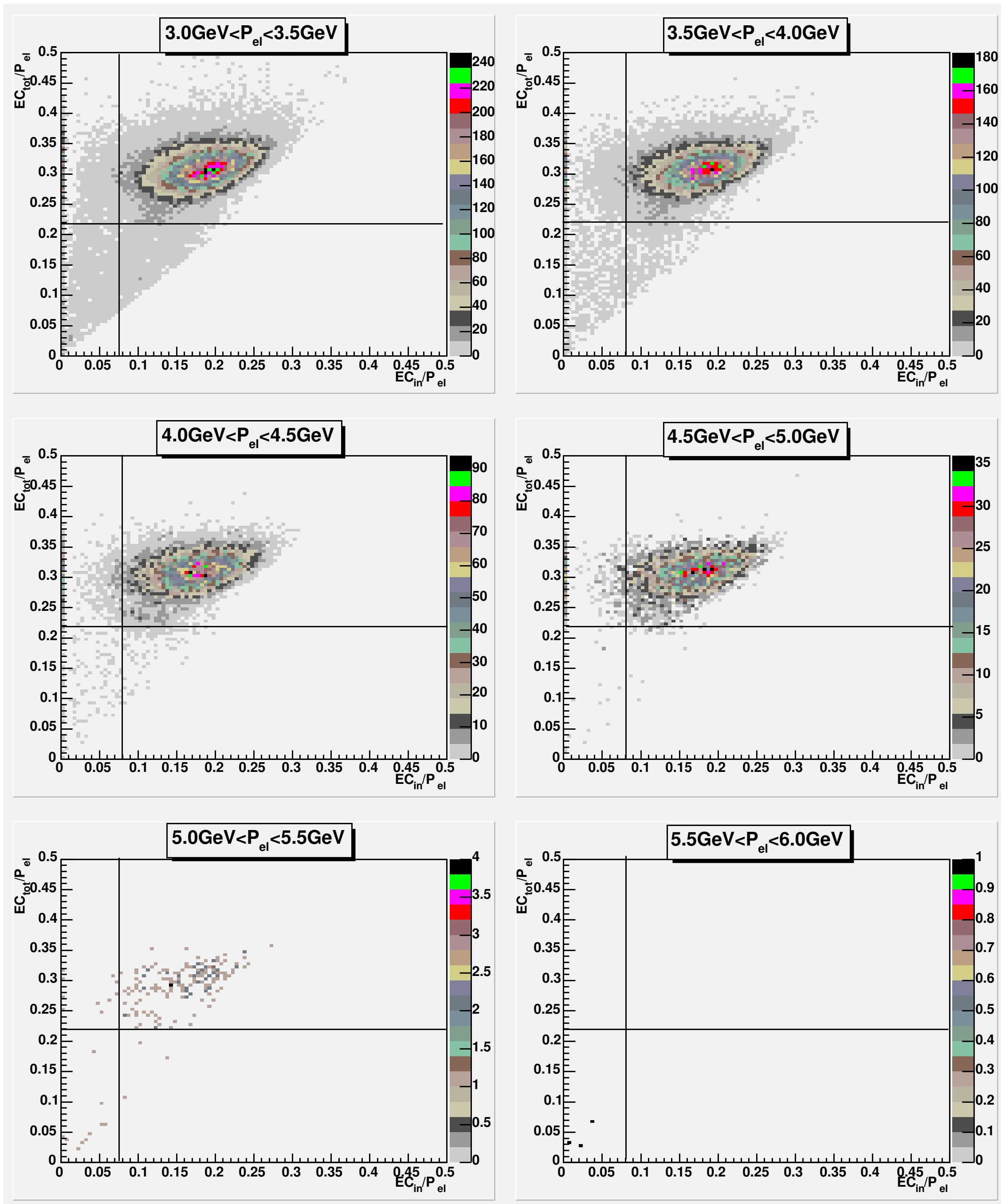

FIG. 39: Total energy deposited in EC vs. energy deposited in the inner layer of EC. Color (shades of grey) represents the number of events in each bin. Solid line indicates an electron ID cut.

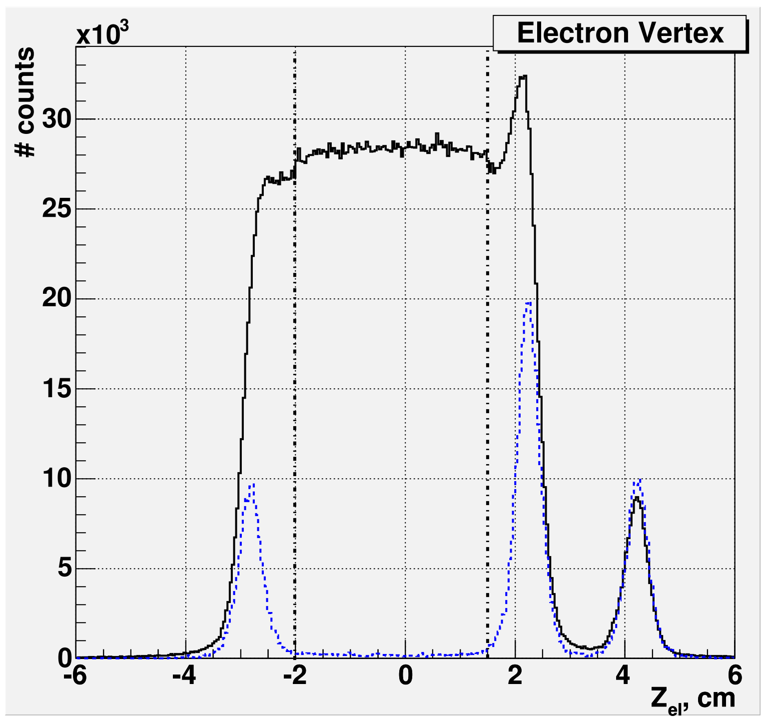

FIG. 40: Electron vertex for the full (solid line) and empty (dashed line) target. Only events with backward proton in coincidence are plotted. Verticle dash-dotted line indicates electron vertex cut.

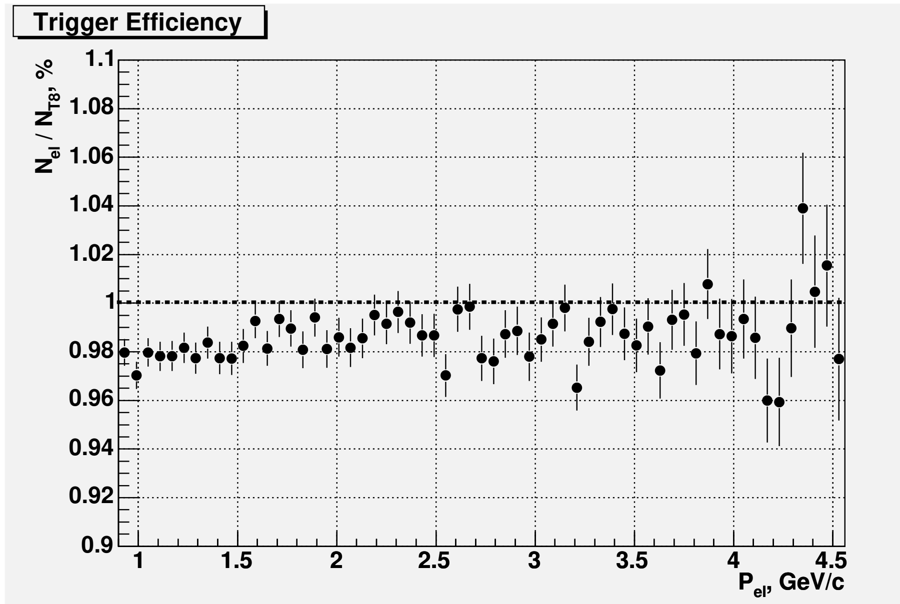

FIG. 41: Trigger efficiency. The ratio of the number of counts in the data set recorded using tight hardware trigger to the number of counts collected with open trigger 8 that pass all software cuts.

with a regular trigger setup and to the prescaled (by a factor of 100) data sample without any hardware thresholds on the electron. The scattered electron momentum and polar angle distributions were then compared for the two to see if there are noticeable trigger inefficiencies in any regions. Based on this study, the trigger was taken to be $98 \pm 2\%$ efficient (Fig. 41).

In the process of data reconstruction, the part of the software code responsible for final data event assembly (known as simple event builder or SEB) always assumed that only the very first particle in the data event can be an electron. However, it is possible to have a situation when the first particle in the event is not really an electron and therefore does not pass the ID cuts. At the same time the real electron might also have been detected and written out in a later position within the event. Those kinds of events were ignored in our analysis. It was estimated by looping over all particles in the event that about 1.4% of the electrons are recorded in secondary positions in the event. This efficiency of $98.6 \pm 1\%$ was used as an overall correction to the data.

A much more complicated task is to estimate the efficiency of the software particle

ID cuts that define a good electron. The electron sample is contaminated with pions and the EC and CC response is used to discriminate negatively charged pions. On the one hand, ID cuts can reject some of the electrons that for one reason or another, although within the region of high detector efficiency, did not have a high enough signal in the detector to pass all the cuts. On the other hand, there is still a fraction of pions that makes it through the ID cuts. Both cases need to be considered, and electron contamination, as well as loss, has to be taken into account.

The CC spectrum of photo-electrons is thought to obey Poisson statistics smeared by finite PMT resolution effects. Based on the measured CC detector spectrum at 1 GeV beam energy the Vlassov parameterization function mentioned earlier was developed by the CC expert. This function was used to simulate the Cherenkov detector response to the scattered electrons. Since the parameterization function was obtained using a data set, taken with slightly different PMT gains, the output of the function had to be multiplied by a constant factor in each of 6 sectors to account for the gain difference and fit our data. The tail of the simulated distribution can be integrated in the region below the software cut to estimate the fraction of electrons that are lost (Fig. 42). It can be seen from Fig. 43 that the electron ID cut on the number of photo-electrons is on average 98% efficient. Instead of applying this correction as a constant scaling factors, the CC detector response was simulated using the Vlassov parameterization function and the CC cut inefficiency was incorporated into the extracted acceptance correction.

"Trigger 8" data was used to select an unbiased sample of pions. The Cherenkov detector spectrum for the number of photo-electrons was produced for pions using the set of EC cuts: $E_{in} < 0.05$, $E_{tot} < 0.1$ (Fig. 44, red dashed line). Then the distribution of photo-electrons for the "perfect" electron was produced using tighter than regular electron ID EC cuts $E_{in}/p > 0.12$ and $E_{tot}/p > 0.23$ (Fig. 44, black solid line). The Cherenkov spectrum of the "perfect" electron was fitted with the sum of the distribution of "golden" pions scaled by factor A and the simulated ideal (no pion contamination) CC response to the incident electrons (Fig. 44, blue dash-dotted line), scaled a factor B. Thus normalized, the "golden" pion spectrum was then integrated above the software ID cuts of 2.5 and 1.0 photo-electrons (depending on the data momentum range) and used to estimate the fraction of pions remaining in the electron sample after the Cherenkov ID cut.

The total fraction of pions relative to the number of good electrons and the

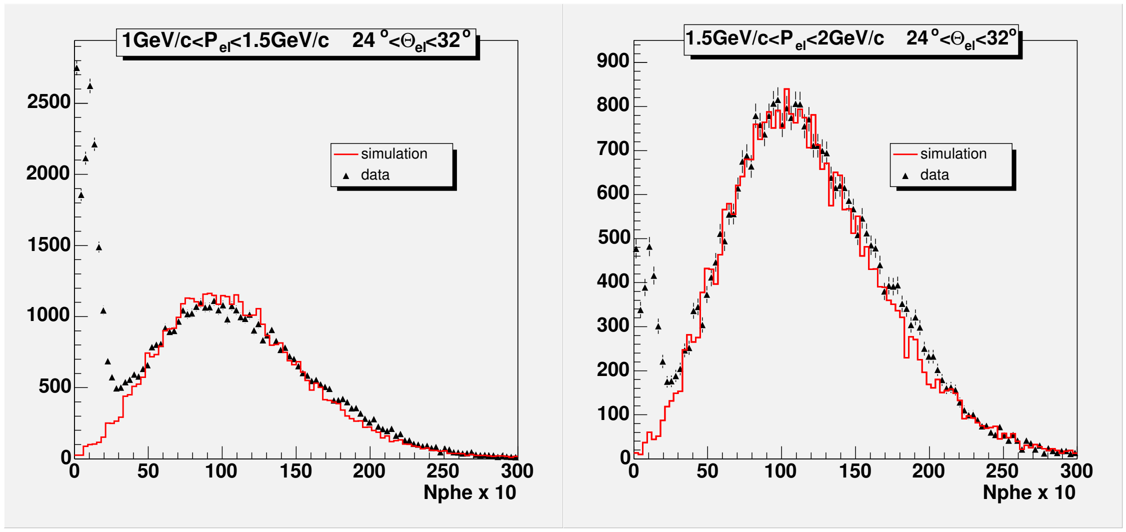

FIG. 42: Example of the simulated Cherenkov detector response to the electron (solid line) overlayed with the electron measured Cherenkov detector response (black triangles).

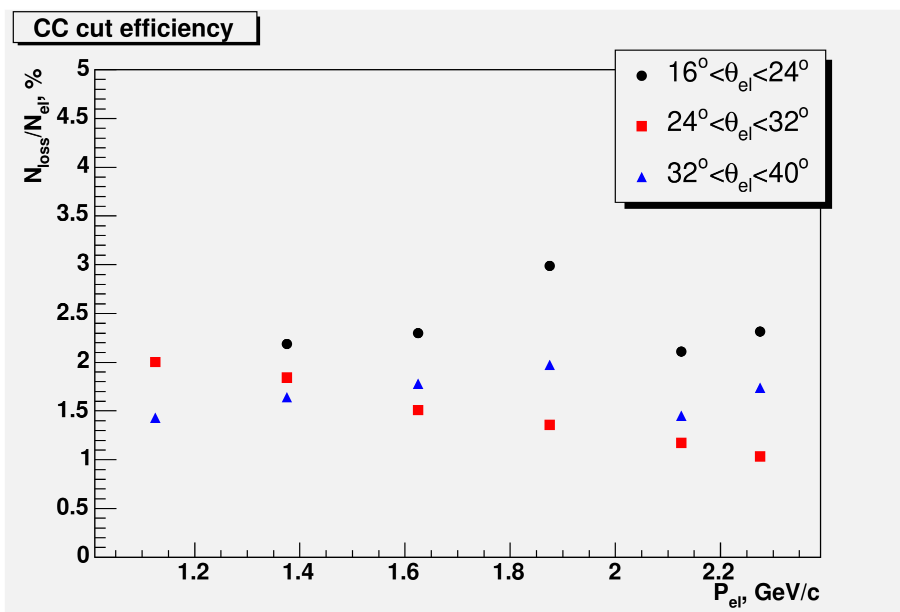

FIG. 43: Loss of the electrons due to the cut on Cherenkov detector spectrum of the electron. The different styles of the points correspond to different ranges in the electron scattering angle.

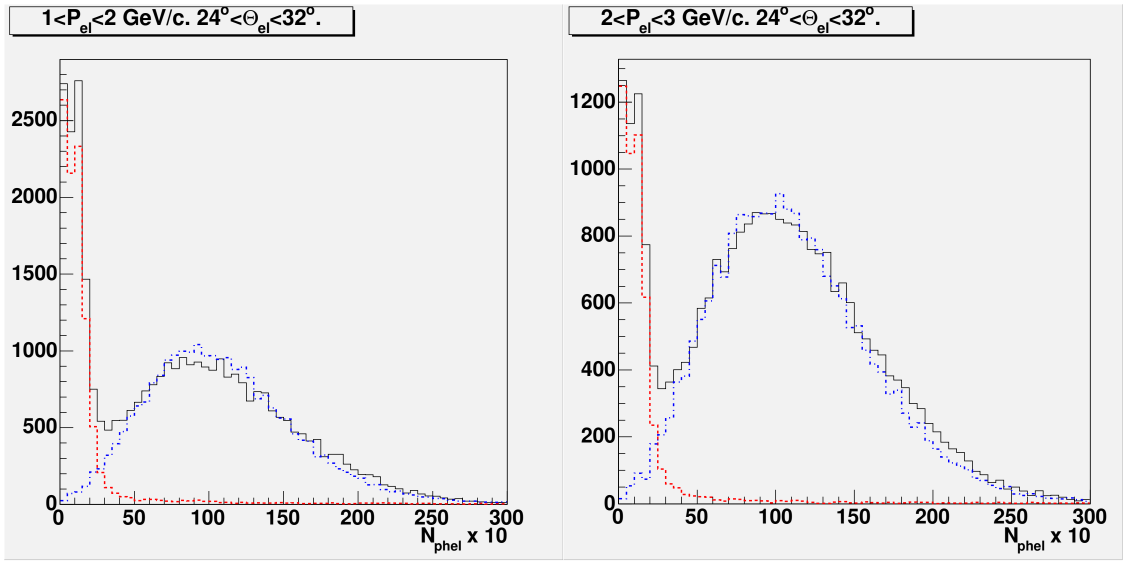

FIG. 44: Example of the electron spectrum from Cherenkov detector (solid line) overlayed with the pion spectrum (dashed line) and CC response simulation (dash-dotted line).

ratio of pions that fall within the CC cuts to the number of good electrons was estimated for the electron momentum range between 1 and 2.6 GeV. The result was then fitted with the function $\frac{N_\pi}{N_{el}} = Ae^{-Bp_{el}}$ (Fig. 46). Using the same functional form, the momentum dependence of the total fraction of pions, relative to the total number of electrons, was extrapolated into the region $P_{el} > 3.0$ GeV/c (Fig. **??**). Since above 2.5 GeV/c the Cherenkov detector cannot efficiently reject pions, an average value between total fraction of pions and pion contamination for a given momentum was used as a conservative upper limit of possible pion contamination. In the region between 2.6 and 3.0 GeV/c the end points of the two functions were linearly interpolated. Obtained functional form for the pion contamination was used to rescale the Monte-Carlo simulation on an event-by-event basis, depending on the momentum of the electron in the event.

The efficiency of the EC cuts was checked by lowering the calorimeter electron ID cuts by 30% with the consequent evaluation of a resulting increase in the number of electrons. To avoid pion admixture, the definition of the electron was simultaneously made more strict by increasing the required number of photo-electrons to the value of 4. From the output of this study, presented in Fig. 47, it can be seen that the EC

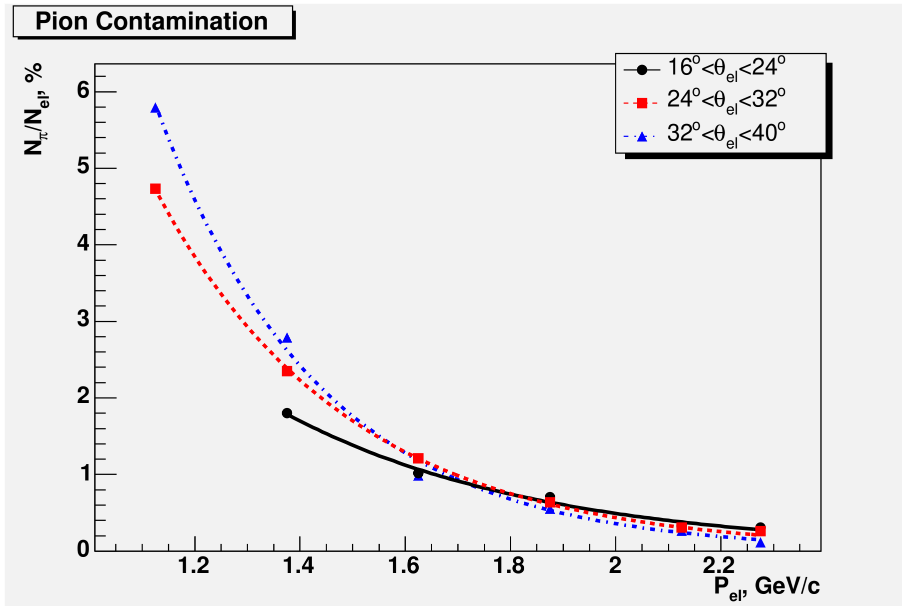

FIG. 45: The fit to the estimated electron spectrum contamination with pion after CC cut. The different curves correspond to different bins in polar angle of the scattered electron.

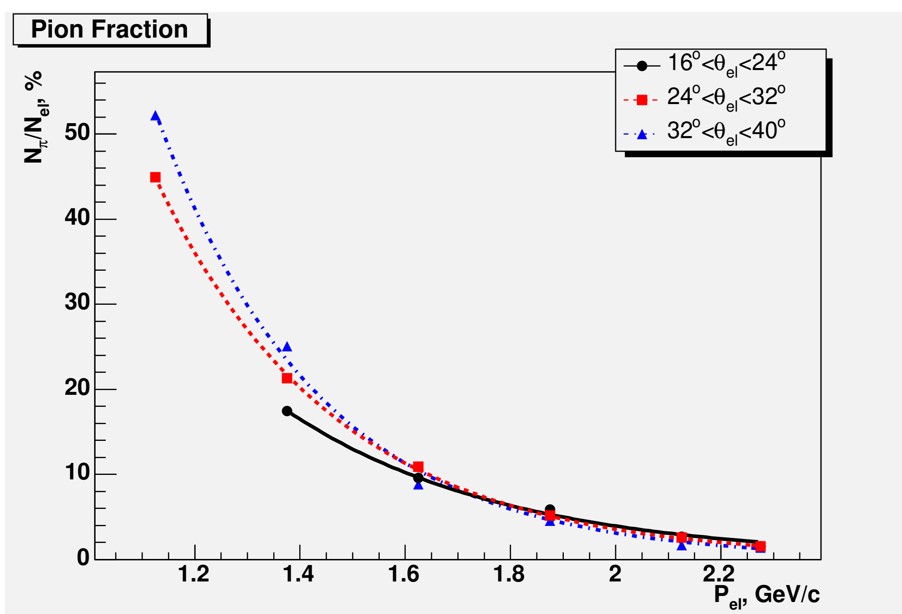

FIG. 46: The fit to the estimated number of pions relative to the number of electrons in the uncut data sample. The different curves correspond to different bins in polar angle of the scattered electron.

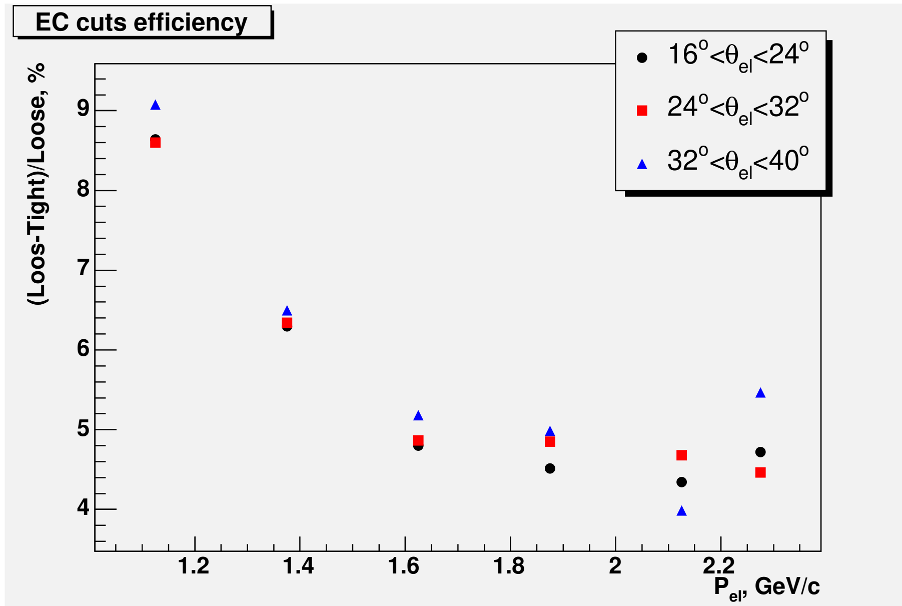

FIG. 47: The relative gain in the number of counts after lowering the EC electron threshold by 30% as a function of electron momentum. The different types of points correspond to different ranges in electron scattering angle.

cut is on average 95% efficient. The increase in the ratio at low electron momenta is believed to be the result of the pion contamination, not cut efficiency fluctuation.

4.3.4 Electron Spectrum Contamination from e^+e^-- pair Production

Another source of contamination of the electron spectrum are the electrons coming from electron-positron pairs, produced from high energy real photons in the $\gamma \to e^+e^-$ process or the Dalitz decay $\pi^0 \to \gamma e^+e^-$. The fraction of that kind of electrons was studied by Peter Bosted for the EG1 experiment. He used the data taken with standard (inbending) magnetic field in the detector volume as well as data taken with the magnetic field in the opposite direction (outbending). The inbending magnetic field bends the negatively charged particles towards the beam line and the outbending magnetic field bends them outwards. The data was separated in 10 bins in momentum and 6 bins in scattering angle ranging between 7 and 40 degrees. Three types of histograms of calorimeter total sampling fraction (E_{tot}/p) were prepared containing: a) electron, using the standard electron ID cuts (similar to those discussed earlier in

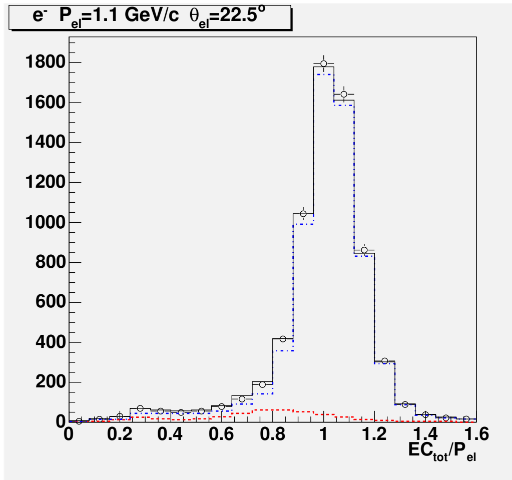

FIG. 48: Electrons. Histograms (a) (black circles), (b) (dot-dashed), (c) (dashed) and the sum of (b) and (c) after fit (black solid). See explanation in text.

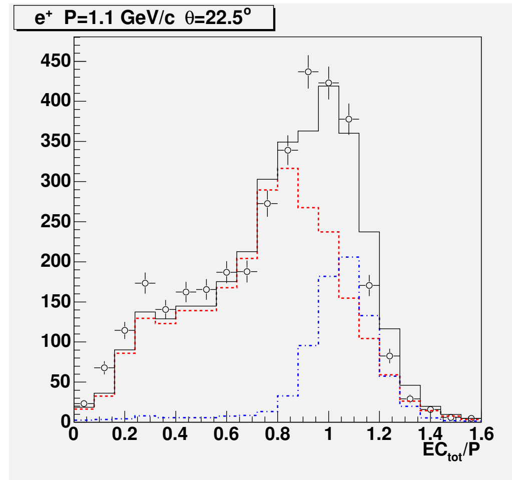

FIG. 49: Positrons. Histograms (a) (black circles), (b) (dot-dashed), (c) (dashed) and the sum of (b) and (c) after fit (black solid). See explanation in text.

this section); b) pions, using CC number of photo-electrons cut: $0.3 < N_{phel} < 1.5$; c) electrons, using a very strict cut $N_{phel} > 6$. The same sets of plots were created for the positrons based on the outbending data set. The two sets of data were cross normalized using the Faraday Cup charge. Histograms (a) were then fitted with the sum of (b) and (c) (see Fig. 48 and 49). The integral of histograms (b) for the positrons was then used as a number of electrons coming from the e^+e^-- pair creation. The integral of histograms (b) for the electrons was used to calculated the ratio.

The obtained ratios were fitted as a function of the electron scattering angle and momentum for convenience of applying a correction. The momentum dependence was first fitted with the exponential function $\frac{e^+}{e^-} = Ae^{-Bp_{el}}$ (Fig. 50). Parameters A and B were then fitted with 3rd and 5th order polynomials respectively to get their dependence as a function of the electron scattering angle. The correction was applied to the Monte Carlo data and became a part of a final correction, extracted together with the detector acceptance.

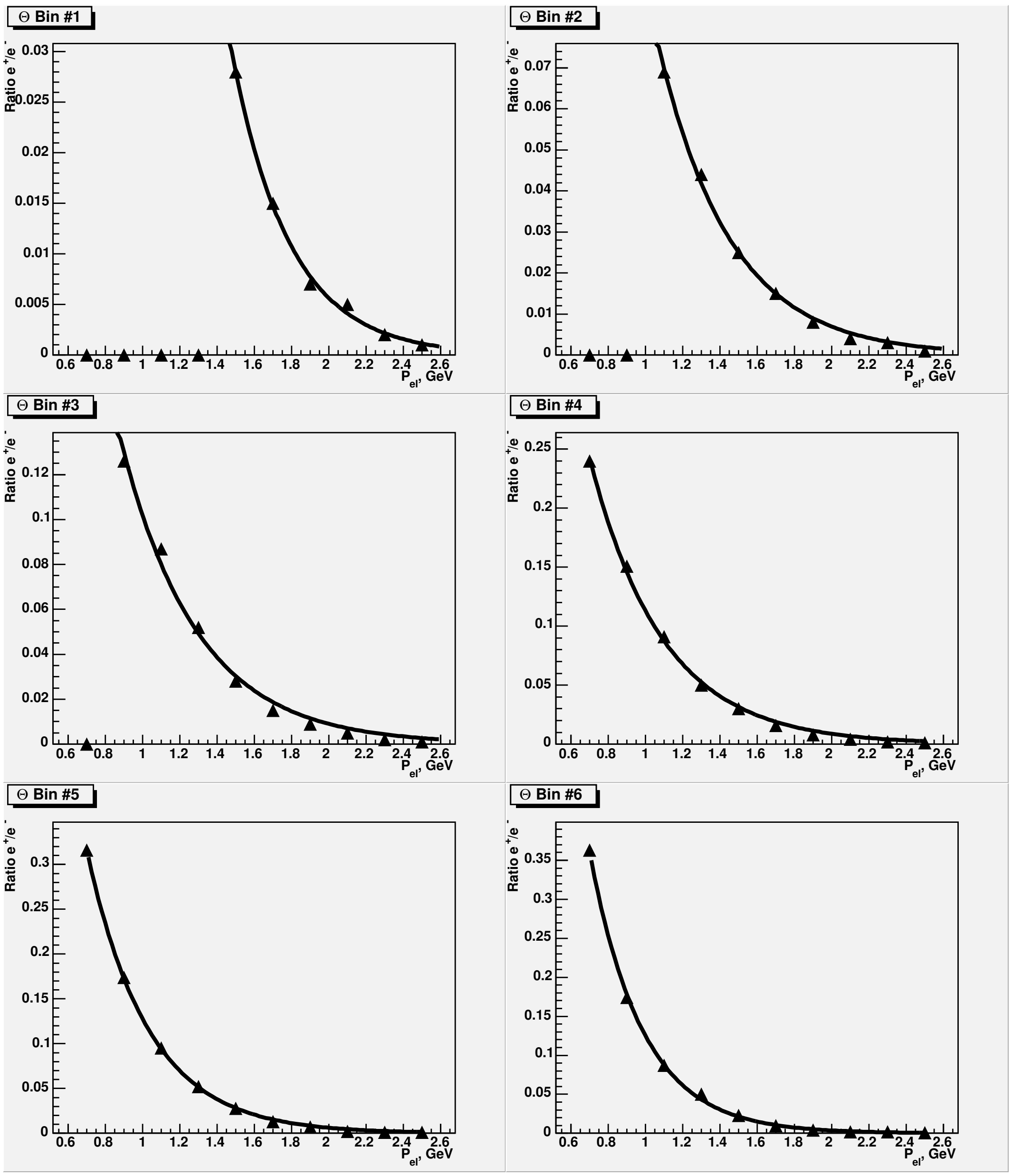

FIG. 50: The fit of the momentum dependence of the positron to electron ratio.

4.4 PROTON IDENTIFICATION

4.4.1 Proton Timing Correction and Selection

Despite being widely advertised as a nearly 4π detector, very few run groups used CLAS to detect particles at very backward angles. As a result, the calibration procedures were never refined for this kinematic region.

When CLAS was constructed a decision was made to equip the last 18 paddles of the SC with only 2 phototubes per pair of paddles. The calibration of these last several paddles is complicated due to the low number of particles that are detected and can be used to calibrate this paddles. The fact that there are 2 actual paddles connected to one PMT on each side makes the ideal calibration almost impossible.

The backward going protons are very important for this study, therefore it was decided to approach the issue of proton identification in this exotic region very carefully. As a result of the study three problems were discovered and resolved: 1) some of the paddles appeared to be inefficient and were excluded from the analysis (an appropriate correction was made to the detector model for the simulation and acceptance calculation); 2) some paddles had an overall time offset ranging from 1 to more than 50 ns; 3) many of the paddles with a paddle ID greater than 39, for which the same set of PMTs is used for read-out, turned out to have two peaks on their time distribution.

As was mentioned, the paddles with low statistics, compared to the same paddles in other sectors of the detector (for example, sector 1 in Fig. 51), were excluded from the analysis. The detector model was also configured not to generate a detector response for these paddles, so that the extracted acceptance would be justified.

Sector 3 in Fig. 51 is a an example of the double peaked time distribution. There is no additional information available, besides paddle ID, to decouple the two maxima. However, there is a variable in the data file that contains the position of the particle as it passes through the SC plane. When plotted as a function of this variable, the timing peaks can be separated by setting a geometrical cut (Fig. 52). After separation, a correction constant can be chosen individually for each of the miscalibrated paddles. The result of the correction is presented in Figs. 53 and 54.

The proton can now be defined as a positively charged particle in any of the secondary positions in the event, detected in the scintillator counter within a -2 to 7 ns window from the expected arrival time of the particle, calculated from its

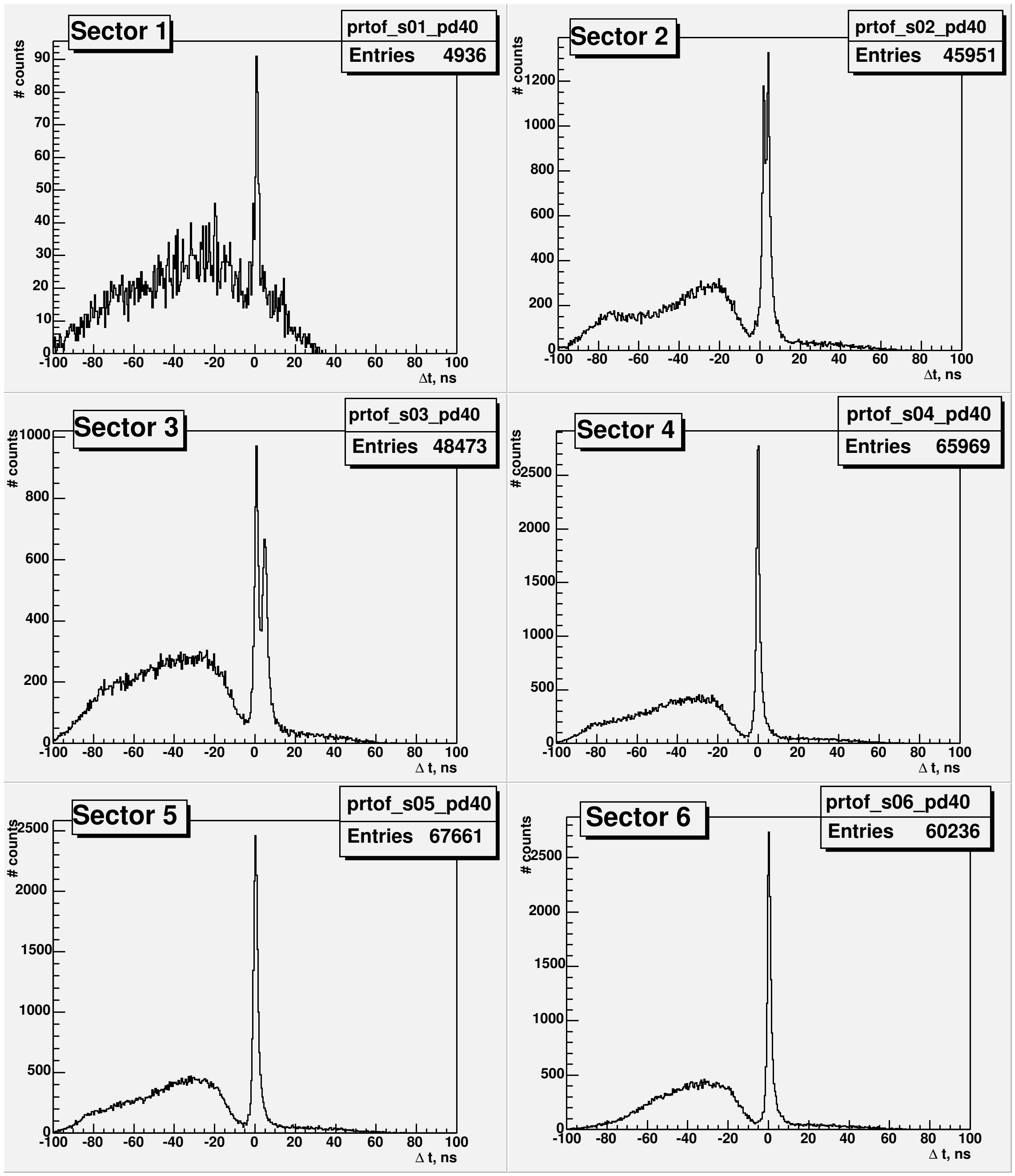

FIG. 51: The proton time vertex, calculated using (45), before the correction for TOF paddle #40.

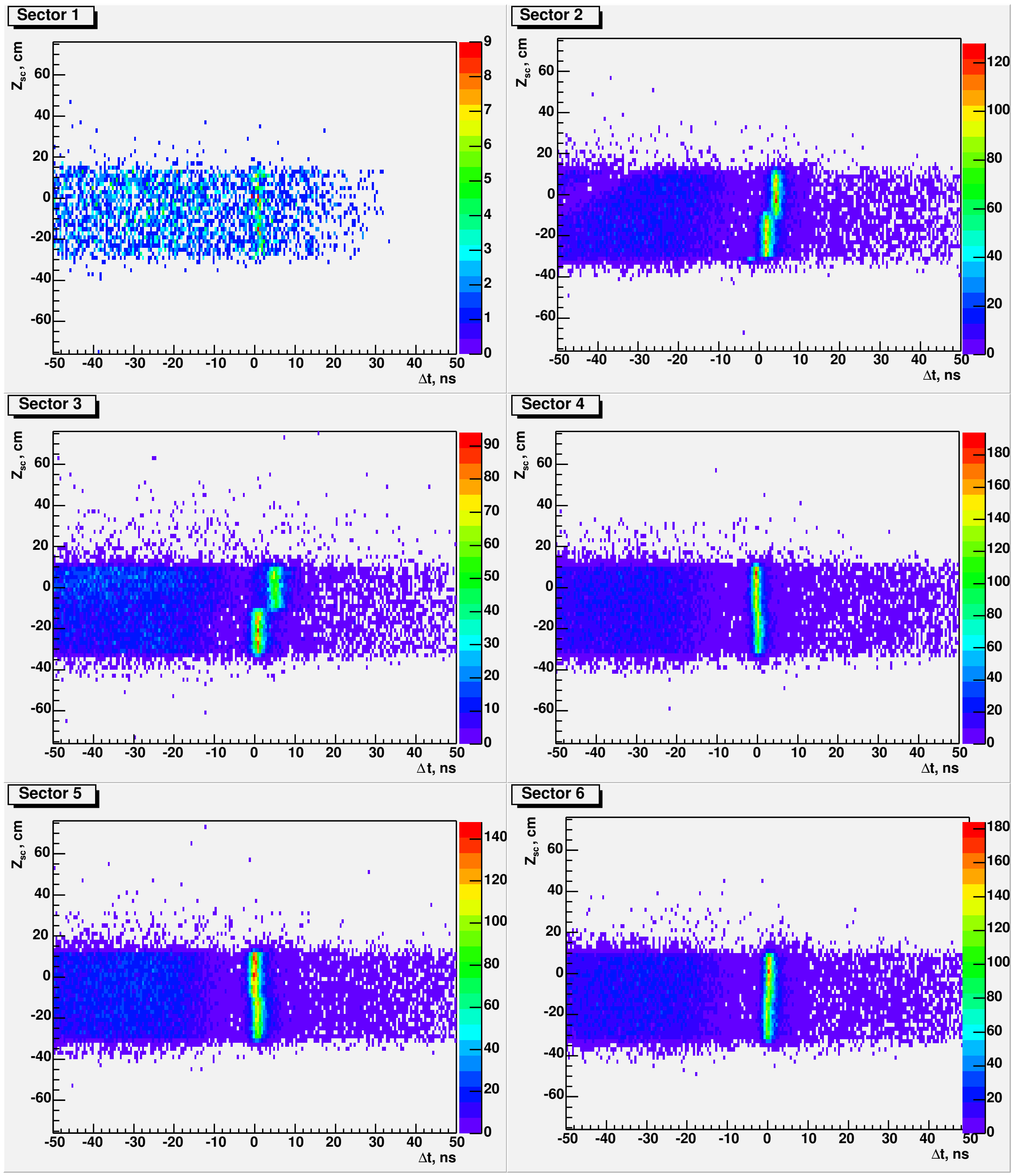

FIG. 52: The particle coordinate on the scintillator plane Z_{sc} [cm] is plotted versus the proton time vertex for TOF paddle #40.

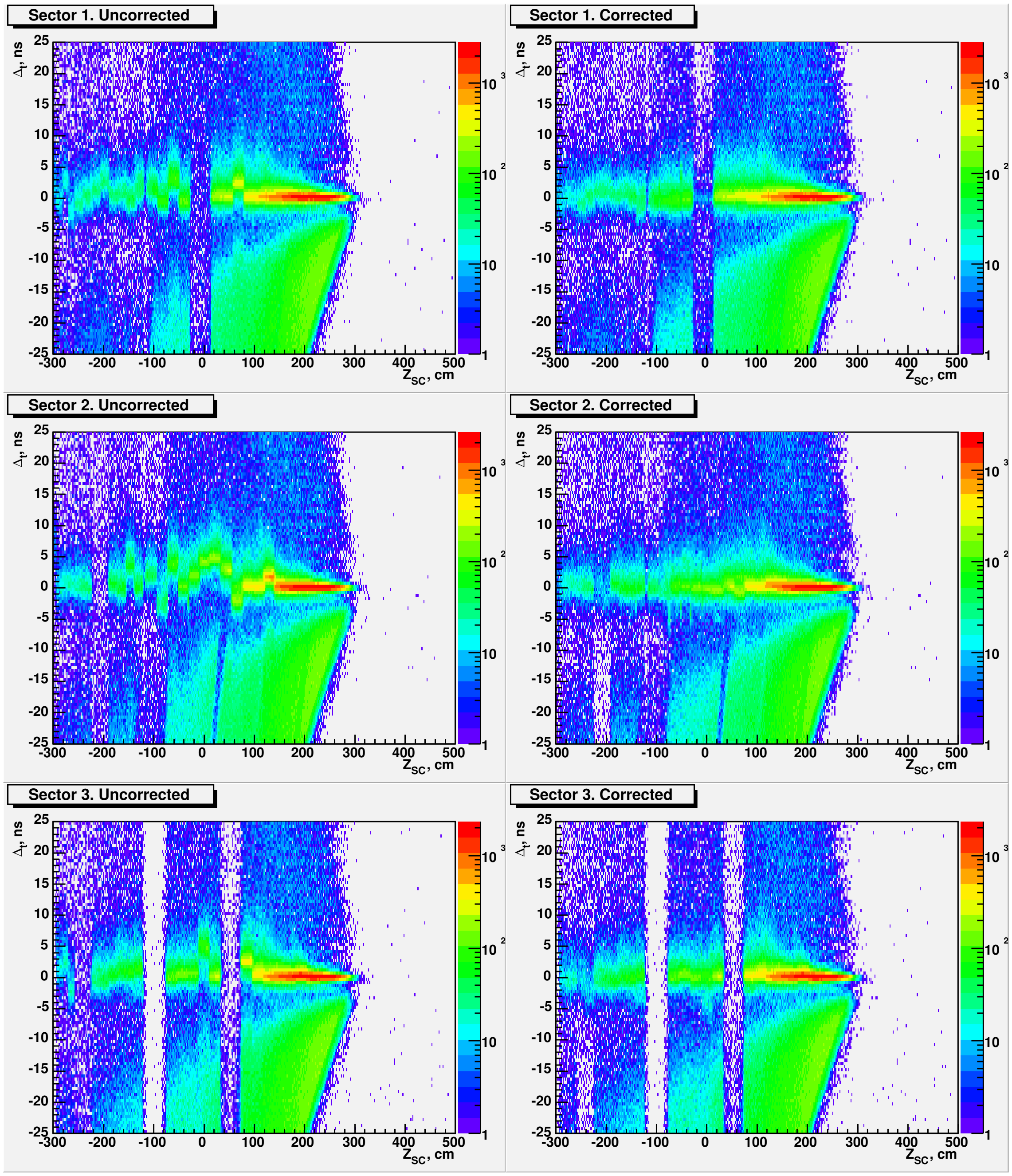

FIG. 53: The proton timing is plotted as a function of the position on the scintillator plane. Before the timing correction (left panel) and after the correction (right panel).

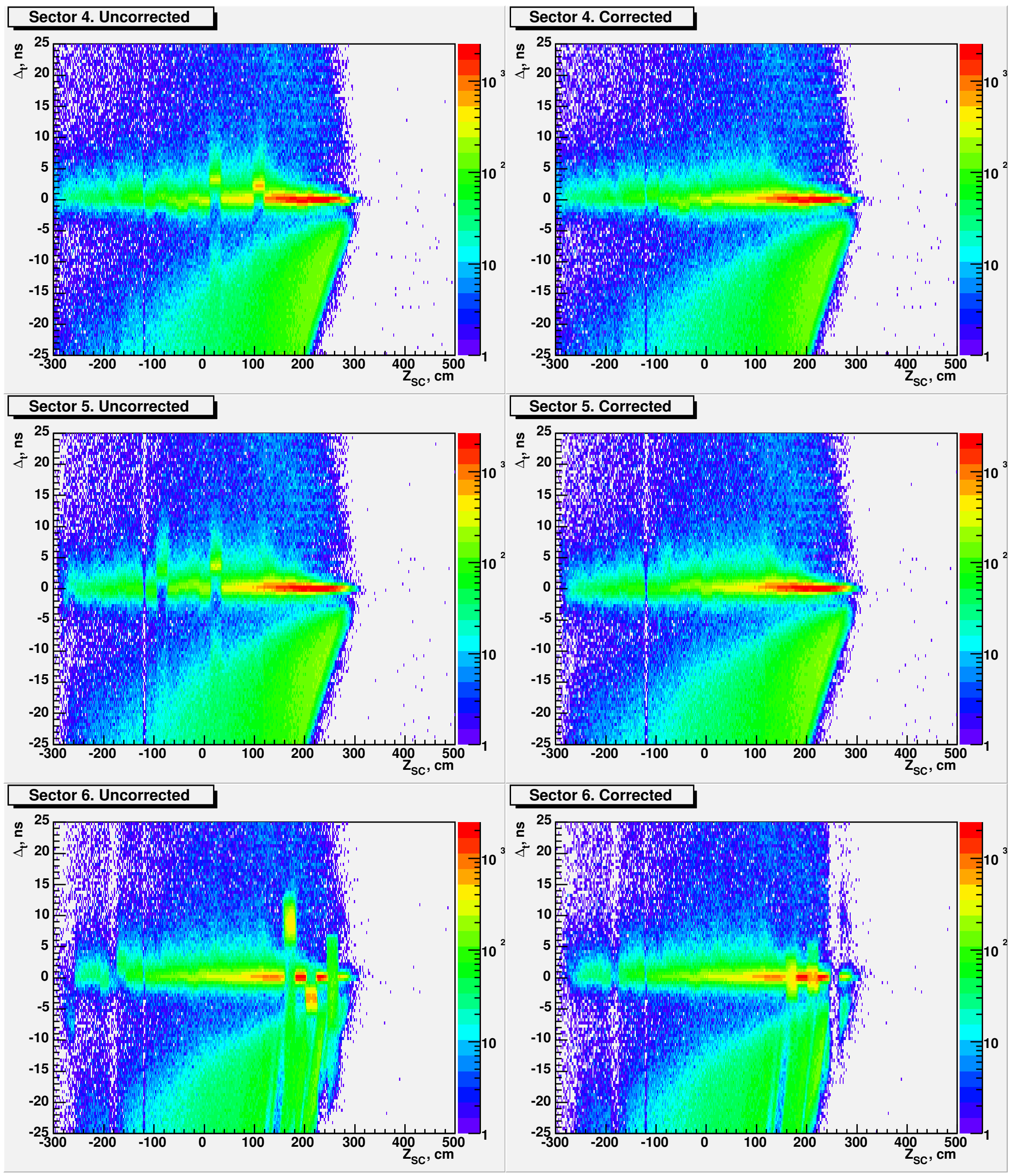

FIG. 54: The proton timing is plotted as a function of the position on the scintillator plane. Before the timing correction (left panel) and after the correction (right panel).

momentum and mass (assuming it had the mass of a proton):

$$\Delta \mathrm{t_{pr}} = \mathrm{t_{sc}} - \mathrm{t_{start}} - \frac{\mathrm{r_{sc}}}{p_{part}/E_{part}} \tag{45}$$

where $\mathrm{t_{sc}}$ is time recorded by the scintillator counters, $\mathrm{t_{start}}$ is the event start time, $\mathrm{r_{sc}}$ is the pathlength of the particle from the target to the scintillator plane, and p_{part} and E_{part} are respectively momentum and energy of the particle as measured by the drift chambers (from the track curvature) and using the mass of the proton to calculate the energy.

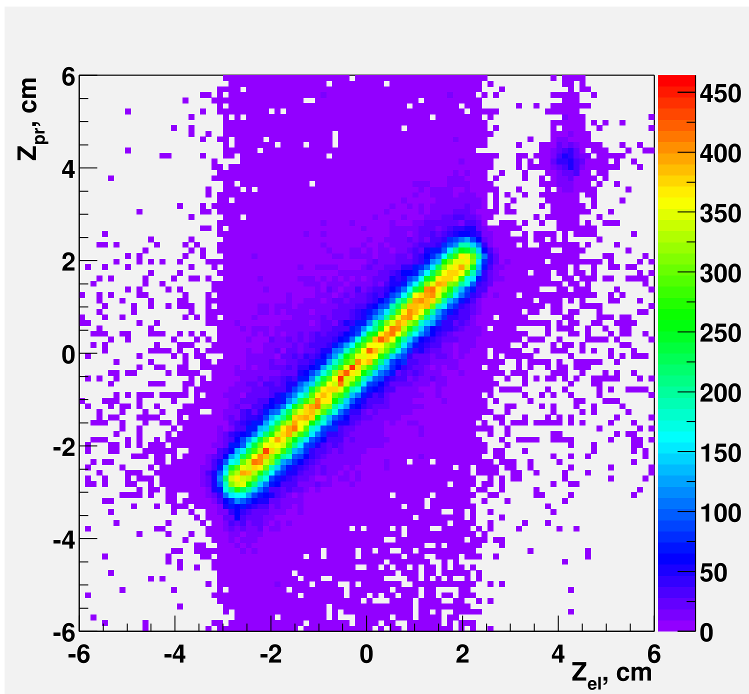

FIG. 55: Electron vertex vs proton vertex.

4.4.2 Proton Vertex Cuts

In the same manner as it is done in the electron identification, a vertex cut has to be used for the detected protons to make sure they are indeed coming from the target cell and not from the target exit windows or support structures. However, a wider cut has to be used for the protons than for the electrons since the vertex resolution for the slow-moving protons of interest is not as good. The proton vertex cut was $-2.5 < Z_{pr} < 2.0$ cm.

To minimize the rate of accidental electron-proton coincidences where the electron is coming from the interaction with the target nucleus and the proton is produced in some other process (deuterium photodisintegration or sequential electron or proton reinteraction with another deuterium nucleus), cut $-1.4 < \Delta Z < 1.4$ cm on the vertex difference between proton and electron was used (Figs. 55,56).

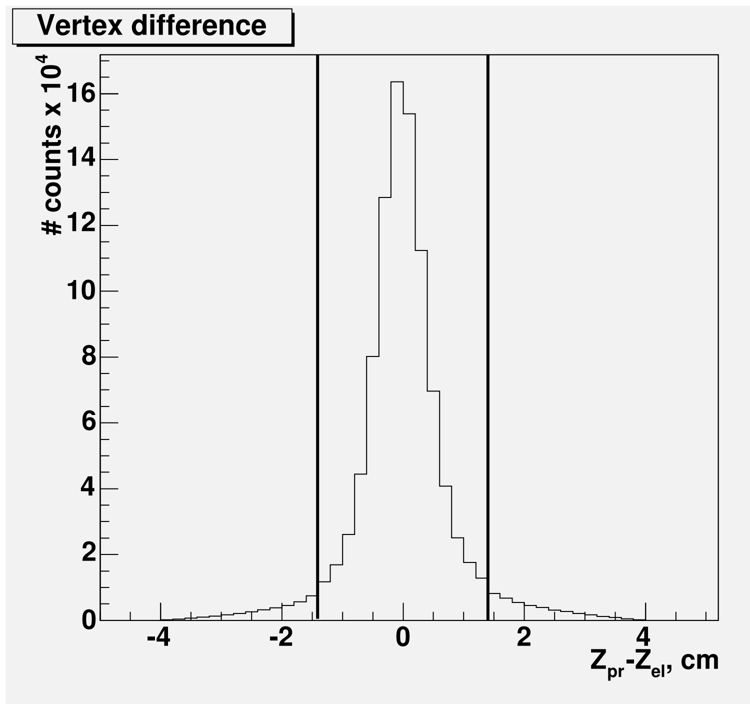

FIG. 56: The vertex difference between proton and electron. The vertical lines indicate the vertex difference cut.

4.4.3 Proton Energy Loss Correction

The proton, as any other charged particle, loses energy while propagating through the detector material, mainly by ionizing atoms it passes near by. The lower the momentum of the proton, the more energy it loses. This process is described by the widely known Bethe-Bloch formula.

The protons of interest have momentum of less then 0.75 GeV/c. If one plots the material penetration range of these low-energy protons versus their kinetic energy on a double-logarithmic scale, it turns out to be almost a straight line. Therefore, the function is roughly exponential and the range (R, g/cm^2) of the particle within a material can be parameterized as a function of the kinetic energy (T_{kin}, MeV) in the form:

$$R(T_{kin}) = b \cdot T_{kin}^{a} \tag{46}$$

which works for a wide variety of materials. If the initial range of a particle is $R_{init} = b \cdot T_{cor}^{a}$, after going through the detector material of thickness τ the range of the reconstructed particle becomes $R_{rec} = R_{init} - \tau = b \cdot T_{rec}^{a}$. This expression can then be rewritten as:

$$T_{cor} = \left\{ T_{rec}^{A} + \frac{B}{\sin\theta_{pr}} + C \right\}^{1/A} \tag{47}$$

where $\tau/b = B/\sin\theta_{pr} + C$ is a parameterization of the thickness of the material the particle goes through. The term $1/\sin\theta_{pr}$ appears to account for cylindrically shaped elements of the target that the particle transverses on its way out, where the amount of the material transversed depends on the scattering angle θ_{pr}. Finally, T_{cor} is the true kinetic energy of the proton after the correction [MeV], T_{rec} is the energy of the proton as it is measured by the detector, A, B and C are the constants to be determined.

To find the parameterization constants the GEANT-based detector simulation code (GSIM) was used. GSIM has an ideal CLAS model built into it and the energy loss of the scattered particle in all layers of the detector (including the target itself) is simulated. Protons were uniformly, randomly thrown at 5 different values of θ_{pr} and in the range of momenta between 200 and 600 MeV/c. The energy loss distribution for each value of θ_{pr} was fitted with the function $(T_{rec}^{A} + \kappa)^{1/A}$ (see Fig. 57). The fit variables κ were then fitted with function of θ_{pr}: $\frac{B}{sin\theta_{pr}} + C$ (see Fig. 58) The following set of energy loss correction parameters was thus obtained: $A = 1.843$, $B = 179.9$ and $C = 54.1$.

4.4.4 Accidental Protons

Despite the vertex cuts there is still a chance of having an accidental coincidence between an electron and a proton in the data sample. The background of accidentals has to be estimated and subtracted from the data. At the same time, the loss of "true" protons due to the time and vertex cuts has to be determined. A pure accidental proton was defined as a positively charged particle with the time-of-flight measured

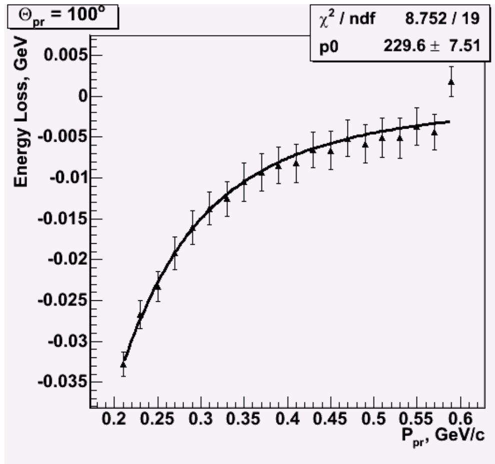

FIG. 57: Fit of function (47) to the energy loss of the proton going at 100° scattering angle in the lab.

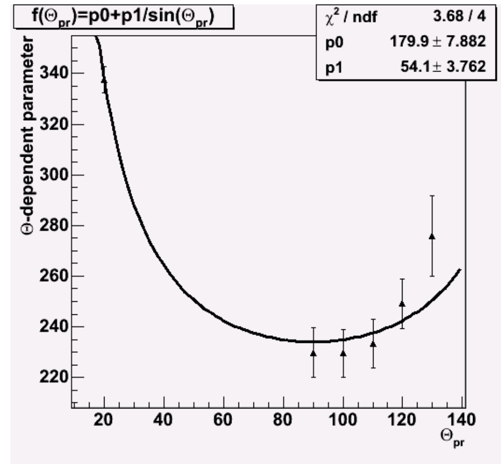

FIG. 58: Fit of function $\frac{B}{\sin(\theta_p)} + C$ to the parameter obtained from the fit of Fig. 57 for different values of proton scattering angle.

by the SC to be at least 12 ns longer than the expected time-of-flight of a proton with that momentum (45). The time window for the accidental proton was taken to be 9 ns, the same as the proton ID time window, so that the expected arrival time for the accidental proton would not be more than 22 ns different from the expected arrival time of the real proton. In the case where the time window of accidentals is less than 5 ns away from when the deuteron (from elastic scattering events) would have had arrived at the TOF counter, the accidental proton is defined to be within a 9 ns window starting at later than 5 ns times after the expected arrival time of a deuterium ion.

The average background of accidental coincidences per nanosecond of the proton time vertex was calculated from the rate in the "accidental" time window described above and compared with the unbiased data sample of coincidences with good proton PID (Fig. 59). The contribution of accidentals was estimated to be, on average, around 7%. The accidental coincidences (scaled by a factor of 1.2 to account for lower detection efficiency of the off-time protons, see section 4.6.3.2) agree well with the wings of the proton time vertex distribution. The level of understanding of accidentals can also be tested using the simulation results. The sum of the accidentals and the simulation should describe the data on good electron-proton coincidences as selected by PID cuts. That will be discussed in section 4.6.3.2 of this dissertation.

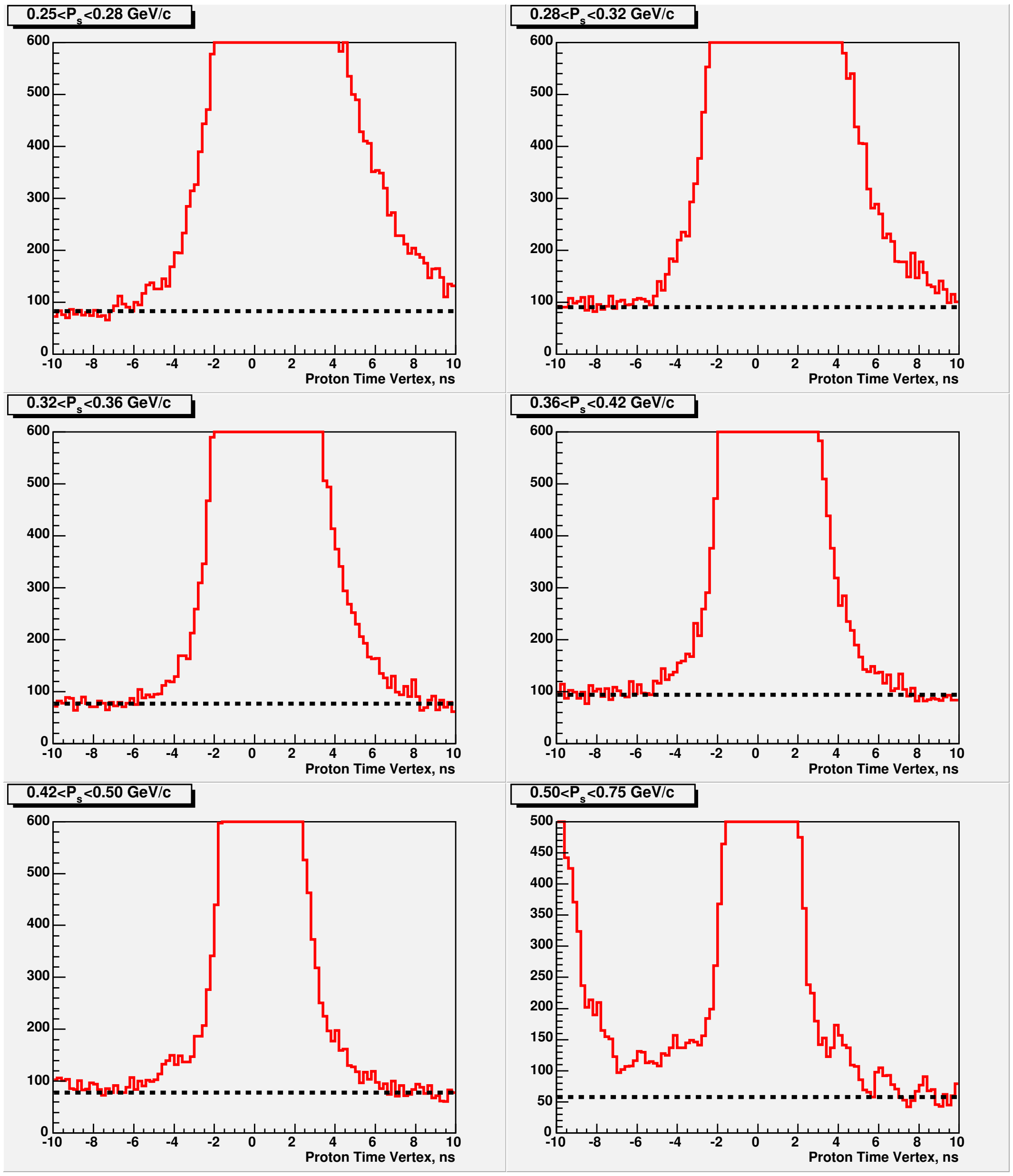

FIG. 59: The proton time vertex distribution for 6 different proton momentum bins. A proton with good PID (solid line) compared with the average background of accidental coincidences (dashed line). The beam bucket structure is visible at large times on the highest momentum plot.

4.5 ADDITIONAL CORRECTIONS AND CUTS

4.5.1 Momentum and Angle Corrections

One of the disadvantages of CLAS is that it does not have a very high momentum resolution. The limitation comes mainly from drift chamber spatial resolution. In addition, the momentum resolution is hurt by the uncertainty in the position of the drift chambers and the magnetic field. Several attempts were undertaken to measure exactly the magnetic field but the question still remains open [68]. Currently, the combination of two different configurations is used in the reconstruction code. Since the drift chambers were installed in 1995, Region 2 was never moved, while some of the sectors of the outermost Region 3 get pulled out almost annually for repair. Region 1 was also occasionally moved, but as a single unit. After removal, a DC sector can be reinstalled with a precision of about 3 mm. This displacement can be accounted for during the track reconstruction process. An alignment code was developed to measure the displacement of the chambers using straight track events (main torus magnets are off). This "alignment" procedure decreases the uncertainty in the relative DC position to about 100 μm [69, 70], however, the absolute position of the chambers can have greater uncertainty.

It is possible to parameterize all of the above unknowns and then try to correct for them using one of the advantages of CLAS $-$ its ability to measure exclusive reactions. In an exclusive reaction all of the products of the reactions are detected and no mass is missing. Therefore, the kinematics of the reaction are fully defined.

The effect of a displacement of the drift chambers and possible discrepancies in the measured magnetic field on the measured scattering angle θ_{rec} and momentum p can be parameterized in the form [72]:

$$d\theta = (c_1 + c_2\phi_{rec})\frac{\cos\theta_{rec}}{\cos\phi_{rec}} + (c_3 + c_4\phi_{rec})\sin\theta_{rec} \tag{48}$$

$$\theta_{cor} = \theta_{rec} + d\theta$$

where c_1,c_2,c_3, c_4 are fit parameters, θ_{rec} is the polar angle of the particle as reconstructed by the tracking software, ϕ_{rec} is the reconstructed (measured) azimuthal angle of the particle and θ_{cor} is the polar angle of the particle after the correction.

$$dp = \left\{(c_5 + c_6\phi_{rec}) \frac{\cos\theta_{cor}}{\cos\phi_{rec}} + (c_7 + c_8\phi_{rec}) \sin\theta_{cor}\right\} \cdot \frac{p_{rec}}{qB_{torus}}$$
$$+c_9 + c_{10}\phi_{rec} + c_{11}\phi_{rec}^2 + (c_{12} + c_{13}\phi_{rec} + c_{14}\phi_{rec}^2) \sin\theta_{cor} + (c_{15} + c_{16}\phi_{rec}) \cos\theta_{cor} \quad (49)$$

$$p_{cor} = p_{rec} + dp$$

where p_{rec} is reconstructed momentum of the particle, q is the charge of the particle normalized to the elementary charge e. B_{torus} is a parameterization of the integral $\int Bdl$ along the path of the track and according to the CLAS conceptual design report [71] is given by:

$$B_{torus} = 0.76 \cdot \frac{I_{torus} \sin^2 4\theta}{3375 \cdot \theta/rad} \quad \text{for} \quad \theta < \frac{\pi}{8}$$
$$B_{torus} = 0.76 \cdot \frac{I_{torus}}{3375 \cdot \theta/rad} \quad \text{for} \quad \theta \geq \frac{\pi}{8}$$

Parameters from c_1 to c_8 parameterize the drift chamber displacements and rotations as a result of which the angle and momentum of the particle is miscalculated in the track reconstruction process. Parameters c_9 through c_{16} parameterize the possible uncertainties in the magnitude of the magnetic field on the path of the particle. More details on this method can be found in CLAS-NOTE 03-005 [72].

The parameters were determined by minimizing a χ^2-like goodness of fit variable using the software package "Minuit". Three reactions were used in minimization: 1) elastic scattering on hydrogen $ep \to e'p$; 2) two-pion production on hydrogen $ep \to e'p\pi^+\pi^-$; 3) pion production off deuterium $ed \to e'pp\pi^-$. Both inbending and outbending torus field data were used. While the first reaction is very clean and has good statistics in the forward region of the detector, the last two reactions ensure that the obtained constants are valid for the full angular and momentum coverage of the spectrometer. The goodness-of-fit parameter was the weighted sum of squared deviations of each component of the total 4-momentum difference $(p^\mu_{initial} - p^\mu_{final})$ from zero.

An improvement of about 9 MeV in the elastic peak width of the invariant mass spectrum was observed for electron scattering on hydrogen (Fig. 60). After fitting all parameters and applying the corrections (48) and (49) the achieved momentum resolution of the experiment is ~32 MeV/c (standard deviation).

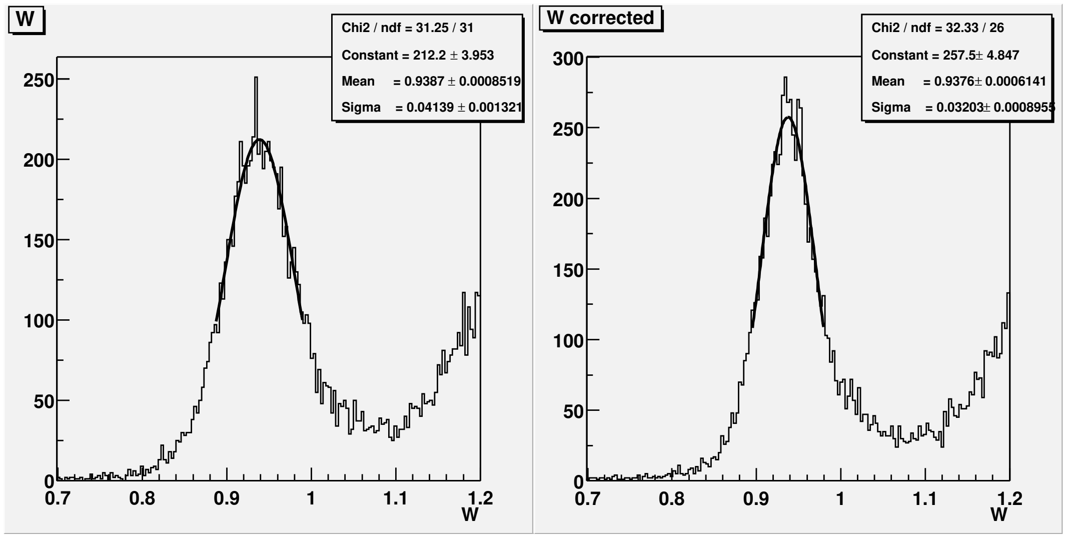

FIG. 60: Uncorrected invariant mass of the proton (left); corrected (right).

4.5.2 Vertex Correction

It is important to know the point along the target from where the detected particle originated. As was mentioned earlier, a vertex cut helps to eliminate false coincidences when the detected electron and proton came from the opposite sides of the target and therefore from two separate reactions. The suppression of background coming from the walls of the target is also done based on the vertex information.

The target cell (Fig. 29) used in the experiment was on average 5 mm in diameter (3−7 mm conical shape) and 5 cm long and was installed in the center of the CLAS. The beam delivered into the experimental Hall is supposed to go through the center of the target cell, but it does not always happen this way. In this experiment the beam was offset leading to a ϕ dependence of the Z vertex reconstruction (left part of Fig. 61). This dependence appears as a result of the tracking software calculating the vertex of the particle by extrapolating the track to the beam axis. The vertex of the electron with the track in a sector towards which the beam is offset will have a negative shift and the vertex of the electron that goes into the sector on the opposite side of the target will be shifted in a positive direction. It can be seen from Fig. 61 that before the correction, the vertex for the electrons in sector 6 ($\phi = -60^o$) had the most negative offset, while the sector 3 ($\phi = 120^o$) was offset in a positive direction.

The correction can be made using simple geometrical considerations and is found to have the functional form:

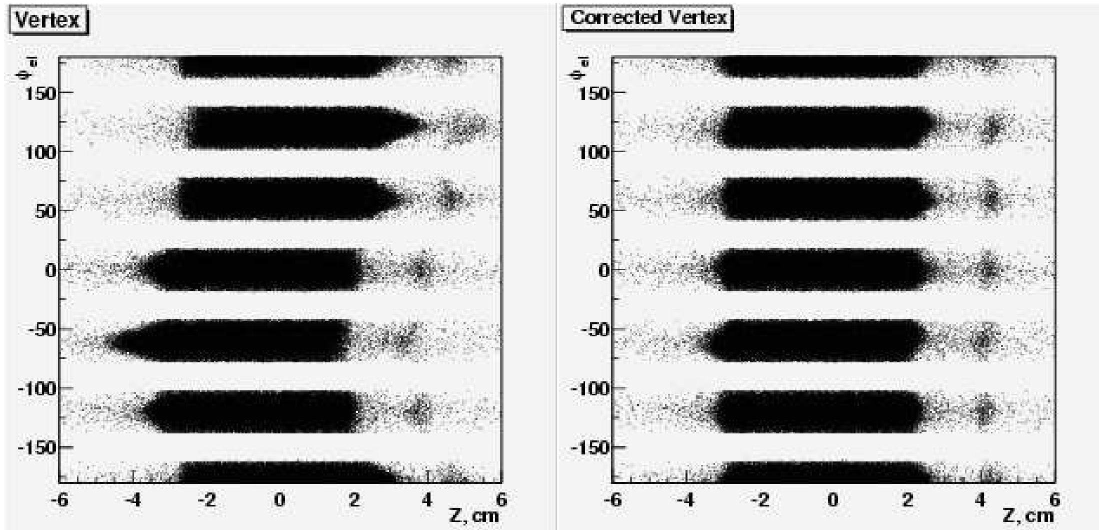

FIG. 61: Uncorrected position along the length of the target cell, where the electron originated from (left); corrected (right).

$$z_{true} = z_{rec} + \frac{r}{\tan\theta}\cos(\phi - \phi_{beam}) \tag{50}$$

where z_{true} is the real point of origin of the particle within the target along its axis, z_{rec} is the uncorrected vertex, θ is the polar scattering angle of the particle, ϕ is the azimuthal angle of the particle, ϕ_{beam} is the azimuthal angle of the direction of the beam offset, r is the distance from the axis along the target to the actual beam line.

The position of the beam defined by ϕ_{beam} and r can be found from the fit to the distribution of average vertex position over 6 sectors. It was established that the beam was offset by 3.29 mm in the direction of sector 6 ($\phi_{beam} = -58^o$). The corrected Z vertex is shown on the right side of Fig. 61. From the empty target data in the region of the target wall (that has an actual thickness of 20 μm) it was estimated that the available vertex resolution of the experiment is of the order of ~ 1.8 mm.

4.6 DATA SIMULATION

To extract any absolute result from experimental data, the detector acceptance has to be evaluated and an appropriate correction applied to the data. Simulation of the well modeled inclusive electron scattering and its comparison with the data also provides an extra check of how well the detector and related inefficiencies are understood. In order to obtain a realistic detector acceptance for a given reaction channel, the input model (event generator) should reproduce the physics of the process reasonably well. External radiation of the incident electron as well as internal radiative effects also have to be taken into the account in the event generator. External radiation of the scattered electrons is considered in the detector simulation code (GSIM).

After the physics of the process is modeled, the corresponding detector response to the final state particles is generated and known detector inefficiencies are introduced. When particle identification inefficiencies (discussed and estimated in Sec. 4.3.3) are applied, the simulated data on inclusive electron scattering should ideally be in agreement with the experimental data. Possible disagreements can be studied and corrected.

Based on the simulation of the semi-inclusive $d(e, e'p_s)X$ reaction, the efficiency of backward proton detection can be studied. Detector inefficiencies in that case can be singled out by comparing the response of the 6 different sectors of the detector.

The acceptance correction for the $d(e, e'p_s)X$ reaction is of particular interest for this analysis. To correct the data for detector acceptance, the experimental data will be divided by the simulated data and then multiplied by the cross section used to generate the simulated data.

4.6.1 Event Generator

The generator used in the simulation was written and is maintained by Sebastian Kuhn. It is based on the code RCSLACPOL that was developed at SLAC [65]. Three different versions of the code were compiled to satisfy our needs for simulation of electron scattering on ^{2}H: 1) elastic scattering on deuterium; 2) elastic scattering on a nucleon; 3) inelastic scattering on a nucleon. The generator is capable of simulating both inclusive and semi-inclusive processes, which is controlled by a configuration file. The events are thrown weighted by the calculated cross section that is normalized to its maximum.

To generate inclusive electron scattering on deuterium the generator is run three times. In the beginning of each generation cycle the electron is randomly thrown within the kinematical boundaries (Q^2 and ν) defined in the configuration file. The first version of the generator then calculates the cross section of elastic electron scattering from deuterium. A parameterization of the deuterium form factors is used to calculate the cross section given by expression (9) and taking F_1 and F_2 to be the form factors of the deuterium nucleus [66]. The value of the cross section is normalized to the maximum cross section within the given kinematical range. A random number determines whether the event is to be accepted or ignored, based on whether the number is smaller or greater than the normalized calculated cross section.

The second version of the generator simulates quasi-elastic scattering from a moving proton or neutron within deuterium using a strict spectator picture. In the spectator approximation the energy and momentum (E_N and $\mathbf{p}_N$) of the off-shell bound nucleon on which the scattering takes place is related to the spectator nucleon momentum $\mathbf{p}_s$:

$$E_N = M_d - \sqrt{M_p^2 + p_s^2} \qquad\qquad \mathbf{p}_N = -\mathbf{p}_s \ . \tag{51}$$

Therefore, the mass of the nucleon that enters the formula for the cross section is now a function of the spectator momentum:

$$M^* = \sqrt{\left(M_d - \sqrt{M_p^2 + p_s^2}\right)^2 - p_s^2}. \tag{52}$$

The initial momentum of the struck nucleon is chosen according to the momentum distribution:

$$P(\vec{p_N}) = |\psi(\vec{p_N})|^2$$

where $\psi(\vec{p_N})$ is a deuterium wave function. The wave function obtained from the Paris potential solution was used [57], rescaled using the light-cone formalism [62]. A comparison of the spectral function calculated from the more modern Argonne v_{18} potential [63] was performed, however no discrepancy of relevant magnitude within the range of momenta of interest ($p_N < 0.7$ GeV/c) was observed. The cross section given by equation (9) was then calculated in the rest frame of the moving nucleon and the events generated accordingly. For full simulation of inclusive scattering on deuterium this version is run separately for the proton and the neutron. In equation (9), F_1 and F_2 are now taken to be the parameterization of proton or neutron form factors from Ref. [56]. The elastic radiative tail is calculated using the equivalent radiator prescription of Mo and Tsai [64]. The reduction of the elastic peak itself

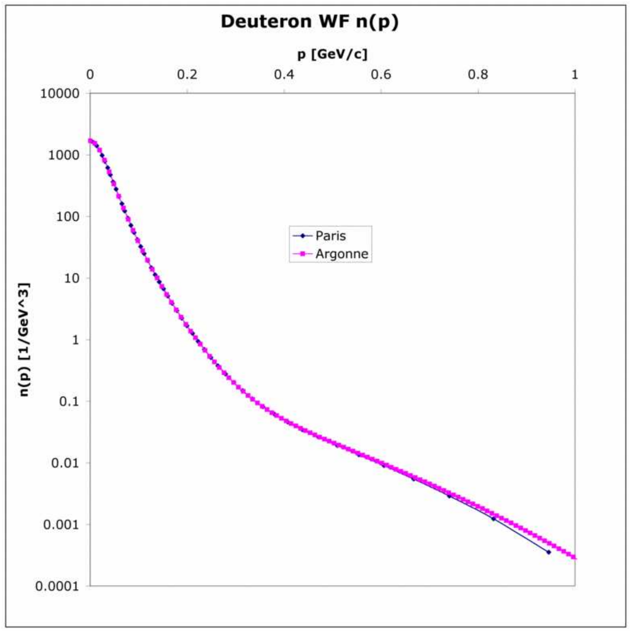

FIG. 62: The spectral function based on Paris potential (dark line) compared with the spectral function from the Argonne v_{18} potential (light points).

due to the internal radiation is given by:

$$\left(\frac{d\sigma}{d\Omega}\right)_{rad} = e^{\delta} \cdot \left(\frac{d\sigma}{d\Omega}\right)_{Born} \tag{53}$$

where the expression for parameter δ is given in Ref. [64]. External radiative losses in the target before the scattering are also simulated, while the losses after the scattering are automatically included in GSIM.

The last part of the simulation for the $d(e,e')X$ reaction is inelastic scattering from a nucleon within deuteron. The cross section here is evaluated in the rest frame of the struck moving nucleon using an equivalent form of expression (17):

$$\frac{d\sigma}{dE'd\Omega} = \sigma_{\mathrm{Mott}} \frac{2MxF_2(x,Q^2)}{\epsilon Q^2}\left[\frac{1+\epsilon R(x,Q^2)}{1+R(x,Q^2)}\right] \tag{54}$$

where $R = \sigma_L/\sigma_T$, σ_L and σ_T are longitudinal and transverse cross sections corresponding to different polarizations of the absorbed virtual photon,

$$\frac{1}{\epsilon} = 1 + 2(1 + Q^2/4M^2x^2)\tan^2(\theta/2)$$

and

$$\sigma_{\text{Mott}} = \frac{4\alpha_{EM}^2 E'^2}{Q^4}\cos^2(\theta/2)\ . \tag{55}$$

The New Muon Collaboration (NMC) fit to SLAC, BCDMS and NMC data on proton and deuteron F_2 structure functions was used [58]. To obtain the neutron structure function, the proton structure function was first smeared with the deuterium spectral function and then subtracted from the deuteron structure function. The parameterization of the ratio σ_L/σ_T from Ref. [59] was used. Radiative effects were simulated using the output of the SLACPOLRAD [65, 67] program. The SLACPOLRAD calculates the ratios of radiated to Born (unradiated) cross section for DIS on a nucleon, without the elastic tail. These ratios were applied to scale the unradiated cross section calculated by the event generator. An event was accepted or rejected randomly based on the calculated cross section, normalized to its maximum value. The inelastic part of the generator was also run for neutron and proton separately. When the event was accepted, an electron momentum four-vector was printed to standard output for further analysis. The five outputs of all three versions of the generator were put together to give the full radiated $d(e,e')X$ inclusive cross section. To simulate the inclusive $p(e,e')X$ cross section, elastic and inelastic versions of generator were run only for the proton.

The same generator was used for the simulation of the semi-inclusive $d(e,e'p_s)X$ reaction, where p_s is a spectator proton detected in a backward direction. In the semi-inclusive run of the generator the backward proton kinematics (minimum momentum and range of angles) were restricted with the appropriate setting in the configuration file. The semi-inclusive version of the generator also prints to the standard output momentum 4-vectors of the scattered electron and of backward going spectator proton. The generator does not model any FSI effects. Two separate outputs - for elastic and deep inelastic scattering - are produced and analyzed together to simulate the $d(e,e'p_s)X$ process in full.

4.6.2 Detector Simulation

An idealized model of all the detector systems is implemented in the open source code known as "GSIM". The program is built on the foundation of the GEANT simulation software package, supported by CERN. GSIM allows simulation of the detector response to the propagating particle, simulating energy loss as well as emission of secondary particles scattered during the passage of the particle through parts of the detector. GSIM was written to accommodate various detector hardware configurations through simple modifications to a configuration file. The only part of the code that has to be frequently rewritten is the target model. Distribution of the events along the target vertex is also done by this part of the program. As an input GSIM, uses momentum 4-vectors of all the particles in the event to be simulated. This is exactly the output of the event generator.

After the response of the ideal detector is simulated, a bit of the reality needs to be introduced. This is done using a separate program called "GPP" (GSIM post-processor). GPP uses precompiled information on dead regions of drift chambers and scintillator paddles to remove the signal for these parts of CLAS from the GSIM output. Information about the dead channels of drift chambers is analyzed by a program known as "PDU". PDU uses raw data BOS banks and makes an appropriate record in a database on the status of every single drift chamber wire. For the dead parts of drift chambers, the first file of run #31794 was chosen as a good representation of the whole run period. The identification of dead SC paddles is done for the scintillator counters by the "P2P" (paddle-to-paddle) program. P2P uses the integrated statistics of part of the run period on electrons in the forward part of SC and pions for the angles $\theta > 45^o$. P2P also stores the information of the inefficient parts of SC in an online database. When GPP is executed, it first reads the database and excludes wires and paddles with bad status from the detector response generated by GSIM. The simulated data with the dead channels removed is then cooked using a standard reconstruction code just like it is done with the actual data.

The simulated data with the dead DC channels removed is compared with the experimental data for sectors 1 through 3 in Fig. 63 and, for sectors 4 through 6 in Fig. 64. It can be seen that most of the nonfunctional regions of the drift chambers are represented by the simulation. There is an inefficiency in region 3 of sector 1 for the first 20 wires (Fig. 63) and an inefficiency in sector 5, region 2 in a forward part as well, that do not show up in the simulation. Since there are some hits in those parts of the drift chambers, PDU does not label them as dead.

The next step was to compare the drift chamber occupancies for run 31794 with a set of random good runs from different periods of the experiment. Runs 31575, 31641, 31901, 32000 and 32091 were chosen to look for possible unaccounted deviations in the efficiency of the drift chambers, appearing as a result of some part of the detector to be malfunctioning temporarily. The drift chamber occupancies for the above mentioned runs are presented in Figs. 65-70. Each Fig. contains occupancies for one sector: sector 1 - Fig. 65, sector 2 - Fig. 66, sector 3 - Fig. 67, sector 4 - Fig. 68, sector 5 - Fig. 69 and sector 6 - Fig. 70. From the listed figures it can be concluded that in terms of DC dead regions sectors 1,2,3 and 4 are remarkably stable throughout the whole experiment. That is verified by the study presented in section 4.1 and the experiment log book. For sector 5 it looks like an inefficiency in the forward part of region 2 (specifically superlayer 3) gets worse at the end of the experiment, so that instead of having fewer counts than the neighboring wires, this part of the chamber has no counts at all. This section was, however, identified by PDU as dead already for 31794 (see Fig. 64), therefore the change in the number of events in those bins is minor. Sector 6 develops 2 large holes in superlayers 5 and 6 (Fig. 70, bottom two sections of the plot). The problem occurred after run #31970 and is can be clearly seen in Fig. 30 used for the selection of good data files. It can now be concluded that run #31974 is indeed a realistic representation of the whole experiment in terms of the dead regions of drift chambers.

To check how well dead or malfunctioning forward paddles of the scintillators were identified by P2P, the plot of the electron time vertex versus paddle number made individually for each sector can be used (Figs. 71 and 72). Sector 1 looks very good with an exception of paddle #16, which might have been miscalibrated. In sector 2 there is a slightly miscalibrated paddle #6. Sector 3 has paddle #11 that is inefficient and is reproduced in the simulation, however paddle #16 has a very broad distribution that is not simulated properly. Paddle #19 in sector 4 (Fig. 72) has an efficiency problem, but does not look as bad in simulation. Sector 5 contains an inefficient paddle #21 that was identified as bad by P2P, that can be seen from the spectrum for the simulated events. Sector 6 has no obvious inefficient paddles. Overall scintillator performance was reproduced by the detector model reasonably well. To make sure the paddles listed above have no impact on the data quality they will be excluded from the analysis.

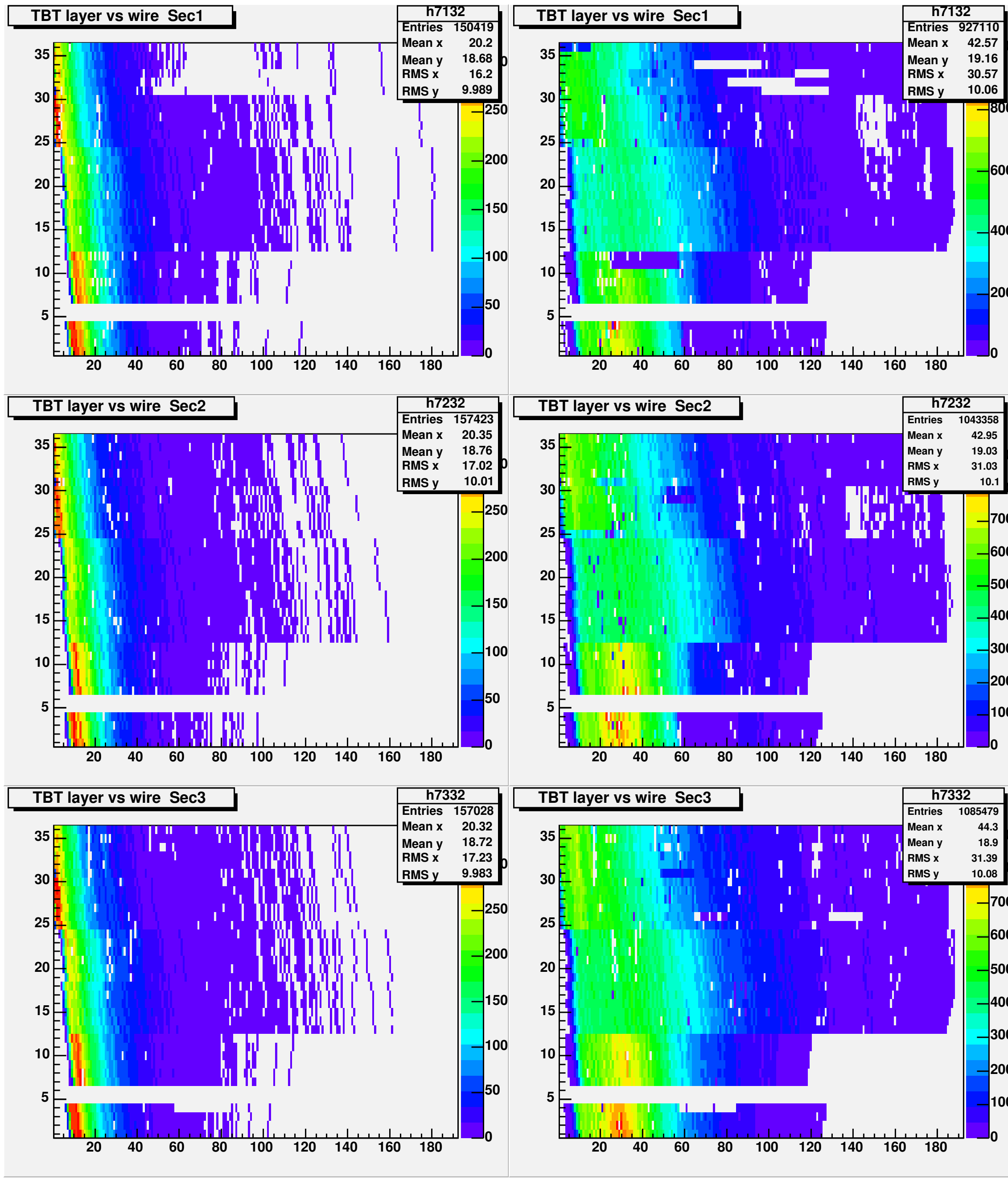

FIG. 63: Drift chamber occupancies. The vertical axis is layer number. The horizontal axis is wire number. The vertical axis is layer number. The horizontal axis is wire number. Comparison of the inclusive simulation, where the electron is the only particle in the event and is thrown in a forward direction (left) with the fully exclusive data, containing all detected particles at all angles (right). Only the forward region (wire number of less than 50) can be compared.

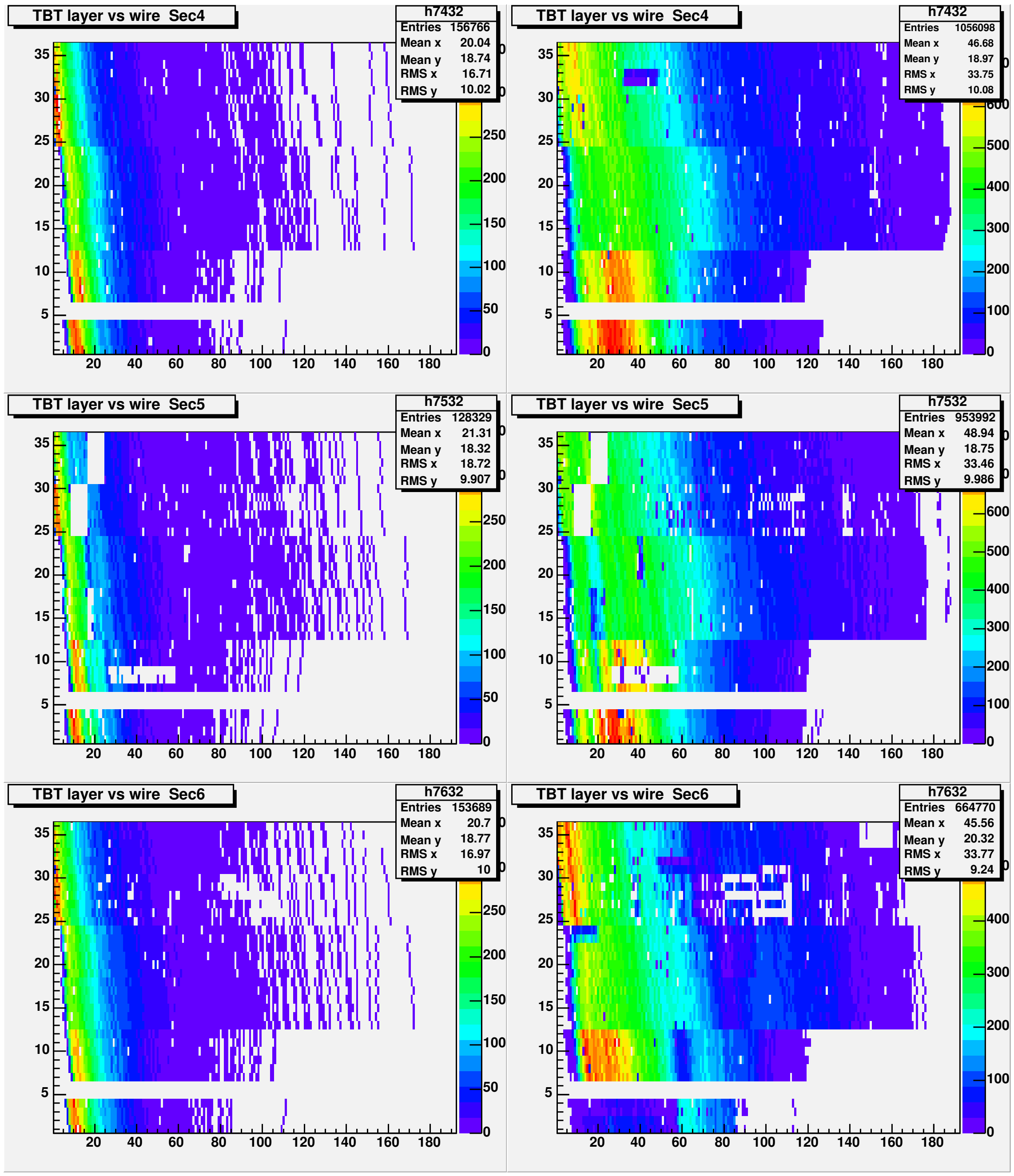

FIG. 64: Drift chamber occupancies. The vertical axis is layer number. The horizontal axis is wire number. The vertical axis is layer number. The horizontal axis is wire number. Comparison of the inclusive simulation, where the electron is the only particle in the event and is thrown in a forward direction (left) with the fully exclusive data, containing all detected particles at all angles (right). Only the forward region (wire number of less than 50) can be compared.

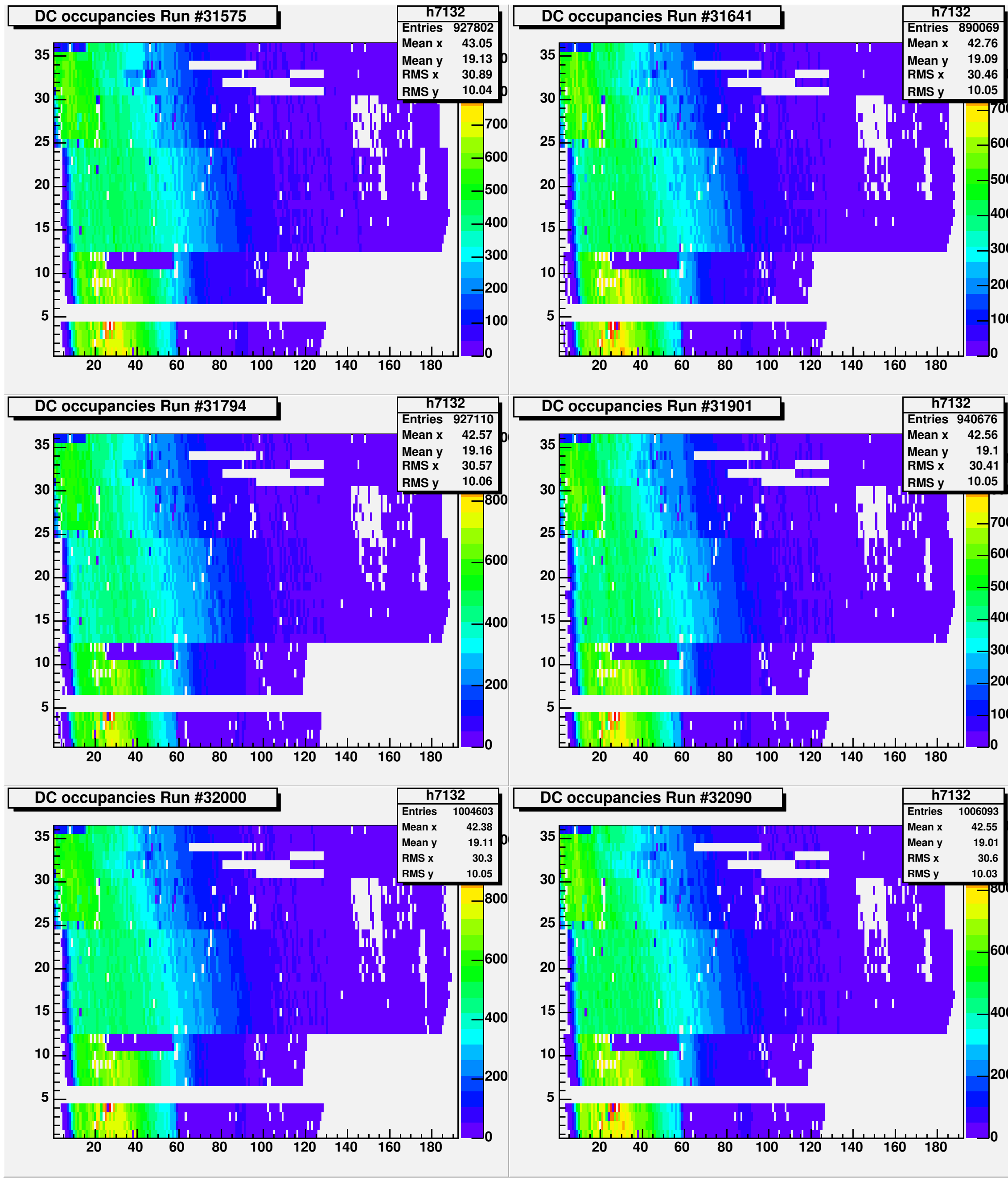

FIG. 65: Sector 1 drift chamber occupancies for 6 different runs throughout the run period. The vertical axis is layer number. The horizontal axis is wire number.

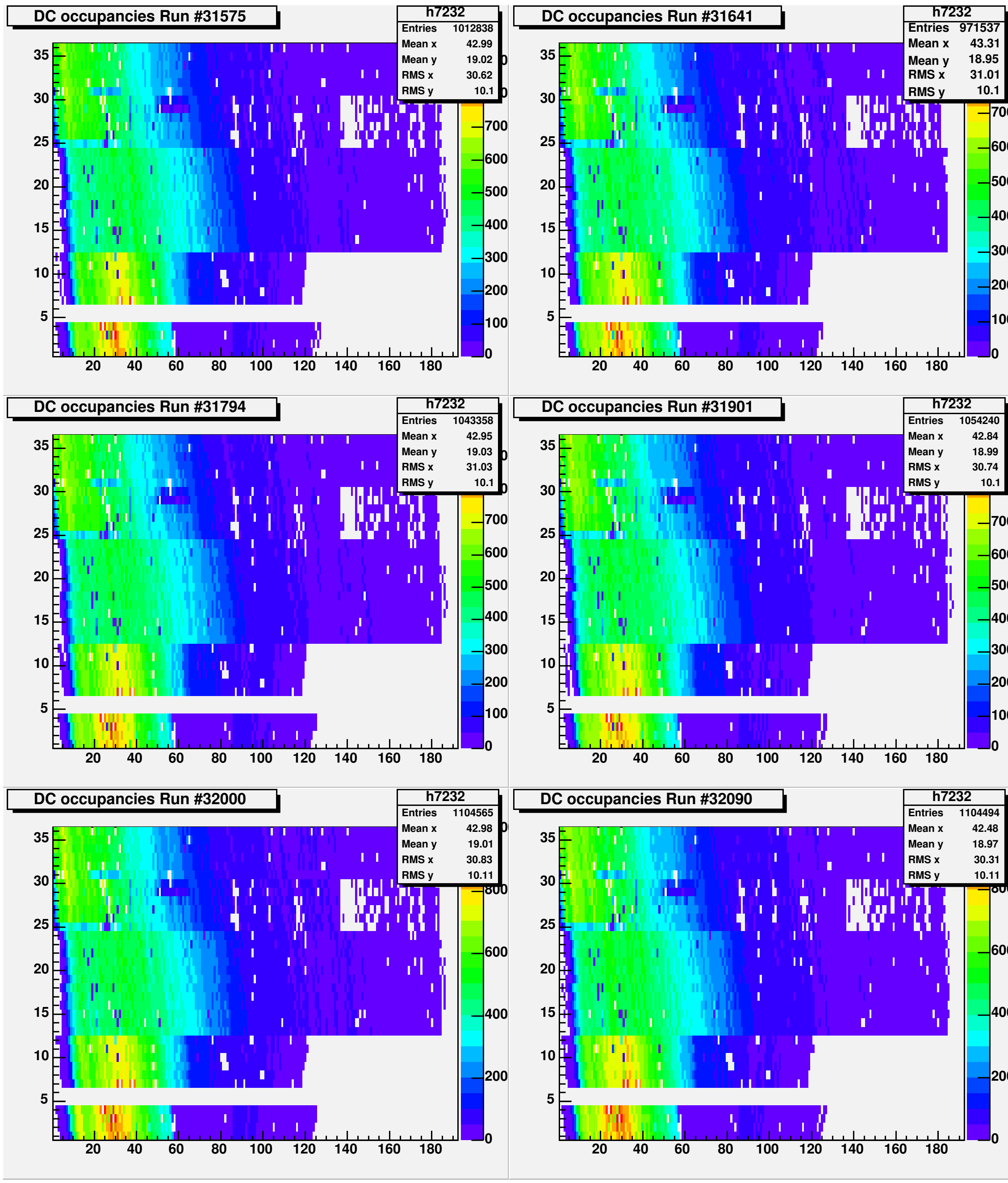

FIG. 66: Sector 2 drift chamber occupancies for 6 different runs throughout the run period. The vertical axis is layer number. The horizontal axis is wire number.

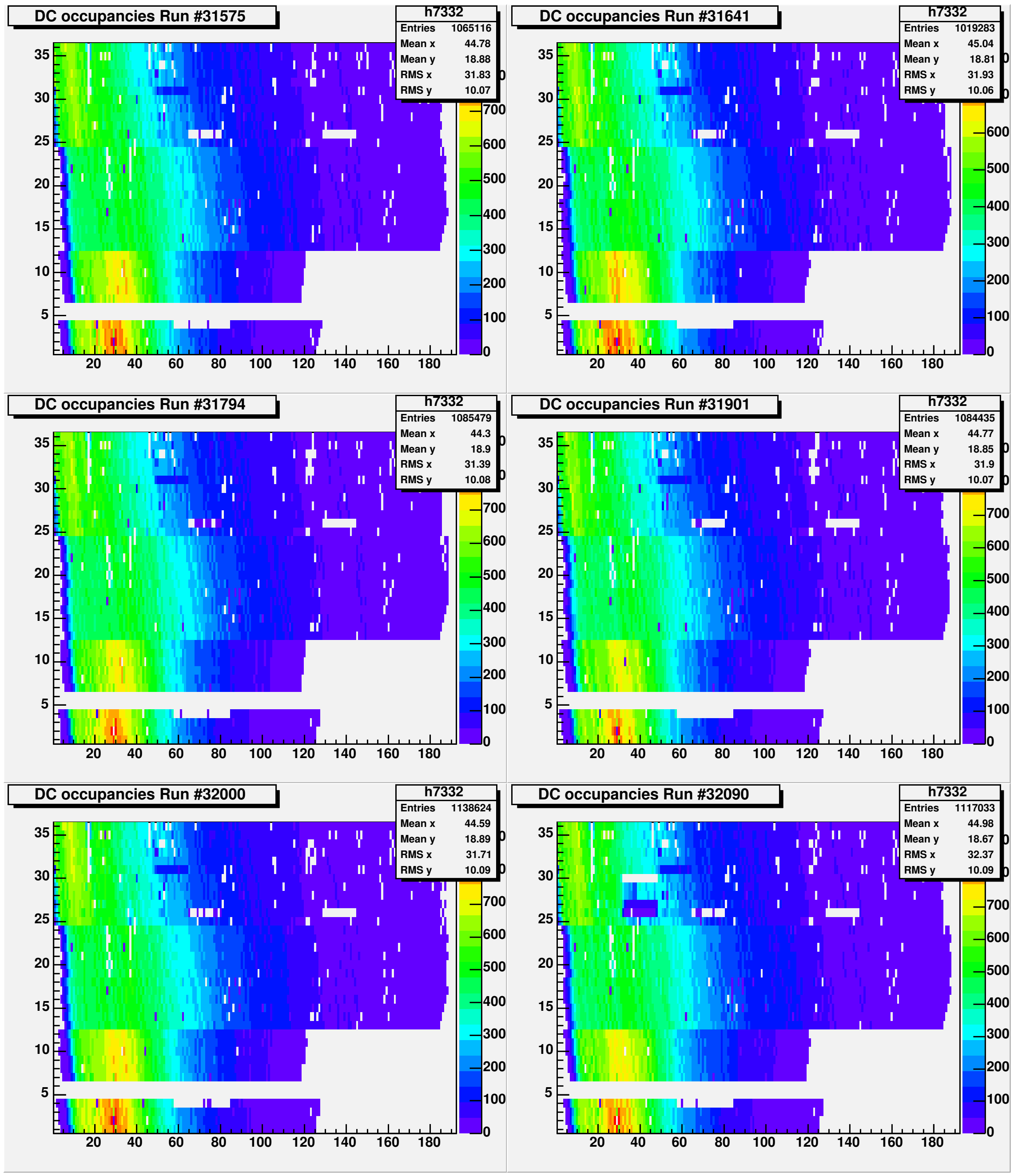

FIG. 67: Sector 3 drift chamber occupancies for 6 different runs throughout the run period. The vertical axis is layer number. The horizontal axis is wire number.

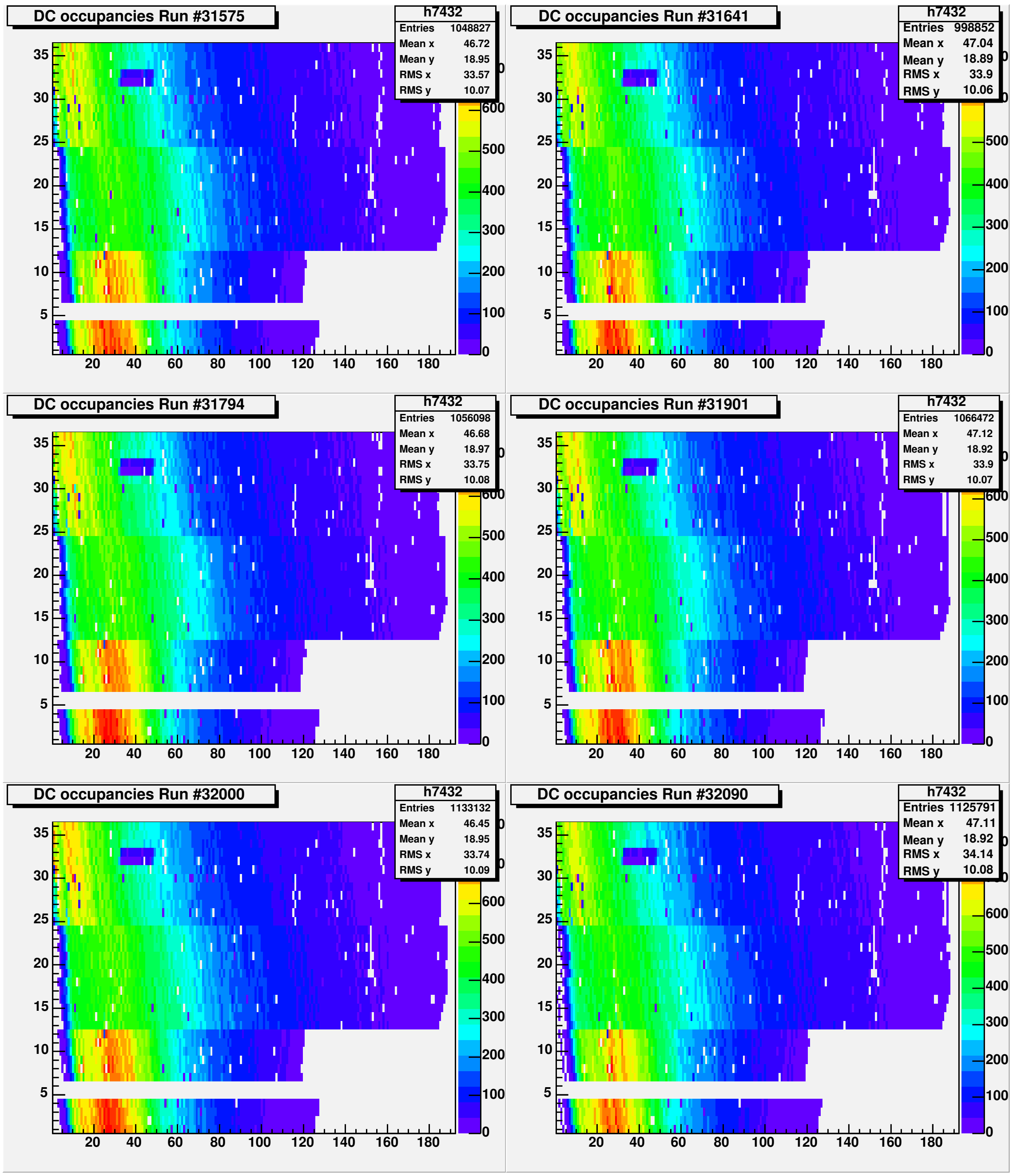

FIG. 68: Sector 4 drift chamber occupancies for 6 different runs throughout the run period. The vertical axis is layer number. The horizontal axis is wire number.

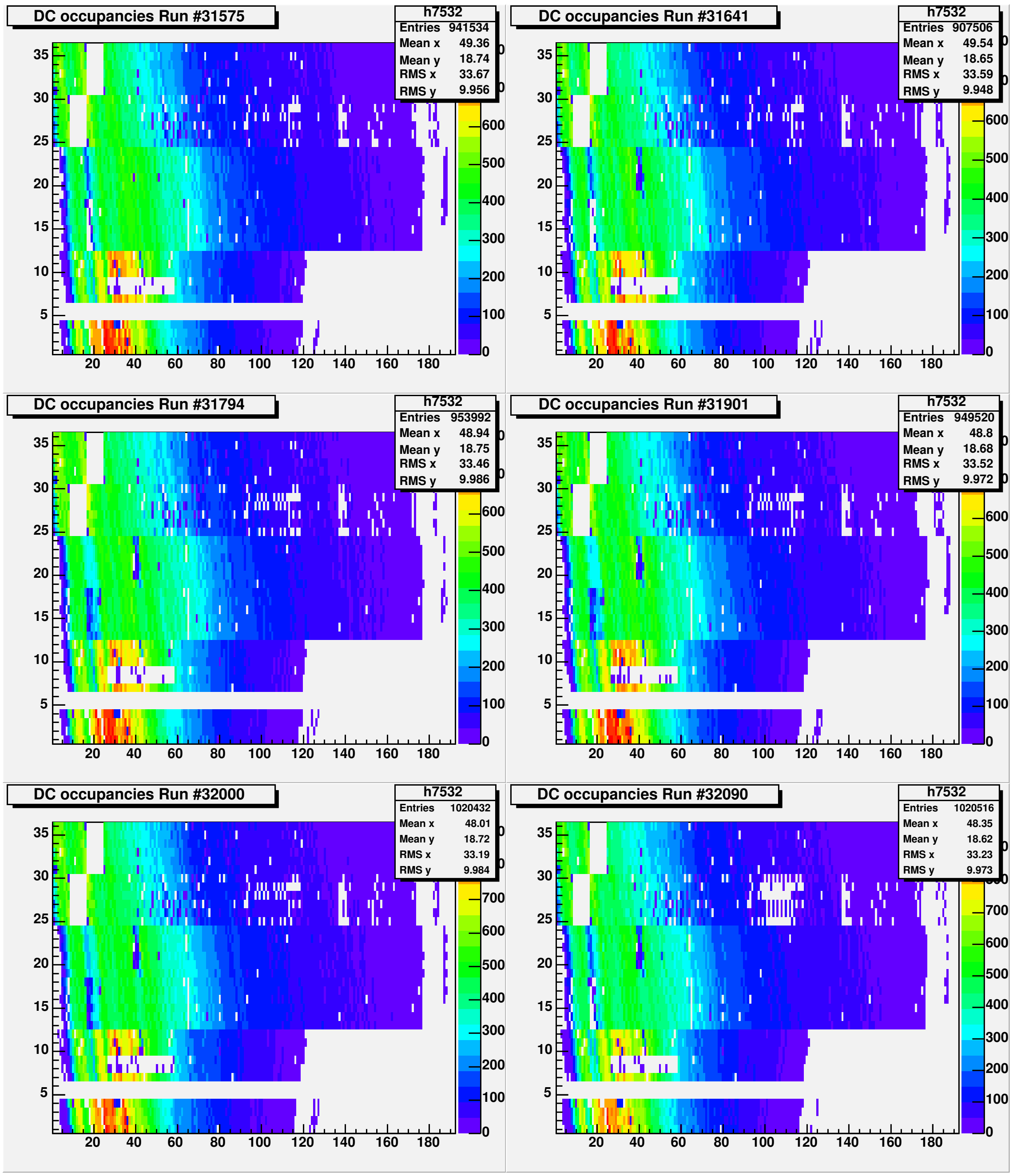

FIG. 69: Sector 5 drift chamber occupancies for 6 different runs throughout the run period. The vertical axis is layer number. The horizontal axis is wire number.

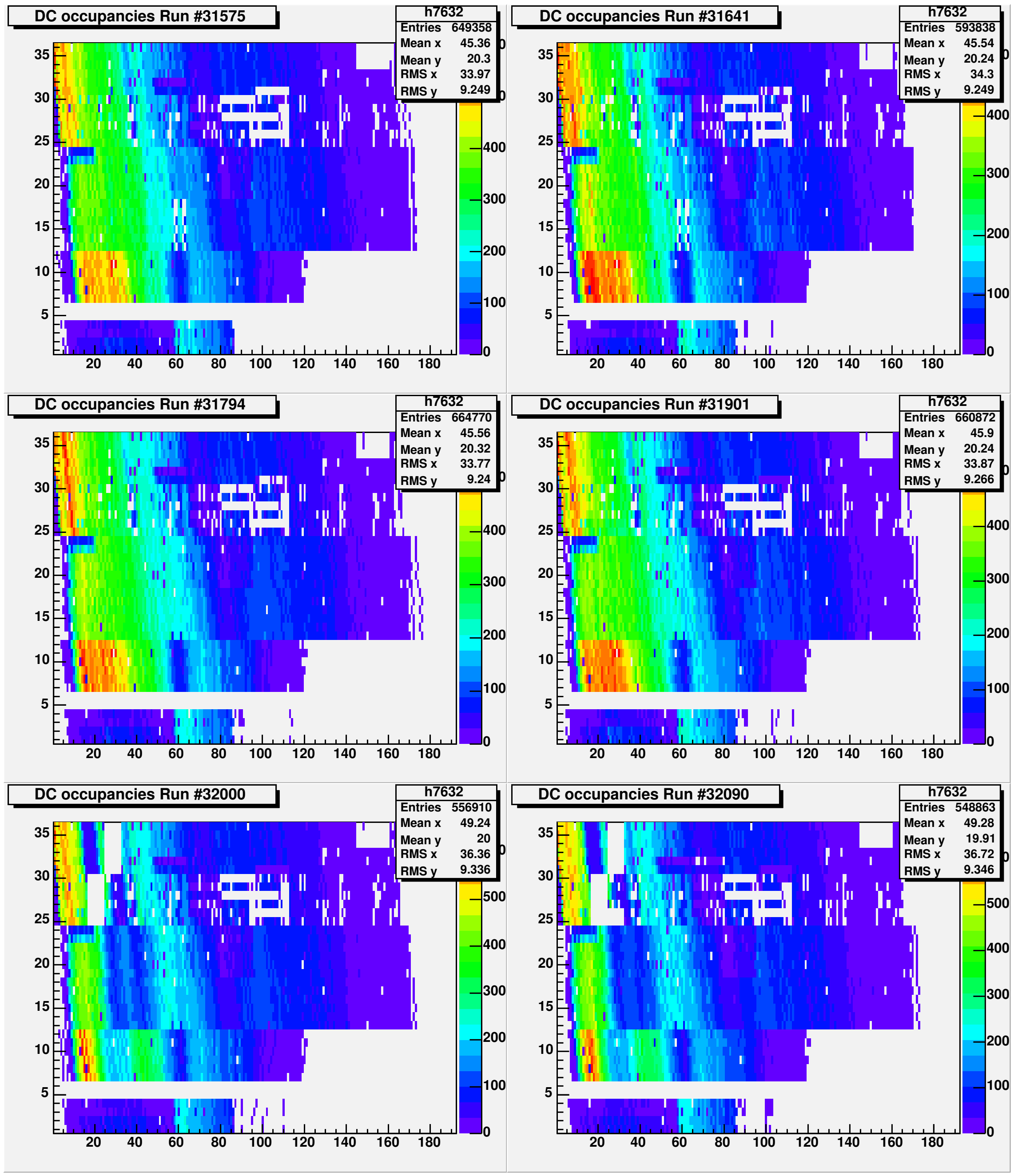

FIG. 70: Sector 6 drift chamber occupancies for 6 different runs throughout the run period. The vertical axis is layer number. The horizontal axis is wire number.

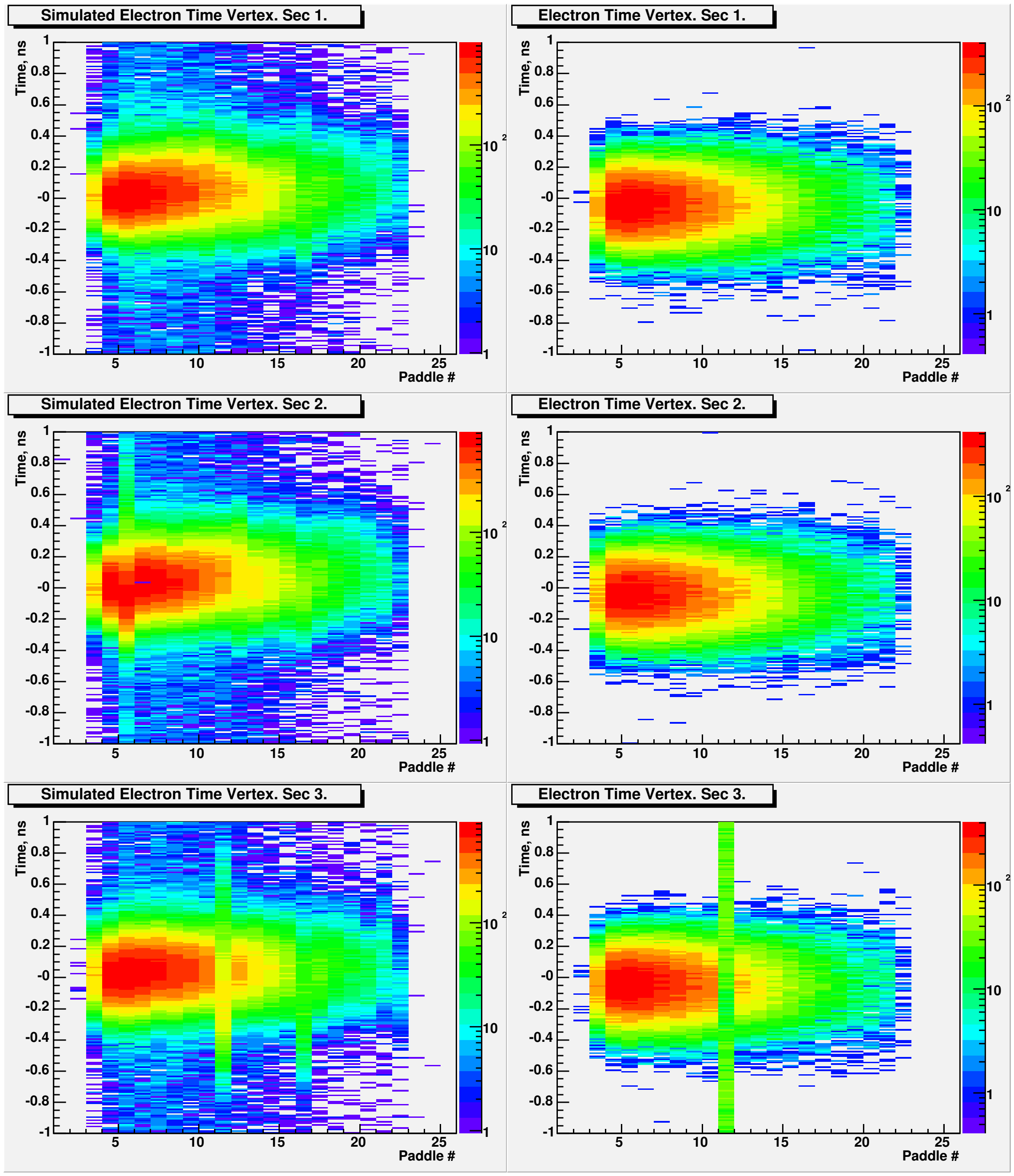

FIG. 71: Electron time vertex plotted versus paddle number for simulation (left) and data (right).

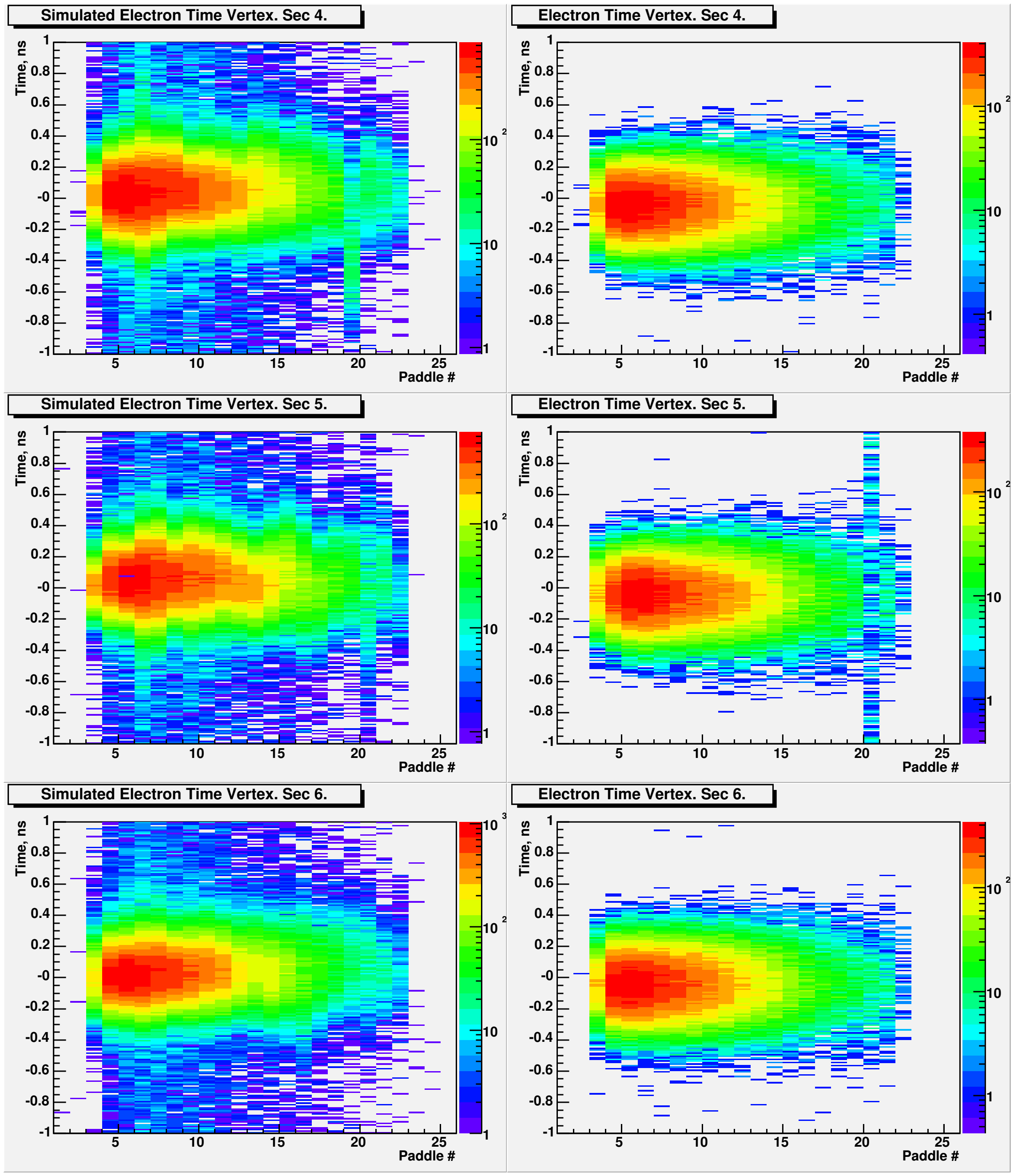

FIG. 72: Electron time vertex plot versus scintillator paddle number for simulation (left) and data (right).

Using GPP, the drift chamber spatial resolution and the TOF timing resolution can be smeared to fit the resolution of the experimental data before running the reconstruction code. The coefficient of smearing is chosen comparing the data with the simulation. Drift chamber resolutions for data and simulation after smearing are presented in Fig. 73. They are in good agreement. The drift chamber smearing coefficients were chosen to be: $a = 1.17$, $b = 1.08$, $c = 1.15$. In the same manner, the time-of-flight resolutions can be smeared. Comparison of simulation with the data, however, has shown that such smearing is not necessary, since (as it can be seen from Fig. 74) the simulated electron time vertex distribution already agrees with the data. To cross-check the choice of smearing coefficients, the invariant mass distribution for the p(e, e')X reaction was fitted with a Gaussian (Fig. 75). The simulated resolution of 32.95 MeV is comparable with the data resolution (after the momentum and angle corrections) of 32.03 MeV (see Sec. 4.5.1).

Now that dead regions of the detector are taken care of, the next step is to make sure that the electron ID Cherenkov and EC cut inefficiencies (section 4.3.3) are reproduced in the simulation. The spectra of the electromagnetic calorimeter and Cherenkov counter should, first of all, look reasonably similar in data and simulation. For electron identification efficiency to be simulated properly, electron ID cuts should also reject approximately the same fraction of good electrons (CC $\approx$ 2% and EC $\approx$ 5%).

The comparison of electromagnetic calorimeter spectra are presented in Figs. 76 and 77. The position of the maximum, for both sampling fraction of the inner part of the calorimeter and the whole detector, is lower in the simulation. The width of the simulated distribution for EC_{in}/P_{el} is in a good agreement with the data. The distribution of EC_{tot}/P_{el} is wider in the data. This can be easily explained by looking at diagnostics plot 34. The sampling fraction of the detector goes up at around run #31700. The left plot in Fig. 77 is integrated over the whole run period, as a result of which the width of a distribution increases by the overlap of two distributions with a slightly offset mean value. Since after run #31700 the sampling fraction is actually higher than for the earlier runs, this is not a concern.

To account for the difference between data and simulation in the mean position of the sampling fraction, the electron ID cut, when applied to the simulation, should be reduced by 22%, which is the EC gain difference between data and simulation. The cuts for the simulation are therefore: $EC_{tot}/P_{el} > 0.172$ and $EC_{in}/P_{el} > 0.063$.

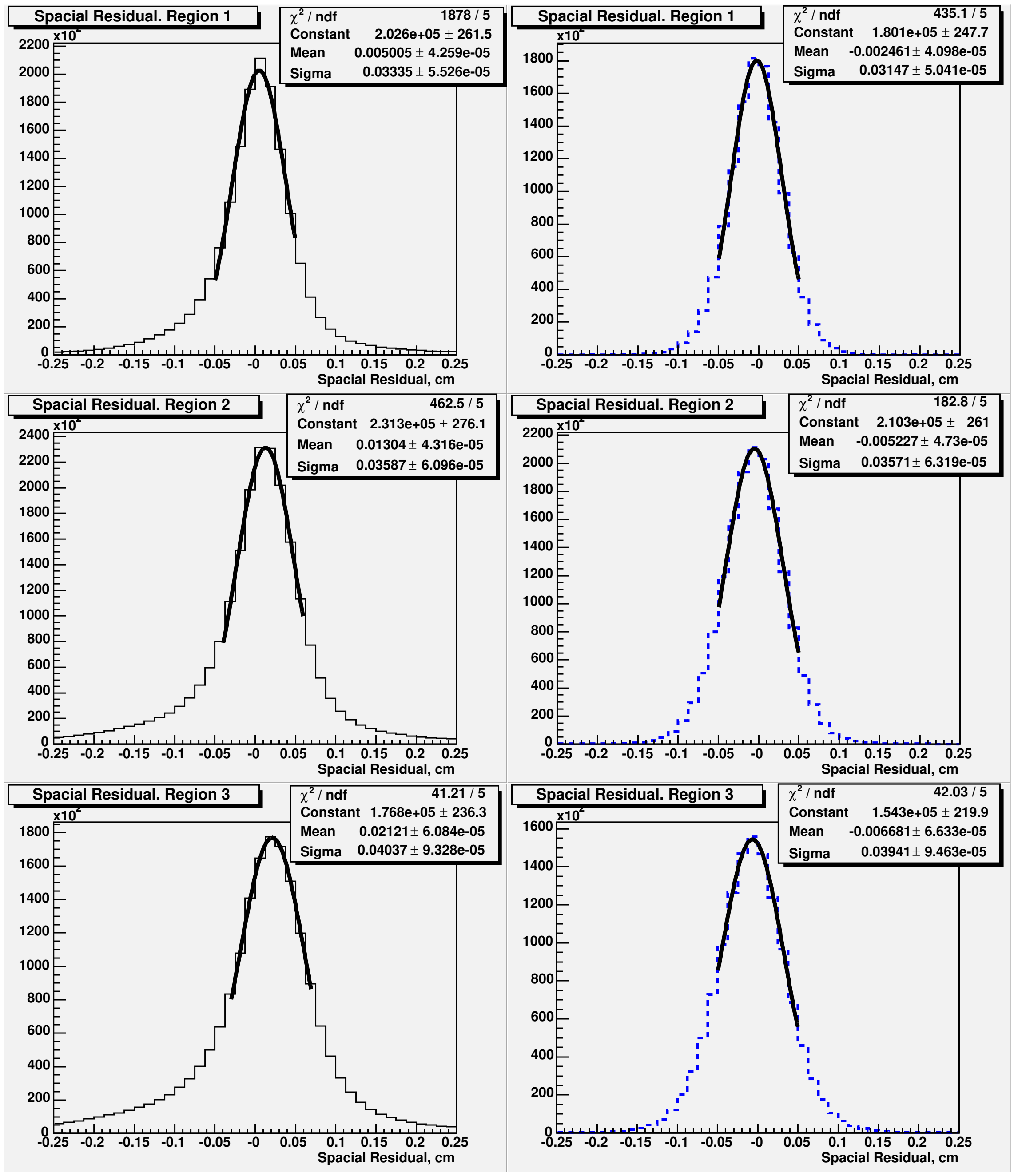

FIG. 73: Drift Chamber spatial residuals for run # 31974 (left) and simulation (right).

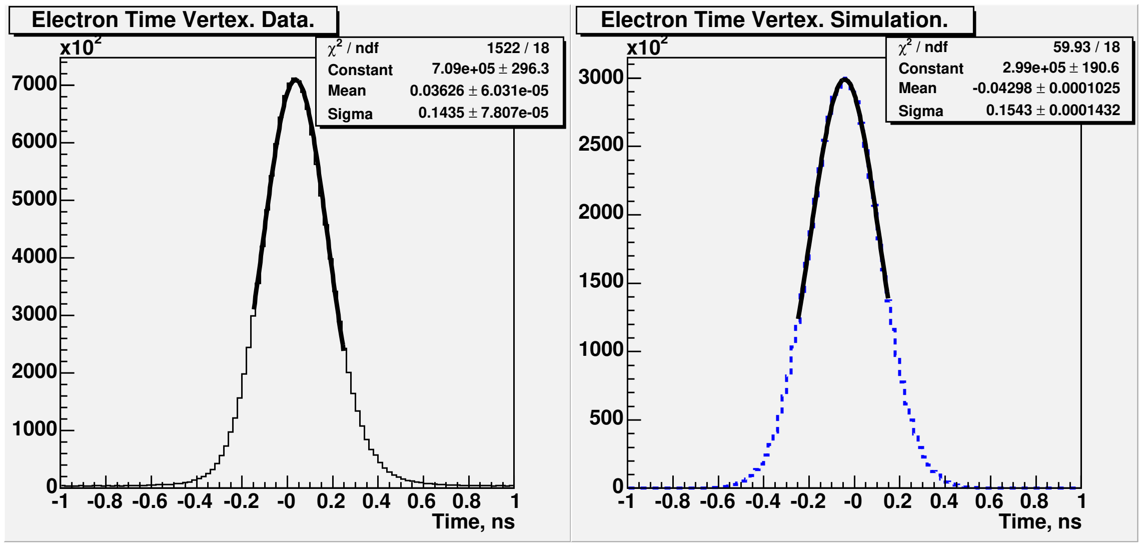

FIG. 74: Electron time vertex for data (left) and simulation (right) (bad scintillator paddles were excluded).

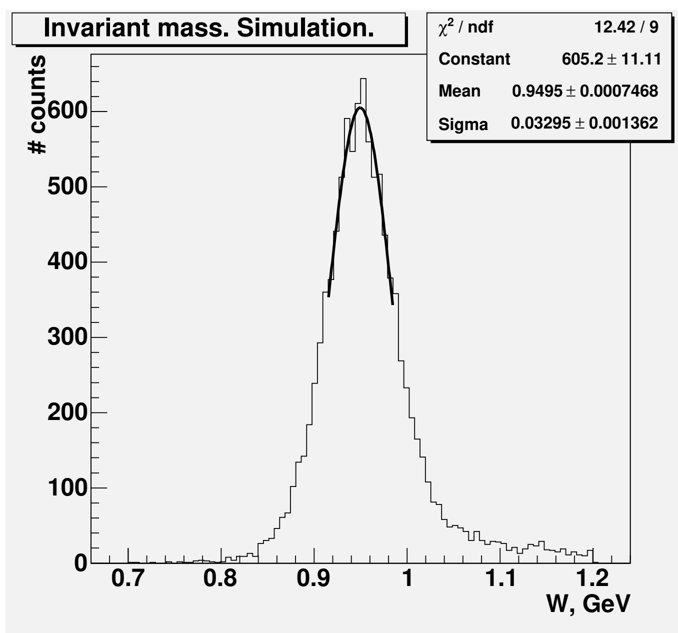

FIG. 75: Simulated invariant mass.

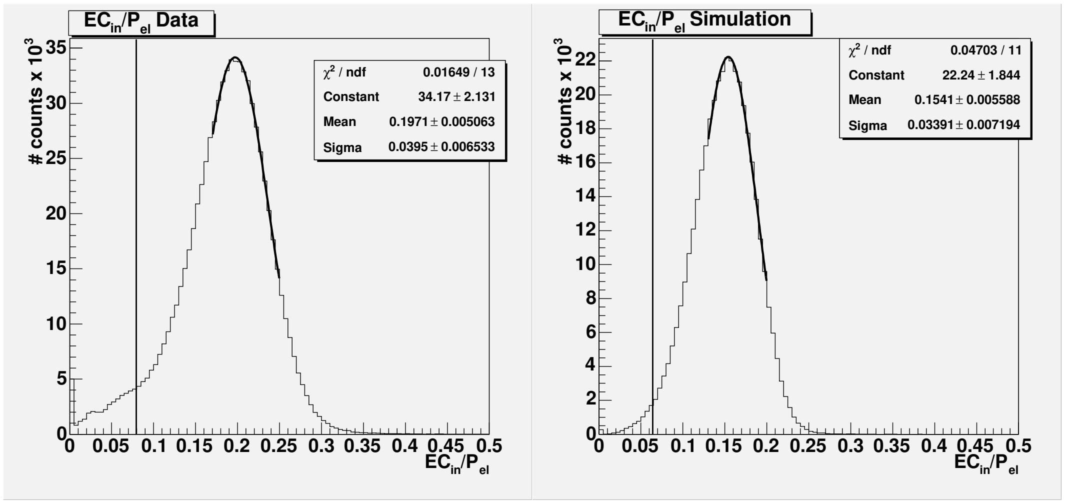

FIG. 76: Energy deposited in the inner layer of the calorimeter

However, as is clearly seen from the Figs. 76 and 77, the EC cut on simulated electrons rejects only a small fraction of good electrons (1.7%). Therefore, an additional correction factor of 0.97 (with 3% systematic error) needs to be applied for the EC cut to have an equivalent effect in the simulation (5% electron loss).

The Cherenkov counter is known not to be simulated properly in GSIM. To simulate the CC response, Vlassov's function (mentioned in section 4.3.1) was used. The average expected number of photo-electrons, given by Vlassov's function, was used as an input of a Poisson random number generator. The spectrum was then scaled by a constant factor for each sector to account for the CC photomultipliers' gain difference between our experiment and the data that were used to parameterize the CC efficiency in Vlassov's function. Figs. 78 and 79 show the comparison of the Cherenkov response in data and simulation. A maximum discrepancy of 10% in the position of the mean of the distribution is acceptable considering the fact that the simulation contains only electrons, while the data are contaminated with a certain fraction of pions (estimated in section 4.3.3). The simulated electron ID CC cut has an efficiency of 2±1% that matches exactly the efficiency estimated for this ID cut when applied to the data. This result is not surprising, since the same function was used to model the CC response in the simulation and to study the CC cut efficiency in the data. No extra correction is required here, after the CC ID cut is applied to

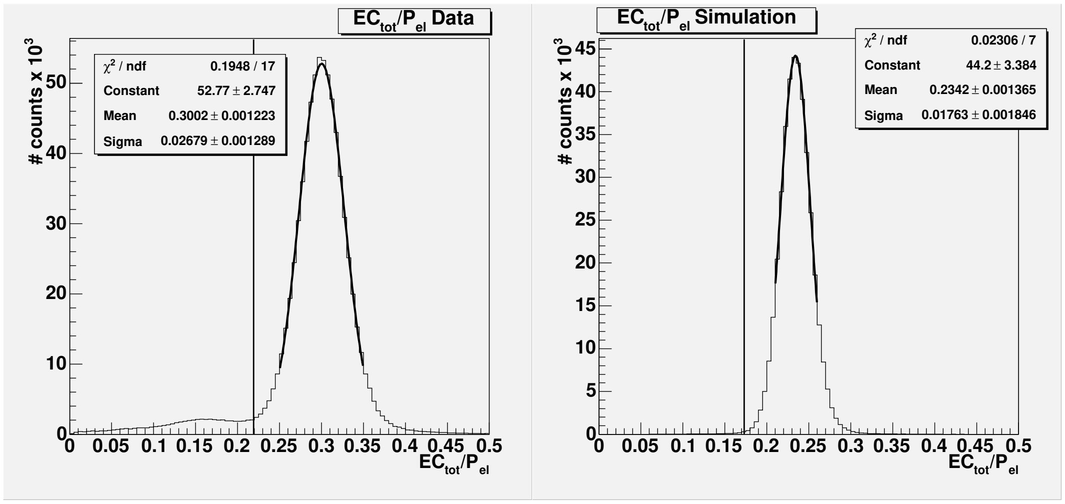

FIG. 77: Total energy deposited in the calorimeter.

the simulated CC response.

One last electron ID cut that is used is the vertex cut. The effect of this cut needs to be compared for data and simulation to make sure the equivalent amount of events is rejected. To compare the data with the simulation, the empty target background was first subtracted from the full target experimental data (Fig. 80). The distribution was then integrated in the limits of the vertex cut used for the electron $-2 < Z_{el} < 1.5$. It was found that after the cut 1.2% more of the simulated events survive the electron vertex cut. Therefore, an overall normalization of 98.8% needs to be introduced when comparing data with the simulation.

4.6.3 Simulation Results

4.6.3.1 Inclusive p(e,e')x and d(e,e')X Reaction Simulation

In this section the results of inclusive electron scattering on hydrogen and deuterium are compared with the simulation based on the parameterized world data. The simulation has all of the corrections discussed above applied to it.

An important question to investigate is how well the detector model, implemented in GSIM, is capable of reproducing the inefficient detector regions and their effect on physics observables. Fig. 82 compares the electron scattering angle in the experimental data with the same distribution in the simulation. At first sight the

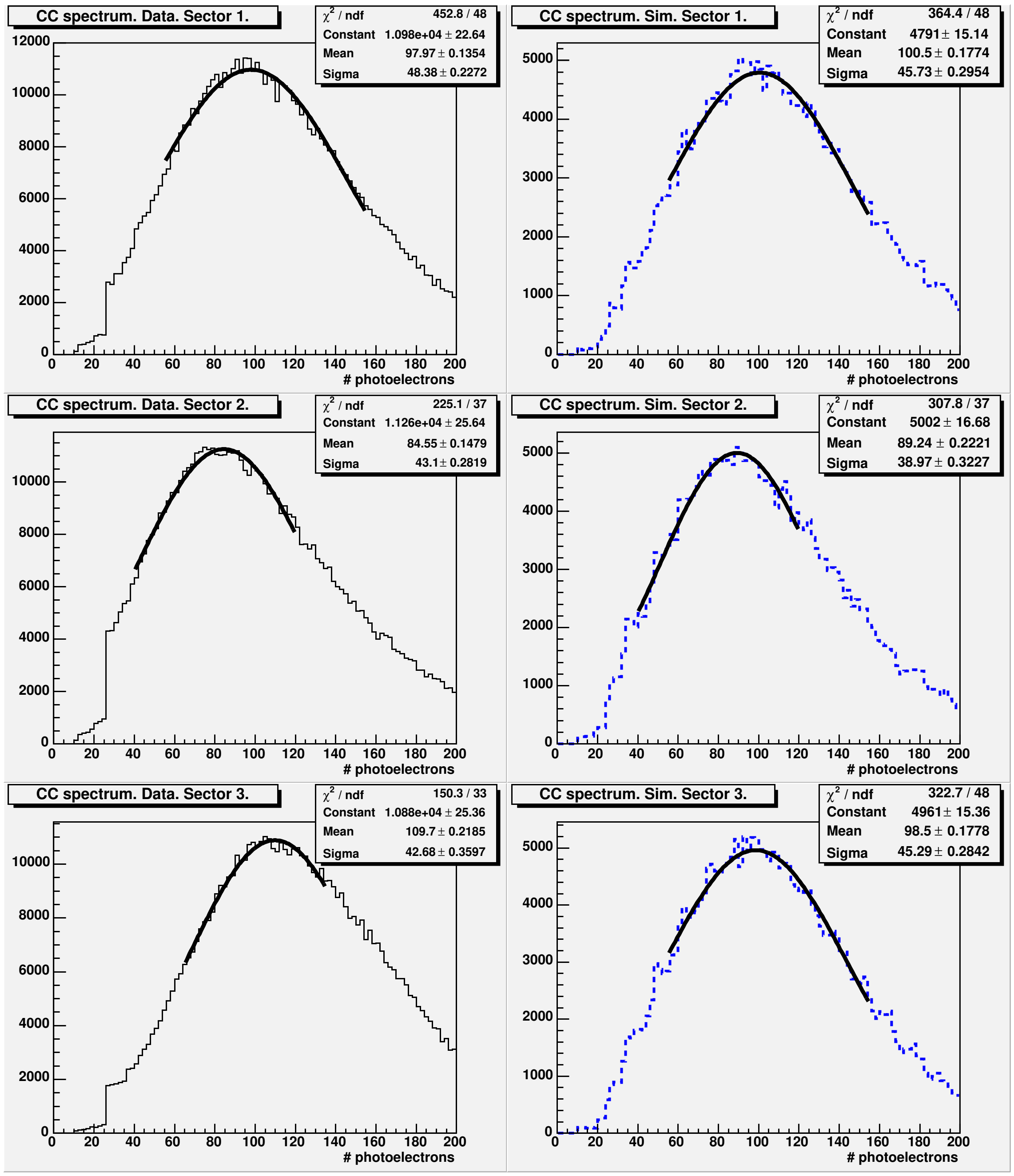

FIG. 78: Cherenkov detector spectrum for data (left) and simulation (right).

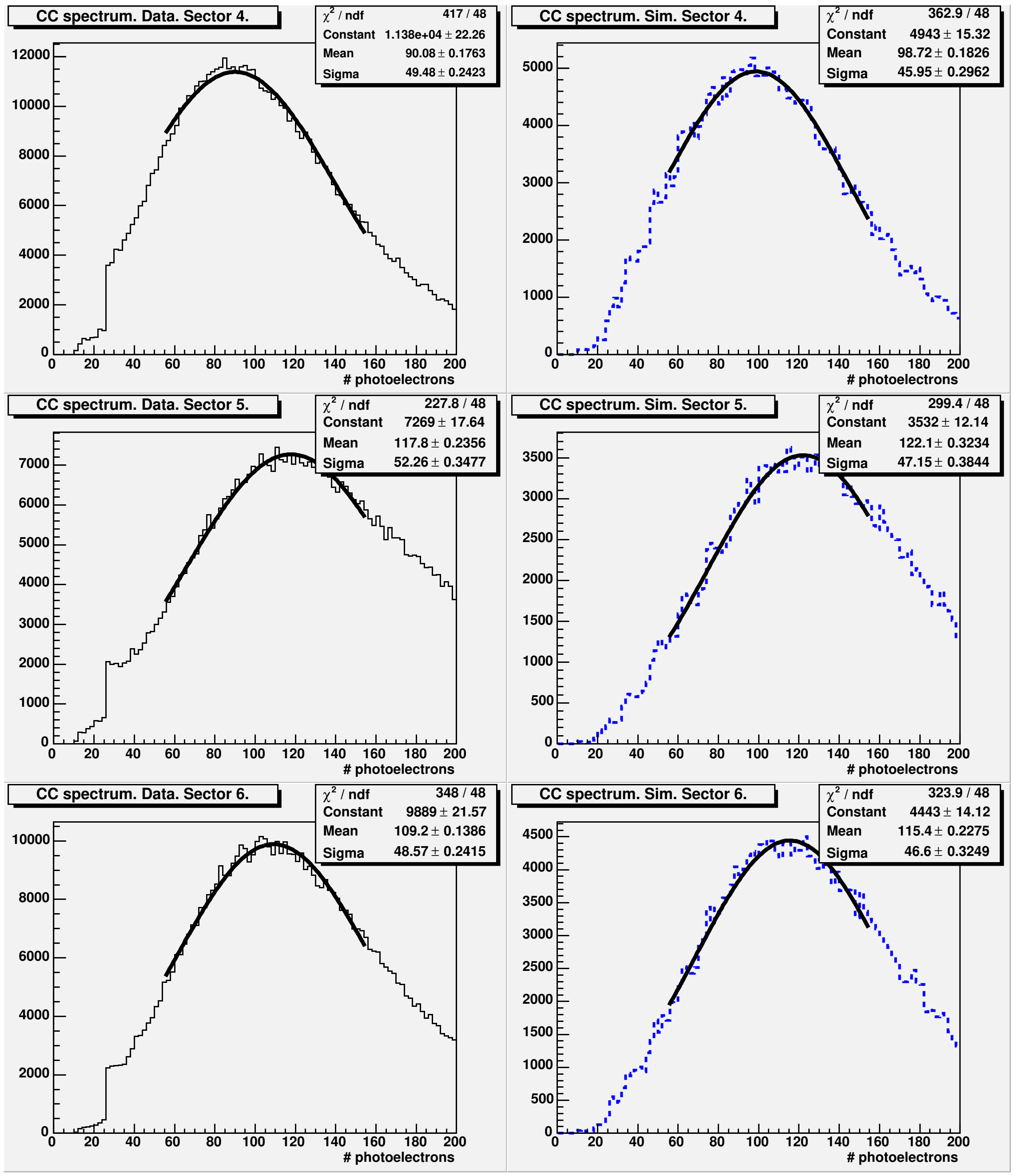

FIG. 79: Cherenkov detector spectrum for data (left) and simulation (right).

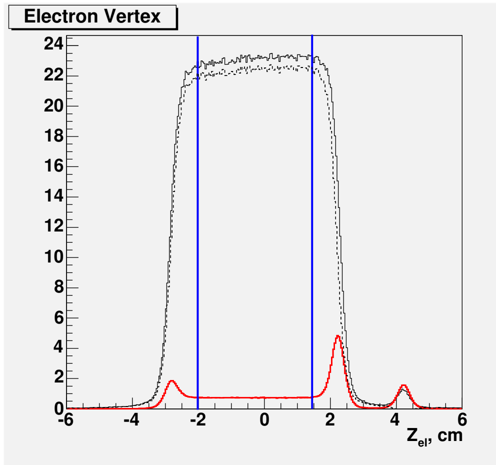

FIG. 80: Target vertex for the experimental data. Plotted are full target (dark solid line), empty target (light solid line) and full target after empty target subtraction (dashed line).

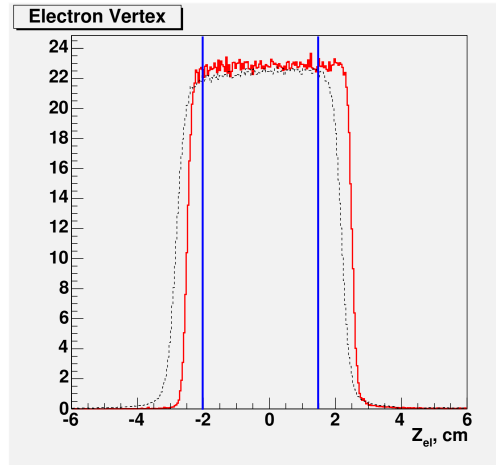

FIG. 81: Target vertex for the data after empty target subtraction (dashed line) and the simulation (solid line).

two curves come very close to each other. However, when the ratio of simulation to data is plotted (Fig. 83), a significant disagreement between the two in sectors 5 and 6 becomes obvious. Since Sectors 1 through 4 appear relatively similar they can be summed and averaged (Fig. 84). This average distribution was then used to normalize sectors where the disagreement was observed (Fig. 85, 86). After this normalization, possible effects coming from model uncertainties cancel out and the remaining discrepancy is only a result of detector inefficiencies that were not simulated properly. The histograms on Figs. 85 and 86 were then transformed into an array of weights and a function was written for event-by-event weighing of the simulated data depending on the electron scattering angle in sector 5 and 6.

The electron kinematics are fully defined if the other variable measured by the detector is considered - electron momentum. Momentum distributions for electrons are shown in Fig. 87. The ratio of data to simulation has to be plotted again to get a better idea of how close the two distributions correlate (Fig. 88). No noticeable major discrepancies are observed in this case and averaging over the whole detector can be performed to improve the statistics (Fig. 89). Using this plot a final statement on the uncertainty of the inclusive process measurement can be made: the $d(e,e')X$ process can be measured within an average error of 7%.

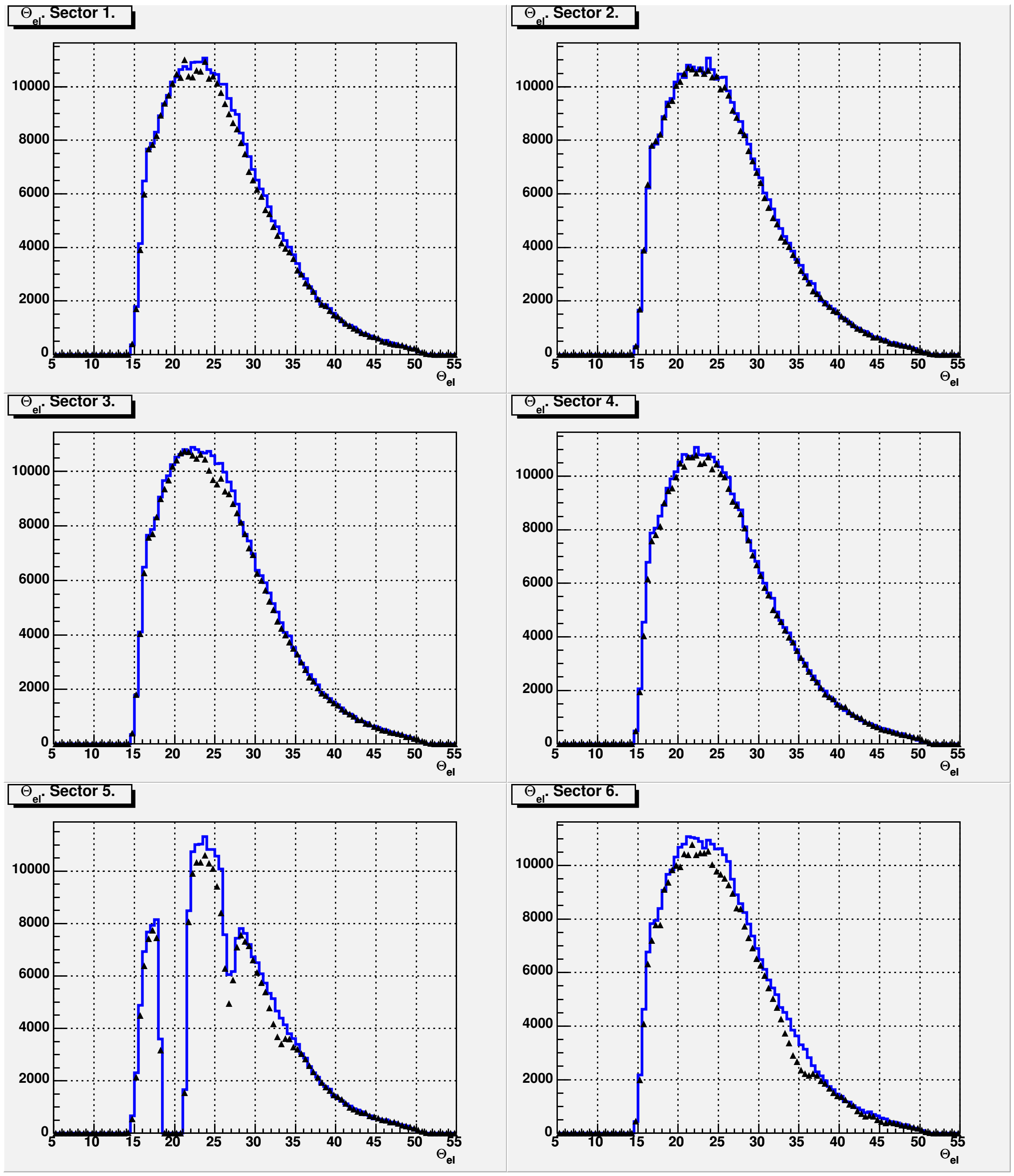

FIG. 82: Electron scattering angle in data (black points) and simulation (solid line).

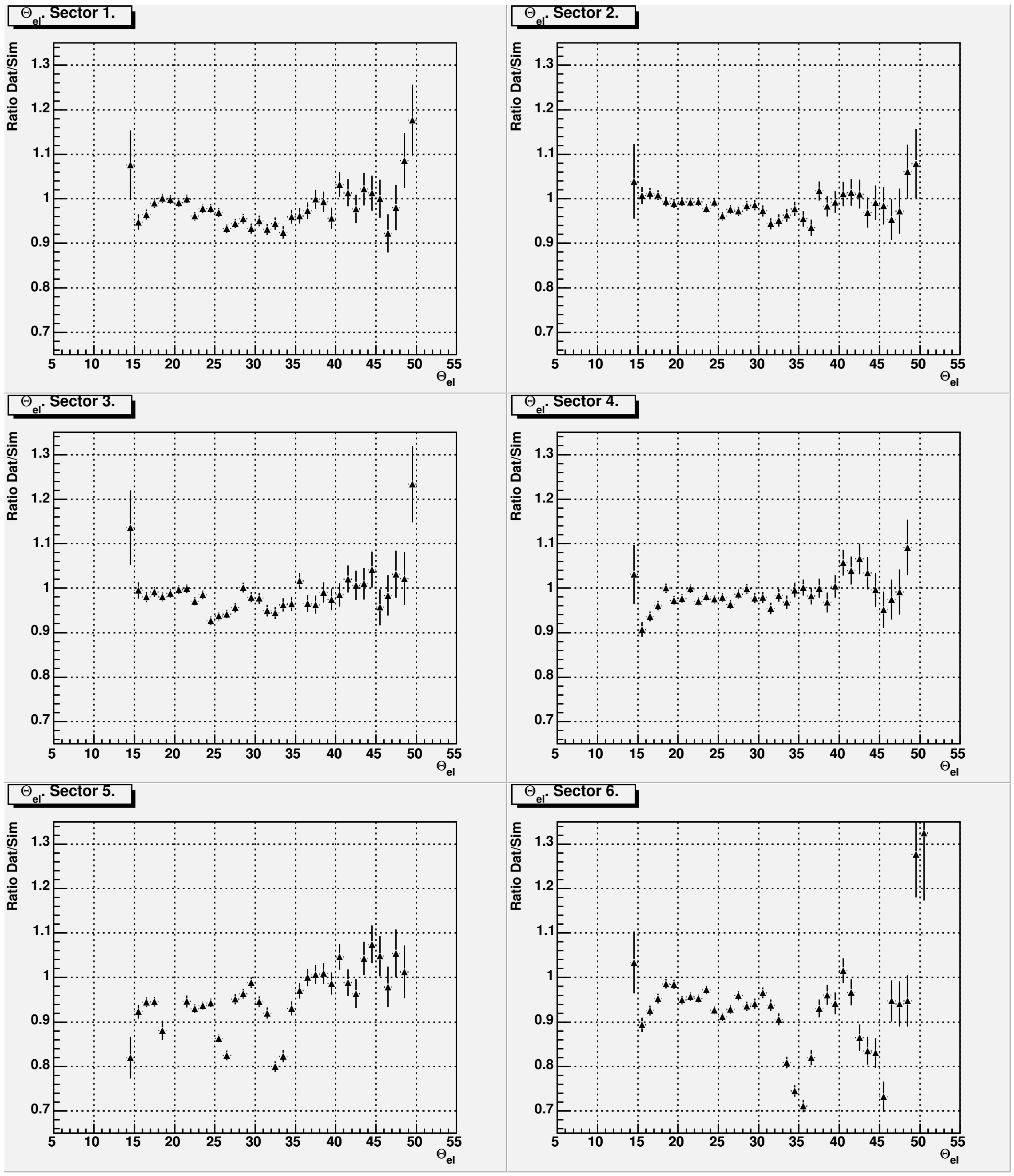

FIG. 83: Electron scattering angle (ratio of data to simulation).

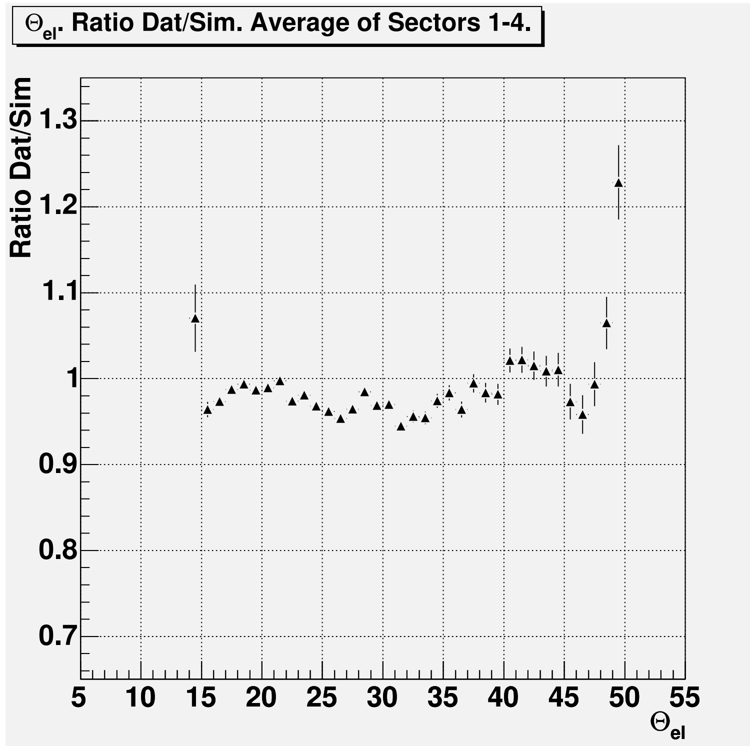

FIG. 84: Scattering angle of the electron: the average ratio of data over simulation for sectors 1 through 4.

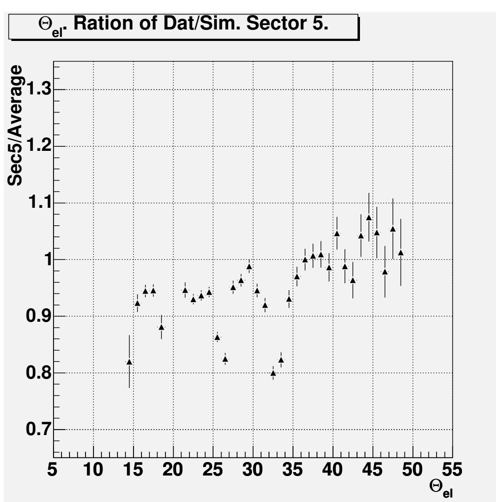

FIG. 85: Sector 5 normalized to the average of first 4 sectors.

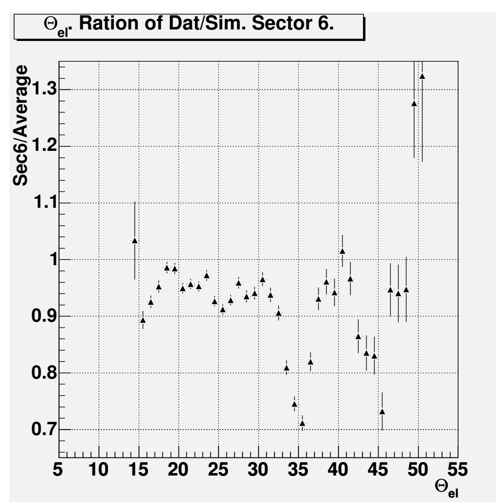

FIG. 86: Sector 6 normalized to the average of first 4 sectors.

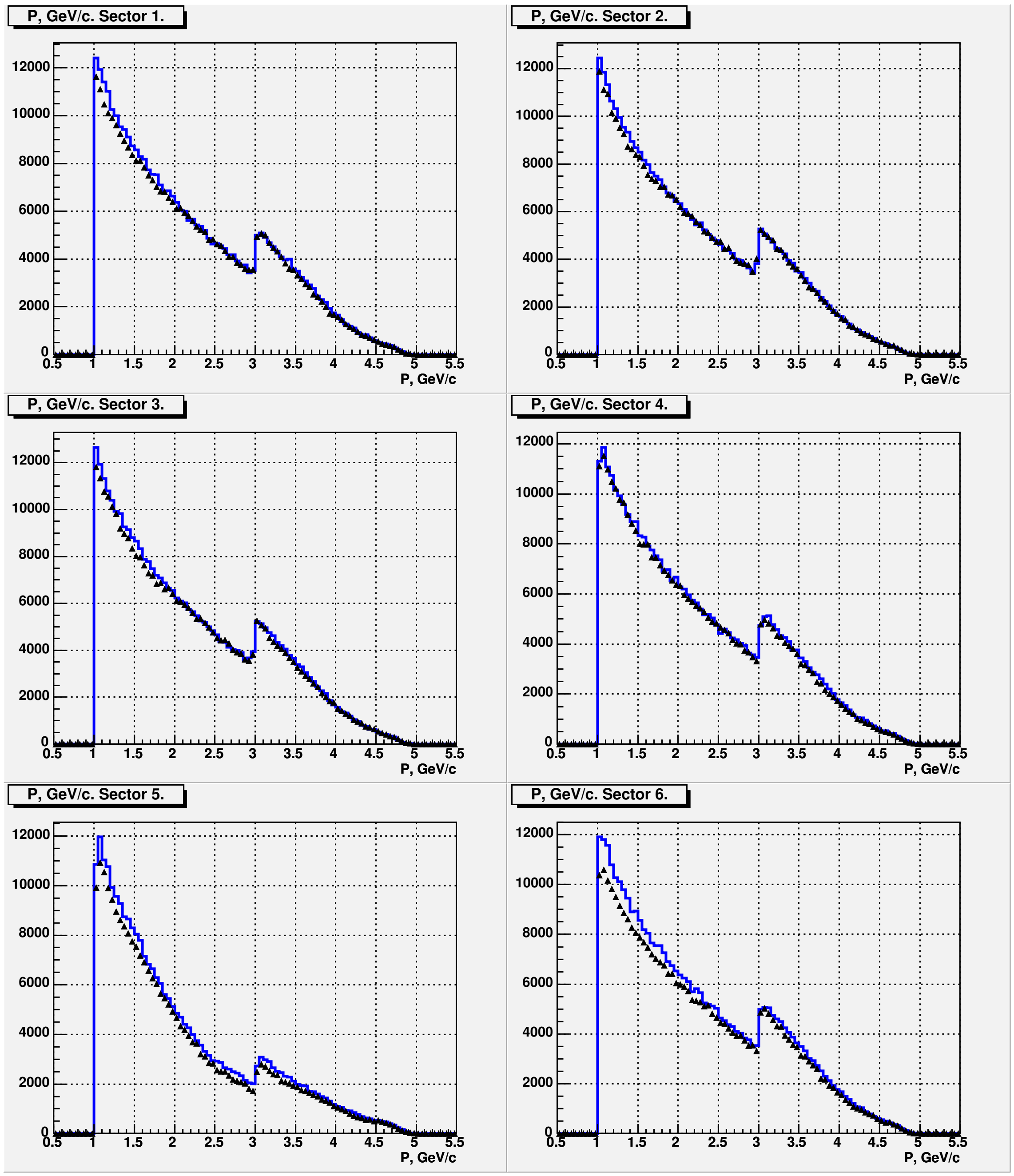

FIG. 87: Electron momentum for data (black points) and simulation (solid line). The step in the distribution is a result of the fiducial cut.

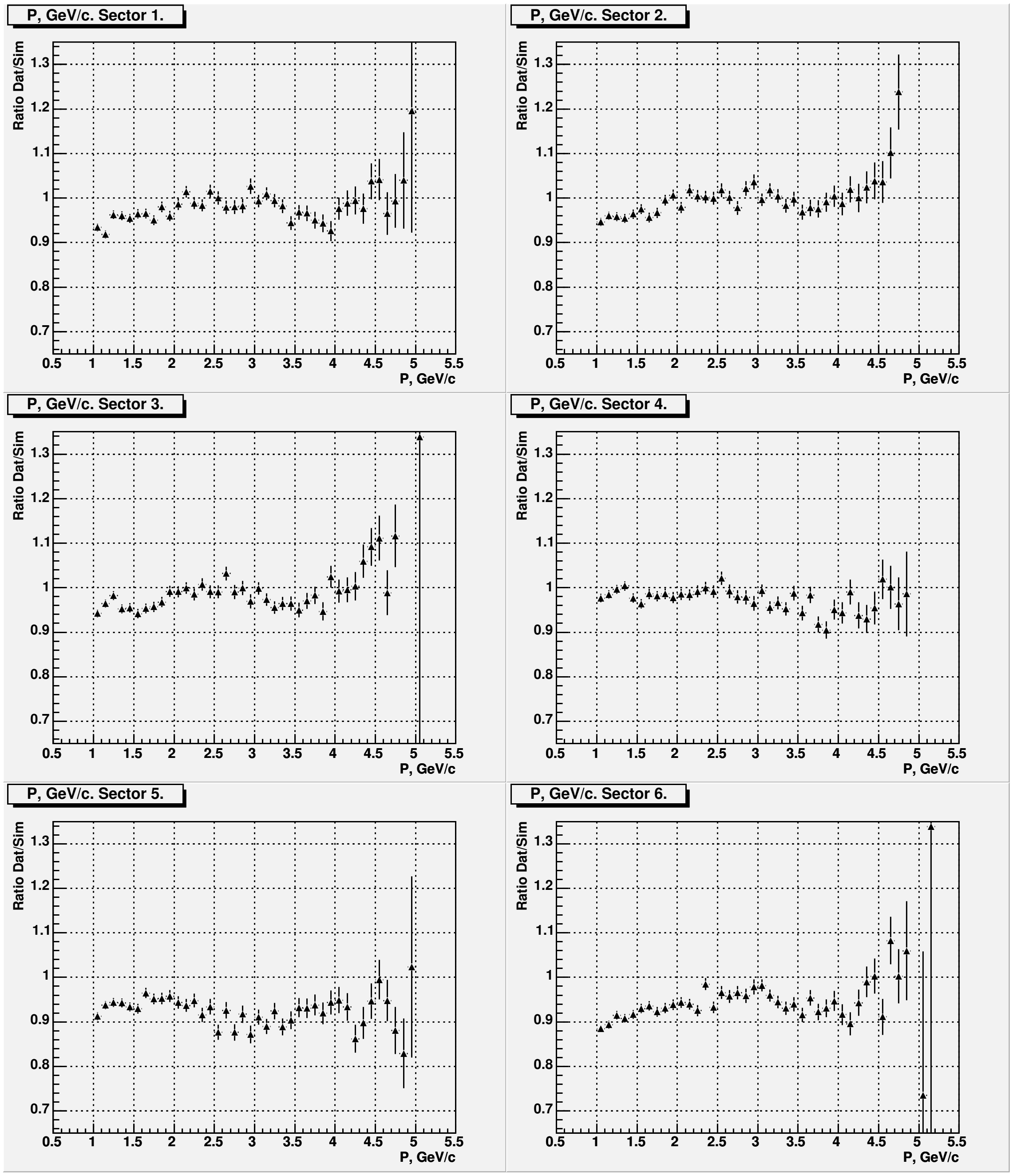

FIG. 88: Electron momentum (ratio of data divided by simulation).

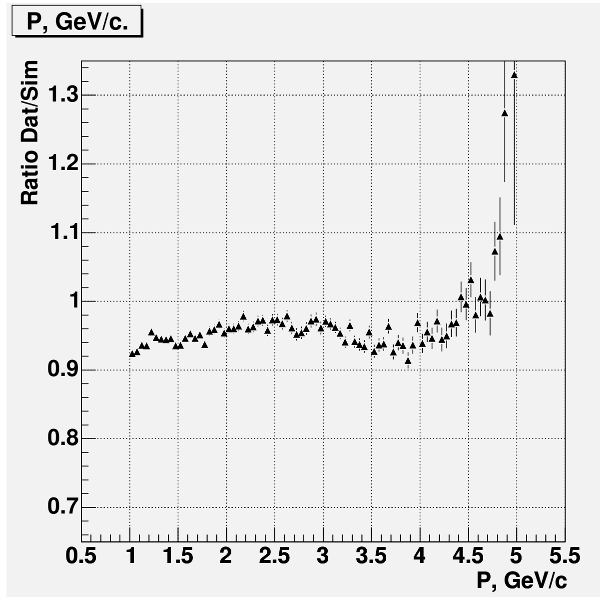

FIG. 89: Electron momentum distribution for all 6 sector of the spectrometer combined. Ratio of data to simulation.

Fig. 90 shows the distribution of data and simulated events versus the invariant mass of the unobserved final state in the $d(e,e')X$ reaction. Fig. 91 is zoomed on the quasi-elastic region. Fig. 92 presents the ratio of the counts in simulation divided by the number of counts found in experimental data. On average, the agreement is within 10%.

To date, one of the best studied cross sections in nuclear physics is that of elastic electron scattering from a free proton. Figs. 93 and 94 show how well the experimental data under discussion are able to reproduce this cross section. To select elastic events a cut on the invariant mass W was used: $0.9 < W < 1.1$ GeV. Unfortunately, the statistics are not high enough to make any firm statements based on these plots. The overall shape is reproduced well and the cross section lies well within 10% at low Q^2 where the statistics are acceptable.

The Q^2 distribution of the inclusive cross section for quasi-elastic scattering on deuterium is also in good agreement with the experimental data (see Fig. 95 and 96). Here the events were also selected using the invariant mass cut $0.9 < W < 1.1$ GeV. In the region of relatively good statistics at low Q^2 the deviation from unity on the ratio plot Fig. 96 does not exceed 10%.

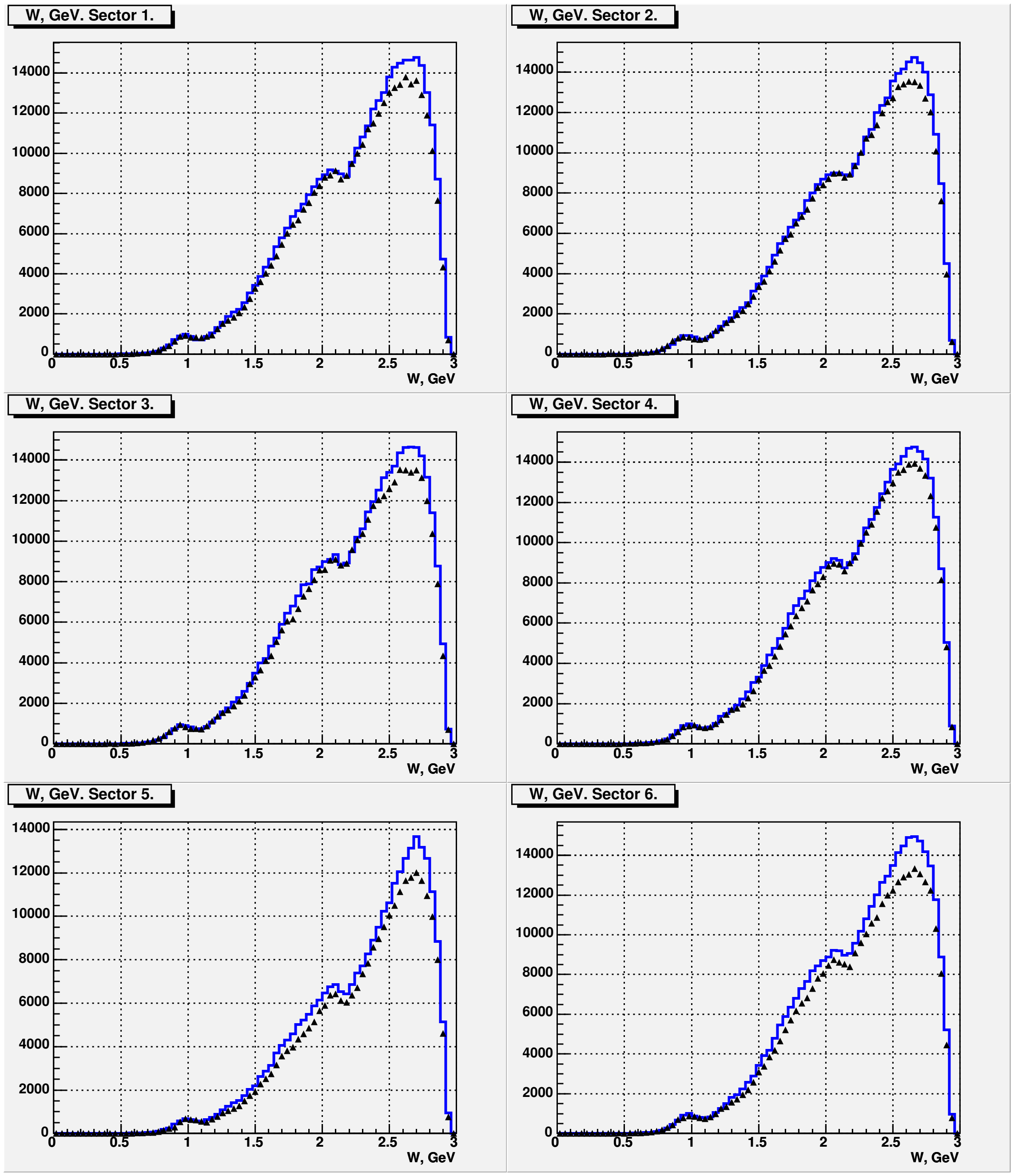

FIG. 90: Invariant mass W (the "step" in the distribution is a result of the fiducial cut).

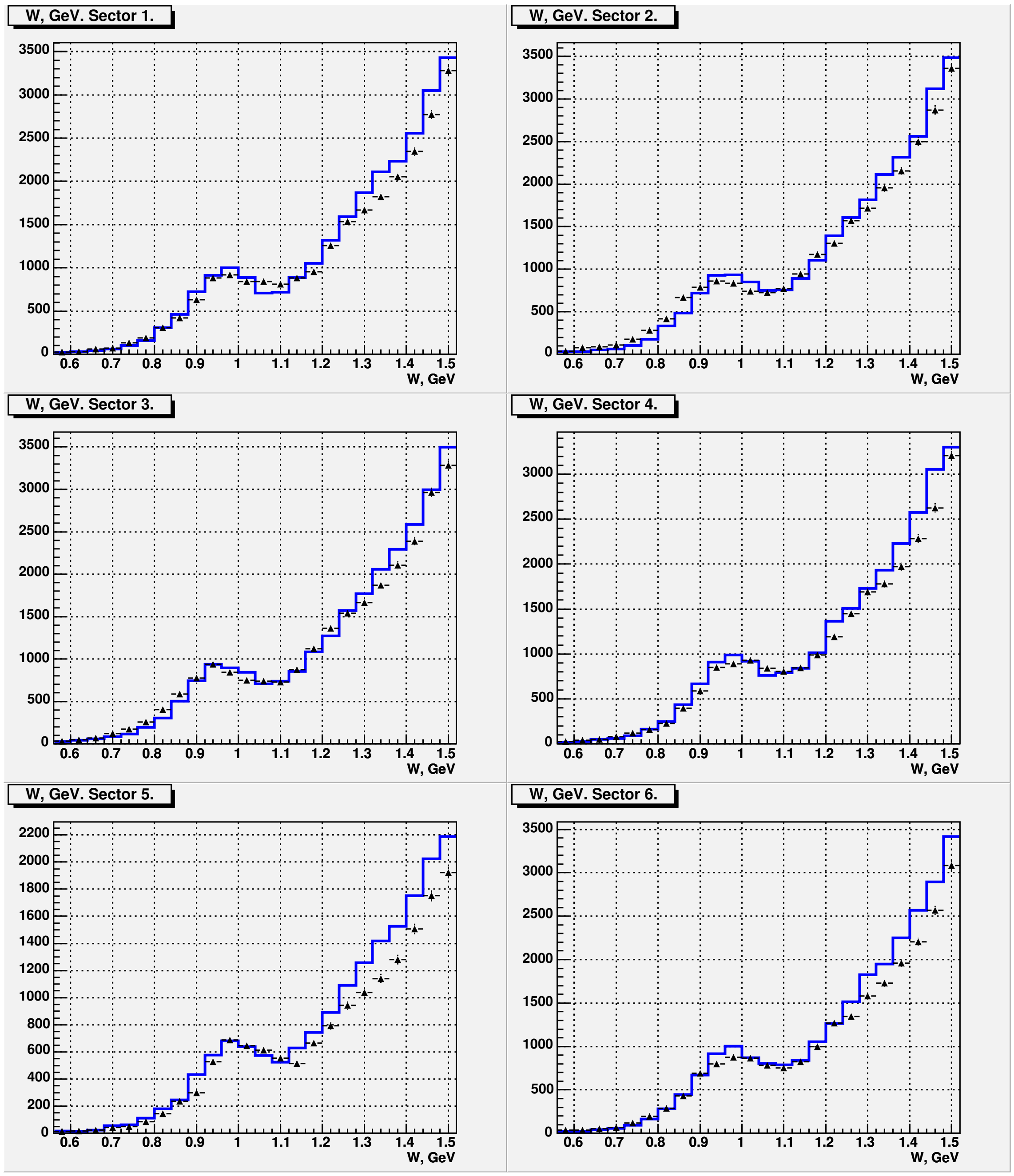

FIG. 91: Same as Fig. 90, with an enhancement of the quasi-elastic region.

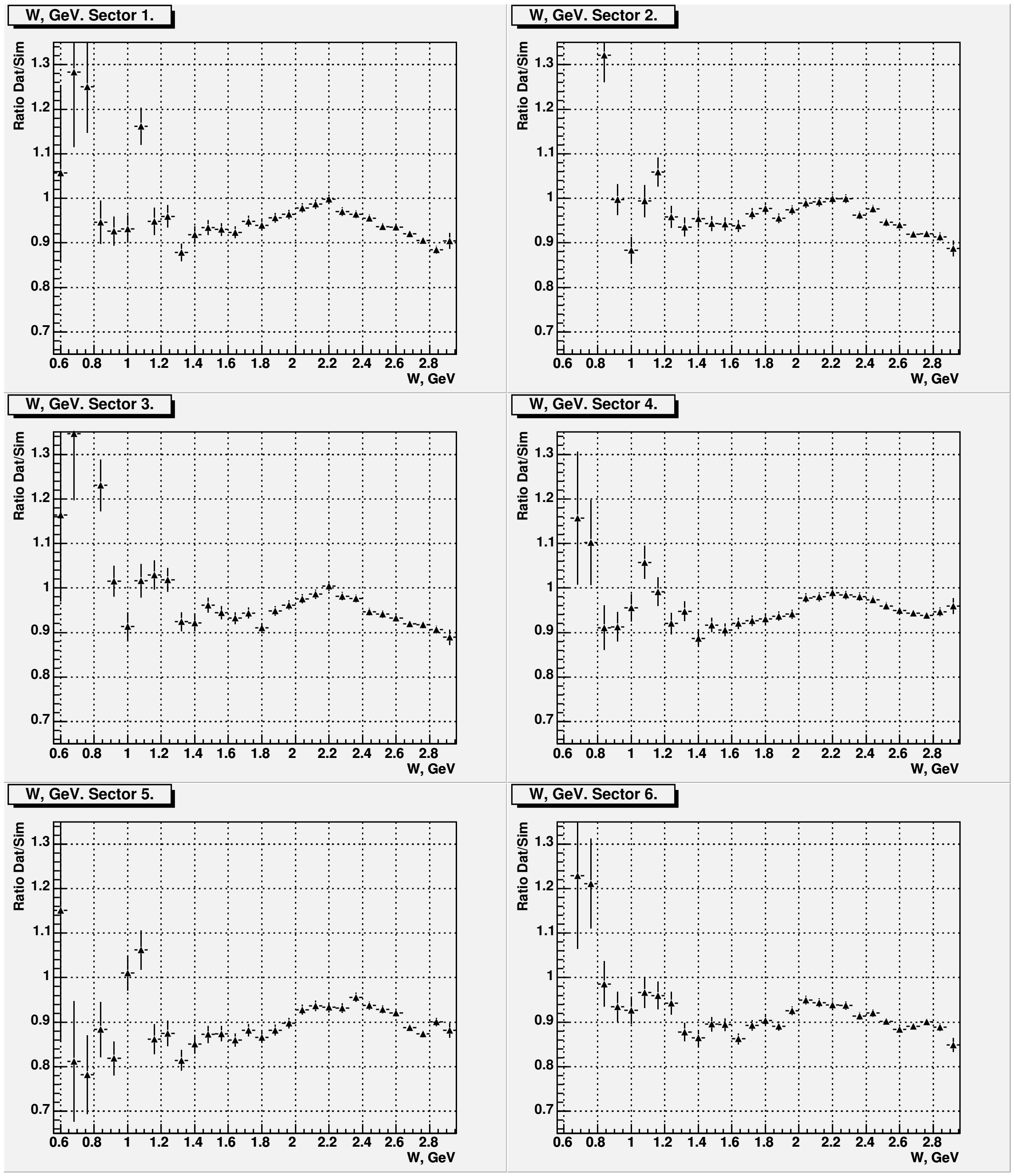

FIG. 92: Ratio of data over simulation for the invariant mass distribution ($d(e,e')X$ reaction).

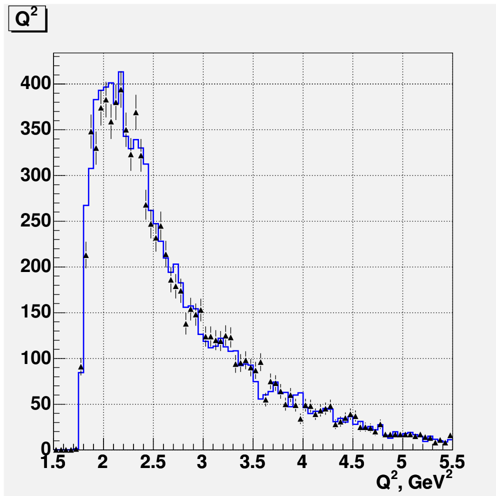

FIG. 93: Q^2 distribution of $p(e,e')p$ scattering for data (triangles) and simulation (solid line).

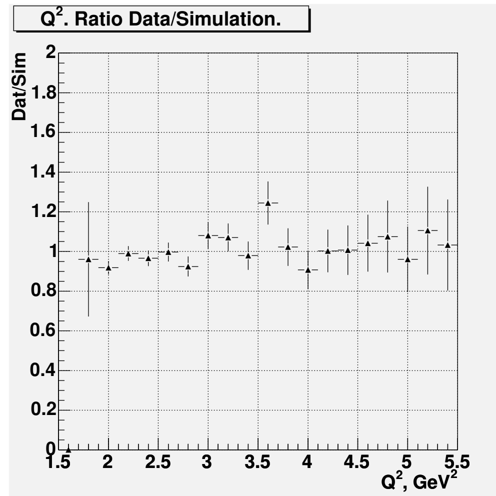

FIG. 94: Ratio of Q^2 distribution of $p(e,e')p$ for data over simulation.

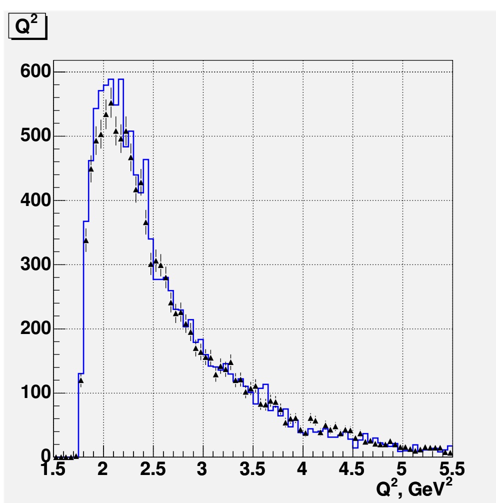

FIG. 95: Q^2 distribution for data (triangles) and simulation (solid line) for $d(e,e')X$ reaction.

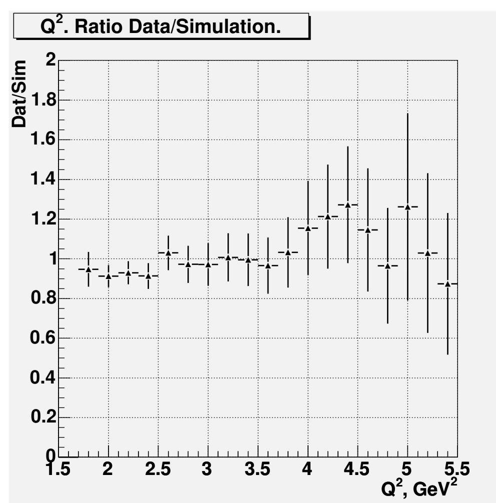

FIG. 96: Ratio of Q^2 distribution for data over simulation for $d(e,e')X$ reaction.

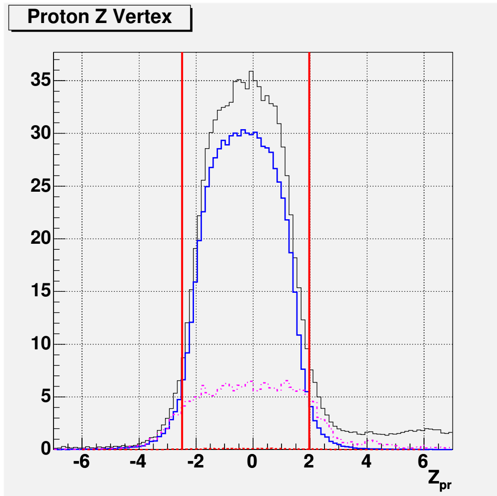

FIG. 97: Proton vertex: data before the background subtraction (thin line); simulation (thick line); accidentals (dot-dashed line). Verticle lines indicate the proton vertex quality cut.

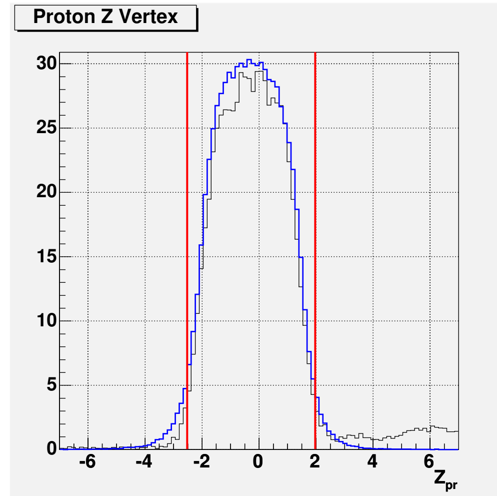

FIG. 98: Proton vertex for data after background subtraction (thin line) and simulation (thick line).

4.6.3.2 Semi-inclusive d(e,e'p) Reaction Simulation

With a good idea of the quality of the electron detection simulation, it is time to narrow down the spectrum of events to the ones of interest, where a backward proton is detected in coincidence with the forward electron. The protons discussed here are required to have a scattering angle of greater than 50^o in the laboratory frame and greater than 72.5^o angle with respect to the momentum transfer vector.

Just as in the case of the electrons, it also has to be verified that the proton vertex cut ($-2.5 < Z_{pr} < 2.$ cm) has the same impact both on data and simulation. The vertex distribution of protons that have an electron in coincidence satisfying all of the electron ID cuts was studied. The reaction was limited to have $Q^2 \geq 1.2$ GeV^2/c^2. To estimate the integrated number of events in the proton vertex distribution, the same distribution was constructed for the accidentals (Fig. 97). The accidentals were then subtracted. Normalized empty target data were used to subtract the remaining small contribution from the target walls. The study showed that 96.85% of data events survive the proton vertex cut, but only 95.64% of simulated events remain after the cut. The difference can be attributed to a minor offset in the simulated vertex as compared to the data vertex.

P_s (MeV/C)	$N_{\Delta T}/N$, Data	$N_{\Delta T}/N$, Sim	$Data/Sim$
250<p<280	0.9370	0.9502	0.9861
280<p<320	0.9505	0.9662	0.9838
320<p<360	0.9676	0.9801	0.9873
360<p<420	0.9798	0.9872	0.9925
420<p<500	0.9843	0.9907	0.9936
500<p<750	0.9808	0.9922	0.9885

TABLE IV: Ratio of the total events to the events within the proton time quality cut for data and simulation. The column contains the ratio between the fraction of events remaining in data over simulation.

Another issue related to the proton ID cuts to be considered is the proton timing cut (discussed in Sec. 4.4.1). The proton time vertex defined in formula (45) can be plotted for different ranges in proton momentum (Fig. 99). The data distribution clearly has a constant background of accidentals that can be subtracted (Fig. 100). The effect of the proton timing cut can now be evaluated for data and simulation. As it can be seen from Table IV an overall correction of $1 \pm 1\%$ is sufficient for the proton time vertex cut to reject equivalent number of events in data and simulation.

It has to be verified that inefficient scintillator paddles in the backward part of the detector are properly excluded in the simulation. For that purpose, a comparison needs to be made between data and simulation of the proton time vertex plotted versus the z-coordinate on the scintillator plane of the point where the proton track intersects with this plane (Z_{sc}). Fig. 101 shows the distributions for sectors 1 through 3. Z_{sc} and paddle number are directly related. In sector 1, the paddle centered at $Z_{sc} = 0$ cm is not reproduced in the simulation. Sectors 2 and 3 look very similar in both simulation and data. A malfunctioning very backward paddle at $Z_{sc} = -250$ cm has some counts in data, but less than neighboring paddles. To avoid unnecessary uncertainties, this region of sector 3 will be completely excluded both from data and simulation. Fig. 102 shows similar plots for detector sectors 4 through 6. Sectors 4 and 5 are identical in data and simulation and need no additional corrections. Sector 6 has inefficiency at $Z_{sc} = -160$ cm. This region will be excluded in data and simulation.

More inefficiencies are revealed if the ratio of simulation to data is plotted as a

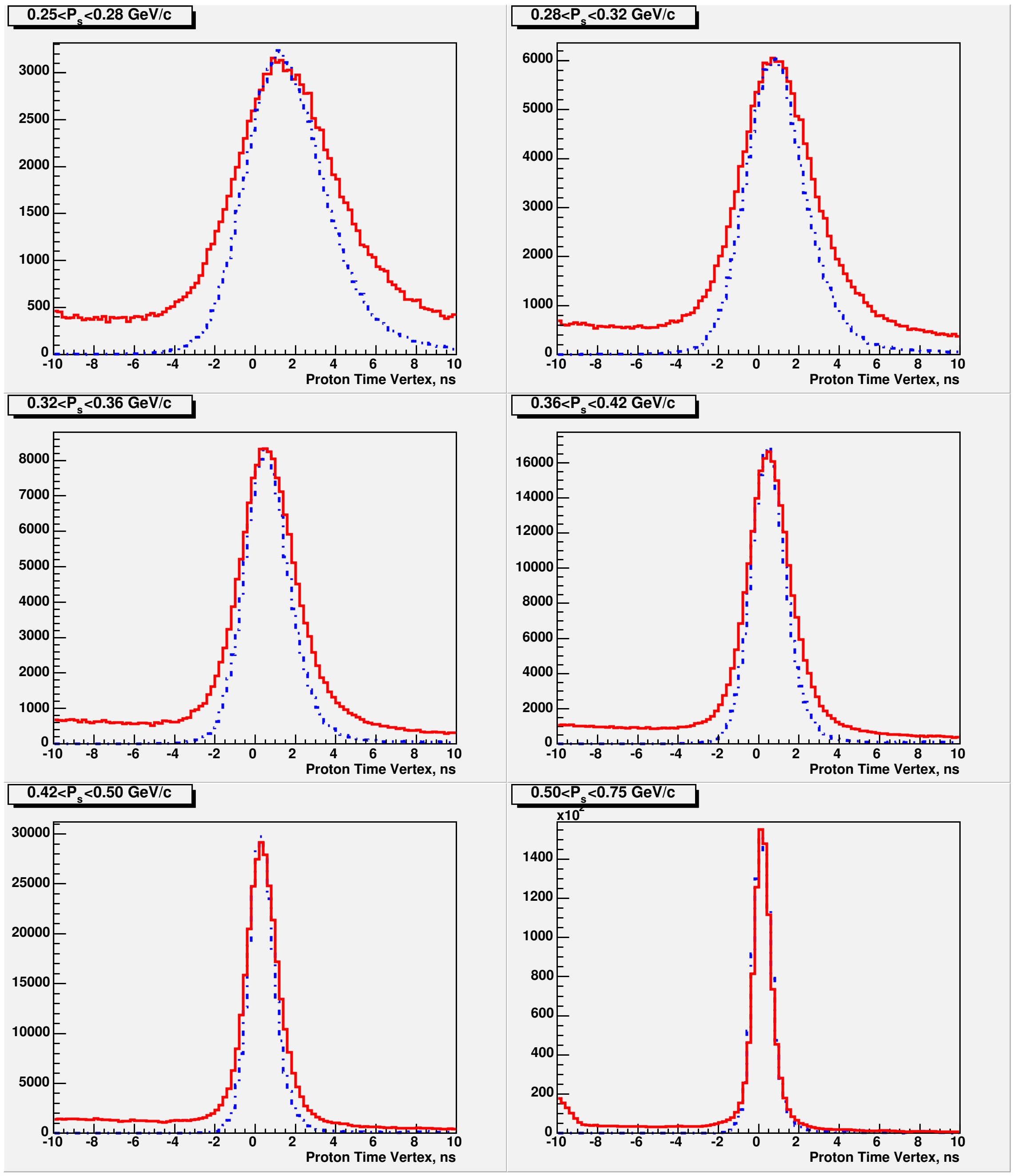

FIG. 99: Proton time vertex: data (solid) and simulation (dot-dashed).

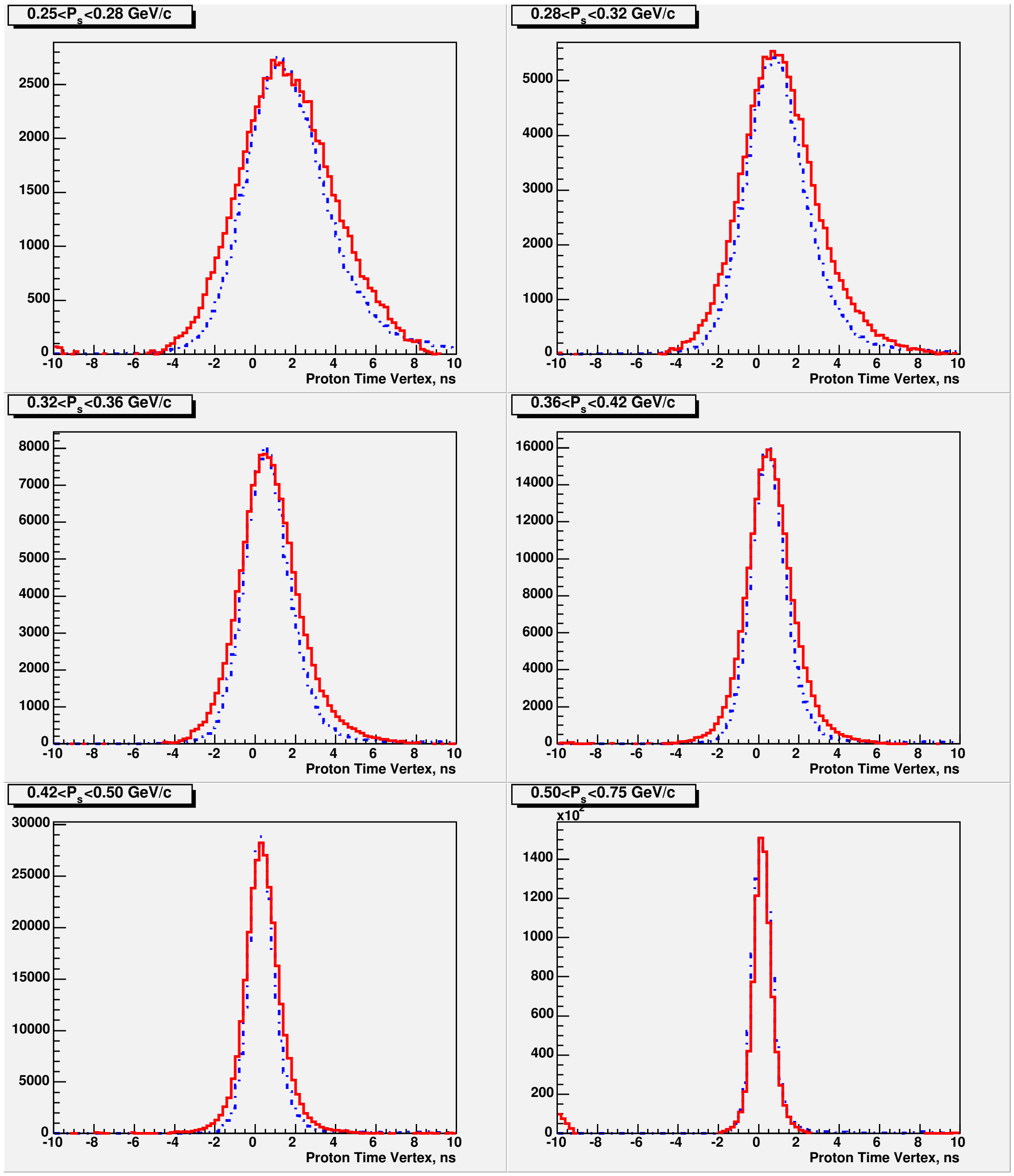

FIG. 100: Proton time vertex after background subtraction for data (solid) compared with simulation (dot-dashed line).

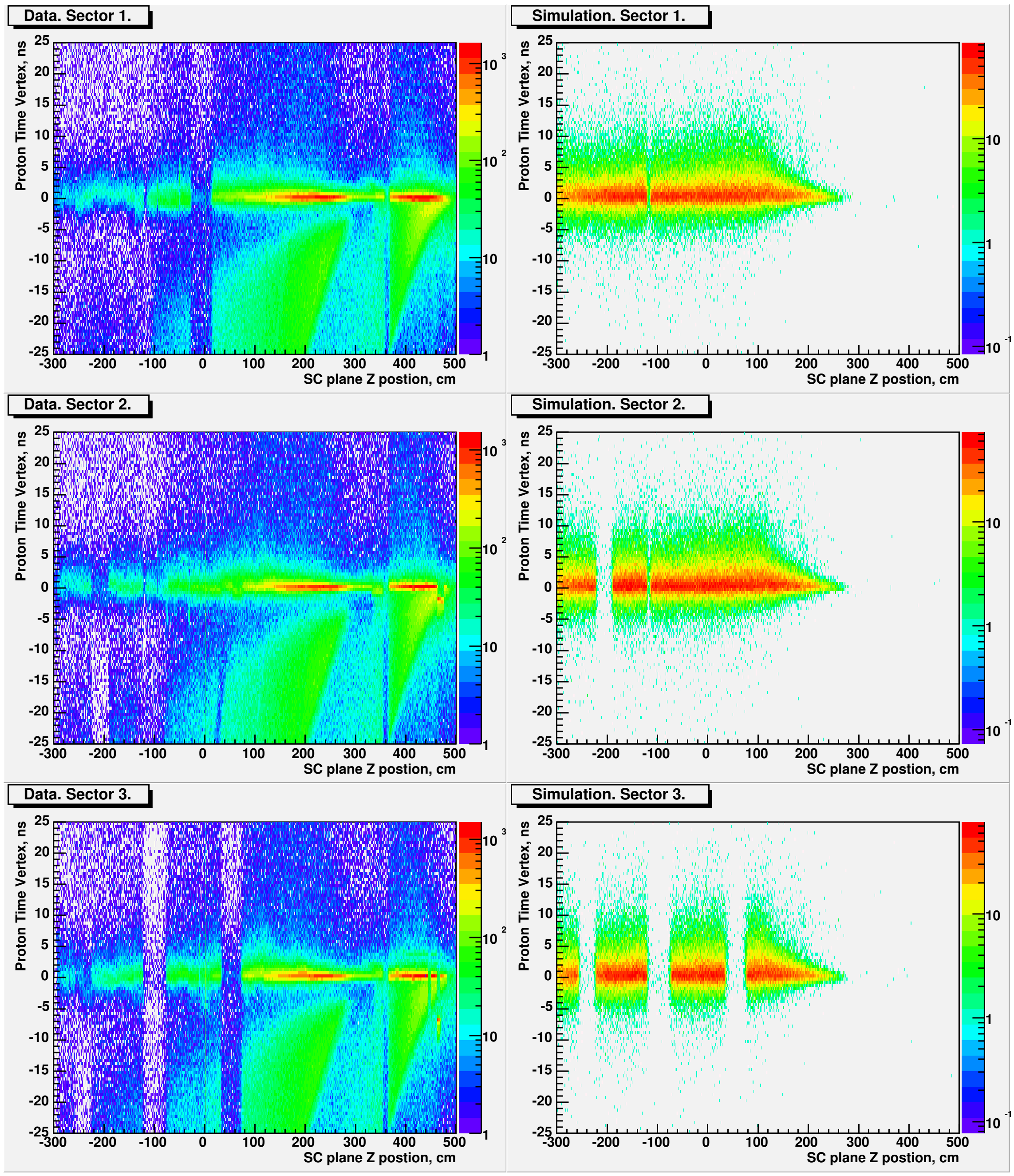

FIG. 101: Proton time vertex plotted as a function of proton position on scintillator plane: data for sectors 1 through 3 is presented on the left panels and simulation on the right.

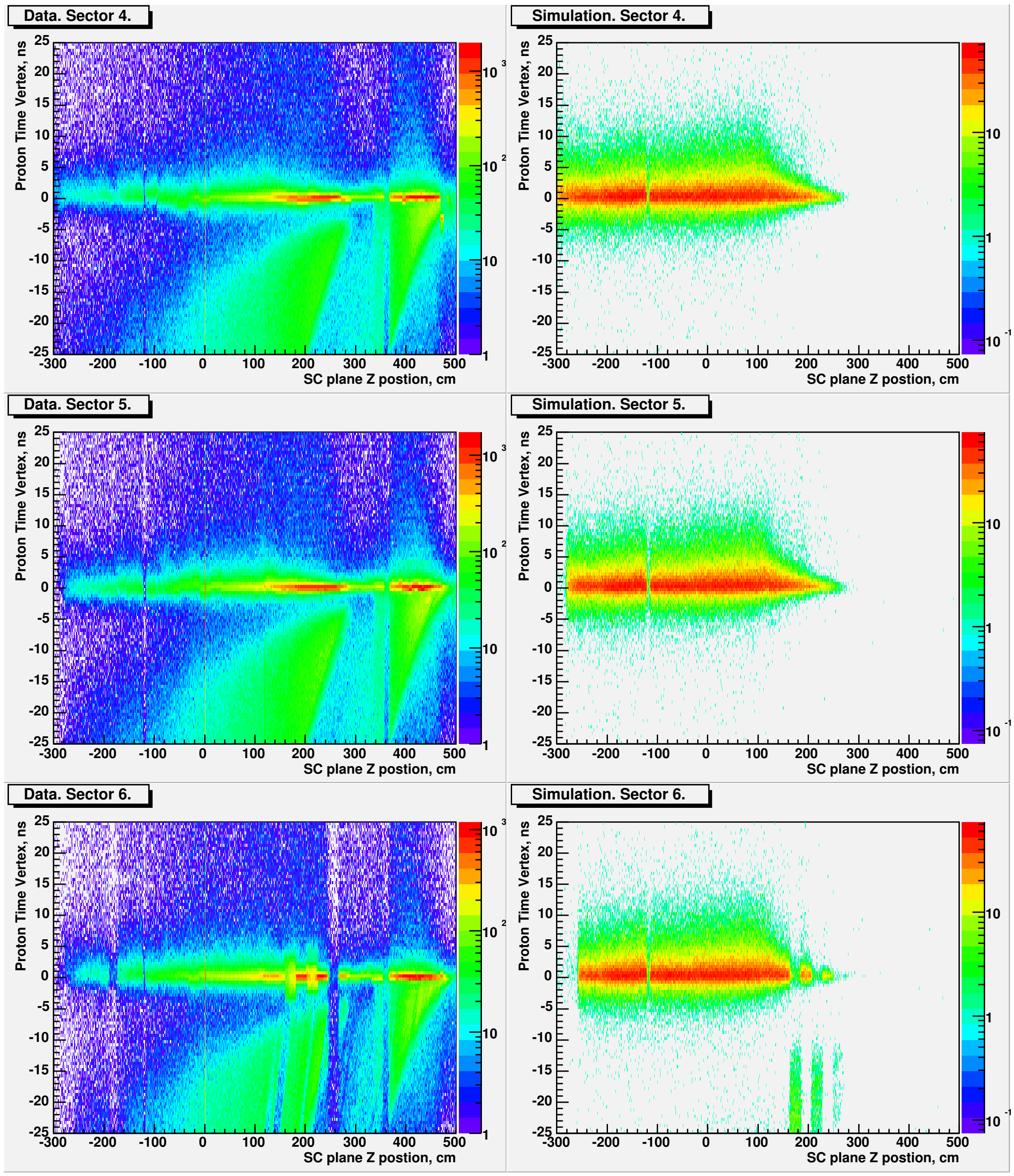

FIG. 102: Proton time vertex plotted as a function of proton position on scintillator plane: data for sectors 4 through 6 is presented on the left panels and simulation on the right.

function of Z_{SC} independently for the 6 sectors where the proton was detected (Fig. 103). Sector 5 and 6 here appear almost flawless. Sector 3 has good efficiency with the exception of the region around $Z_{sc} = -200$ cm. The ratio is not necessarily unity because the PWIA model used in in simulation does not describe the total proton yield perfectly. The first 3 sectors are more problematic. There are two general types of mismatches in efficiency between data and simulation. The dead paddles that were introduced by GPP have a slightly different width in Z_{sc} in simulation, as a result of which there are spikes in the ratio of simulation to data right on the boundary of these paddles. Regions where the scintillator counters are operating, but are not as efficient for low-momentum backward protons as is expected from the detector model, have to be excluded from the analysis as well. Those appear as bumps relative to the overall trend of the distribution given by the last three sectors, that are mostly efficient. The final set of excluded regions is presented in Fig. 104.

The resulting proton distribution should be tested using observables that were not explicitly used to reject inefficient data. Fig. 105 shows the proton angular distribution for all 6 sectors after all the inefficient regions of SC were excluded. The average ratio of data to simulation was calculated using the last three sectors to determine a correction for the detector-independent (model-dependent) component. The simulation for all six sectors was then divided by the obtained ratio. There is a very good agreement in sectors 4, 5, and 6 as expected. The first three sectors, especially sector 2, still have a few inefficiencies.

Out of the observables of interest, the most sensitive to SC uncertainties is the proton angular distribution with respect to the direction of the momentum transfer, θ_{pq}. If the simulation is scaled with the ratio of data to simulation for the best sectors 4 and 5 to account for the inability of the model to fully describe the data, an agreement with an uncertainty of better than 5% is reached (see Fig. 106 and 107). Thus, the uncertainty coming from the proton detection efficiency is comparable with the uncertainties seen for the electron detection efficiency convoluted with the model uncertainties. Therefore it was decided not apply any more corrections and cuts and instead include the remaining discrepancies in the overall systematic error.

To test the validity of the approach used to study the background of accidental coincidences between the backward proton and forward electron, results of the $d(e, e'p_s)X$ simulation can be used. The simulation does not contain any accidental

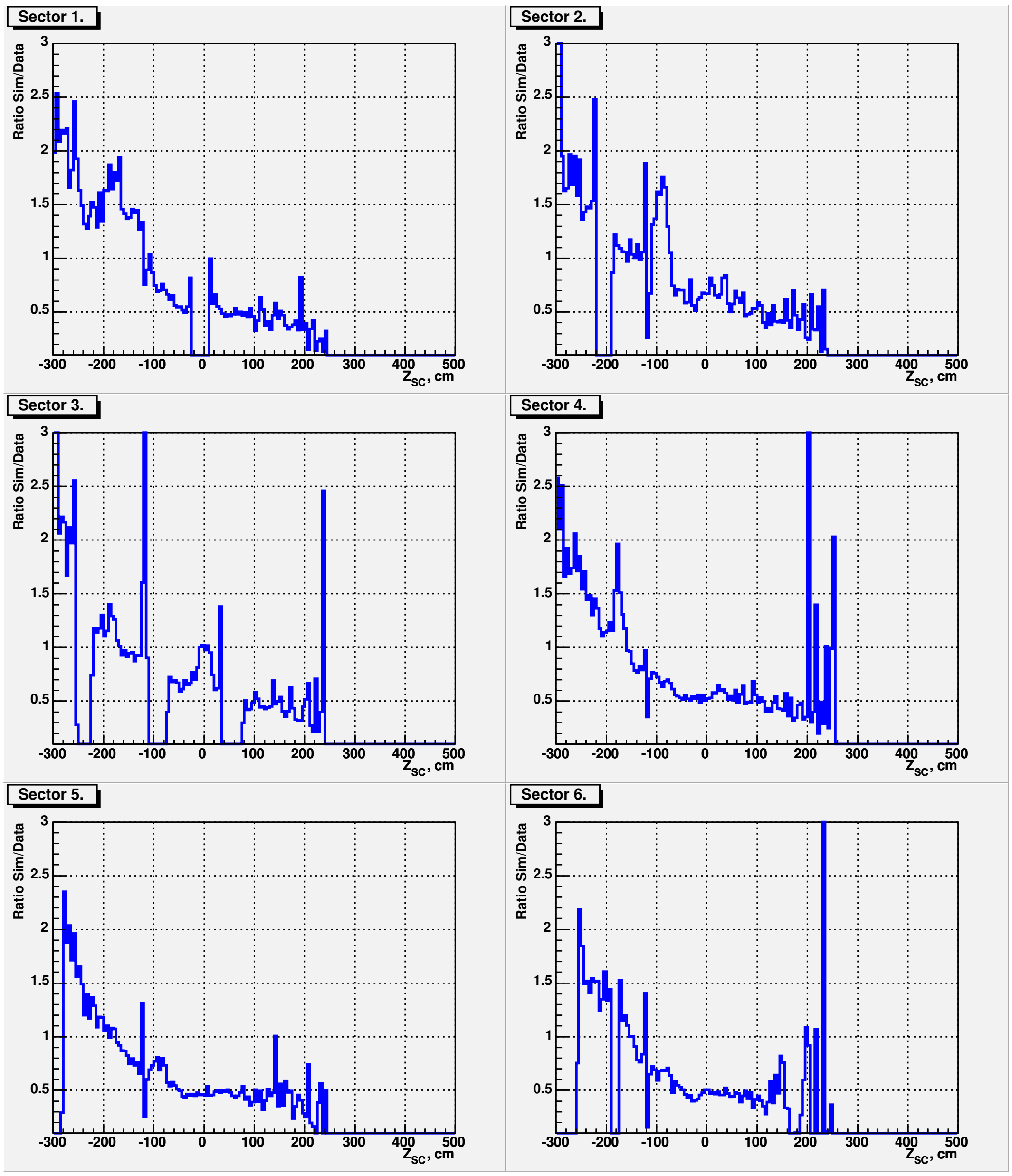

FIG. 103: Ratio of simulation divided by data plotted as a function of Z_{SC}.

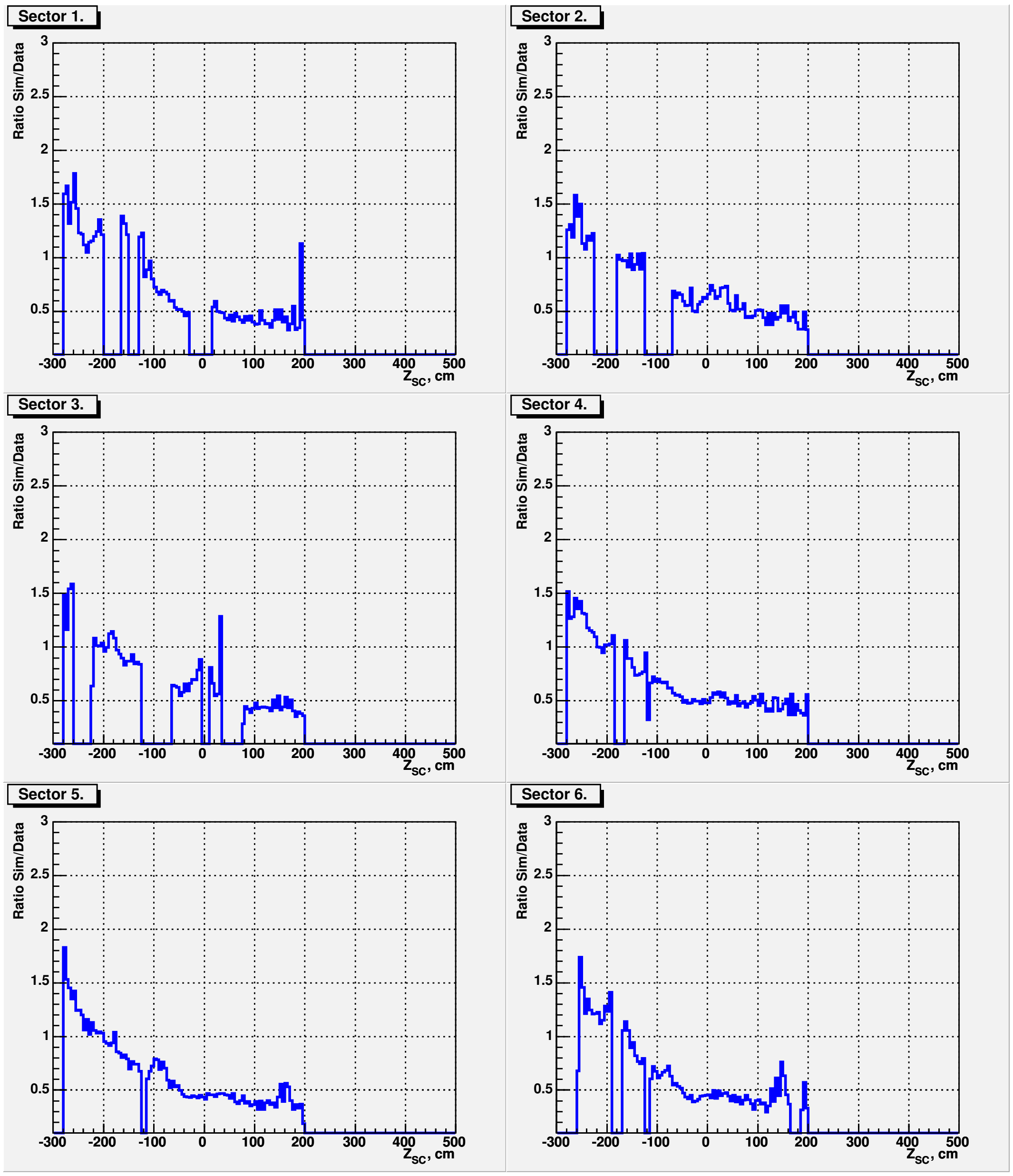

FIG. 104: Ratio of simulation divided by data plotted as a function of Z_{SC} after most of the inefficient regions were removed (breaks in the histograms).

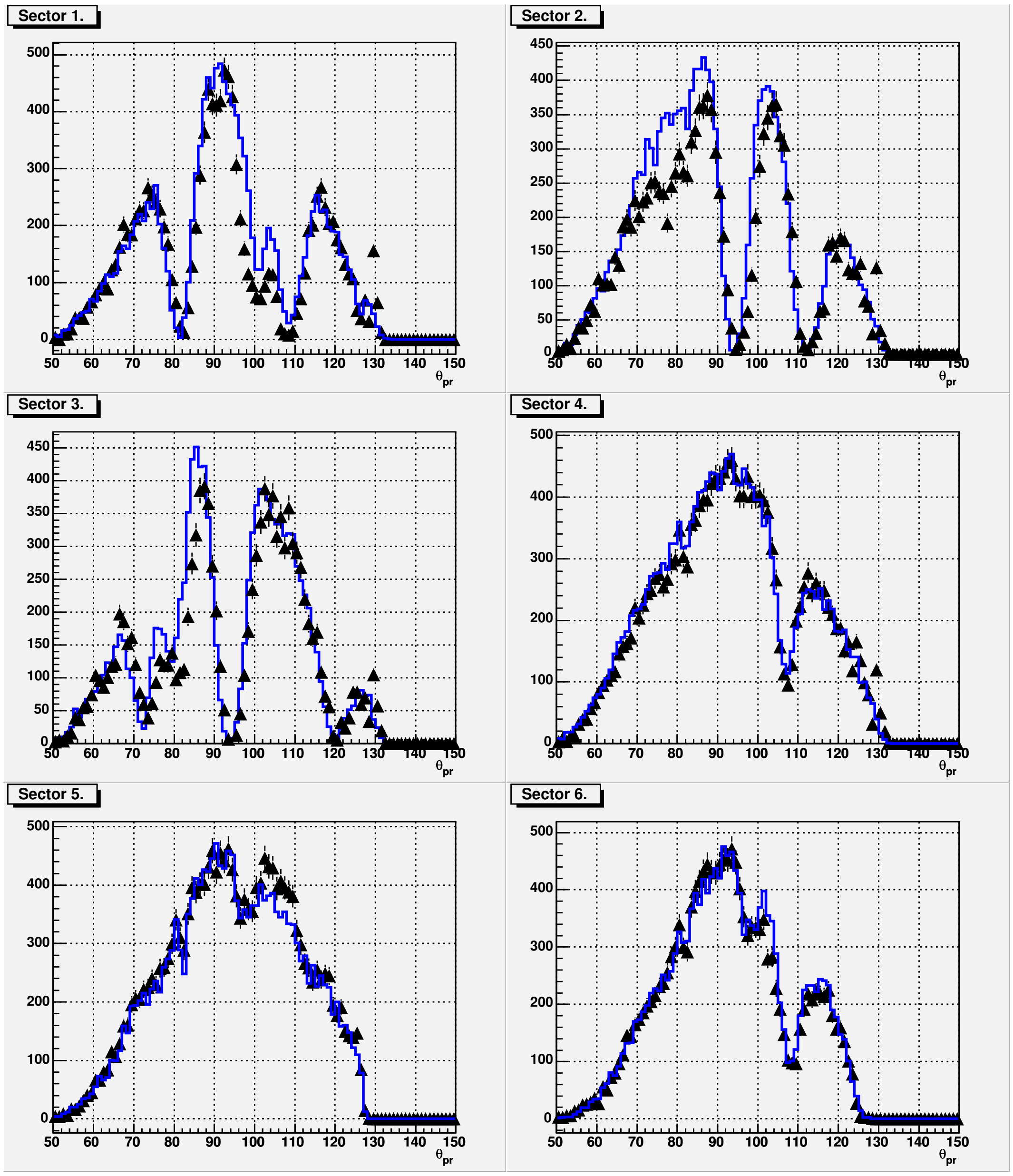

FIG. 105: Proton scattering angle distribution after inefficient regions identified from Z_{SC} plot were removed. The proton is required to have scattering angle and make an angle $\theta_{pr} > 50^o$ with the direction of a momentum transfer $\theta_{pq} > 72.5^o$.

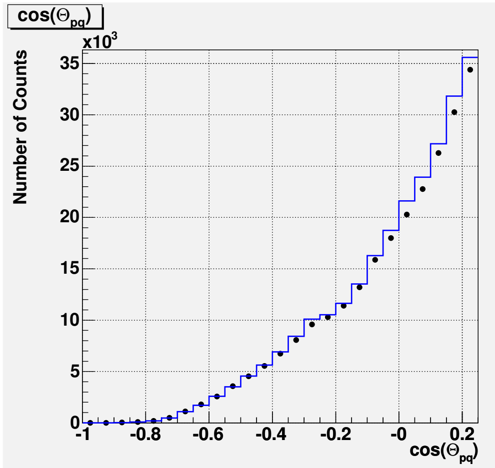

FIG. 106: Cosine of proton angle with respect to the momentum transfer direction for data (black triangles) and simulation (blue solid line). The model input has been divided out.

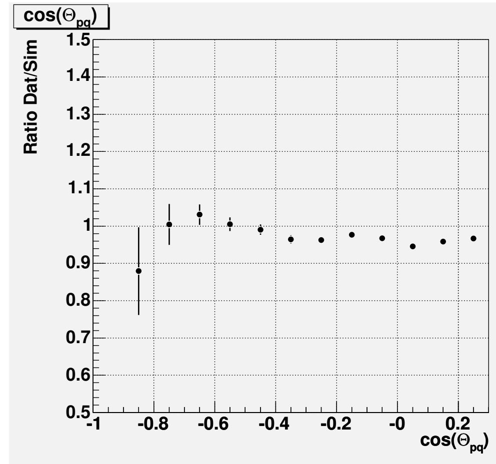

FIG. 107: Ratio of data to simulation for the cosine of the proton angle with respect to the momentum transfer direction. The model input has been divided out.

coincidences, therefore, simulated data together with a sample of pure accidentals selected from data (Sec. 4.4.4) should fit the shape of distributions sensitive to accidental coincidences. The background of accidentals is best seen in the proton time vertex distribution and target vertex difference between proton and electron. The simulation has a better resolution in these two variables and therefore has to be convoluted with a Gaussian distribution. Fit examples of the function $N_{acc} \cdot a + F_{gauss} \otimes N_{sim} \cdot b$ are presented in Figs. 108 and 109 for two different ranges in the momentum of the backward proton. A constant scaling factor of 1.2 was used for the parameter a. An error of 20% is set on this parameter. The need for this scaling is a result of the way an accidental coincidence was defined. A proton far off-time is taken to be accidental. However, the further in time the particle is from the event start time, the worse is the tracking efficiency. As a result, a fraction of the accidentals is simply rejected at the time of event reconstruction. From the plots presented it is clear that the fit is much better in describing the background on the negative side of the vertex difference distribution. That happens because the data contain a type of two-step process accidentals, where a particle originating from the electron vertex reinteracts further along the target cell, liberating another (backward) proton which arrives on-time to the TOF. Protons produced in such a way enhance the positive side

P_s (MeV/c)	Scale
250<p<280	0.18
280<p<320	0.24
320<p<360	0.49
360<p<420	0.69
420<p<500	0.95
500<p<750	1.13

TABLE V: Scaling factor for different ranges in momentum introduced for two-step accidentals, defined as an on-time proton with $\Delta Z > 1.4$ cm.

of the vertex difference distribution, defined as $Z_{pr} - Z_{el}$. The selected sample of accidentals contains off-time events, and therefore does not fully reproduce the shape of the vertex difference distribution. To subtract a proper fraction of accidentals, those types of events should be added to the sample of pure accidentals coincidences, defined using off-time protons. A two-step accidental distribution was defined using the sample of on-time protons in coincidence with an electron with $\Delta Z > 1.4$ cm, properly scaled (see Table V) for the integral of these events not to exceed the integral of the difference between data and simulation plus off-time accidentals in the region -1.4 cm $< \Delta Z <$ 1.4 cm.

The vertex difference cut is one of the proton ID cuts, therefore it is important that the same fraction of good non-accidental protons remains after this cut both in data and in simulation. The Gaussian smearing of the simulated data ΔZ distribution, performed for the purpose of the study discussed above, is not done in the data analysis. That leads to a minor difference in the integral of events within the vertex difference quality cut. The ratio of the total number of events to the number of events after $|\Delta Z_{pr-el}| < 1.4$ cm cut was estimated. The difference in Table VI in the effect of the vertex difference cut on data and simulation has to be corrected. A constant factor of 0.965 with an error of 2% applied to the simulation takes care of this discrepancy.

It is also of interest to estimate the approximate fraction of accidentals relative to the number of good coincidences. The numbers are shown in the Table VII. The number of accidental protons drops with increasing momentum as expected.

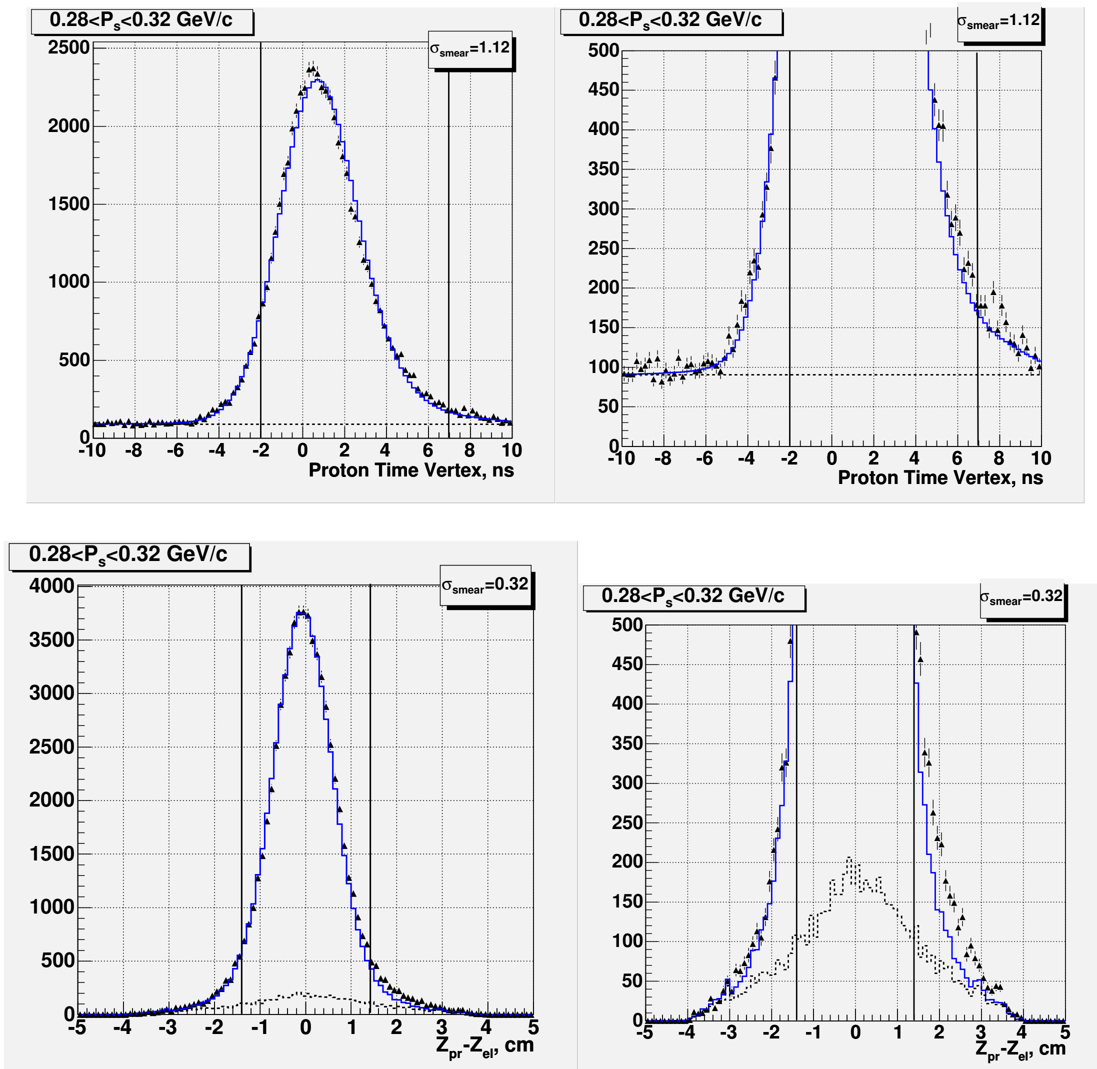

FIG. 108: The fit (solid line) of accidentals (dashed line) and simulation smeared with Gaussian (with σ shown in the right upper corner of each plot) overlaid with the data (black triangles). Presented are the proton time vertex distribution (top panels) and target vertex difference between proton and electron (bottom panels). Plots on the right side are zoomed to better see the region of low number of counts. The results shown are for protons between 280 and 320 MeV/c momentum. Vertical lines indicate the ID cut.

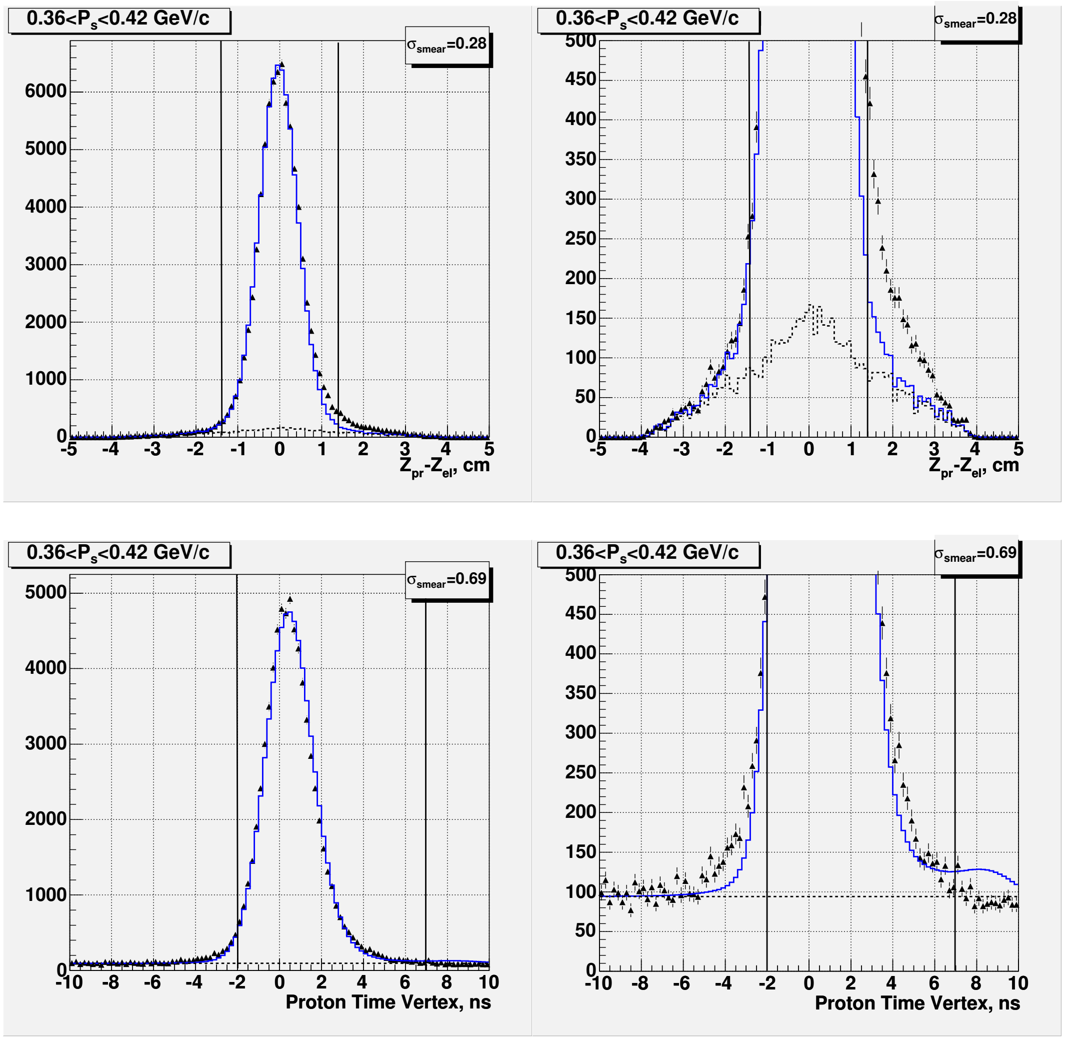

FIG. 109: Same as Fig. 108, except for proton momenta between 360 and 420 MeV/c; vertical lines indicate the ID cut.

P_s (MeV/c)	$N_{\Delta Z}/N_{total}$, Data	$N_{\Delta Z}/N_{total}$, Sim	Correction
250<p<280	88%	91%	97%
280<p<320	92%	95%	96%
320<p<360	94.%	98%	96%
360<p<420	96%	99%	97%
420<p<500	96%	99%	97%
500<p<750	97%	99%	97%

TABLE VI: The fraction of events surviving the vertex difference cut in data and simulation. The last column contains a correction factor that needs to be applied to the simulation to account for the discrepancy.

P_s (MeV/c)	Acc,%
250<p<280	14%
280<p<320	9.7%
320<p<360	8.0%
360<p<420	7.4%
420<p<500	6.6%
500<p<750	4.6%

TABLE VII: Estimated total fraction of accidentals in a given momentum bin.

CHAPTER 5

RESULTS AND DISCUSSION

In this chapter all the key steps leading to the extraction of final results are first summarized. The statistical error and total systematic uncertainty are evaluated. The results of the experiment are then compared with the prediction of the PWIA model. The general trends in deviation of the data from the PWIA calculation are discussed and compared with the trends predicted by more sophisticated theoretical models. Tentative conclusions on the possible nature of the observed deviations are presented.

5.1 APPLIED CORRECTIONS AND ERROR ESTIMATION

The simulated data discussed at the end of the previous section was used to correct the experimental data for detector acceptance. To simplify the statistical error calculation, all the corrections for the detector inefficiencies and data sample contamination (except for accidentals and the radiative elastic tail) were applied to the simulated events.

The efficiency of the CC electron ID cut is well reproduced in the simulation using Vlassov's function. A 1% systematic uncertainty enters here to account for the observed deviation of the cut efficiency from sector to sector. The EC ID cut efficiency is reproduced only partially. The efficiency of the cut in data was found to be 95%, however the same cut, applied to the simulation, is 98% efficient. The difference might be a result of data being contaminated with pions, despite the increased CC threshold. The simulated data were scaled down by a constant factor of 0.97 to account for the difference in the effect of the cut. A 2% systematic uncertainty was assigned to this factor due to the uncertainty about the source of the deviation. A variable factor that ranges from 1.06 to less than 1.01 was used to introduce pion contamination into the simulation. The factor varies with the particle scattering angle and momentum. A variable factor was also applied to the electron spectrum in the simulation to introduce electrons coming from electron-positron pair creation. The resulting systematic uncertainty was estimated by varying these factors by 50%. The resulting change in the distribution in each of the final histograms was used as an estimate of the systematic uncertainty of these corrections.

An additional factor of 0.98 with 2% error appears to account for the estimated hardware trigger inefficiency. A factor of 0.986 with 0.7% uncertainty enters to account for the loss of the electrons in the secondary positions in the event data bank. The difference in the effect of the electron vertex cut in data and simulation was accounted for by multiplying the simulated data with a factor 0.988, with 0.6% systematic uncertainty assigned to it. The error on the correction to the inefficiencies in sectors 5 and 6 was calculated by reducing the correction by 50%. The systematic uncertainty on the electron radiative effects in the inelastic region was taken to be 50% of the observed difference between the simulated radiated and unradiated spectra for studied distributions.

Many fewer corrections were applied to the proton spectrum. A constant factor of 0.99 was introduced to reflect the difference in the effect of the proton timing ID cut. The systematic uncertainty of 0.5% on this number accounts for momentum dependence of the effect. A factor dependent on the proton momentum was applied to the simulated data to account for the discrepancy between data and simulation in the effect of the cut that was set on the difference between electron and proton vertex. The systematic uncertainty here is evaluated individually for each histogram, by varying the correction by 50%.

Before extraction of the final results the data were also reduced by the proton accidentals, protons originating from a two-step proton knock-out and elastic radiative tail (whenever inelastic data is analyzed). Normalization factors are applied to each of these contributions before the subtraction. The systematic uncertainty here is estimated by varying the deviation of these normalization factors from unity by 50%.

The comparison of the inclusive and semi-inclusive experimental data and simulation, after all the corrections discussed above were applied, showed a variable 7% deviation of the ratio between the two. The uncertainty in the input model of the simulation itself is partially responsible for this deviation. In general, the absolute cross sections were never measured with CLAS to better than 5% uncertainty. An additional systematic uncertainty of 5% was assigned to the whole data set to incorporate the errors from the effects that cannot be easily studied. That includes possible unknown (not fully reproducible) detector and tracking inefficiencies, minor variations in the target density, uncertainty in the FC charge measurement, etc.

A summary of the applied corrections and systematic errors can be found in

Correction	Magnitude	Systematic Error
EC ID Cut	0.97	2%
Trigger Efficiency	0.98	2%
Secondary Electrons	0.986	0.7%
Electron Vertex ID Cut	0.988	0.6%
Proton Timing ID Cut	0.99	0.5%
CC Efficiency	-	1%
Other Unaccounted Inefficiencies	-	5%
Total Constant Error		5.9%

TABLE VIII: Constant correction factors applied to the data and systematic errors associated with various sources of uncertainty.

Table VIII. The overall systematic uncertainty that is not momentum, angle, or sector dependent was estimated to be 5.9% and can be considered as an overall scale uncertainty.

5.2 EXTRACTION OF THE RESULTS

The events from the data set were sorted in seven main sets of one-dimensional histograms. The histograms in the first two sets each contain 26 bins in the variable $\cos(\theta_{\rm pq})$, in the range between -1 and 0.3 (where θ_{pq} is the angle between the scattered proton and the direction of the momentum transfer $\hat{q}$). The first set consists of 72 histograms of $\cos(\theta_{\rm pq})$ selected for different ranges of invariant mass of the unobserved final state W^*, momentum of the scattered proton p_s, momentum transfer Q^2 and relative orientation of hadronic and leptonic planes ϕ_s (see Table IX). The second set has 120 histograms in it divided in bins of p_s , Q^2 and the scaling variable x^* (see Table X). The third set of histograms contains twelve one-dimensional distribution of the invariant mass of the unobserved final state W^* for six different values of p_s and two bins in Q^2 (see Table XI). Another set of 12 histograms has a distribution of a scaling variable x^*, binned in spectator proton momentum p_s and momentum transfer Q^2 (see Table XII). The last two sets of 192 histograms contain light-cone fraction of the spectator proton distribution α_s for six values of transverse proton momentum p_T, different ranges in the invariant mass of the unobserved final state W^*(six values) and scaling variable x^* (six values), and two values of momentum

Observable	Range	Number of bins	Bin size
$\cos(\theta_{pq})$	-1 - +0.3	26	constant
p_s, GeV/c	0.25-0.7	6	0.25-0.28-0.32-0.36-0.42-0.5-0.7
W^*, GeV	0.9-2.7	6	$<$1.1,1.1-1.35-1.6-1.85-2.2,$>$2.2
Q^2, GeV^2/c^2	1.2-5.0	2	$<$2.1,$>$2.1

TABLE IX: Bin division for the first set of histograms.

Observable	Range	Number of bins	Bin size
$\cos(\theta_{pq})$	-1 - +0.3	26	constant
p_s, GeV/c	0.25-0.7	6	0.25-0.28-0.32-0.36-0.42-0.5-0.7
x^*, GeV	0.0 - 1.0	10	constant
Q^2, GeV^2/c^2	1.2-5.0	2	$<$2.1,$>$2.1

TABLE X: Bin division for the second set of histograms.

transfer Q^2 (see Table XIII, XIV).

To extract the final results, the above sets of histograms were created separately for the following categories of events: 1) experimental data with all the standard electron and proton ID cuts; 2) accidental electron-proton coincidences based on experimental data; 3) coincidences with the rescattered protons; 4) simulated data for the elastic scattering on a bound neutron; 5) simulated data for the inelastic scattering on a bound neutron. Accidental coincidences and coincidences with rescattered protons were then subtracted from the data on a bin-by-bin basis. Simulated elastic

Observable	Range	Number of bins	Bin size
W^*	0.0 - 3.0 GeV	60	constant
p_s, GeV/c	0.25-0.7	6	0.25-0.28-0.32-0.36-0.42-0.5-0.7
Q^2, GeV^2/c^2	1.2-5.0	2	$<$2.1,$>$2.1

TABLE XI: Bin division for the third set of histograms.

Observable	Range	Number of bins	Bin size
x^*	0.0 - 1.0	40	constant
p_s, GeV/c	0.25-0.7	6	0.25-0.28-0.32-0.36-0.42-0.5-0.7
Q^2, GeV^2/c^2	1.2-5.0	2	$<$2.1,$>$2.1

TABLE XII: Bin division for the fourth set of histograms.

Observable	Range	Number of bins	Bin size
α_s	0.95 - 1.7	15	constant
p_T, GeV/c	0.05-0.65	6	constant
W^*, GeV	0.9-2.7	6	$<$1.1,1.1-1.35-1.6-1.85-2.2.$>$2.2
Q^2, GeV^2/c^2	1.2-5.0	2	$<$2.1,$>$2.1

TABLE XIII: Bin division for the fifth set of histograms.

Observable	Range	Number of bins	Bin size
α_s	0.95 - 1.7	15	constant
p_T, GeV/c	0.05-0.65	6	constant
x^*, GeV	0.0 - 1.0	10	constant
Q^2, GeV^2/c^2	1.2-5.0	2	$<$2.1,$>$2.1

TABLE XIV: Bin division for the sixth set of histograms.

scattering data were also used to subtract the elastic radiative tail from the experimental data. For this purpose both data and simulation were first integrated in the range of the invariant mass of the unobserved final state W^* from 0.5 to 1.1 GeV. The elastic radiative tail in the simulation was then scaled by the ratio of the data to the simulation and subtracted. The scaling for the first three ($\cos(\theta_{pq})$ distributions) and the last two (α_s distributions) sets of histograms was done as a function of $\cos(\theta_{pq})$ or α_s respectively. The radiative tail for the remaining two sets of histograms (containing $W^*$and x^* distributions) was scaled with a constant factor.

As was previously discussed, in the spectator picture, the cross section for the off-shell nucleon can be factorized as a product of the bound nucleon structure function and the nuclear spectral function, multiplied by a kinematic factor (see Eq. (27)). Using the data of this experiment, it is possible to extract this product, and, in the region where FSI are small and the spectral function is well described by the model, even the off-shell structure function by itself. To do that, the experimental data (with accidentals, rescattered proton events, and elastic radiative tail subtracted) were first divided by the simulated data. The simulated events were generated using the cross section (27) with full consideration of radiative effects. To extract the product of structure and spectral functions, the ratio of data to simulation was multiplied with the product $F_{2n}(x^*, Q^2) \times S(\alpha, p_T)$, calculated using the same model that was used in the generator. Therefore, the dependence of the extracted data on the specific model for the simulation is minimized, since the "input" (F_{2n} and $S(\alpha, p_T)$) cancels to first order. To extract just the structure function, the ratio of data to simulation was multiplied with the free nucleon structure function $F_{2n}(x^*, Q^2)$. This assumes that the spectral function used in the simulation is reasonably accurate. Basically, this procedure corrects the data for the detector acceptance, bin migration and radiative effects, and divides out the kinematic factor $\frac{4\pi\alpha_{EM}^2}{x^*Q^2}$ as well as the factor in square brackets in Eq. (27) (which depends weakly on the ration $R = \sigma_L/\sigma_T$) individually for each of the 408 final distributions.

The statistical error was calculated for each data point as:

$$\frac{\sqrt{Number\ of\ Events\ in\ Data}}{Number\ of\ Simulated\ Events}$$

In addition to the 5.9% constant systematic error discussed earlier, the systematic uncertainty of the variable corrections had to be estimated. These variable corrections include accidentals, rescattered protons, and elastic radiative tail subtraction, as well as correction for pion contamination, contamination with e^+e^--pairs, and variable correction for the difference in effect of the vertex difference cut between data and simulations. The error estimation was done separately for each of these corrections. The six standard sets of histograms were produced twice for each of the corrections, first for the correction factor reduced by 50%, then for the factor increased by 50%. The average difference between the two for each data point in each of the 408 distributions was taken as a systematic error for a given correction. The errors were summed in quadrature to get the total systematic error for variable corrections. The absolute value of systematic error for a given plot, originating from the variable corrections, is plotted as a red bar at the bottom of all histograms discussed in the next section.

5.3 RESULTS AND DISCUSSION

As a quantum mechanical process, only probability statements can be made about the interaction of the beam electron with the target nucleus, as well as about the state of the nucleon inside of the nucleus at the instant of interaction. The experimentalist has no control over the internal nuclear momentum the neutron has at the moment of interaction, or how much energy the electron transfers to the neutron. However, the probability of the interaction products (scattered electron and the recoiling proton) to be found in a certain kinematics can be studied. In a simple PWIA picture, for particular electron kinematics, this probability is proportional to the product of the interacting neutron structure function (that, in the parton model, depends on a distribution of quarks and gluons within a neutron, at the moment of interaction) and the deuterium spectral function (that, in the nuclear spectator model, gives the probability for the neutron to be found within the deuteron with a certain momentum and off-shell mass). In real life, the detected recoil proton also reinteracts with the scattered neutron (in the case of quasi-elastic scattering) or the neutron debris (inelastic scattering). Using the available data we can try to decouple the competing effects in the interaction process. The undistorted deuterium spectral function in the Eq. (27) does not depend on the electron kinematics (e.g., W^* and x^*). Thus the behavior of the structure function $F_{2n}(x^*, Q^2)$ can be studied as a function of these two variables (in principle, F_{2n} could also depend on the off-shell mass M^*).

On the other hand, the deuterium spectral function and FSI effects can be studied by plotting the dependence of the product $F_{2n} \times S^{FSI}$ as a function of the recoiling proton kinematic variables (p_s, p_T, $\cos(\theta_{pq})$, α_s).

By comparing the calculations based on a simple spectator model (Sec. 4.6) with the data, general conclusions can be made regarding the possible underlying effects governing the observed behavior of the structure and spectral functions. Full calculations for the electron scattering from a bound nucleon as well as calculations of the effect FSI have on the spectral function are available for slightly different kinematic conditions. However, a general trend in these models can be discussed and compared with the trends, observed in the data.

5.3.1 Deuterium Momentum Distribution

The two models of FSI discussed in Sec. 2.5 (see Figs. 9 and 11) give different predictions for the behavior of the distorted spectral function S^{FSI} as a function of the recoiling proton momentum and the scattering angle (also directly related to the proton light-cone fraction $\alpha_s = \frac{E - p_s \cos(\theta_{pq})}{M}$ and transverse momentum $p_T = p_s \sin(\theta_{pq})$). The DWIA model of FSI [47] predicts a reduction of as much as 25% in the spectral function due to FSI effects at the of $\alpha_s \approx 1$ and values of $p_T \leq$ 300 MeV/c. Beyond $p_T = 300$ MeV/c, this model shows that FSI effects start to invert and the spectral function is enhanced by about 5% at $p_T = 400$ MeV/c. At e intermediate values of α_s of $1.2 - 1.3$, FSI are expected to reduce the spectral function by less than 5%, almost independent of p_T. In the deep inelastic region, the DWIA FSI model predicts almost no or very slow variation of FSI with x^*.

On the other hand, the hadronization model of FSI [48] predicts a very strong increase (beyond 100%) in the spectral function due to FSI for deep inelastic scattering at $p_s > 300$ MeV/c for proton scattering angles around $\theta_s = 90^o$. A somewhat slower growth in the FSI spectral function at $\theta_s = 90^o$ is predicted for the quasi-elastic process, where FSI increase the spectral function by more than 100% at $p_s > 350$ MeV/c. This calculation shows that at $\theta_s = 180^o$ in DIS, the FSI reach their maximum of 40% above the PWIA spectral function at $p_s = 300$ MeV/c, and then drop to the values of the FSI-free spectral function at $p_s = 400$ MeV/c. FSI effects of $\pm 10\%$ in the range between 300 and 400 MeV/c proton momentum are observed for the quasi-elastic scattering. The model also shows an increase in FSI with the increase of the momentum transfer Q^2.

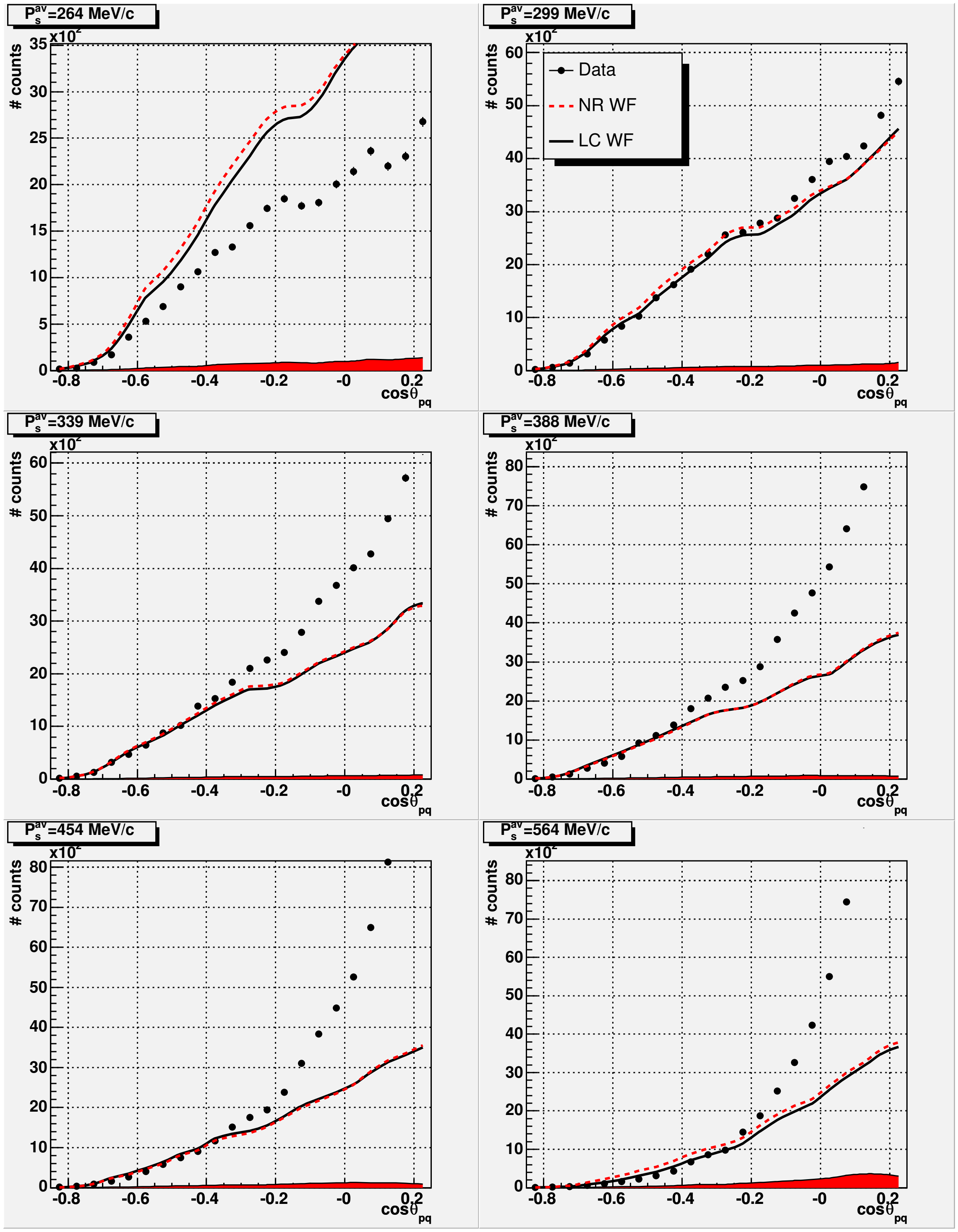

FIG. 110: Cosine of the proton scattering angle with respect to the direction of momentum transfer. Different sections of the plot correspond to the different average value of the proton momentum. The data shown are integrated over all electron kinematics.

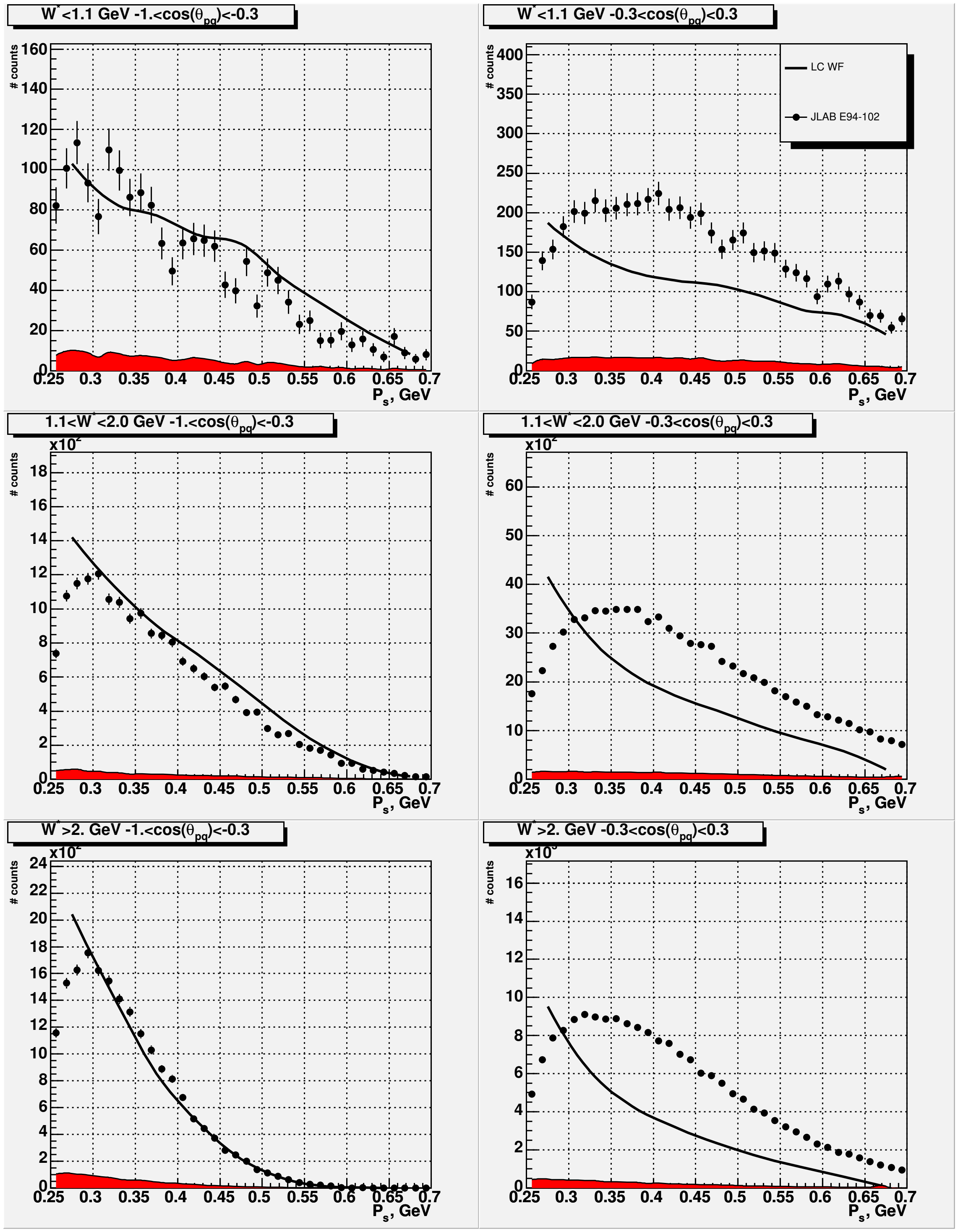

FIG. 111: Momentum distribution of the scattered proton for different ranges of scattering angles and invariant mass of the unobserved final state.

The signatures of final state interactions are already observed on the θ_{pq} distributions (where θ_{pq} is the proton scattering angle relative to the momentum transfer direction) integrated over electron kinematics (Fig. 110). Since a strong dependence of FSI on proton momentum is expected, it is instructive to plot the angular distribution separately for different values of proton momentum. The solid curve on Fig. 110 is the prediction based on the spectator approximation and using the light-cone spectral function. The dashed curve is obtained using the non-relativistic Paris potential wave function in the covariant instant-form approach. In both cases the free neutron structure function was used, extracted as described in Sec. 4.6. Since no attempt to model FSI was undertaken to produce either of the model curves, it is very likely that the large discrepancy in the region of smaller θ_{pq} (greater $\cos(\theta_{pq})$) is due to the FSI contribution. The plots for all values of proton momentum, with the exception of the very first one, follow the same pattern; the discrepancy at forward angles gets bigger as proton momentum increases. At the same time both models are in reasonably good agreement with the data at $\cos(\theta_{pq}) < -0.3$. It can be concluded that the FSI (or whatever other effect makes the data rise at forward angles) are small beyond this point or cancel out with competing effects. The data for the lowest value of momentum (top left plot on Fig. 110) lie far under the simulated data for the whole range of scattering angles. The data in this plot lie on the very edge of the proton momentum detector acceptance and the observed deviation is most likely a result of an efficiency problem.

Fig. 111 shows the recoiling proton momentum distribution for two ranges in $\cos(\theta_{pq})$: less than -0.3, where the models agree fairly well with data, and greater than -0.3, where a huge discrepancy is observed. For the back angle plots, the shape of the recoiling proton momentum distribution is well reproduced down to values of $p_s = 300$ MeV/c (left panel of Fig. 111), where the data drop but the simulated data keep rising. The disagreement with data at $\cos(\theta_{pq}) > -0.3$ is model independent, since both non-relativistic and light-cone calculations agree with each other in this region. The drop in the momentum distribution in data is likely due in part to a detector inefficiency up to proton momenta of 280 MeV/c.

To study the cross section in more detail, the data were divided into additional kinematic bins in the observables of interest. The data were corrected for the acceptance and all the other effects discussed in Sec. 4, and presented as the product of structure function F_{2n} with the "effective" probability $P(\vec{p_s})$ of finding the spectator

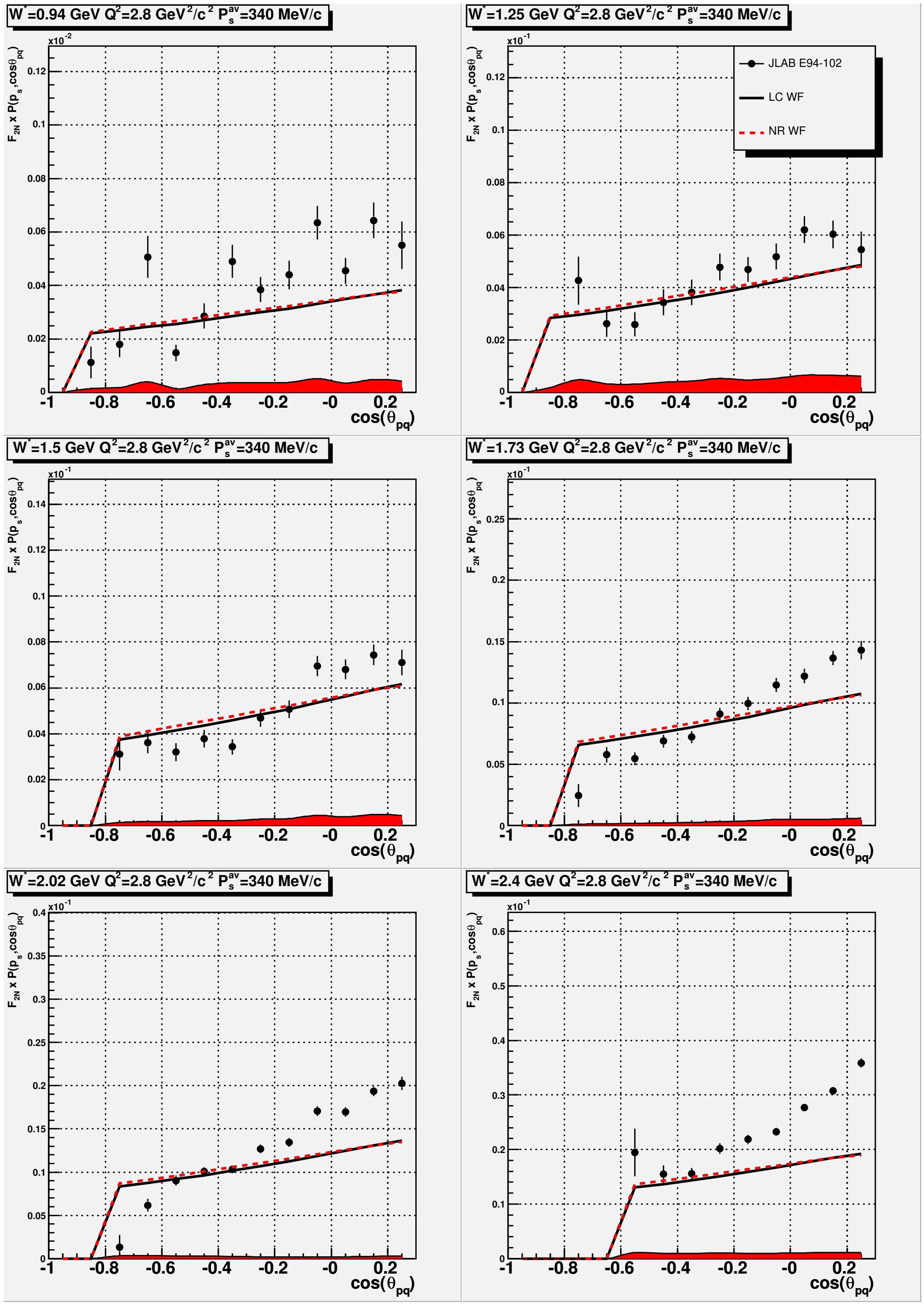

FIG. 112: $F_{2n}(W^*, Q^2)$ times $P(\vec{p_s})$ versus the cosine of the proton scattering angle with respect to the direction of momentum transfer. Different sections of the plot correspond to the different ranges of the invariant mass W^*. The data shown are for the upper Q^2 bin $(2.1 - 5.0\ \ \mathrm{GeV}^2/c^2)$ and proton momenta between 320 and 360 MeV/c.

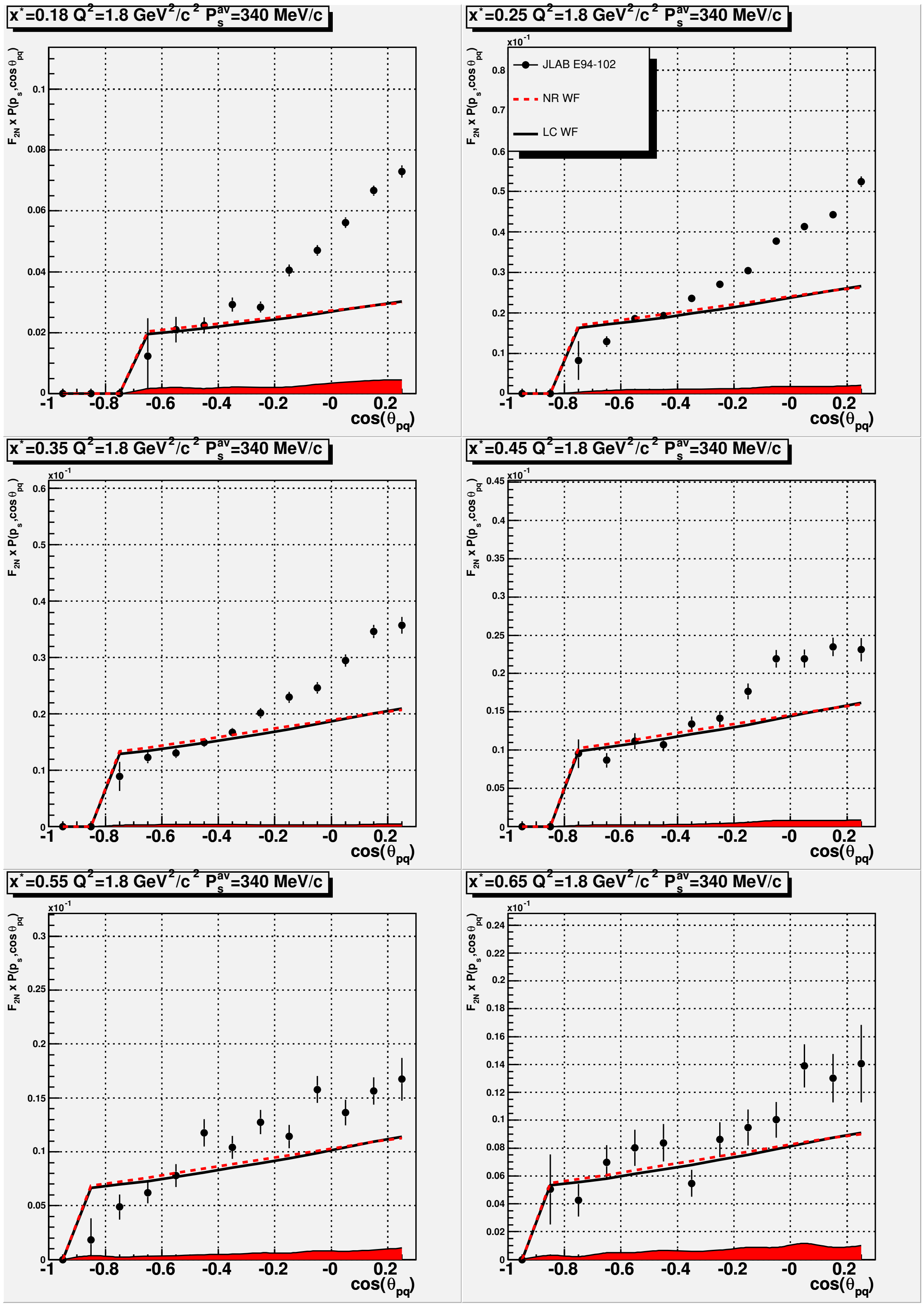

FIG. 113: $F_{2n}(x^*, Q^2)$ times $P(\vec{p_s})$ versus the cosine of the proton scattering angle with respect to the direction of momentum transfer. Different sections of the plot correspond to the different ranges of the invariant mass W^*. Here, the lower Q^2 bin was selected ($1.2 - 2.1$ GeV^2/c^2), but the same momentum bin as in Fig. 112.

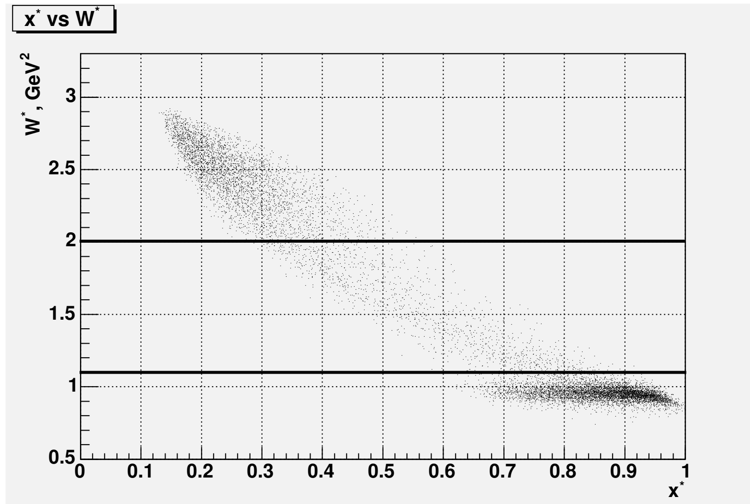

FIG. 114: Invariant mass of the unobserved final state W^* potted versus scaling variable x^*.

nucleon with 3-momentum $\vec{p_s}$. The extracted reduced cross section can be independently compared to a full calculation or the data from another experiment. The probability $P\left(\vec{p_s}\right)$ is related to the non-relativistic wave function and spectral function (26), which is expressed in terms of the light-cone variables, through the expression: $P\left(\vec{p_s}\right) = |\psi_{NR}(\vec{p_s})|^2 = \frac{1}{J \cdot E_s} S(\alpha_s, p_T)$, with $E_s = \sqrt{p_s^2 + M^2}$ and flux factor $J = \frac{(2-\alpha_S)M_D}{2(M_D - E_S)}$. The full set of histograms, showing the product $F_{2n} \times P\left(\vec{p_s}\right)$, plotted as a function of proton scattering distribution with respect to the direction of the momentum transfer, appear in Appendix A. In addition to proton momentum, the plots were also separated into six ranges in the invariant mass of the unobserved final state W^* and two ranges in the momentum transfer Q^2 (Table IX, Figs. 127-136). Independently, a set of plots was created for six different ranges in the scaling variable x^* and two values of Q^2 (Table X, Figs. 137−146). The same data were extracted as a product of structure function F_{2n} and the light-cone spectral function $S(\alpha_s, p_T)$. The product $F_{2n} \times S(\alpha_s, p_T)$ was plotted as a function of light-cone fraction of the spectator proton α_s for different ranges in the transverse component of the proton momentum p_T. The full set of these distributions, overlayed with the calculations (based on the non-relativistic wave function and light-cone spectral function), can

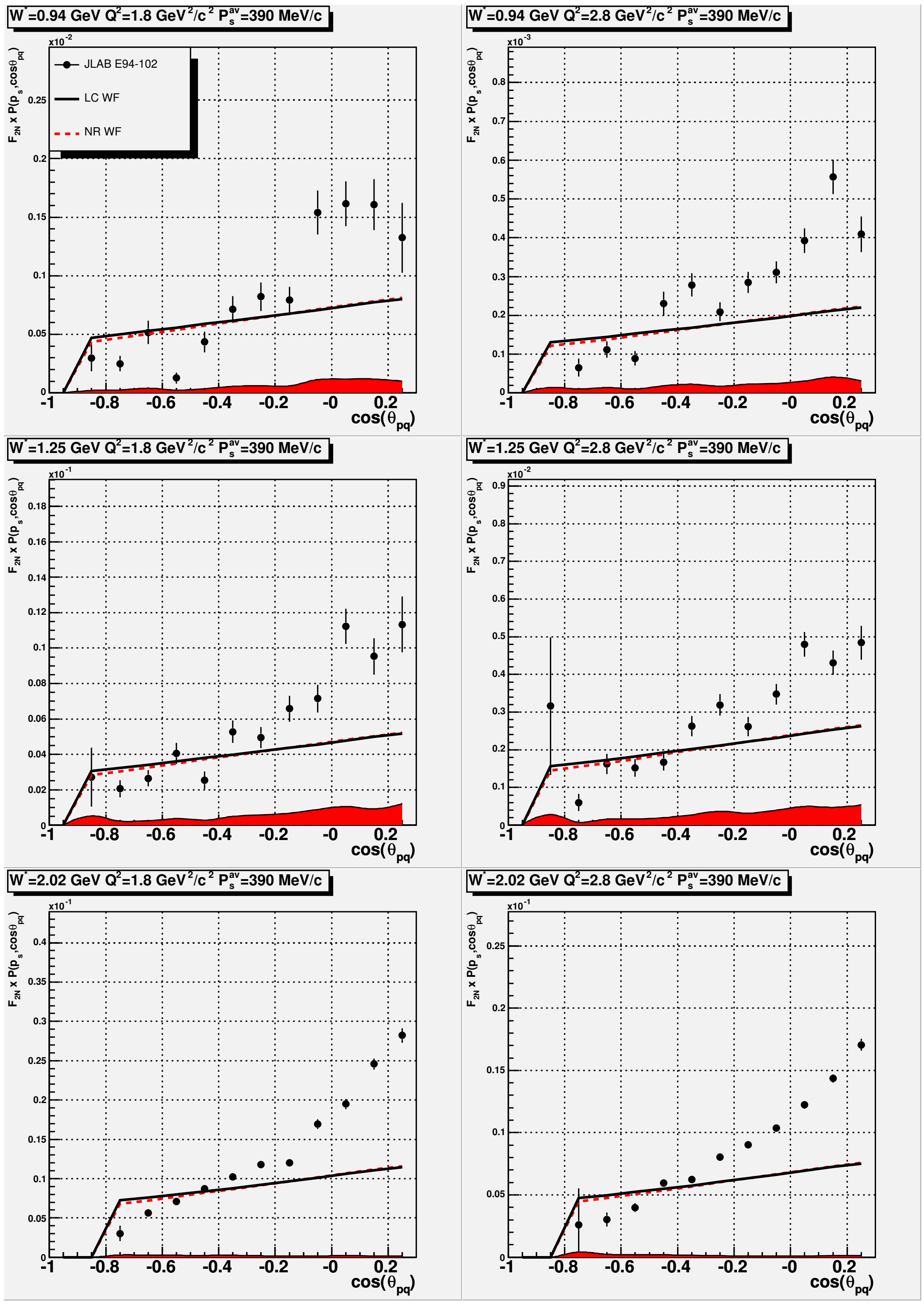

FIG. 115: $F_{2n}(W^*, Q^2)$ times $P(\vec{p_s})$ versus the cosine of the proton scattering angle with respect to θ_{pq} for two different values of Q^2. The left side of the plot contains histograms for the data in the low Q^2 range and the right one - for the high Q^2 range.

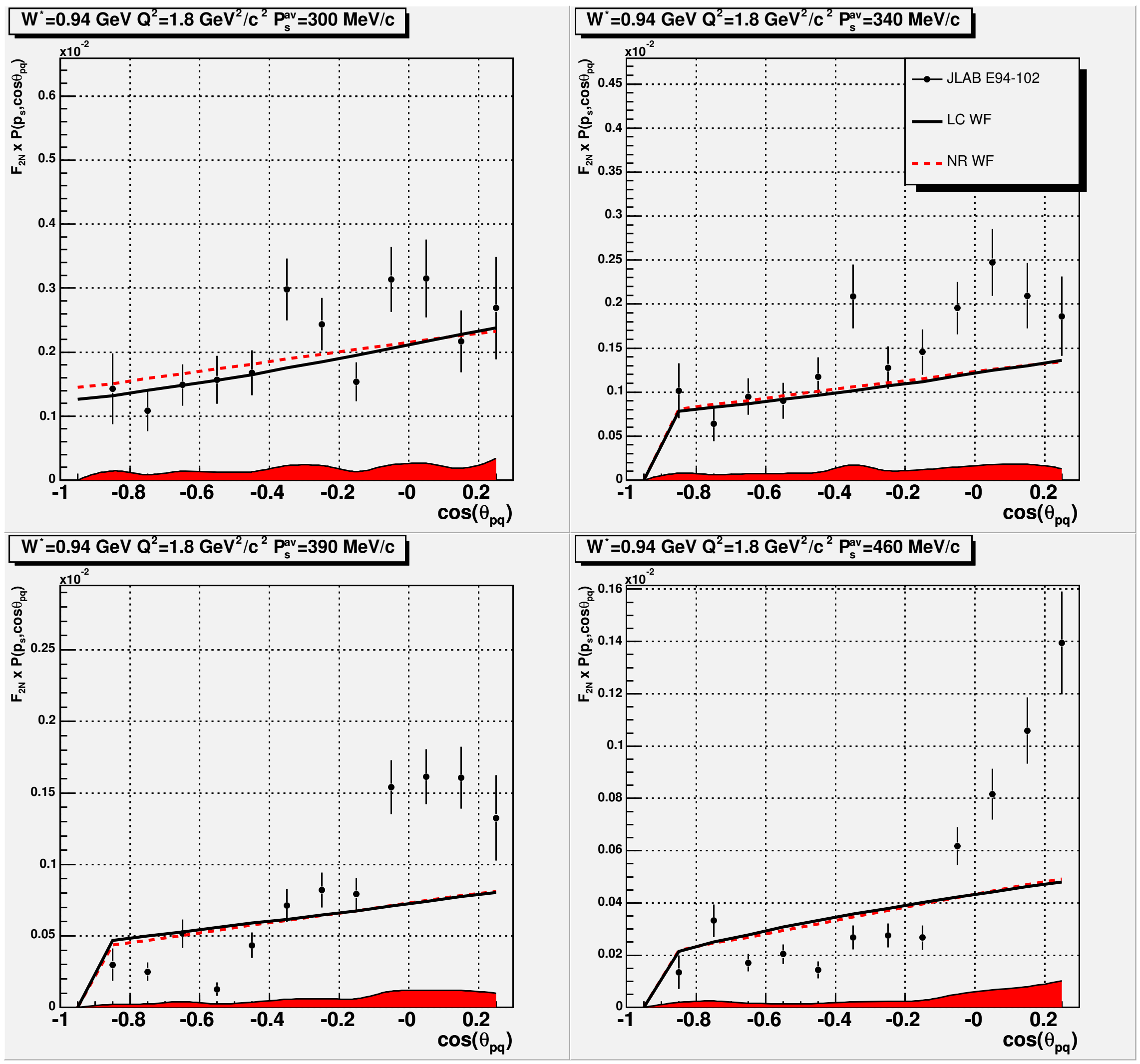

FIG. 116: $F_{2n}(W^*, Q^2)$ times $P(\vec{p_s})$ versus $\cos(\theta_{pq})$ for four different values of proton momentum, but for the same value of $W^* = 0.94$ GeV and $Q^2 = 1.8$ GeV^2/c^2.

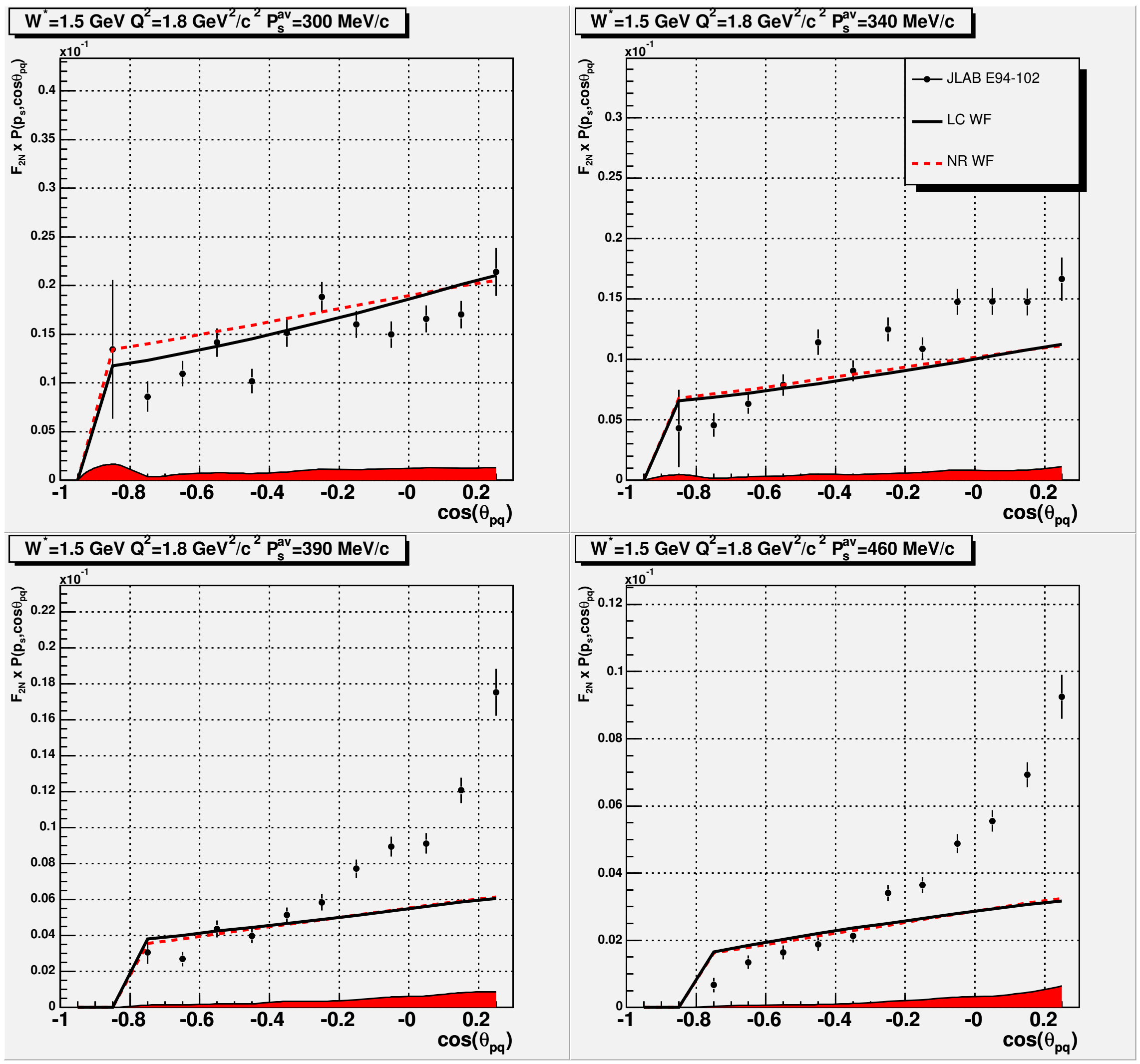

FIG. 117: $F_{2n}(W^*, Q^2)$ times $P(\vec{p_s})$ versus $\cos(\theta_{pq})$ for four different values of proton momentum, but for the same value of $W^* = 1.5$ GeV and $Q^2 = 1.8$ GeV^2/c^2.

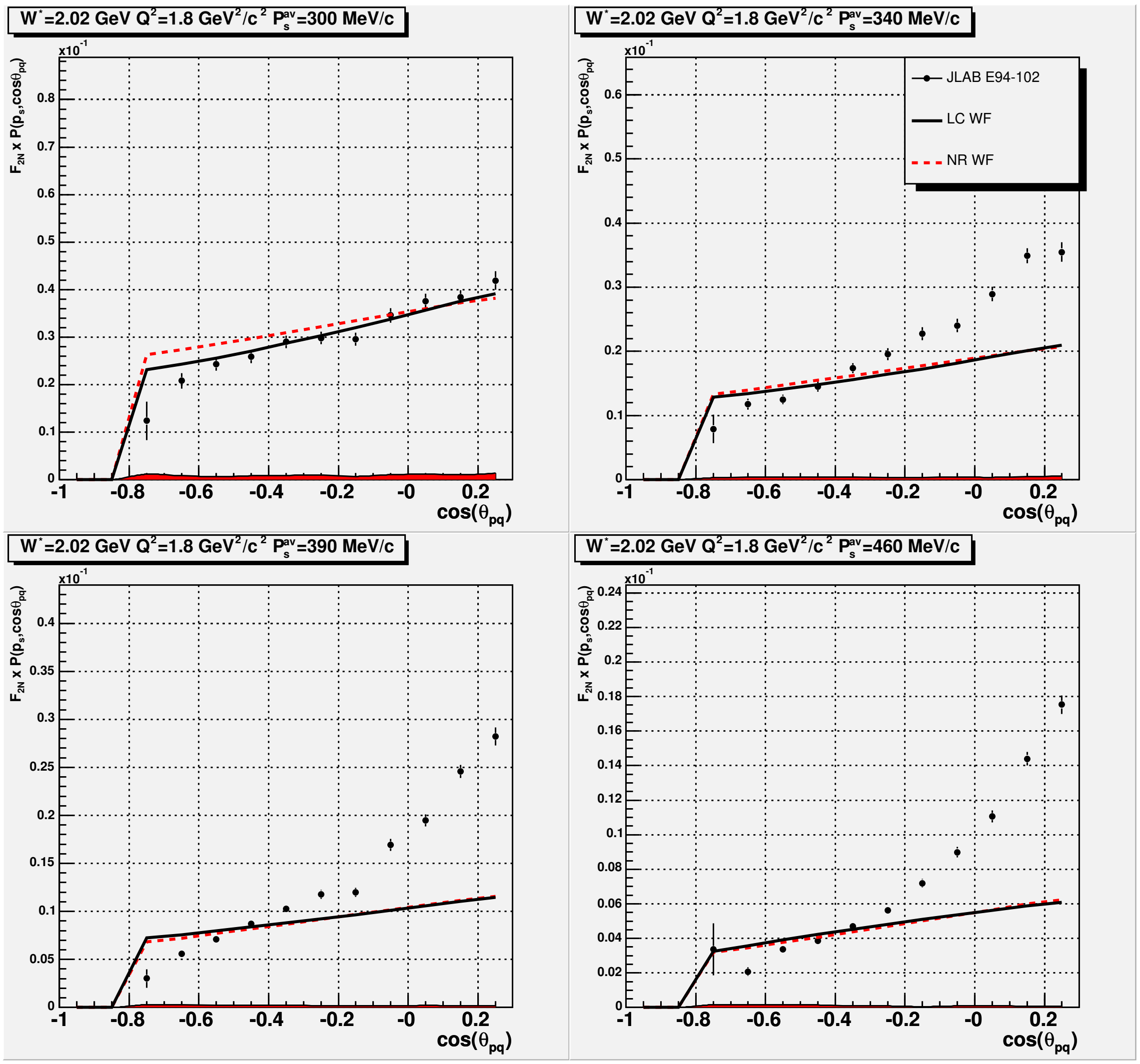

FIG. 118: $F_{2n}(W^*, Q^2)$ times $P(\vec{p_s})$ versus $\cos(\theta_{pq})$ for four different values of proton momentum, but for the same value of $W^* = 2.02$ GeV and $Q^2 = 1.8$ GeV^2/c^2.

be found in Appendix A. Again, the histograms of the product $F_{2n} \times S(\alpha_s, p_T)$ were created for different ranges in W^* (Fig. 157-165) and scaling variable x^* (Fig. 147-156) and for two bins in the momentum transfer Q^2.

The enhancement in data at high values of $\cos(\theta_{pq})$ increases with invariant mass of the unobserved final state W^* (Fig. 112) or, equivalently, with decreasing value of the scaling variable x^* (corresponding to increasing values of W^*) (Fig. 113). The bottom right plot on Fig. 113 for values of $x^* = 0.65$ already contains a small contribution from quasi-elastic events, significantly offset by the effects of Fermi motion from their on-shell value of $x = 1.0$ (Fig. 114). For this reason F_{2n}, structure function data will not be discussed in the region $x^* > 0.7$. At $p_s = 300$ MeV/c there is good agreement between the calculated cross sections and the data as a function of $\cos(\theta_{pq})$ for all values of W^* (Figs. 116, 117, 118). As was observed in the distributions integrated over electron kinematics (Fig. 110), the discrepancy in the region $\cos(\theta_{pq}) > -0.3$ gets bigger as proton momentum increases for all values of W^*.

Basically the same trends are observed for the product $F_{2n} \times S$ plotted as a function of light-cone variable α_s: at transverse proton momentum $p_T = 300$ MeV/c, the biggest discrepancy between the models and the data is observed at low values of α_s and for the lowest and highest values of W^* (Fig. 119). The data rise sharply as p_T increases to 400 MeV/c, and continue to grow relative to the model, as p_T increases further (Fig. 120, 121) for all values of W^*. The same behavior of $F_{2n} \times S$ is observed on the plots for different values of the scaling variable x^* (Fig. 122).

Overall, the DWIA model of FSI is not supported well by the observations; in fact, in this model, the FSI are expected to peak in the region of quasi-elastic scattering. Also, the FSI contribution appears to be noticeably different for different values of scaling variable x^* in contradiction to the DWIA FSI model results. The hadronization FSI model predicts that the effective cross section for the FSI in the DIS region is substantially greater than the one in the quasi-elastic region. Indeed, as the invariant mass of the final state W^* increases, it contains more and more particles and the particle momenta in the center of mass also get bigger. This can be pictured as a kind of explosion, with the density of the debris cloud and the speed at which it expands getting larger as W^* increases. As the invariant mass of the unobserved final state W^* decreases, it contains fewer and fewer particles, so that in the quasi-elastic region the proton can reinteract only with a struck neutron. The

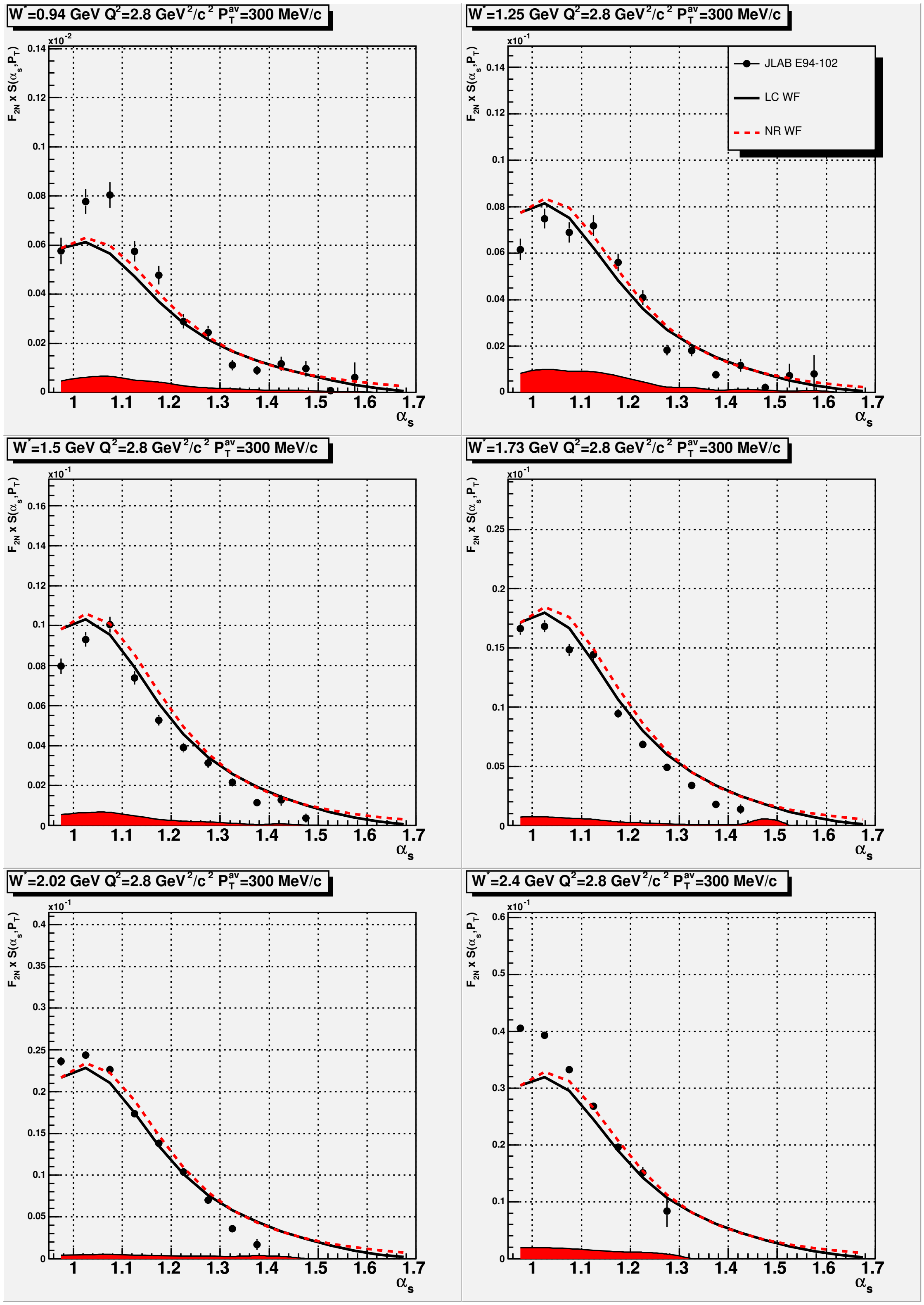

FIG. 119: $F_{2n}(W^*, Q^2)$ times $S(\alpha_s, p_T)$ versus α_s for different ranges of the invariant mass W^*, for the upper Q^2 bin ($2.1 - 5.0$ GeV^2/c^2) and p_T between 250 and 350 MeV/c.

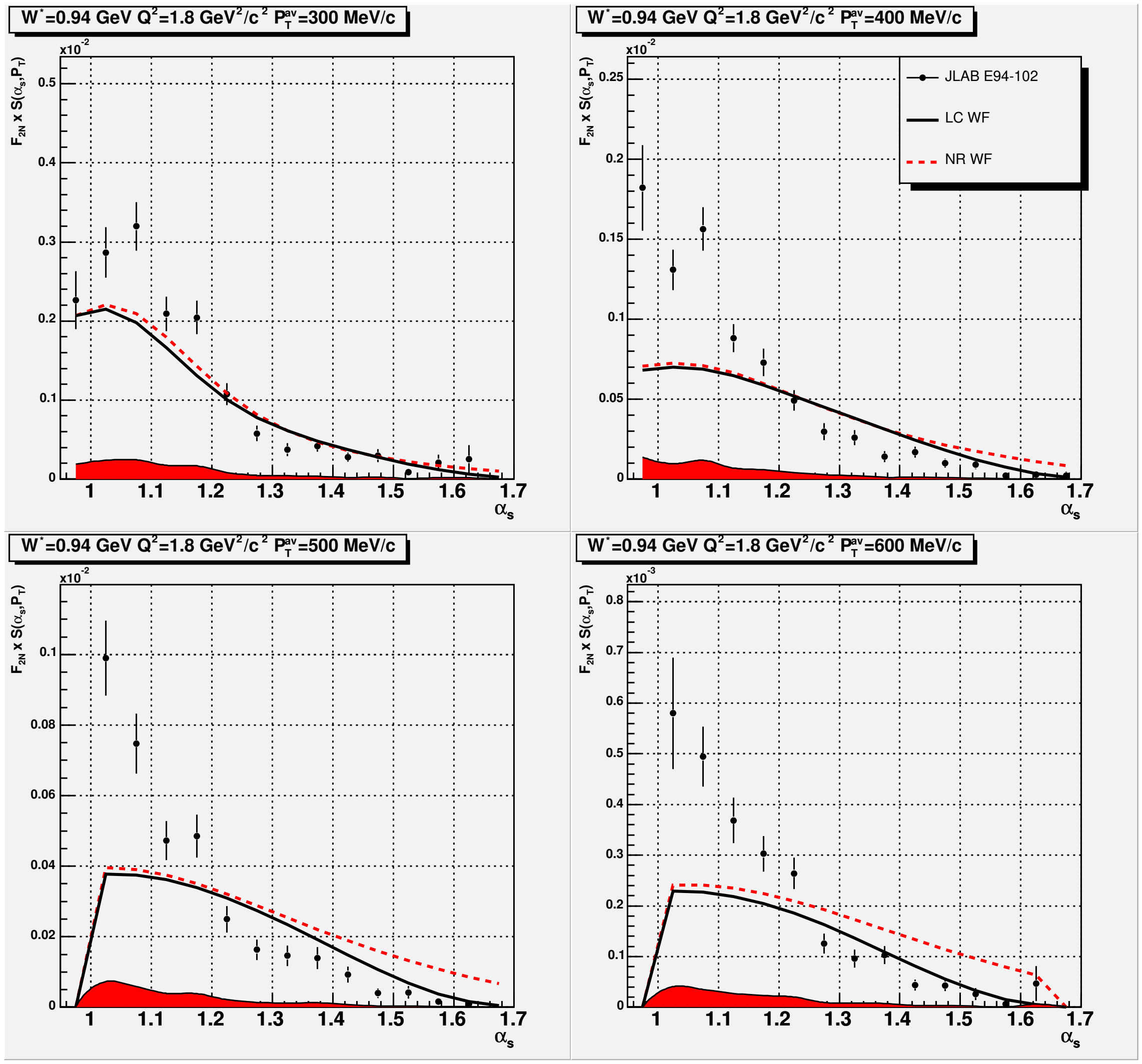

FIG. 120: $F_{2n}(W^*, Q^2)$ times $S(\alpha_s, p_T)$ versus α_s for four different values of proton momentum, but for the same value of $W^* = 0.94$ GeV and $Q^2 = 1.8$ GeV^2/c^2.

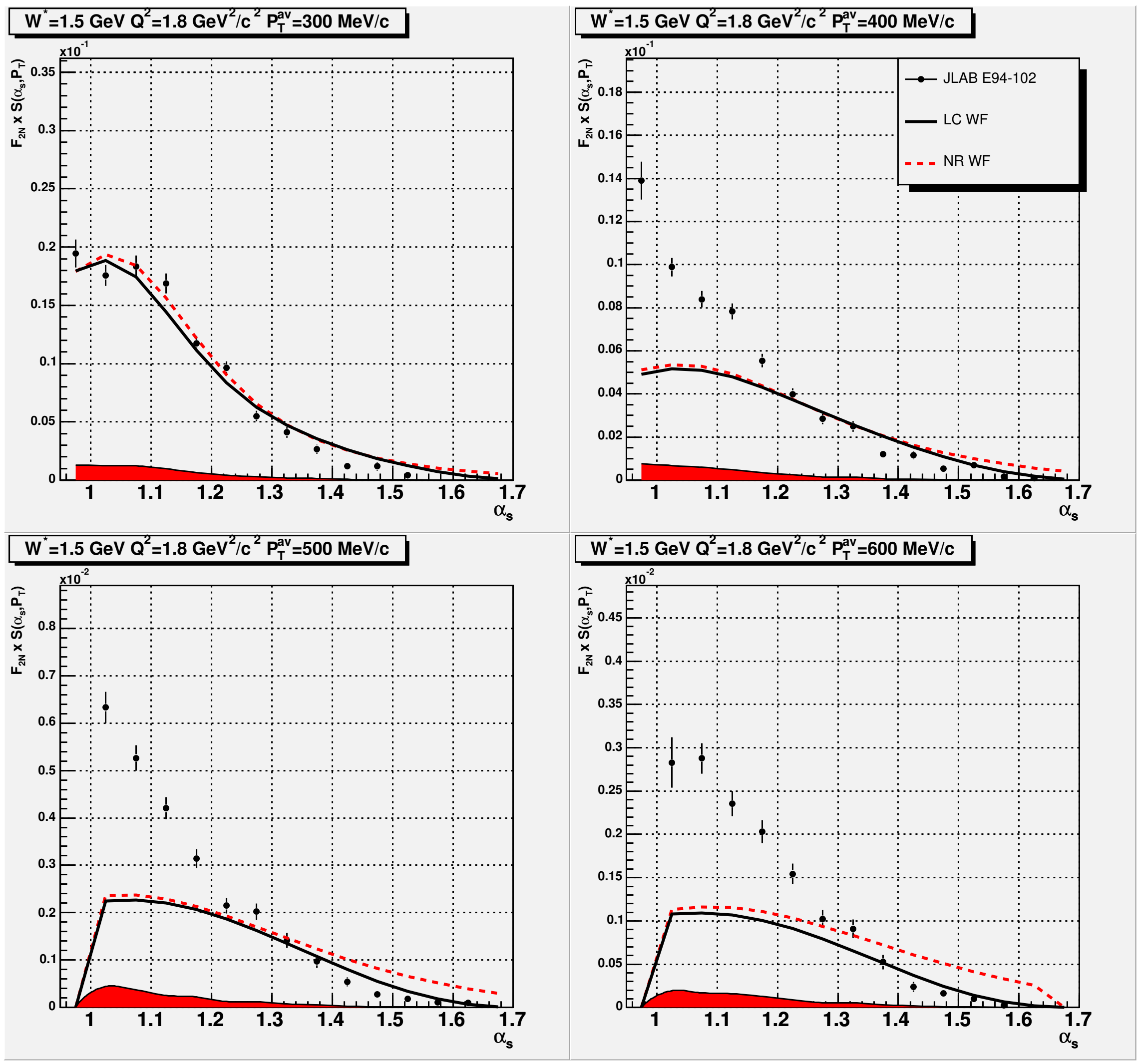

FIG. 121: $F_{2n}(W^*, Q^2)$ times $S(\alpha_s, p_T)$ versus α_s for four different values of proton momentum, but for the same value of $W^* = 1.5$ GeV and $Q^2 = 1.8$ GeV^2/c^2.

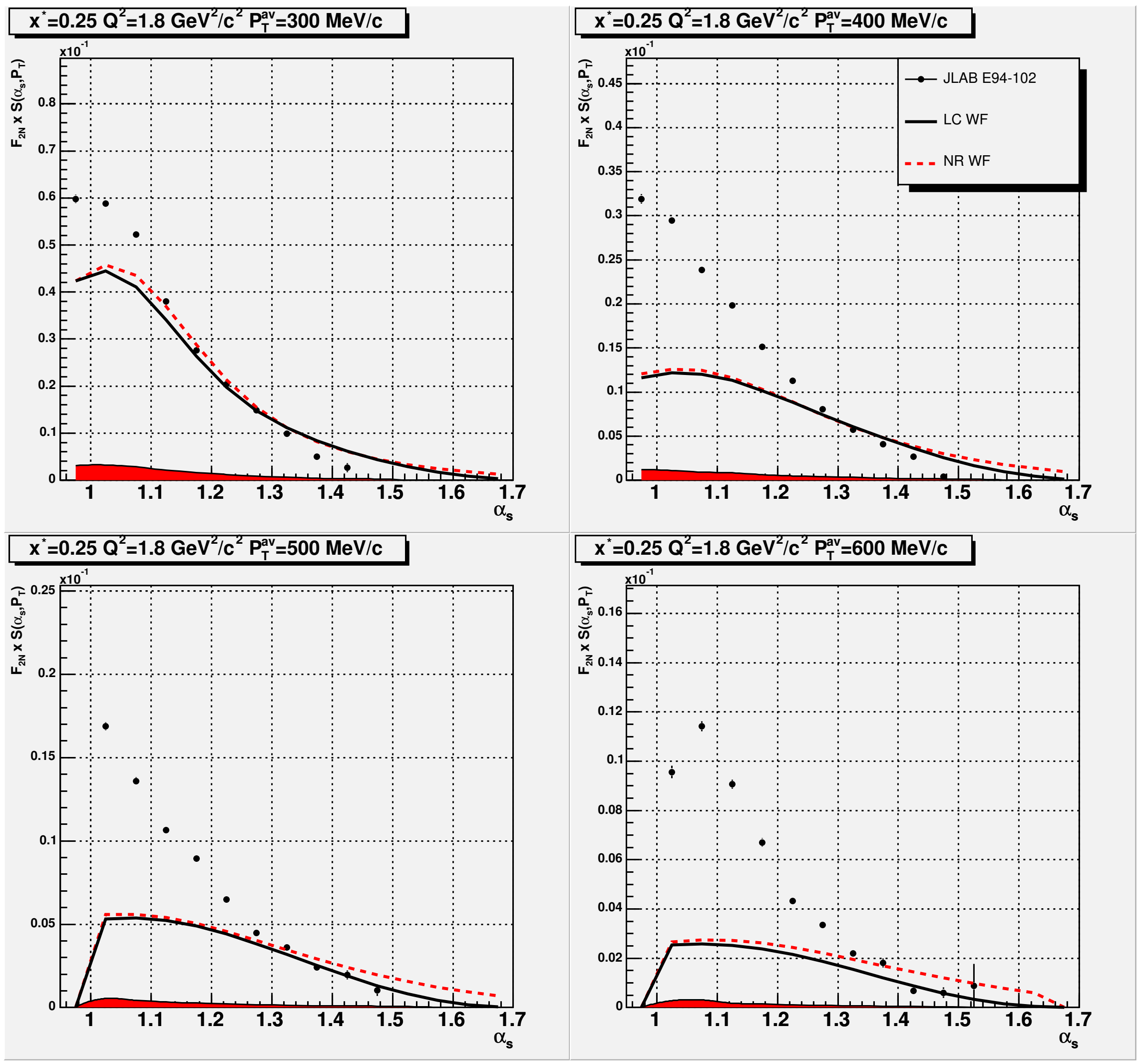

FIG. 122: $F_{2n}(x^*, Q^2)$ times $S(\alpha_s, p_T)$ versus α_s for four different values of proton momentum, but for the same value of $x^* = 0.25$ and $Q^2 = 1.8$ GeV^2/c^2 .

relative magnitude of the models compared to the data in the region of forward angles also seems to be dynamically changing with Q^2. As it can be seen from Fig. 115, the increase in the momentum transfer for a given W^* value, reduces the excess of the data over the model curves. A naive interpretation of this effect relates the size of FSI to the transverse size of the final state as it reinteracts with the spectator. The velocity of the final state center of mass can be expressed as $\beta_W = q/E_W$, where $q = \sqrt{Q^2 + \nu^2}$ is a momentum transfered and $E_W = \sqrt{W^2 + q^2} = \sqrt{M^2 + 2M\nu + \nu^2}$ is the total lab energy of the final state. As Q^2 increases, so does the velocity of the center of mass and the cone of the emerging final state particles starts to get narrower. However, at fixed x^*, if Q^2 increases, the energy transfer increases as $\nu \sim Q^2/x^*$, so that the increase in the final state velocity is accompanied by an even stronger increase in W^*. This agrees qualitatively with the hadronization FSI model, where the effective cross section of reinteraction increases as Q^2 increases at fixed x^*.

The behavior of the data in the region $\cos(\theta_{pq}) > -0.3$ is qualitatively described by the hadronization model of FSI, while the DWIA FSI model is less successful. At the same time, the region of backward angles ($\cos(\theta_{pq}) < -0.3$) is thought to be almost free of FSI, compared to the region of forward angles, discussed in the previous paragraph. Both FSI models predict minor effects in the region $\cos(\theta_{pq}) < -0.3$, where the data roughly agree with the PWIA models. The DWIA FSI model predicts a small (5%) reduction in the cross section, due to the FSI effects at high (greater than 1.3) values of light-cone fraction α_s (corresponding to very negative values of $\cos(\theta_{pq})$ and large values of p_s). The hadronization model shows an increase in the magnitude of the distorted spectral function at large backward angles in the range of momenta 300−400 MeV/c and then small or no reduction at larger momentum values. However, the data on $\cos(\theta_{pq})$ and α_s distributions, for a given range in W^* or x^* , show some depletion relative to the PWIA calculations at very negative values of $\cos(\theta_{pq})$ and high α_s.

5.3.2 Bound Neutron Structure

As established by the European Muon Collaboration, the cross section of electron scattering from a bound nucleon is reduced relative to the cross section of a free nucleon. If the source of the EMC-effect lies in the modification of the nucleon structure itself (as some models suggest), the cross section for the recoiling spectator proton would be reduced as well, since it is correlated with the struck off-shell neutron. As the momentum of the recoil proton increases, the neutron goes further off-shell and the structure modification effect should become more pronounced. Different models have very different predictions for the magnitude of the reduction in the structure function. Even if final state interactions do vary with electron kinematics, both FSI models discussed predict that in the extreme backward kinematics and at certain values of momenta, the recoiling spectator protons do not experience a distortion of greater than 10%. Thus, in this region, the PLC suppression and the binding models, that predict respectively 50% and 25% reduction in the structure function, can be tested.

Using the assumption that at large backward angles the FSI of the recoil proton are small, the bound neutron structure function F_{2n} was extracted. The dependence of F_{2n} as a function of W^* was obtained by multiplying the ratio of data to simulation with the free nucleon structure function used to generate the simulated data. This way in addition to the kinematic factor (containing the Mott cross section), the PWIA spectral function is also divided out from the cross section. The structure function was extracted for six different values of proton average momentum and for low and high momentum transfer (Figs. 123 and 124). The data were compared with the calculation using the free nucleon structure function (solid curve). In general, the model lies fairly close to the data points for all values of W^*, p_s and Q^2. However, at low Q^2 in the region of the quasi-elastic peak, large changes in the data relative to the model are observed (Fig. 123) with the increase of average proton momentum p_s. The model goes from being about 10% lower than the data at $p_s = 300$ MeV/c and 340 MeV/c, to more than 50% higher than the data at the highest proton momentum of 560 MeV/c. At higher momentum transfer in the quasi-elastic region, the model is in good agreement with the data up to $p_s = 390$ MeV/c. As the momentum increases, the model prediction grows faster than data and the two disagree by about 15% at $p_s = 560$ MeV/c. The region of the $\Delta-$resonance ($W^* = 1.2$ GeV) follows the same trend as the quasi-elastic peak: the model goes from being slightly below the data at lower momenta, to overshooting the data as p_s increases. In the rest of the resonant region at low Q^2, the model describes the data reasonably well up to the values of W^* around 2.0 GeV for $p_s = 300$ MeV/c. At $W^* > 2$ GeV, the data dips below the model and the two disagree by as much as 10%. At higher p_s =340 and 390 MeV/c, the data falls slightly below the model, but then increases as W^* enters the DIS region. This increase in the deep inelastic region might be a signature

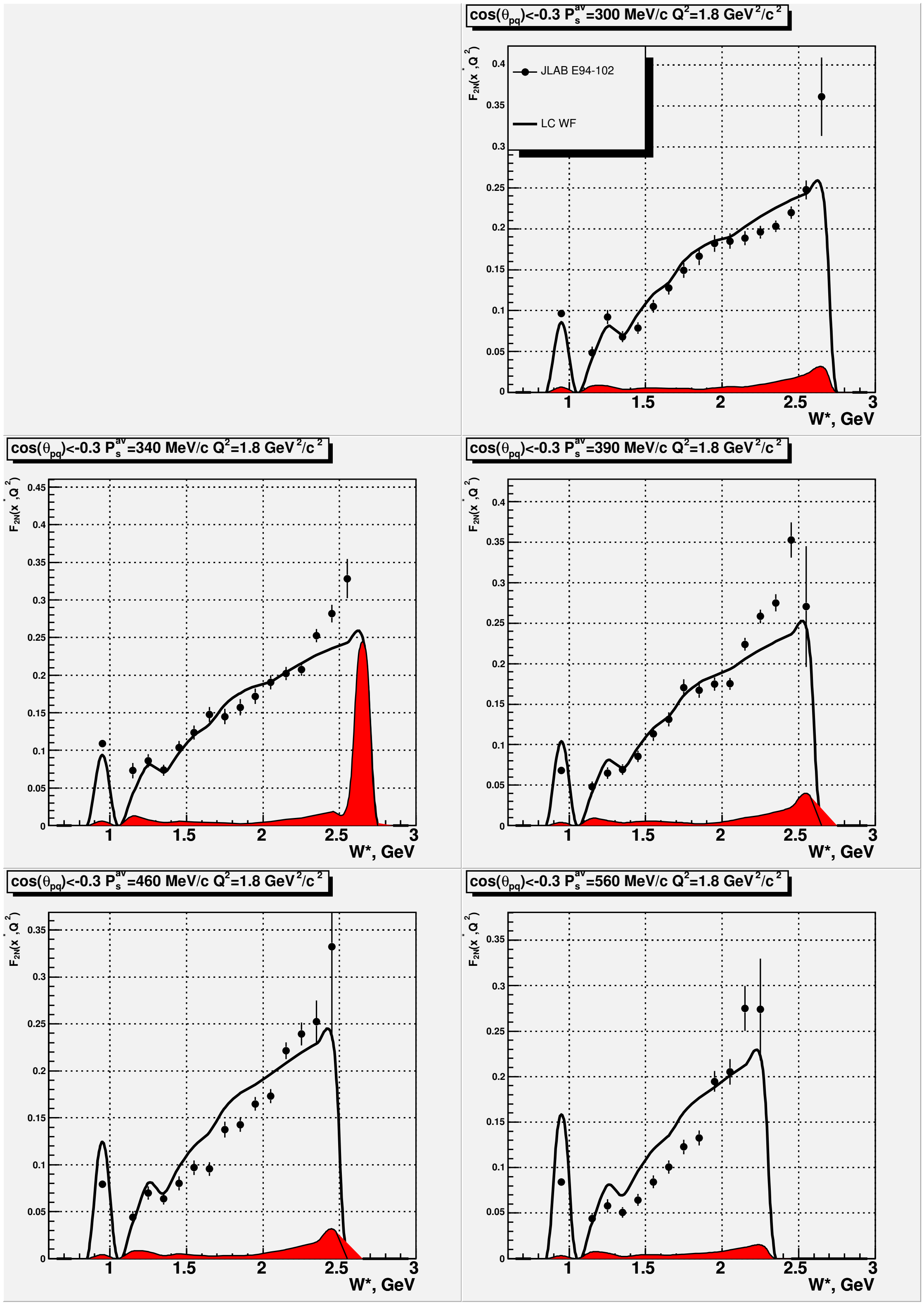

FIG. 123: Structure function $F_{2n}(W^*, Q^2)$ versus the invariant mass of the unobserved final state W^* for the lower bin in $Q^2 = 1.8$ Gev^2/c^2. Different sections of the plot correspond to the different values of the proton average momentum. The quasi-elastic peak was scaled up by a factor of 10.

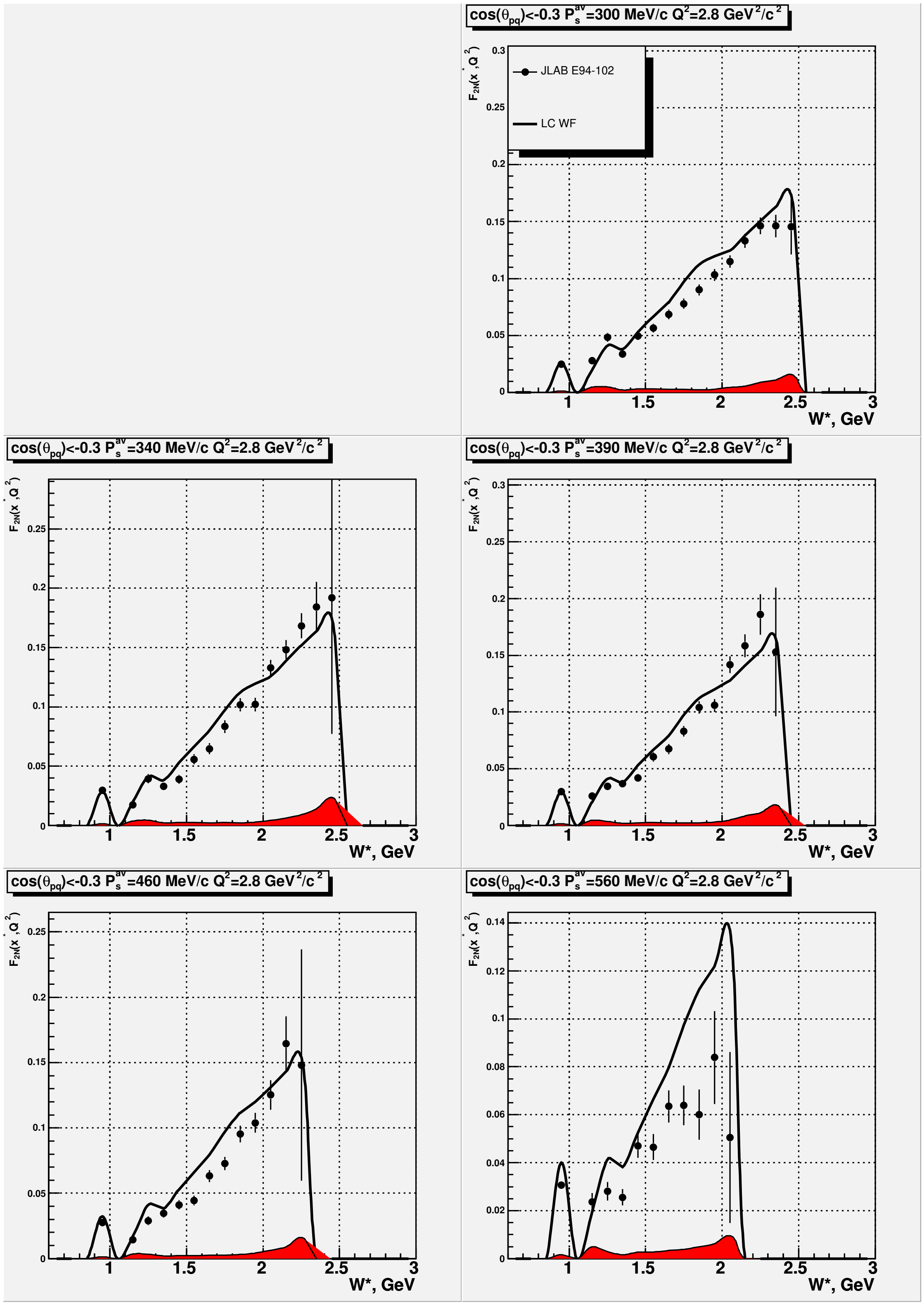

FIG. 124: Structure function $F_{2n}(W^{*}, Q^{2})$ versus the invariant mass of the unobserved final state W^{*} for the upper bin in $Q^{2} = 2.8$ Gev^{2}/c^{2}. Different sections of the plot correspond to the different values of the proton average momentum. The quasi-elastic peak was scaled up by a factor of 10.

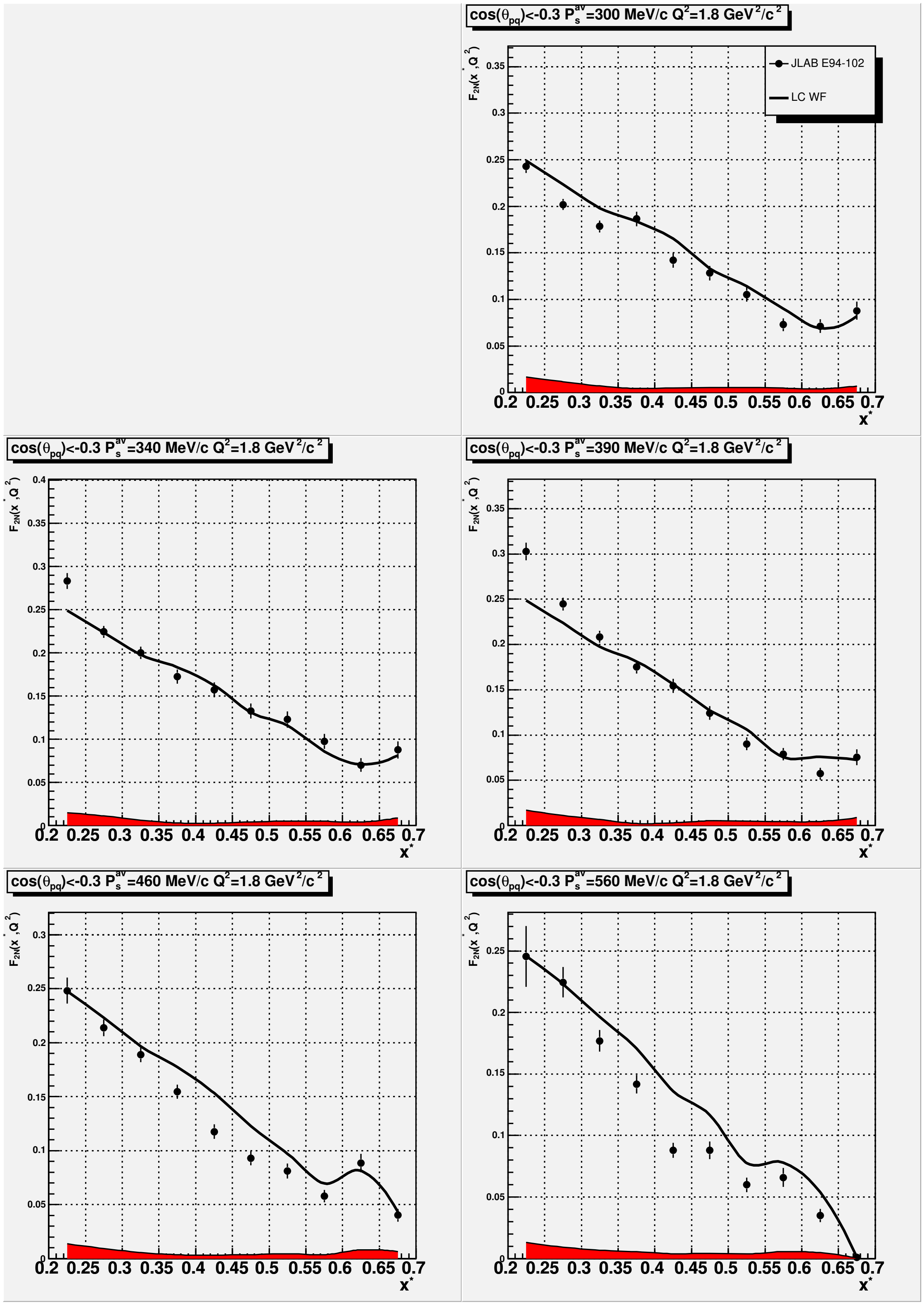

FIG. 125: Structure function $F_{2n}(x^*, Q^2)$ versus the scaling variable x^* for the lower bin in $Q^2 = 1.8$ Gev^2/c^2. Different sections of the plot correspond to the different values of the proton average momentum.

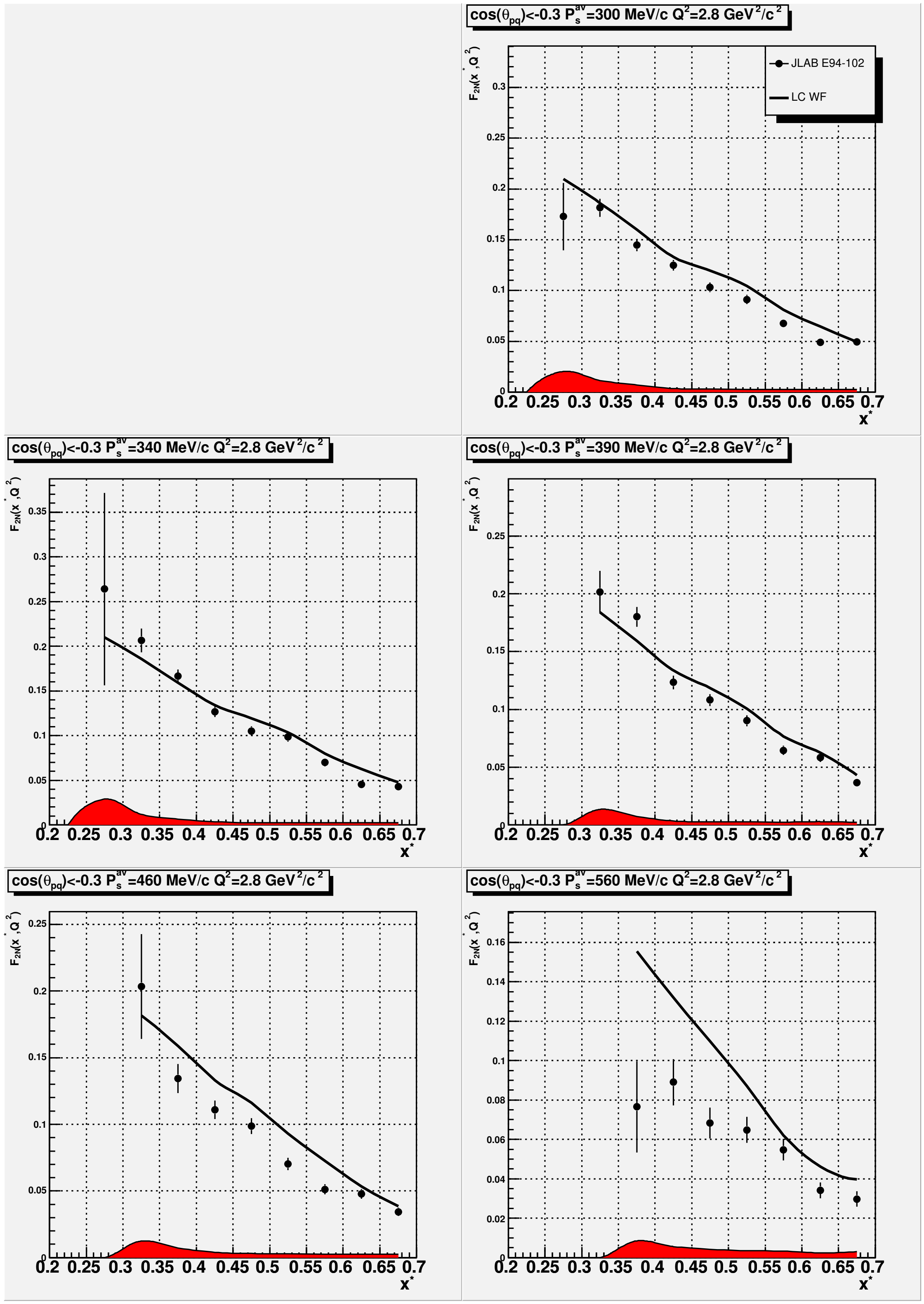

FIG. 126: Structure function $F_{2n}(x^*, Q^2)$ versus the scaling variable x^* for the upper bin in $Q^2 = 2.8\ \ \mathrm{Gev}^2/\mathrm{c}^2$. Different sections of the plot correspond to the different values of the proton average momentum.

of final state interactions that were seen (in the previous subsection) to be stronger at higher W^*. For the highest two values of momentum (and low Q^2), the model overestimates the value of F_{2n} for the whole resonant region, but seems to work better at $W^* > 2$ GeV. The agreement in the DIS region again might be only an illusion, created by two competing effects (for example, nucleon structure modification and FSI) canceling each other. At high Q^2 the model lies above the data in the resonant region for all values of momentum, but usually gives better agreement at $W^* > 2$ GeV.

The scaling variable x^* is directly related to the invariant mass W^*. High values of W^* correspond to low values of x^*, while above $x^* = 0.4 - 0.5$ most of the data lie in the resonance region ($W^* = 1.1 - 1.85$ GeV). Nevertheless, it is instructive to investigate the behavior of F_{2n} as a function of x^* as well (Figs. 125 and 126). Here, the model is in good agreement with data almost throughout the whole x^* range for both high and low values of Q^2 and for the proton momenta between 300 and 390 MeV/c. At $p_s = 340$ MeV/c and 390 MeV/c the two lowest x^* points in the data lie above the calculation. However, the systematic uncertainty at low values of x^* (the bar at the bottom of Figs. 125 and 126) is also bigger. The disagreement at low x^* can be interpreted as a competition between FSI and general decrease of F_{2n} as spectator momentum p_s increases. For the highest two values of proton momentum a dip is observed in the F_{2n} distribution as a function of x^* in the range from 0.3 to 0.6 (Fig. 125). A similar behavior is noted at higher momentum transfer (Fig. 126). The observed behavior might be an indication of structure modification of the nucleon or some other underlying effect. The reduction in F_{2n} at intermediate x^* is clearly more pronounced as the momentum of the recoiling proton increases, which in spectator approximation means that the struck neutron is further off its mass shell.

CHAPTER 6

SUMMARY

Taking advantage of the large solid angle acceptance of the CEBAF Large Acceptance Spectrometer, an overwhelming (compared to previous measurements) amount of data (≈500K events) were collected on the reaction $d(e, e'p_s)X$ in the exotic region of extreme backward proton kinematics. The data range from 1.2 to 5 GeV^2 in momentum transfer Q^2 and reach values of the missing mass of the unobserved final state W^* of up to 2.7 GeV. Protons with momentum p_s as low as 280 MeV/c and up to 700 MeV/c were detected, at angles relative to the direction of the momentum transfer as large as 140°. In terms of the light cone variables, the data span values of the light-cone fraction α_s up to about 1.7, with the minimum proton transverse momentum, relative to $\hat{q}$ of 150 MeV/c and up to 600 MeV/c.

Absolute cross sections were extracted as a function of $\cos(\theta_{pq})$, W^*, x^* and α_s for a variety of kinematic conditions, allowing us to test future theoretical calculations against the presented data. Comparison with a simple PWIA model shows that the kinematic region of $\cos(\theta_{pq}) < -0.3$ is relatively free from FSI. In the region of proton scattering angles $\cos(\theta_{pq}) > -0.3$, the FSI are strong and seem to depend on p_s, W^* and x^* as well as Q^2. The FSI increase as proton momentum p_s and invariant mass W^* increase, but are somewhat reduced at increased Q^2. This behavior is in qualitative agreement with models that describe the strength of FSI in terms of the transverse size of the final state X. The angular (θ_{pq}) and momentum (p_s) dependence of the observed strength in the cross section in quasi-elastic region (where X is a neutron in its ground state) is also in qualitative agreement with detailed calculations showing a transition from destructive interference below $p_s = 300$ MeV/c to a strong enhancement at $p_s > 400$ MeV/c around $\cos(\theta_{pq}) = 0$.

A depletion in the data, compared to the PWIA model, is observed in the data at $\cos(\theta_{pq}) < -0.3$ and for high p_s, where the struck neutron is far off its mass shell. The reduction in data in these kinematics is a lot stronger than that predicted by the FSI models and might be an indication of some other underlying effect (for example, nucleon structure modification). It is especially strong in the region of moderate x^* which largely overlaps with the nucleon resonance region. However, a uniform depletion for all values of x^* (or W^*), which may be somewhat masked by remaining FSI-induced enhancement at high, cannot be ruled out. It remains to be seen whether detailed theoretical calculations including off-shell effects can reproduce these data.

BIBLIOGRAPHY

[1] S.E. Kuhn *et al.,* PR 94-102 experiment proposal.

[2] H.C. Urey, F.G. Brickwedde and G.M. Murphy, Phys. Rev. **39**, 164(L) (1932).

[3] F. Halzen, A.D. Martin, *Quarks and Leptons: an Introductory Course in Modern Particle Physics,* John Wiley & Sons, Inc. (1984).

[4] R.G. Roberts, *The Structure of the Proton: Deep Inelastic Scattering,* Cambridge University Press (1990).

[5] S.E. Kuhn. *Nucleon Structure Functions: Experiments and Models,* HUGS Lecture Series (1997).

[6] Panovsky W.K.H. Rapporteurs talk, in *International Conference on High Energy Physics*, Vienna, ed. J. Prentki and J. Steinberger (CERN, Geneva) (1968).

[7] J.D. Bjorken, Phys. Rev. **179**, 1547 (1969).

[8] R.P. Feynman, Phys. Rev. Lett. **23**, 1415 (1969).

[9] E.D. Bloom *et al.*, Phys. Rev. Lett. **23**, 930 (1969).

[10] M. Breidenbach *et al.*, Phys. Rev. Lett. **23**, 935 (1969).

[11] C.G. Callan and D. Gross, Phys. Rev. Lett. **22**, 156 (1969).

[12] Berge J.P. *et al.*, Phys. Rev. **D18**, 1367 (1978).

[13] Efremenko V.I. *et al.*, Phys. Rev. **D22**, 2581 (1980).

[14] M.M. Sargsian *et al.*, J. Phys. **G29**, R1 (2003).

[15] J.J. Aubert *et al.*, Phys. Lett. **B123**, 275 (1983).

[16] A. Bodek *et al.*, Phys. Rev. Lett. **50**, 1431 (1983); **51**, 534 (1983).

[17] R.G. Arnold *et al.*, Phys. Rev. Lett. **52**, 727 (1984).

[18] G. Bari *et al.*, Phys. Lett. **B163**, 282 (1985).

[19] D.M. Alde et. al. Phys. Rev. Lett. **66**, 2479 (1990).

[20] S.D. Drell, T.-M. Yan, Phys. Rev. Lett. **25**, 316 (1970).

[21] S. Dieterich et.al., Phys. Lett. **B500**, 47 (2001).

[22] S. Strauch et. al., Phys. Rev. Lett. **91,** 052301 (2003); S. Dieterich *et al.*, Nucl. Phys. **A690**, 231 (2001); R.D. Ransome, Nucl. Phys. **A699**, 360c (2002).

[23] C.E. Carlson et. al., Phys. Rev. **D63**, 117301 (2001).

[24] E545 Collaboration, T. Kafka et.al., Bull. Am. Phys. Soc. **28**, 756 (1983).

[25] S.M. Wong, *Introductory Nuclear Physics*, 2nd. ed., John Wiley & Sons Inc. (1998).

[26] S. Okubo and R.E. Marshak, Ann. Phys. **4**, 166 (1958).

[27] J. Carlson, R. Schiavilla, Rev. Mod. Phys. **70**, 743 (1998).

[28] Pudliner et al., Phys. Rev. Lett. **74**, 4396 (1995).

[29] R.V. Reid, Ann. Phys. **50**, 411 (1968).

[30] R. Machleidt, K. Holinde and Ch. Elster, Phys. Rep. **149**, 1 (1987).

[31] R. Machleidt, F. Sammarruca and Y. Song, Phys. Rev. **C53**, R1483 (1996).

[32] V.G.J. Stocks et al., Phys. Rev. **C49**, 2950 (1994).

[33] T. de Forest Jr., Nucl. Phys. **A392**, 232 (1983).

[34] H. Meier-Hajduk, U. Oelfke, P.U. Sauer, Nucl. Phys. **A499**, 637 (1989).

[35] O. Benhar, V. Pandaripande, I. Sick, Phys. Lett. **B410**, 79 (1997).

[36] Quoted in E. Matsinos *et al.*, Z. Phys. **C44**, 79 (1989).

[37] M. Garcon, J.W. Van Orden, Adv. Nucl. Phys. **26**, 293 (2001).

[38] G.A. Miller and J.R. Smith, Phys. Rev. **C65**, 015211 (2002).

[39] D.S. Koltun., Phys. Rev. **C57**, 1210 (1998).

[40] W. Melnitchouk, A.W. Shreiber, A.W. Thomas, Phys. Rev. **D49**, 1183 (1994).

[41] W. Melnitchouk, A.W. Shreiber, A.W. Thomas, Phys. Lett. **B335**, 11 (1994).

[42] P.G. Blunder and G.A. Miller, Phys. Rev. **C54**, 359 (1996).

[43] D.H. Lu, A.W. Thomas, K. Tsushima, A.G. Williams and K. Saito, Phys. Lett. **B417**, 217 (1998).

[44] L.L. Frankfurt, M.I. Strikman, Nucl. Phys. **B250**, 143 (1985).

[45] F.E. Close *et al.*, Phys. Rev. **D31**, 1004 (1985).

[46] C.E. Carlson, K.E. Lassila, Phys. Rev. **C51**, 364 (1995).

[47] W. Melnitchouk, M. Sargisian, M.I. Strikman, Z. Phys. **A359**, 99 (1997).

[48] C. Cioffi delgi Atti, L.P. Kaptari, B.Z. Kapelovich, Eur. Phys. J. **A19**, 145-151 (2004).

[49] E.S. Smith, T. Carstens *et al.*, Nucl. Inst. and Meth. **A432**, 265 (1999).

[50] M. Amarian, G. Asryan *et al.*, Nucl. Inst. and Meth. **A460**, 239 (2001).

[51] M.D. Mestayer, D.S. Carman *et al.*, Nucl. Inst. and Meth. **A449**, 81 (2000).

[52] M.D. Mestayer *et al.*, Nucl. Inst. and Meth. **A367**, 316 (1995).

[53] G. Adams, V. Burket *et al.*, Nucl. Inst. and Meth. **A465**, 414 (2001).

[54] R. Prydz, *The Thermodynamic Properties of Deuterium*, Nat. Bur. of Stand. **9276** (1967).

[55] R.G. McCarty, J. Hord, and H.M. Roder, *Selected Properties of Hydrogen (Engineering Design Data)* (Washington D.C. U.S. Gov. Printing Office, 1981; Nat. Bur. of Stand. Monograph 168).

[56] P.E. Bosted, Phys. Rev. **C51**, 409 (1994).

[57] M. Lacombe, J. Cote, *et al.*, Phys. Rev. **C21**, 861 (1980).

[58] M. Arneodo *et al.*, Phys. Lett. **B364**, 107 (1995).

[59] K. Abe *et al.,* Phys. Lett. **B452**, 194 (1999).

[60] S.J. Brodsky, Nucl.Phys.Proc.Suppl. **108**, 327-339 (2002).

[61] G.A. Miller, in Baryons 2002. *Proceedings of the 9th International Conference on the Structure of Baryons*, World Scientific (2003).

[62] L.L. Frankfurt, M.I. Strikman, Phys. Rep. **76**, 215 (1981).

[63] R.B. Wiringa, V.G.J. Stocks, R. Schiavilla, Phys. Rev. **C51**, 38 (1994).

[64] L.W. Mo and Y.S. Tsai, Rev. Mod. Phys. **41**, 205 (1969).

[65] K. Abe et. al., Phys. Rev. **D58**, 112003 (1998).

[66] R.G. Arnold et. al. Phys. Rev. Lett. **58**, 1723 (1987).

[67] I. Akushevich, A. Ilyichev, N. Shumeiko et. al. hep-ph/9706516.

[68] H. Egiyan, *Minutes of the CLAS CALCOM Analysis Meeting*, (1997).

[69] R. Feuerbach, *CLAS Drift Chamber Alignment*, CLAS-NOTE 01-022 (2001).

[70] S.A. Morrow, M.D. Mestayer, *Drift Chamber Alignment*, CLAS-NOTE 02-010 (2002).

[71] B. Mecking *et al.*, Nucl. Inst. and Meth. **A503/3**, 513 (2003).

[72] S.E. Kuhn, A.V. Klimenko, *Momentum Corrections for E6*, CLAS-NOTE 03-005 (2003).

[73] D. Lawrence, M.D. Mestayer, *CLAS Drift Chamber Calibration Procedures*, CLAS-NOTE 99-018 (1999).

[74] E. Smith et. al., *Calibration of CLAS Time-of-Flight System*, CLAS-NOTE 99-011 (1999).

[75] A. Vlassov et. al., *CLAS Cherenkov Detector Calibration*, CLAS-NOTE 99-005 (1999).

APPENDIX A

FULL SET OF FINAL HISTOGRAMS

This appendix contains all of the extracted distributions, overlayed with two different simple models of the scattering from a deuterium nucleus. The data on all the plots is represented with black circles with error bars. All plots also contain two model curves, calculated using free nucleon structure function (and form factors) and a non-relativistic spectral function (dashed line) or with a light-cone spectral function (solid line). No final state interactions were included in any of the models.

The data were corrected for the acceptance, backgrounds and radiative effects, using a GSIM simulation based on the model with the light-cone spectral function, which gives the best agreement with the data in most cases. The data should be directly comparable to theoretical calculations. The red bar at the bottom of each distribution represents the absolute value of the systematic error and does not include a kinematics-independent overall scale error estimated to be 5.9%.

The four sets of plots show the extracted cross section for the reaction $d(e, e'p_s)X$ integrated over various ranges of momentum transfer $Q^2 = -q^\mu q_\mu$, invariant mass $W^* = \sqrt{(p_D - p_s + q)^\mu (p_D - p_s + q)_\mu}$ of the unobserved final state X or relativistically invariant scaling variable $x^* = \frac{Q^2}{2(p_D - p_s)^\mu q_\mu}$. The first two sets of plots are binned in backward proton momentum p_s and the other two sets are binned in transverse proton momentum p_T. The cross sections on all the plots are divided by normalization factor $\frac{4\pi\alpha_{EM}^2}{x^* Q^4}$ and the kinematic factor (see Eq. (27)):

$$K = \left(1 - y^* + \frac{y^2/2 + M^{*2} x^{*2} y^{*2} (1-R)/Q^2}{(1+R)}\right)$$

where $M^{*2} = (p_D - p_s)^\mu (p_D - p_s)_\mu$ is the off-shell mass of the struck neutron (in the spectator picture), $y^* = \frac{(p_D - p_s)^\mu q_\mu}{(p_D - p_s)^\mu k_\mu} \approx \frac{\nu}{E}$, $R = \sigma_L/\sigma_T$ (taken from a parameterization of free structure functions) and $k^\mu = (E, \mathbf{k})$ is the incoming electron 4-momentum. In a pure spectator picture without final state interactions, the extracted cross section equals the product of spectral function $S(\alpha_s, p_T)$ or the proton momentum distribution $P(\vec{p_s})$ with the (off-shell) structure function $F_{2n}(x^*, Q^2)$ or $F_{2n}(W^*, Q^2)$. In the case of quasi-elastic final state ($W^* = M_n$), the structure function is replaced with $\frac{G_{En}^2 + \tau G_{Mn}^2}{1+\tau}$ with $\tau = Q^2/4M^2$. The first two sets of plots contain the product

$F_{2n} \times P(\vec{p_s})$ plotted as a function of cosine of the angle the scattered proton makes with the virtual photon q. The other two sets contain the distribution of the product $F_{2n} \times S(\alpha_s, p_T)$ as a function of light-cone fraction of the spectator proton α_s.

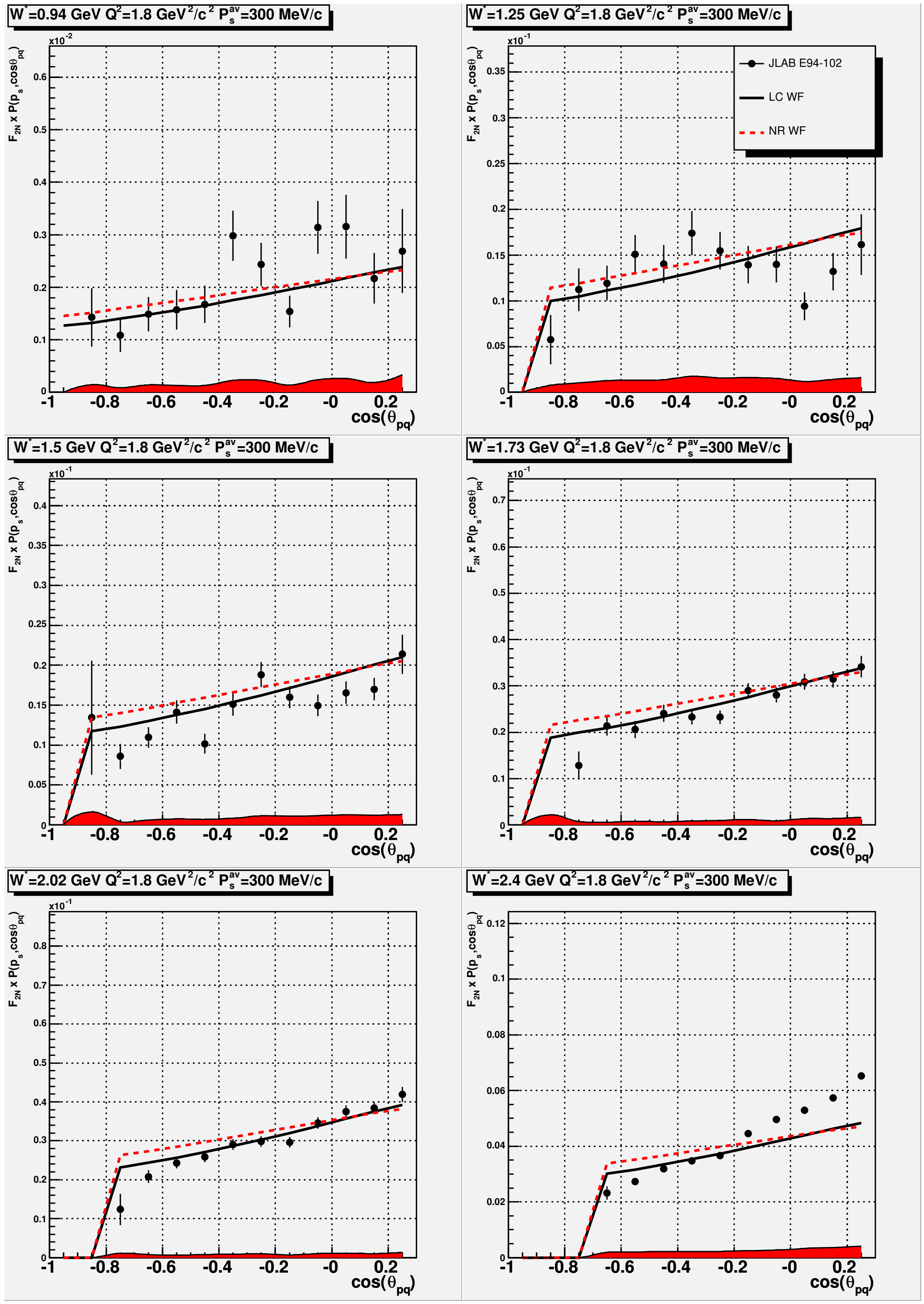

FIG. 127: $F_{2n}(W^*, Q^2)$ times $P(\vec{p_s})$ versus $\cos(\theta_{pq})$ for different ranges of the invariant mass W^*, for lower Q^2 bin (1.2-2.1 GeV^2/c^2) and for the lowest proton momentum bin $(280 - 320\ \text{MeV/c})$.

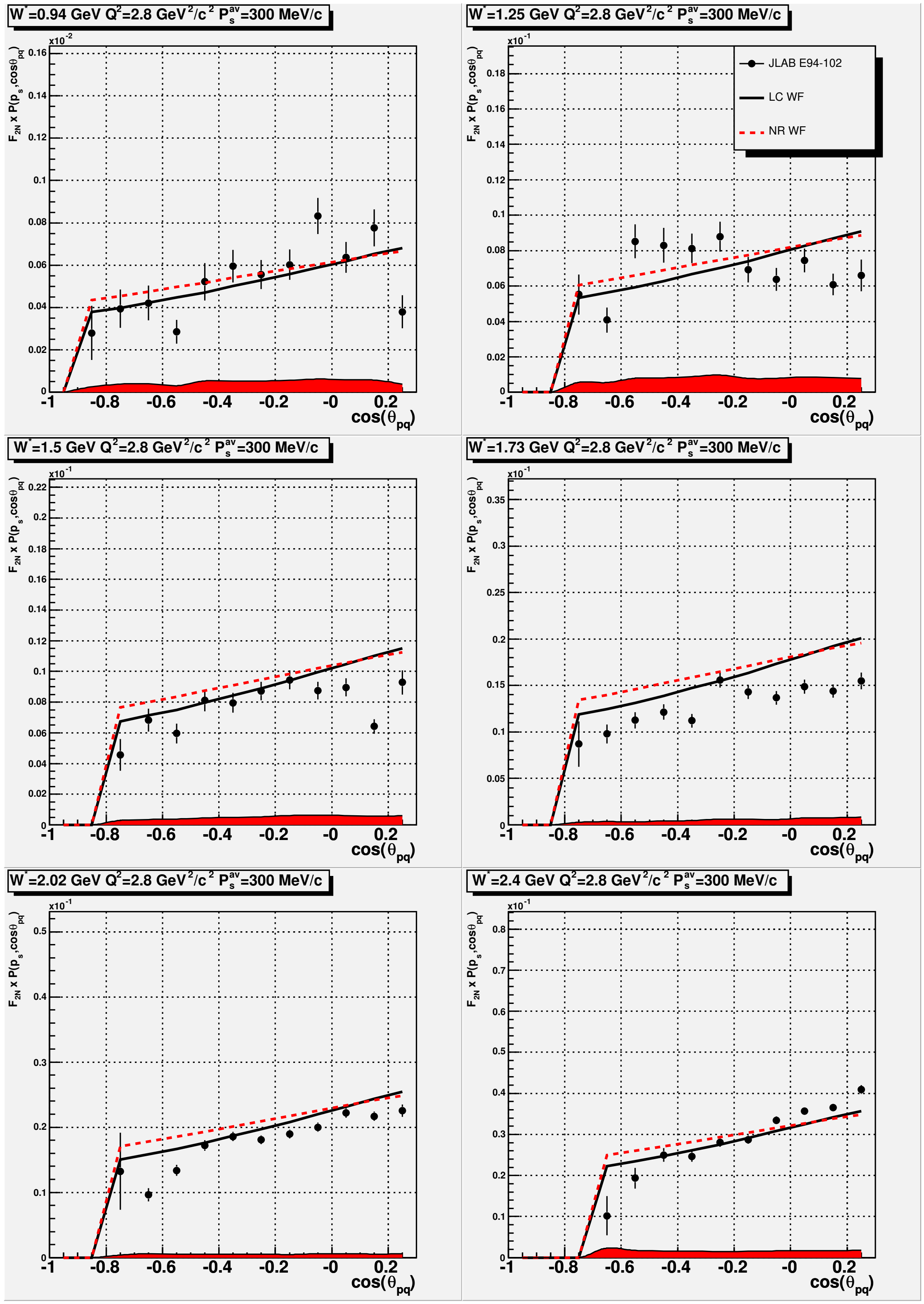

FIG. 128: The same as Fig. 127, but for the higher momentum transfer Q^2 bin $(2.1 - 5.0\ \mathrm{GeV}^2/c^2)$.

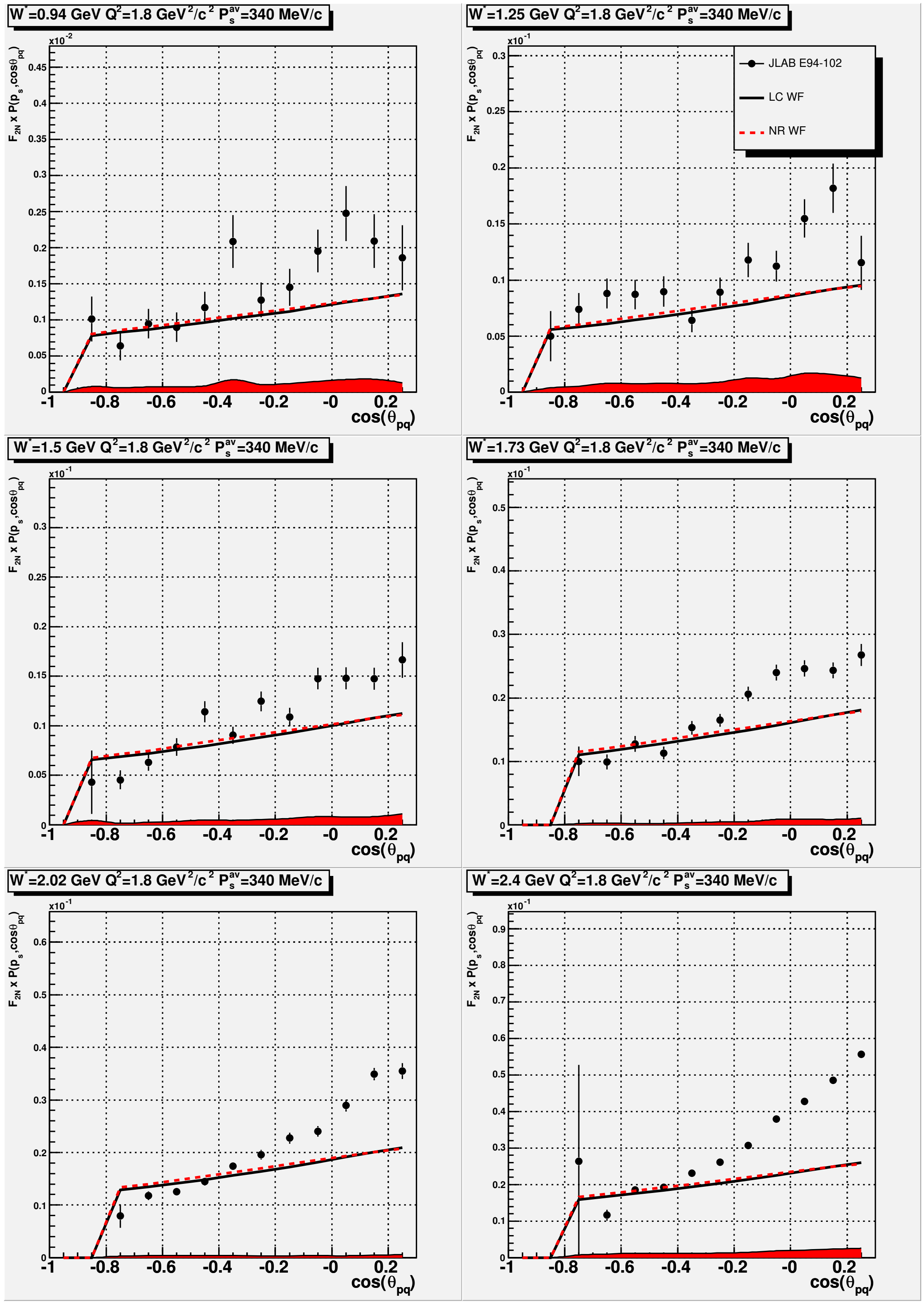

FIG. 129: The same as Fig. 127, but for the higher proton momentum p_s bin $(320 - 360$ MeV/c).

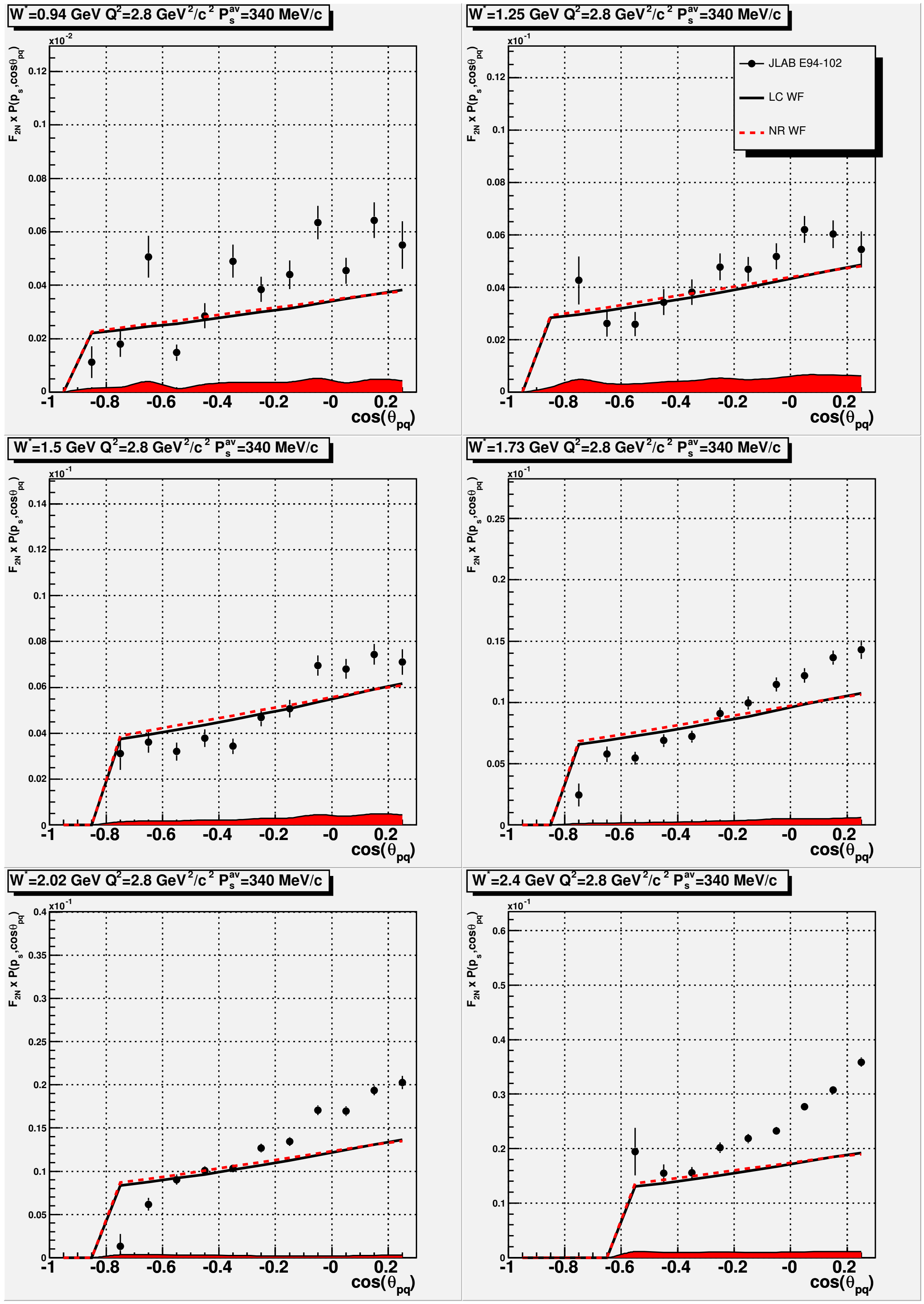

FIG. 130: The same as Fig. 129, but for the higher momentum transfer Q^2 bin $(2.1 - 5.0\ \mathrm{GeV}^2/\mathrm{c}^2)$.

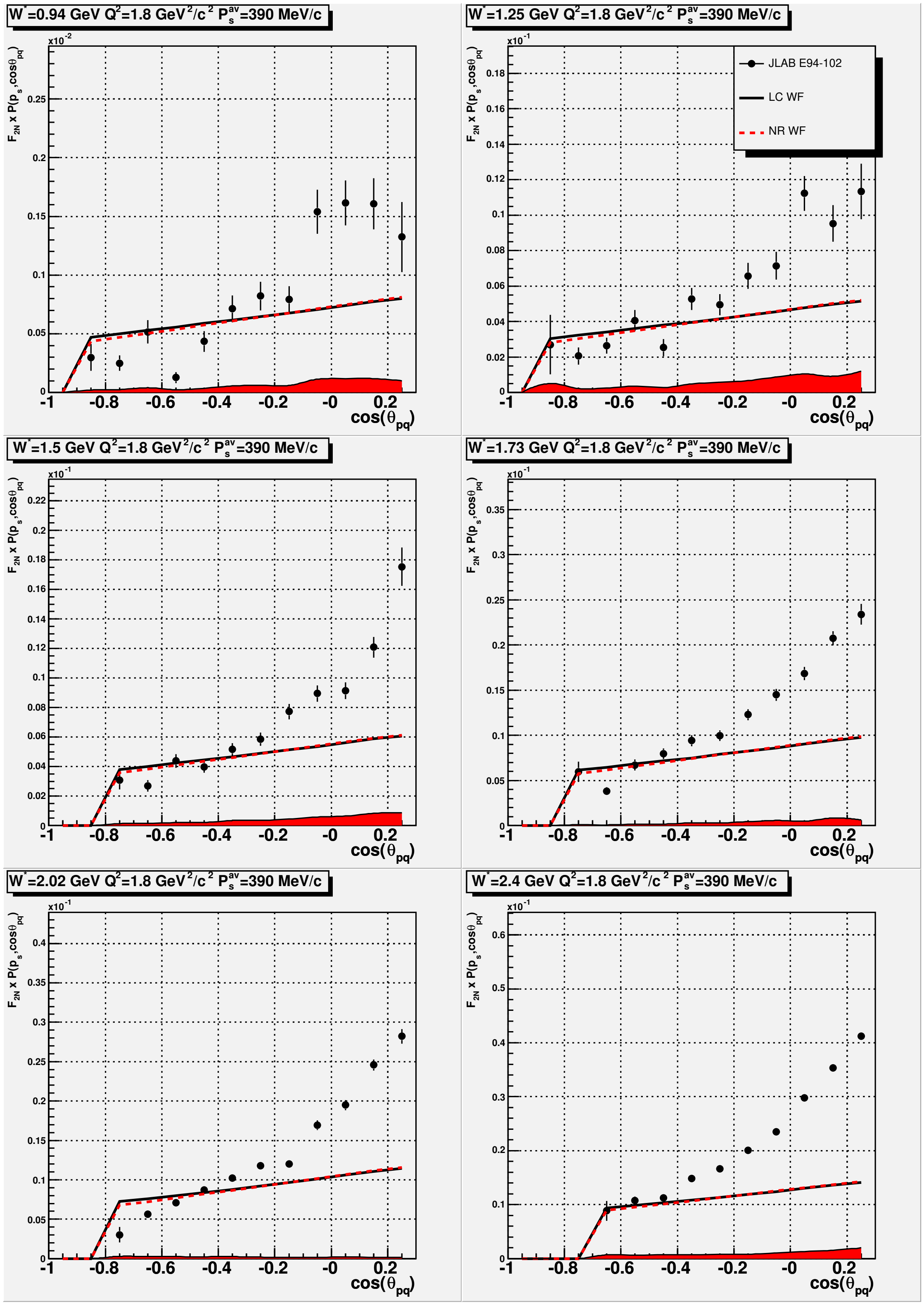

FIG. 131: The same as Fig. 127, but for the higher proton momentum p_s bin $(340 - 420\ \mathrm{MeV/c})$.

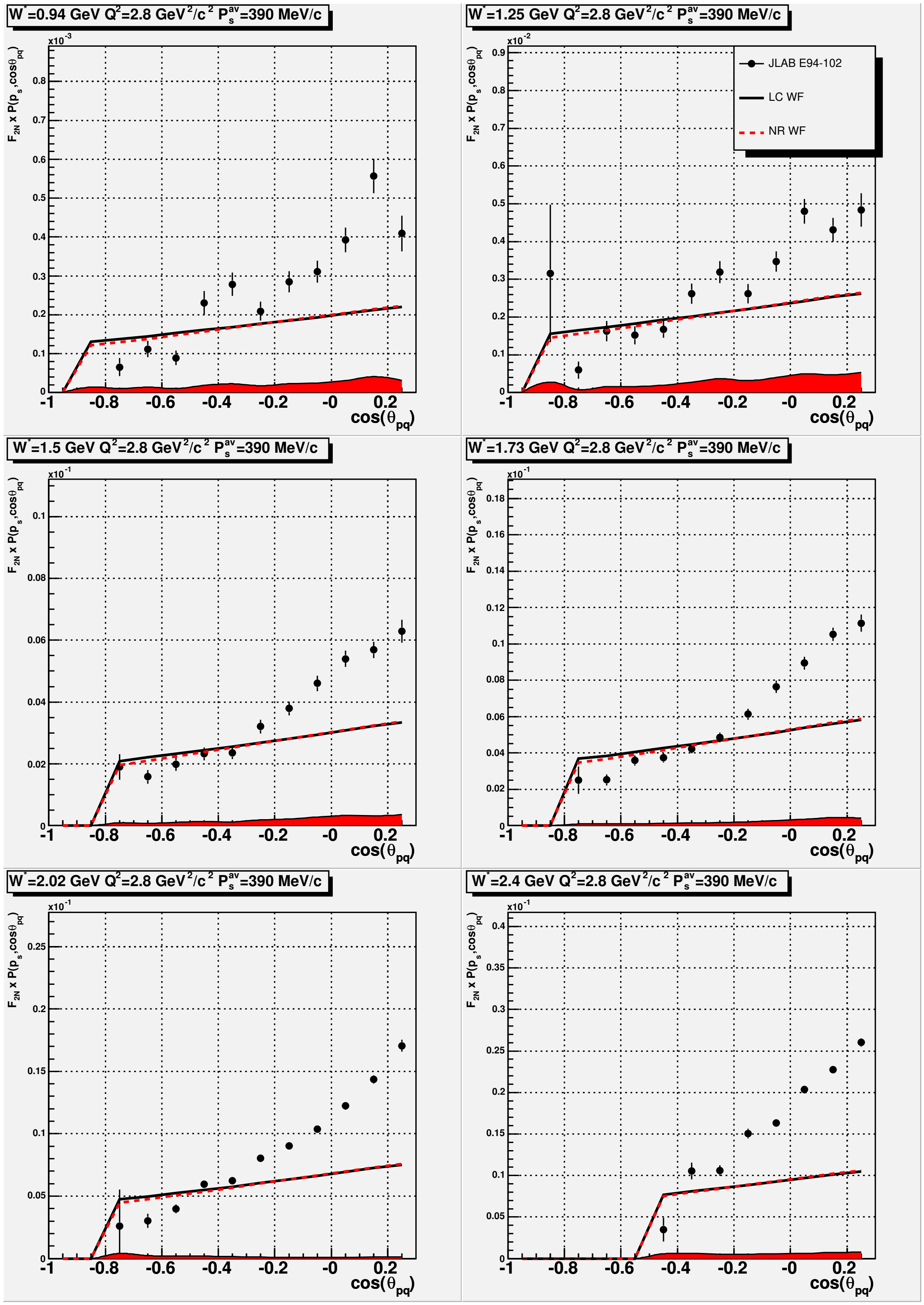

FIG. 132: The same as Fig. 131, but for the higher momentum transfer Q^2 bin $(2.1 - 5.0\ \mathrm{GeV}^2/\mathrm{c}^2)$.

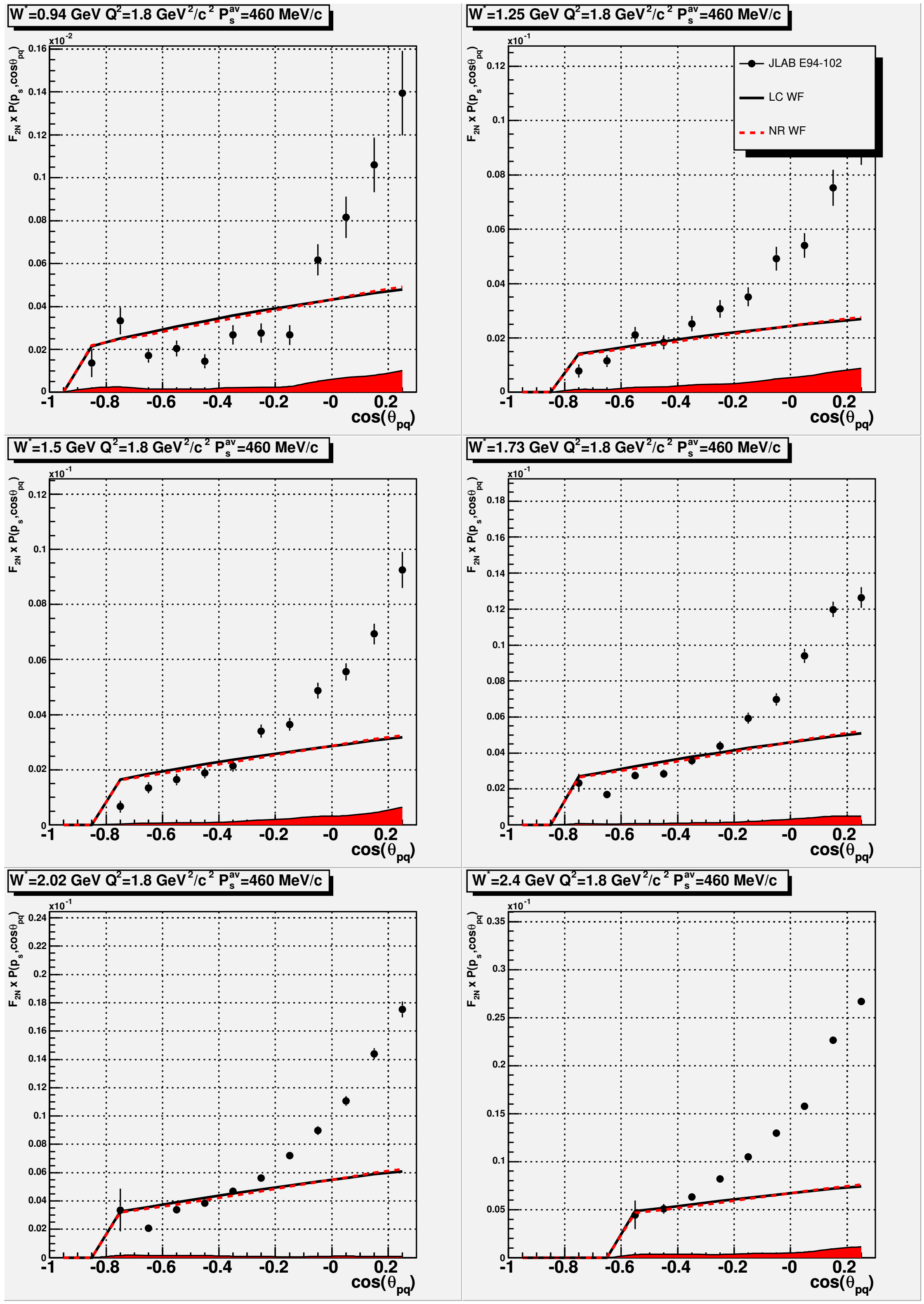

FIG. 133: The same as Fig. 127, but for the higher proton momentum p_s bin $(420 - 550$ MeV/c).

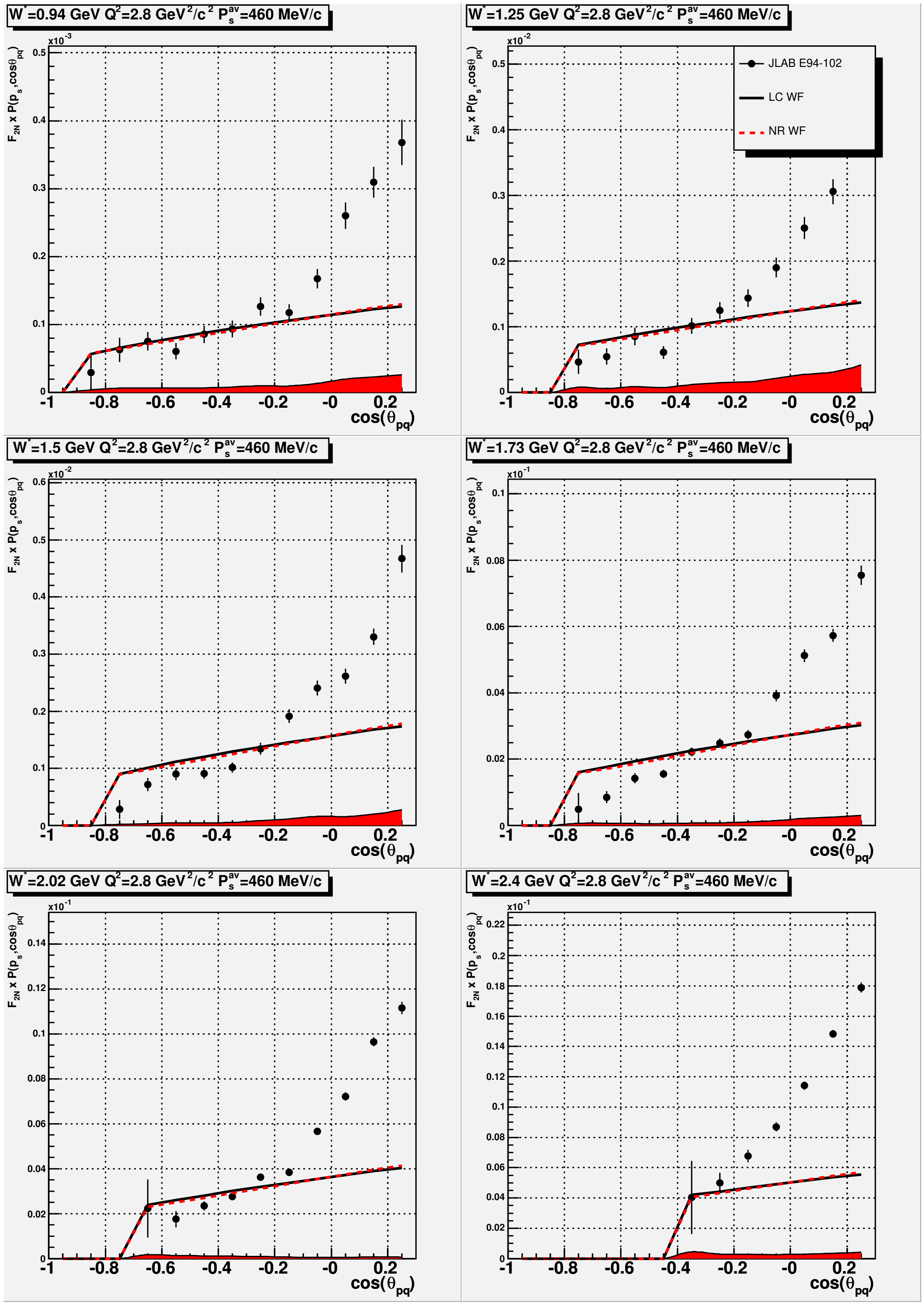

FIG. 134: The same as Fig. 133, but for the higher momentum transfer Q^2 bin $(2.1 - 5.0\ \mathrm{GeV}^2/\mathrm{c}^2)$.

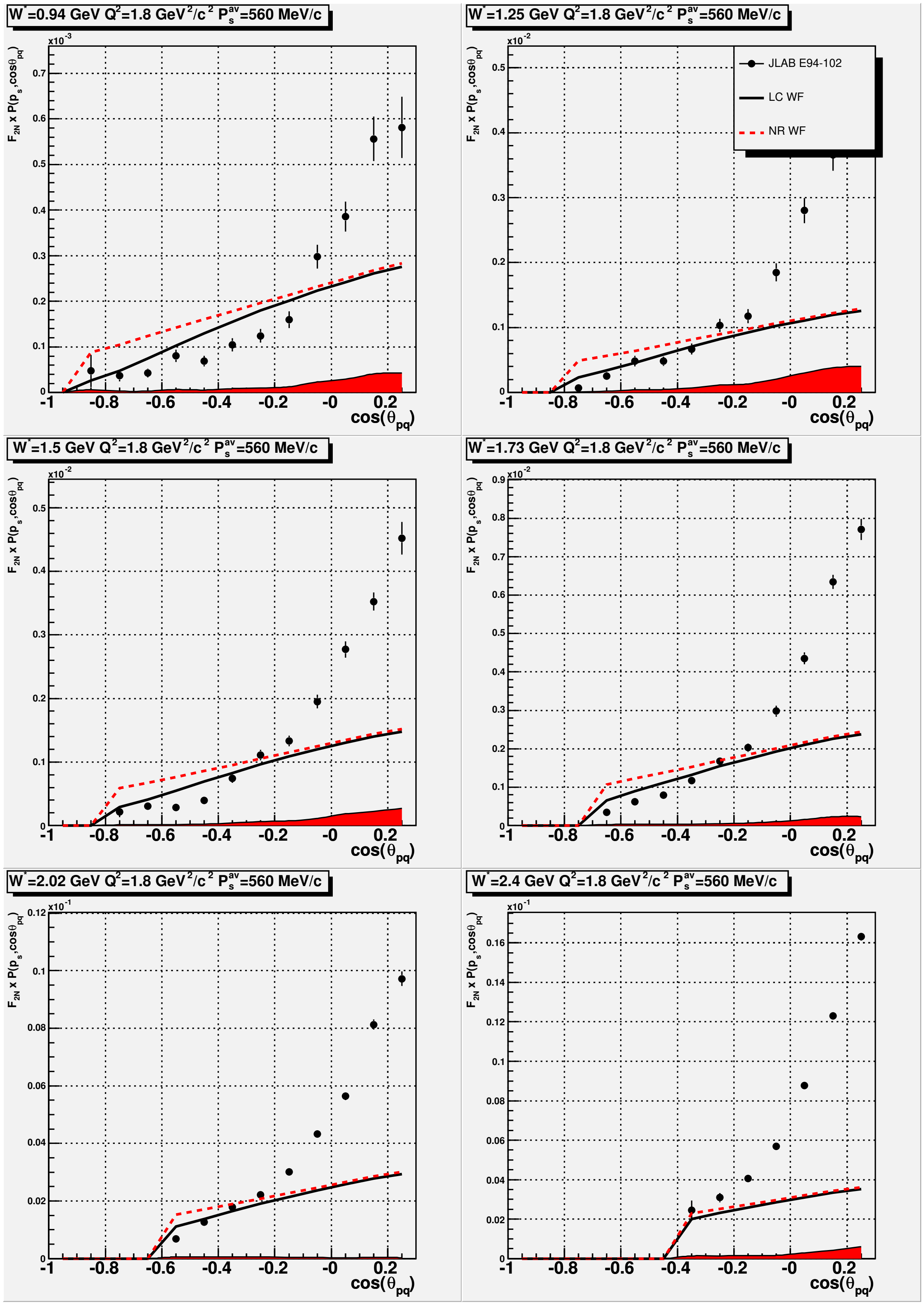

FIG. 135: The same as Fig. 127, but for the higher proton momentum p_s bin $(550 - 700$ MeV/c).

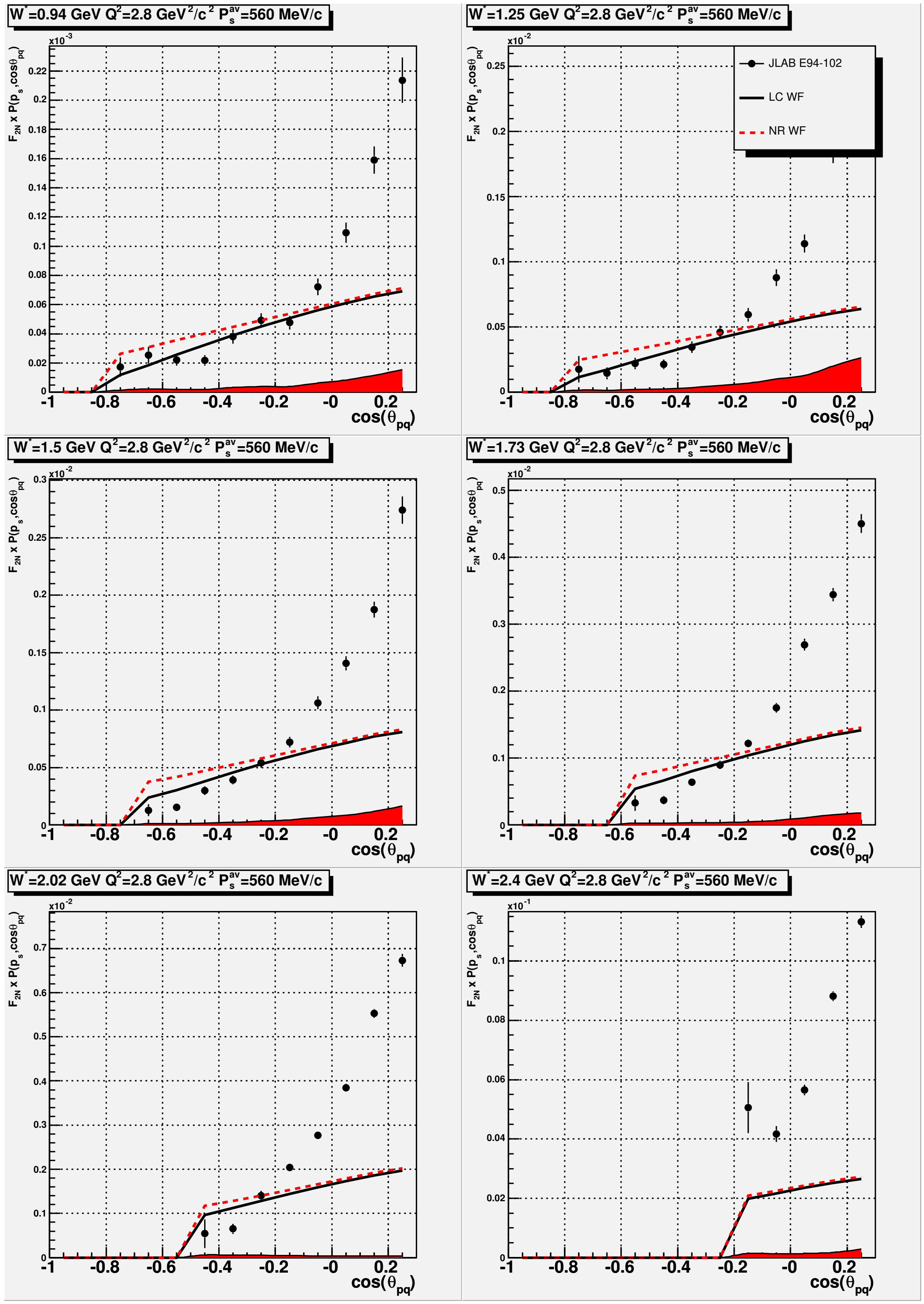

FIG. 136: The same as Fig. 135, but for the higher momentum transfer Q^2 bin $(2.1 - 5.0\ \mathrm{GeV}^2/\mathrm{c}^2)$.

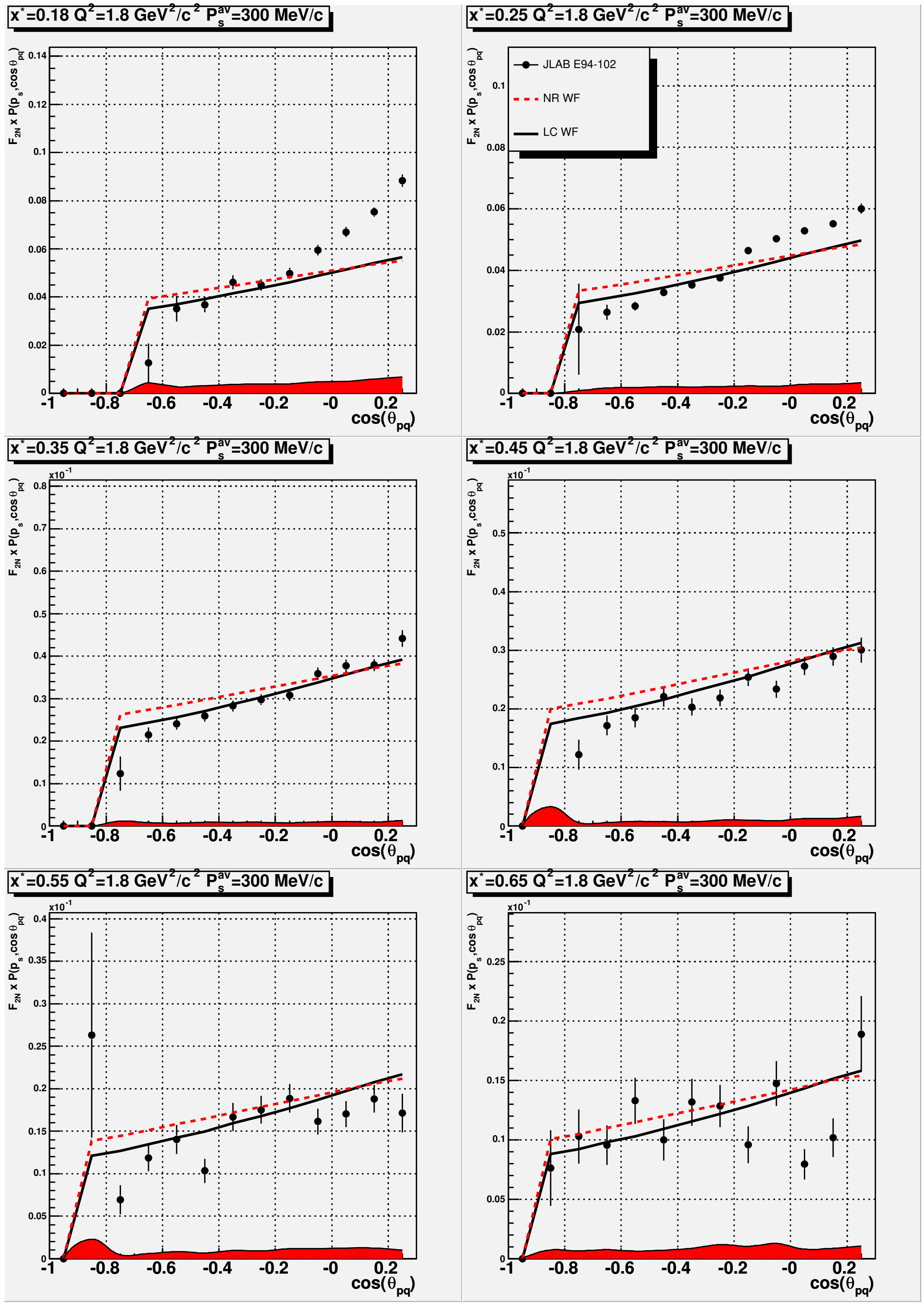

FIG. 137: $F_{2n}(x^*, Q^2)$ times $P(\vec{p_s})$ versus $\cos(\theta_{pq})$ for different ranges of the scaling variable x^*, for the lower Q^2 bin (1.2-2.1 $\mathrm{GeV}^2/\mathrm{c}^2$) and for the lowest proton momentum bin $(280 - 320\ \mathrm{MeV/c})$.

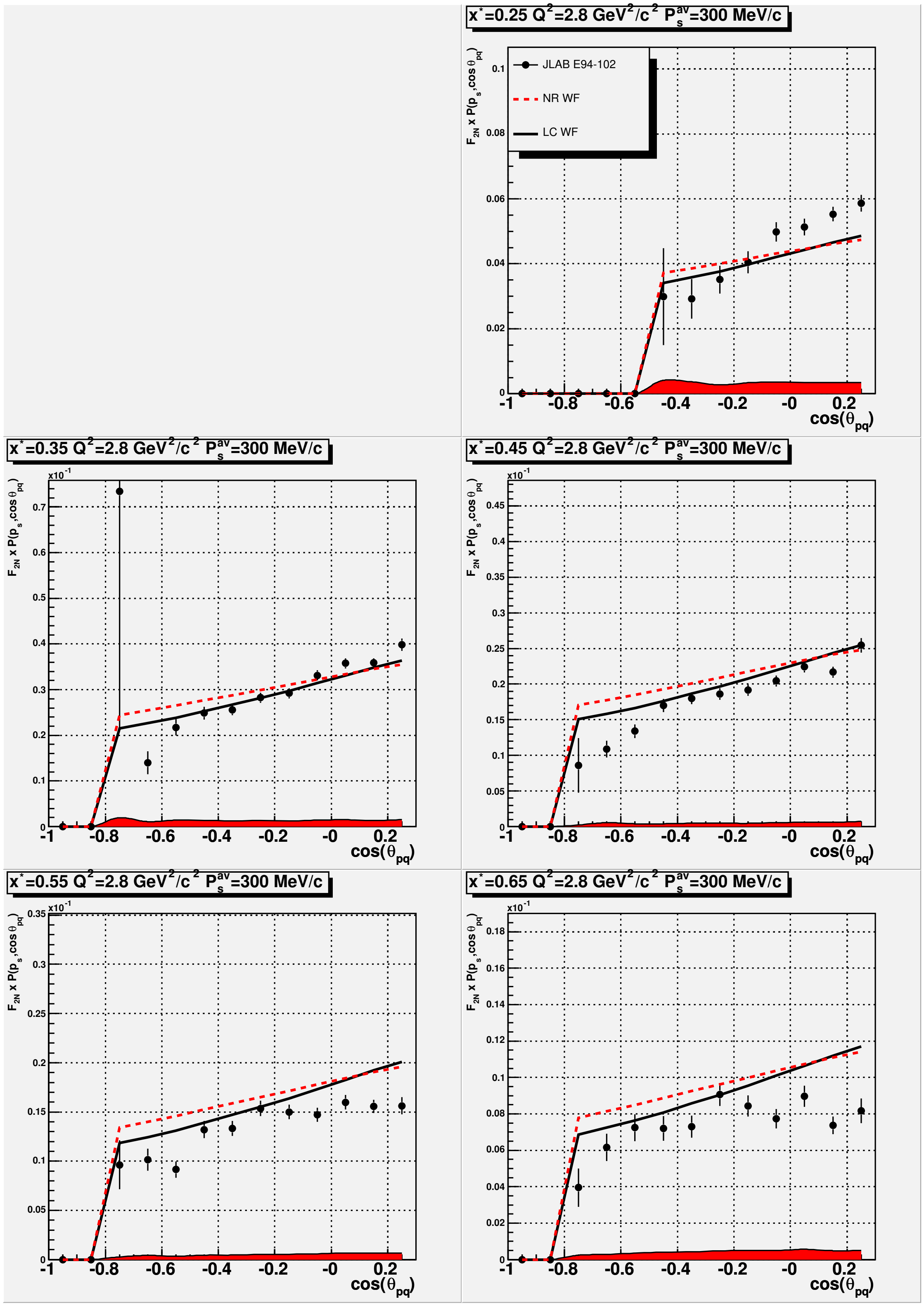

FIG. 138: The same as Fig. 137, but for the higher momentum transfer Q^2 bin $(2.1 - 5.0\ \mathrm{GeV}^2/\mathrm{c}^2)$.

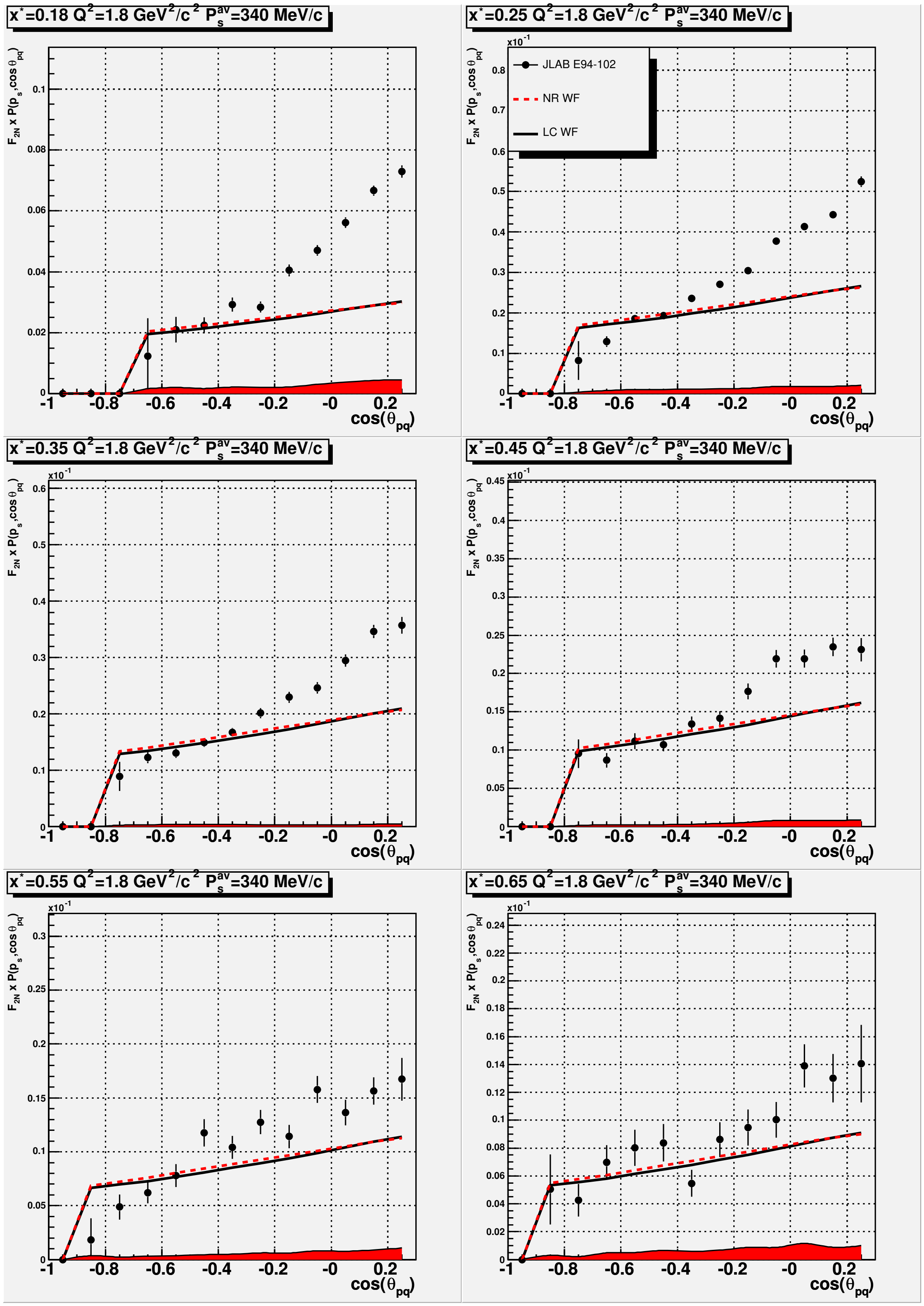

FIG. 139: The same as Fig. 137, but for the higher proton momentum p_s bin $(320 - 360$ MeV/c).

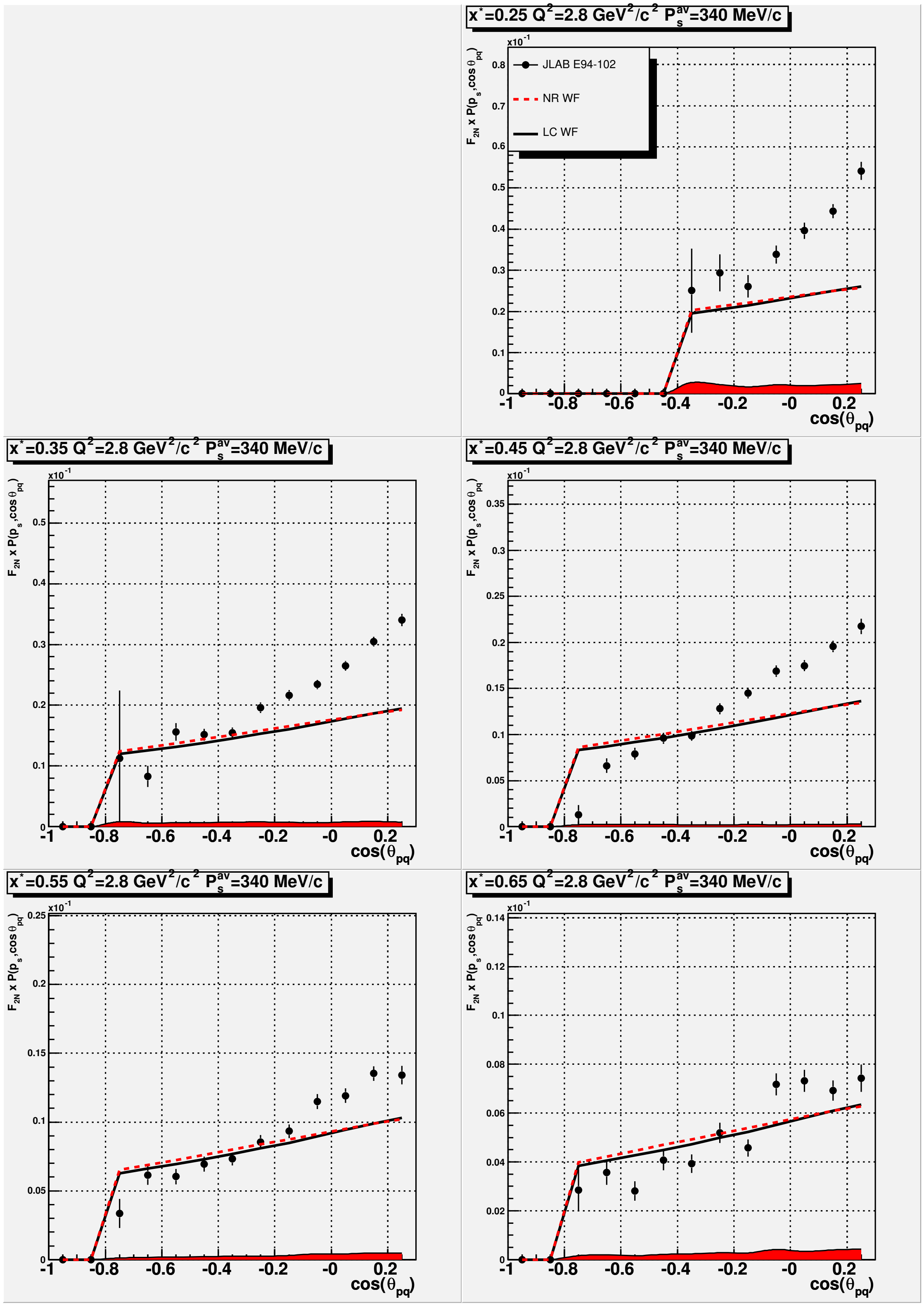

FIG. 140: The same as Fig. 139, but for the higher momentum transfer Q^2 bin $(2.1 - 5.0\ \mathrm{GeV}^2/\mathrm{c}^2)$.

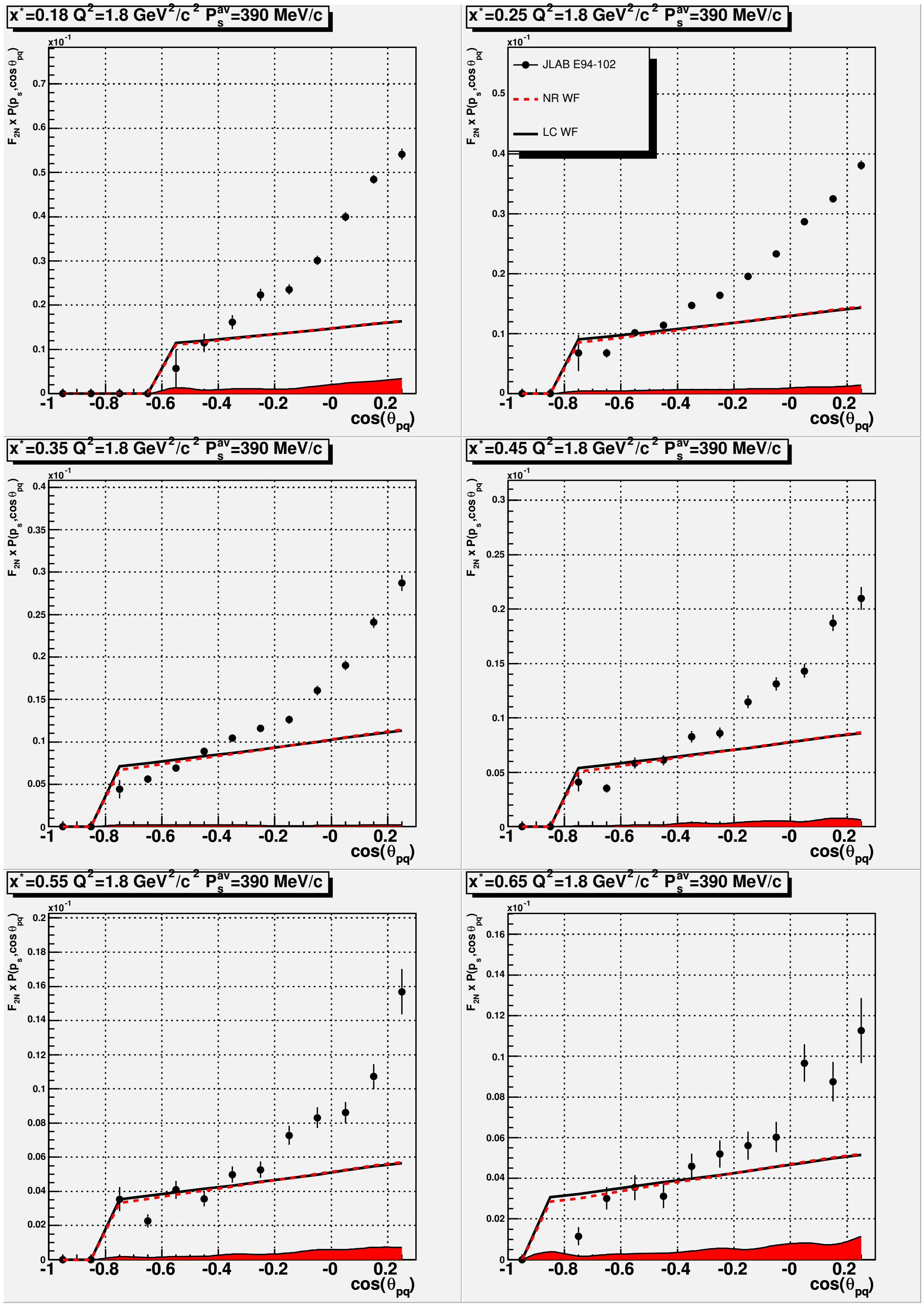

FIG. 141: The same as Fig. 137, but for the higher proton momentum p_s bin $(360 - 420$ MeV/c).

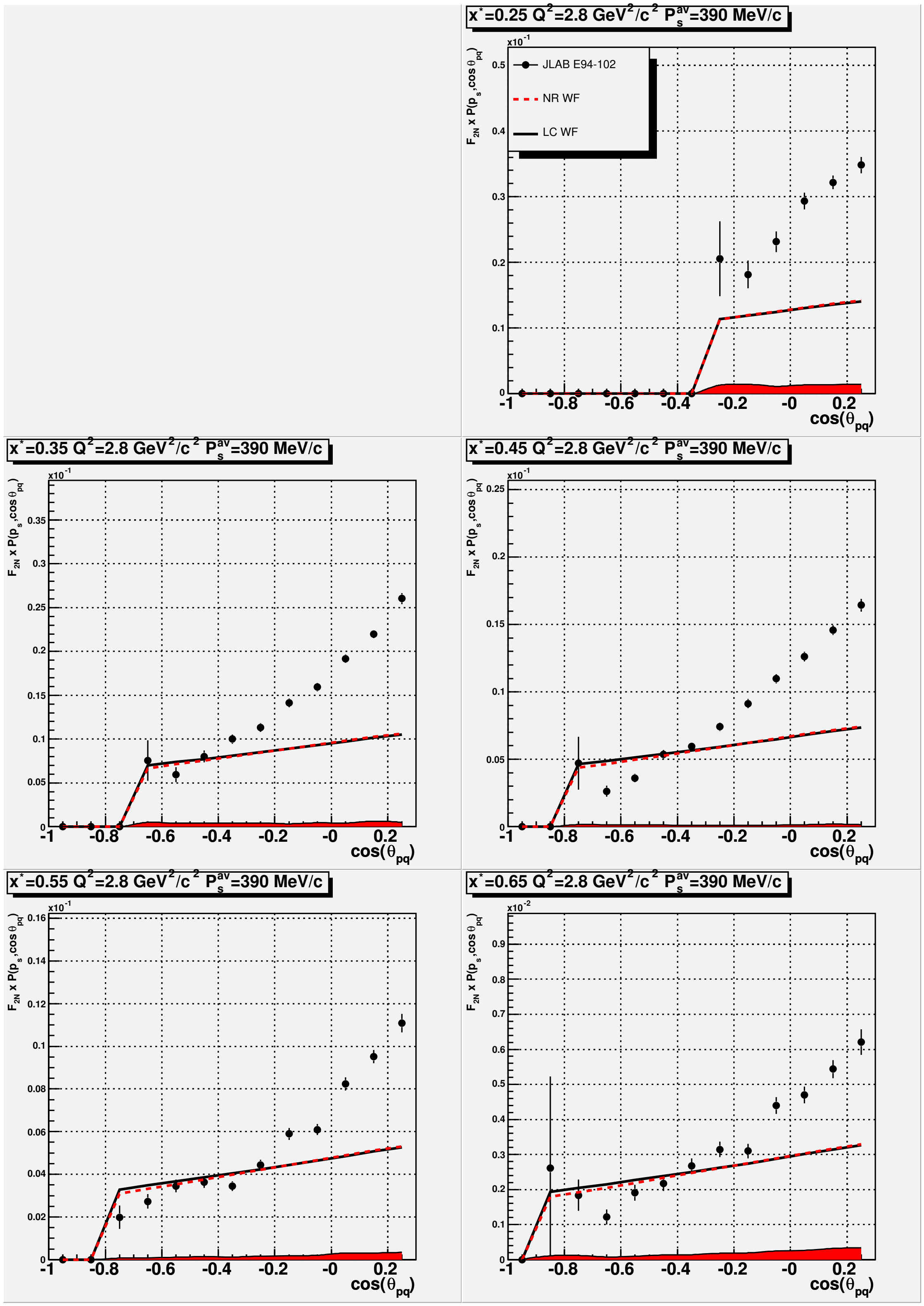

FIG. 142: The same as Fig. 141, but for the higher momentum transfer Q^2 bin $(2.1 - 5.0\ \mathrm{GeV}^2/c^2)$.

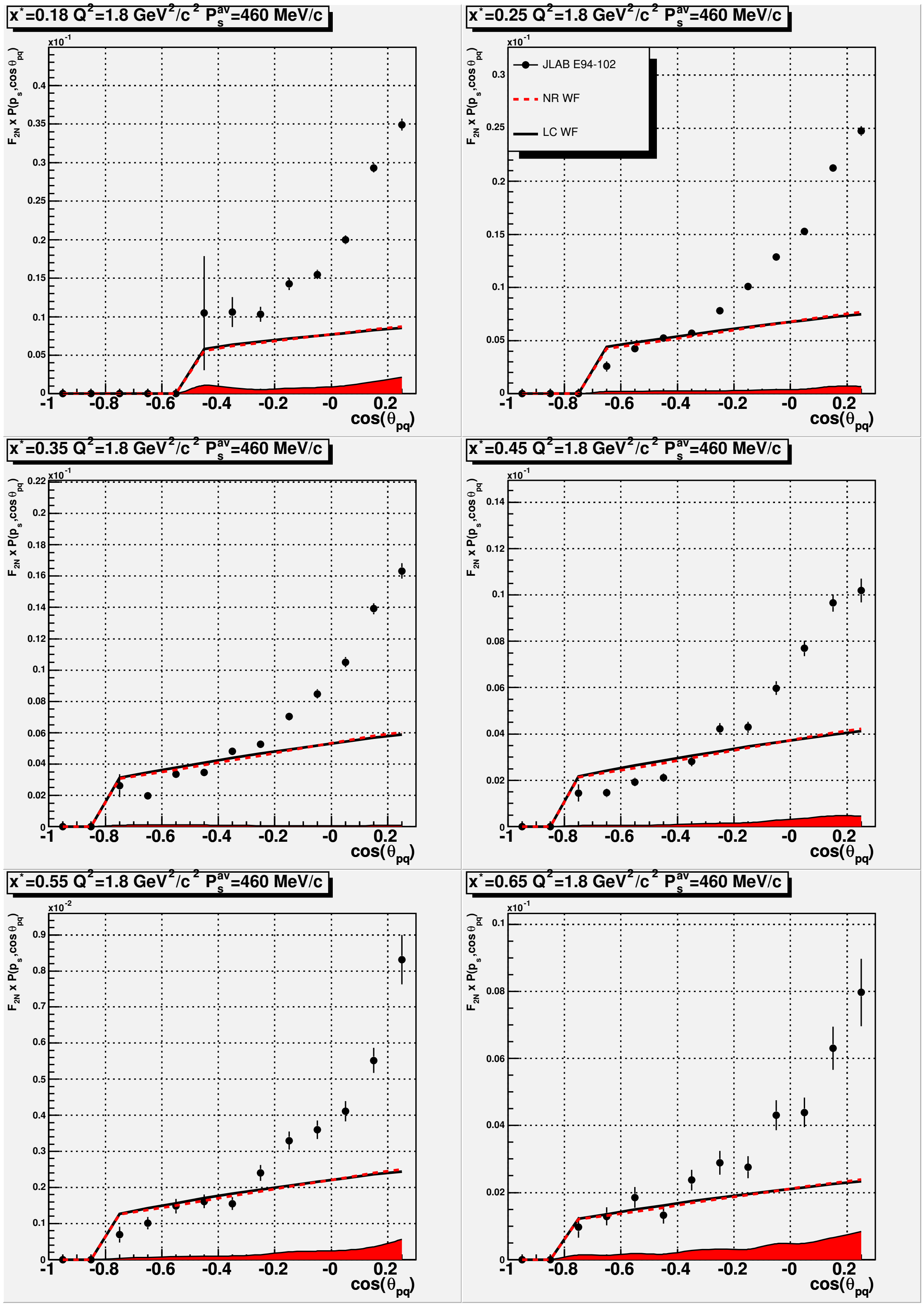

FIG. 143: The same as Fig. 137, but for the higher proton momentum p_s bin $(420 - 550$ MeV/c).

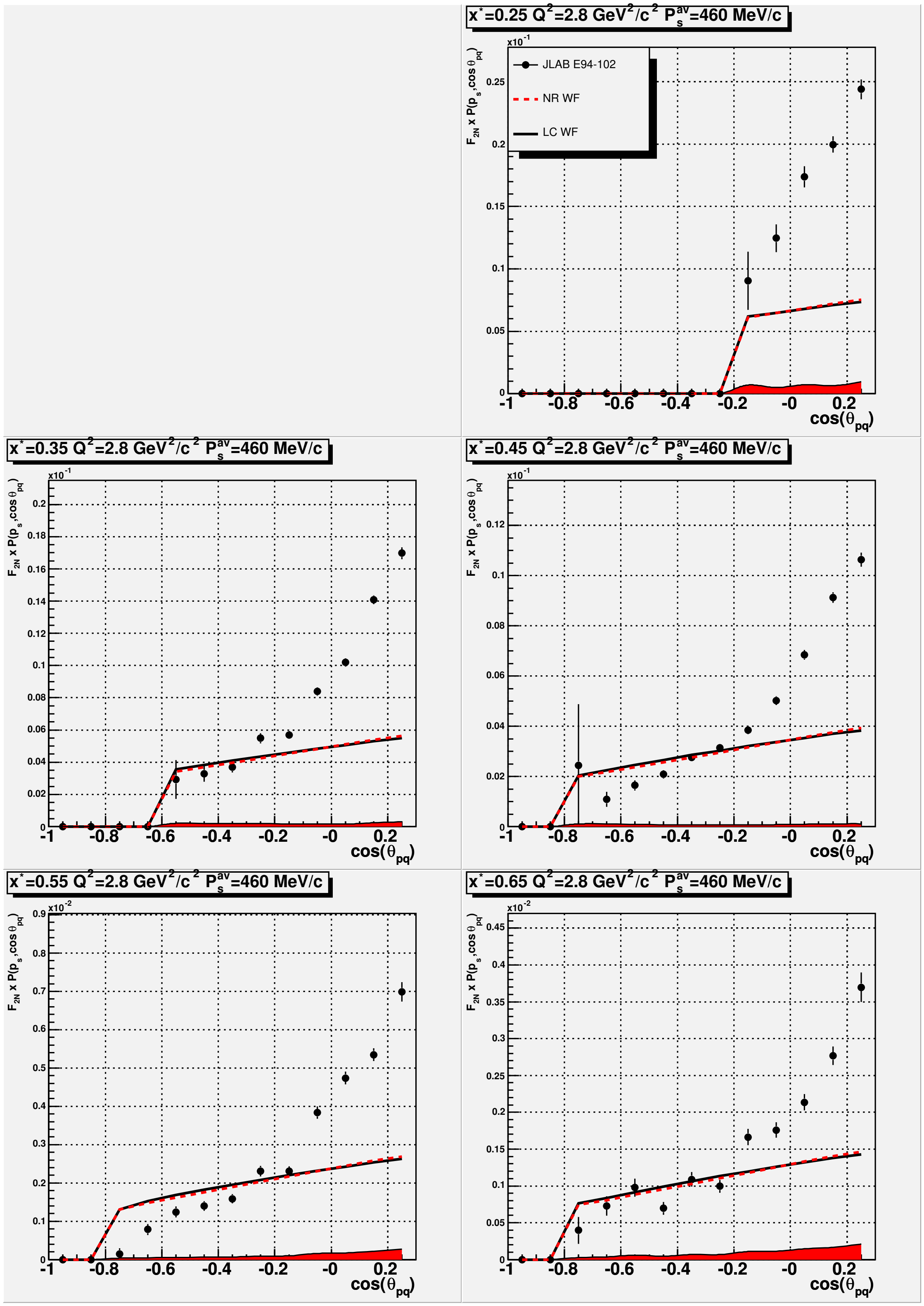

FIG. 144: The same as Fig. 143, but for the higher momentum transfer Q^2 bin $(2.1 - 5.0\ \mathrm{GeV}^2/\mathrm{c}^2)$.

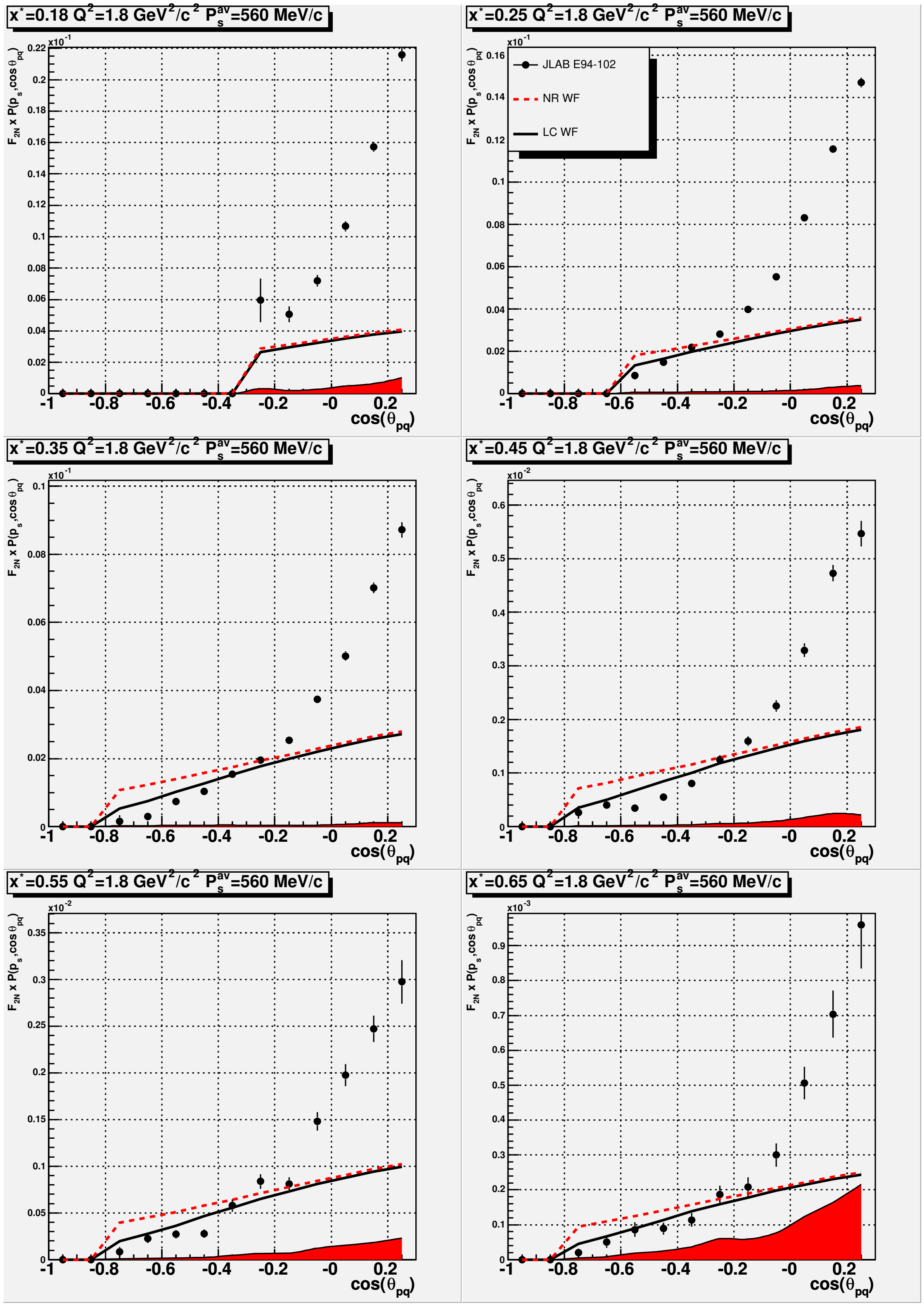

FIG. 145: The same as Fig. 137, but for the higher proton momentum p_s bin ($550 - 700$ MeV/c).

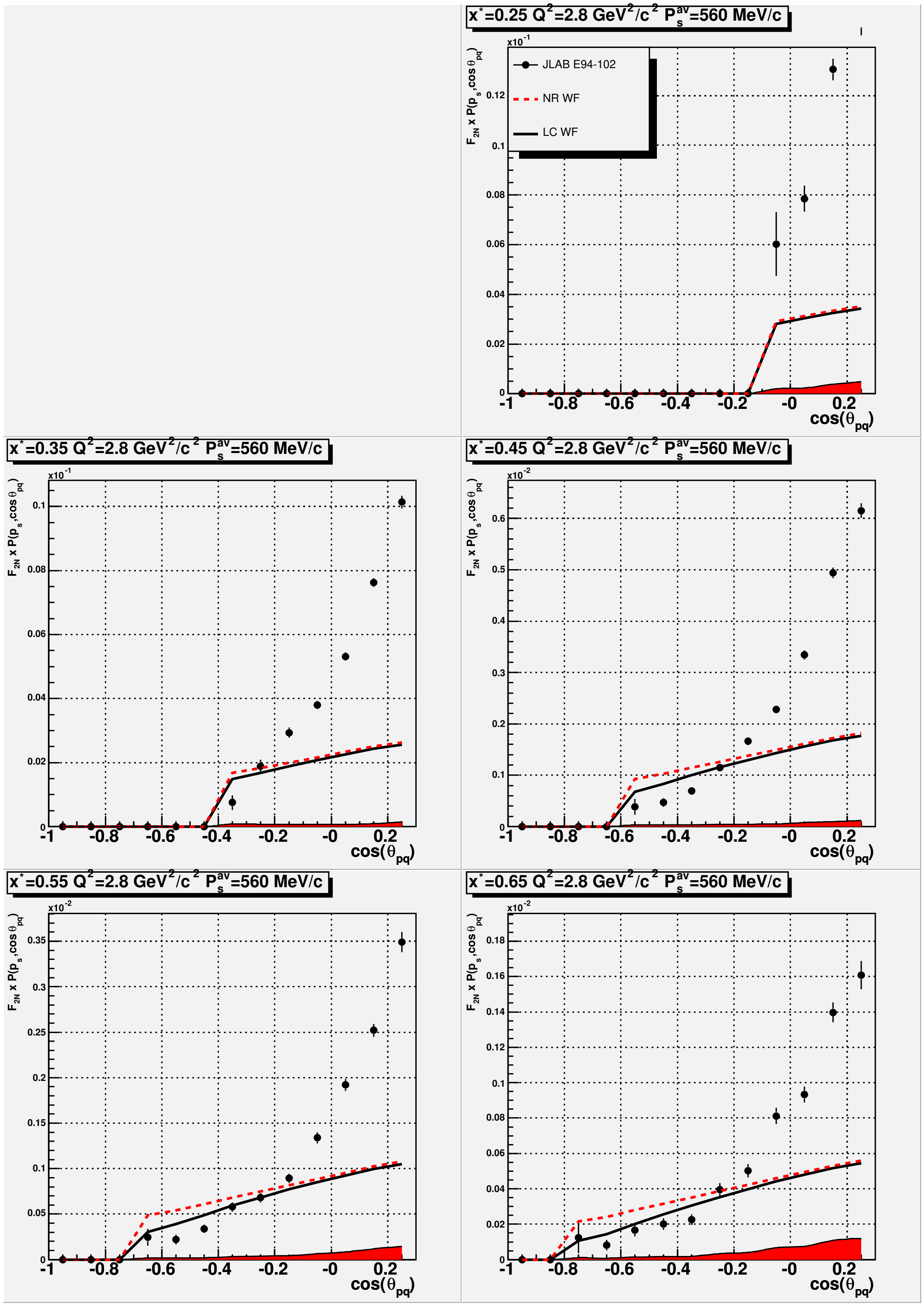

FIG. 146: The same as Fig. 145, but for the higher momentum transfer Q^2 bin $(2.1 - 5.0\ \mathrm{GeV}^2/\mathrm{c}^2)$.

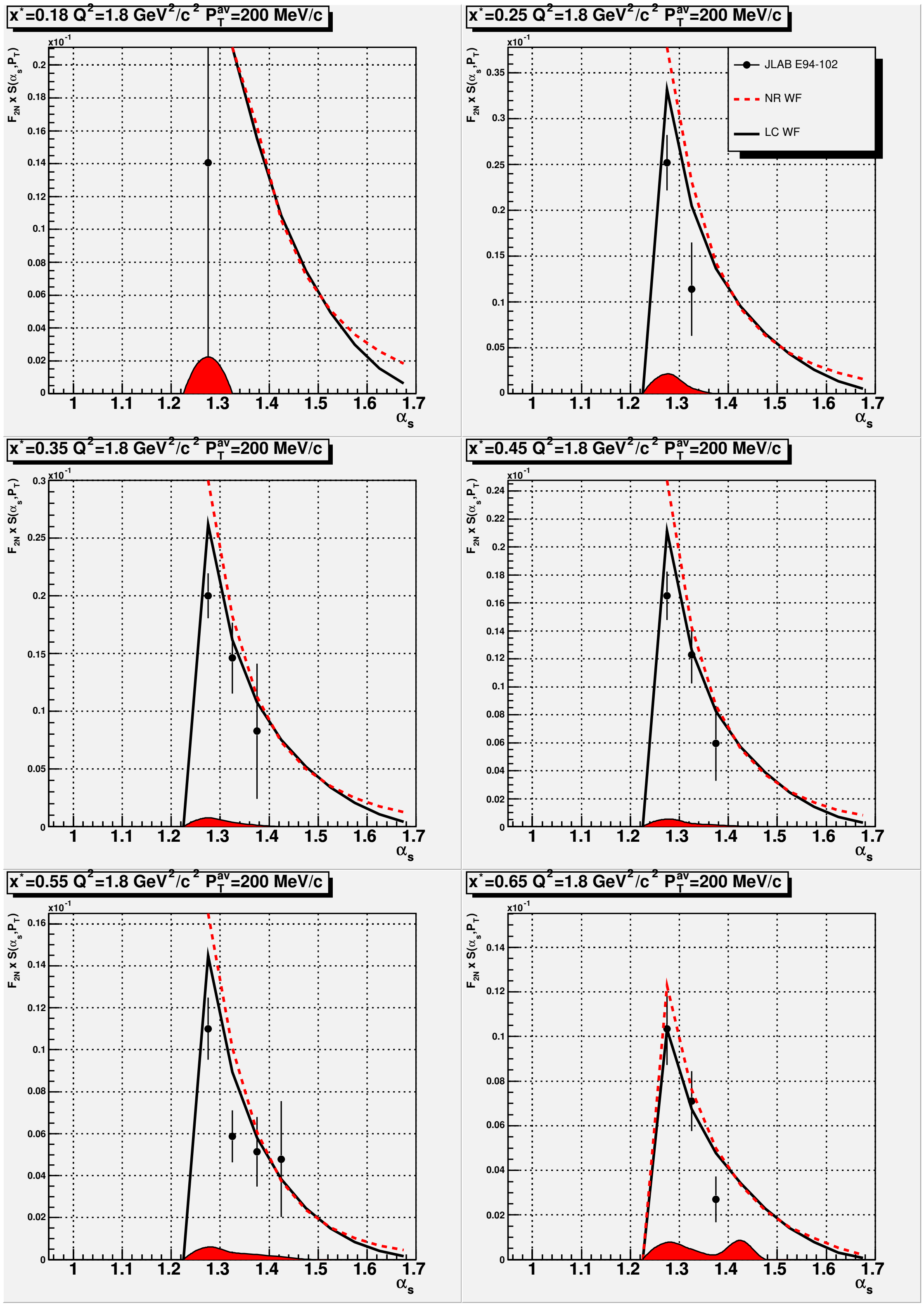

FIG. 147: $F_{2n}(x^*, Q^2)$ times $S(\alpha_s, p_T)$ versus α_s for different ranges of the scaling variable x^*, for the lower Q^2 bin (1.2-2.1 GeV^2/c^2) and for the lowest proton transverse momentum bin $(150 - 250\ \text{MeV/c})$.

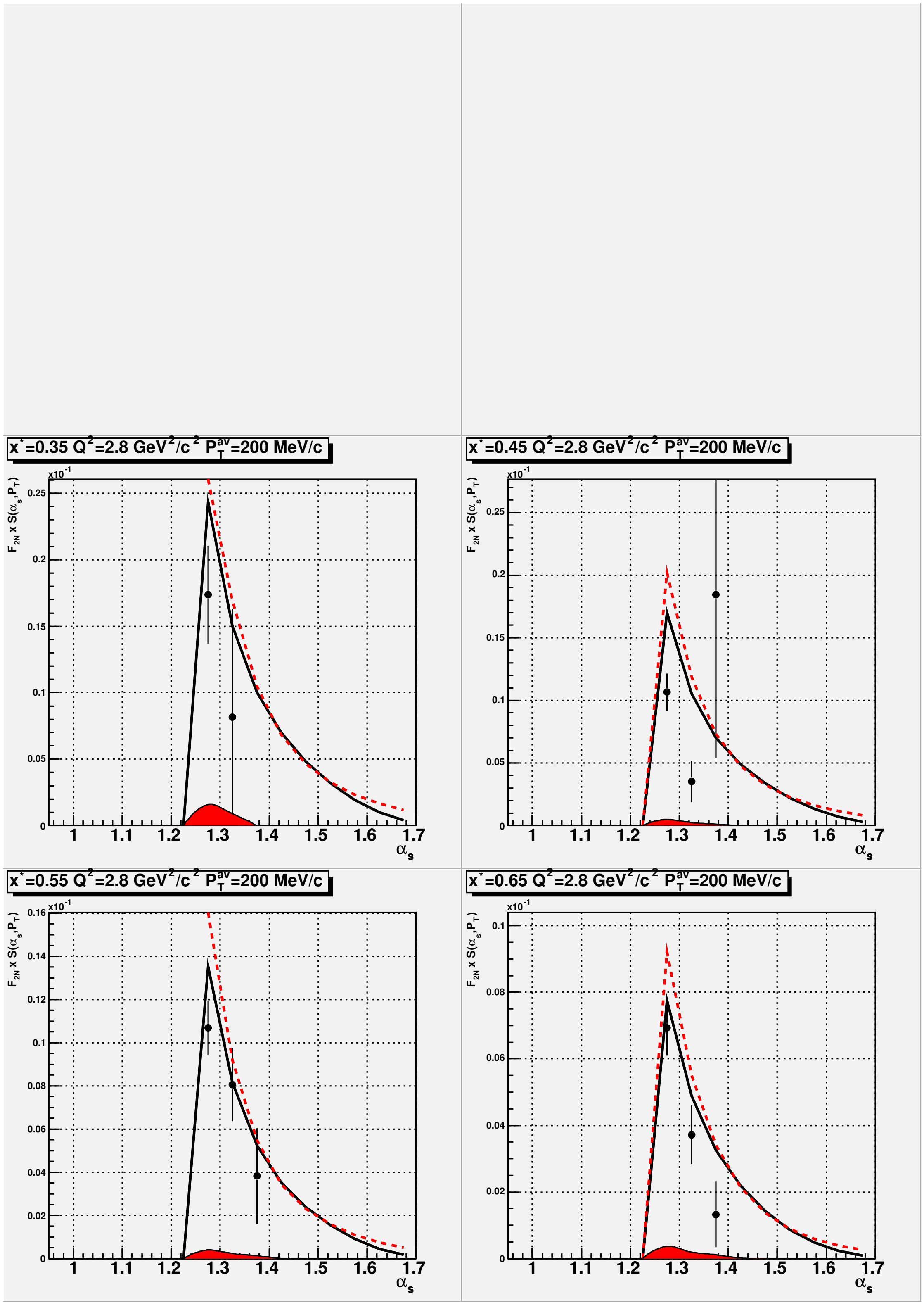

FIG. 148: The same as Fig. 147, but for the higher momentum transfer Q^2 bin $(2.1 - 5.0\ \mathrm{GeV}^2/\mathrm{c}^2)$.

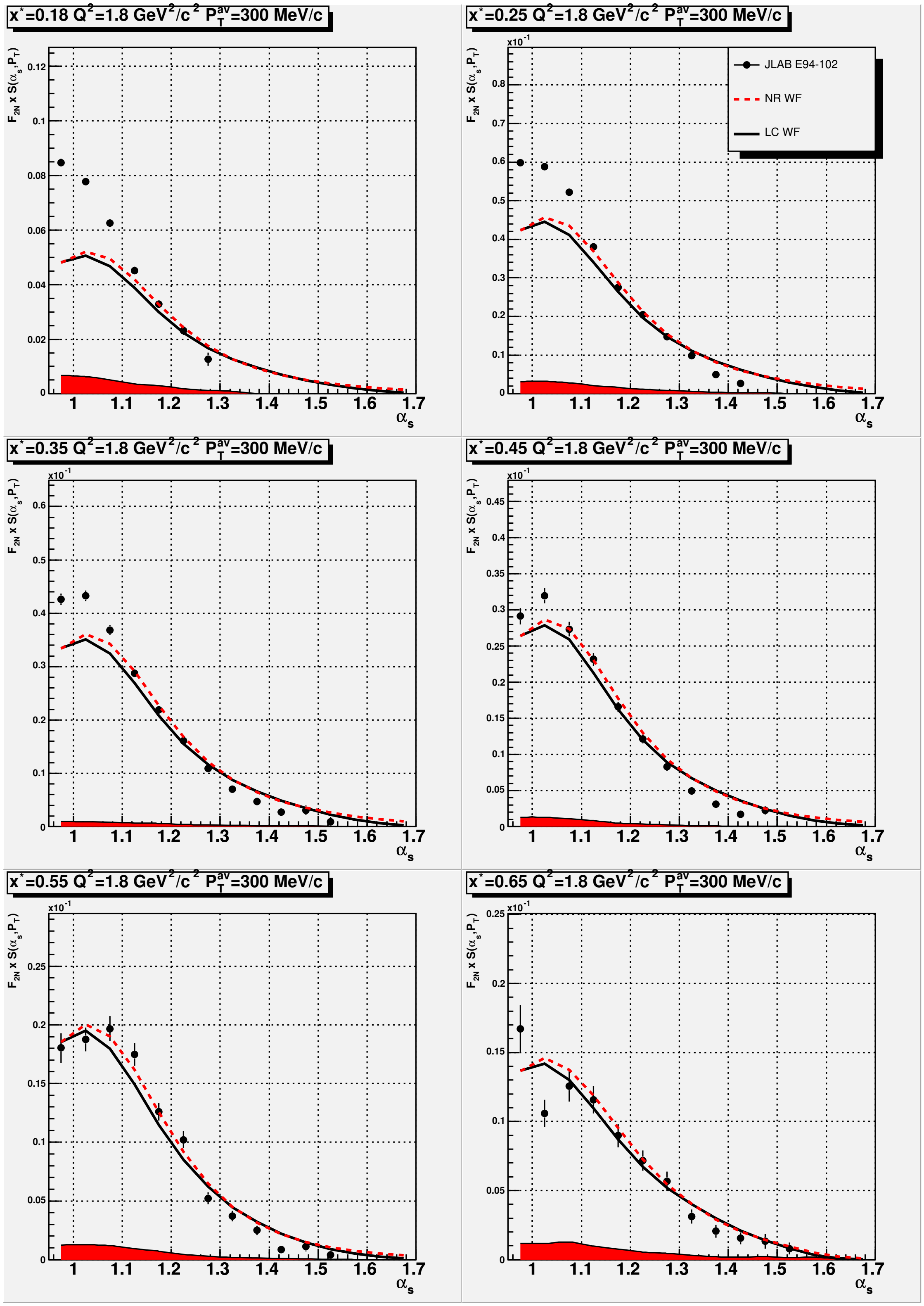

FIG. 149: The same as Fig. 147, but for the higher proton transverse momentum p_T bin $(250 - 350$ MeV/c).

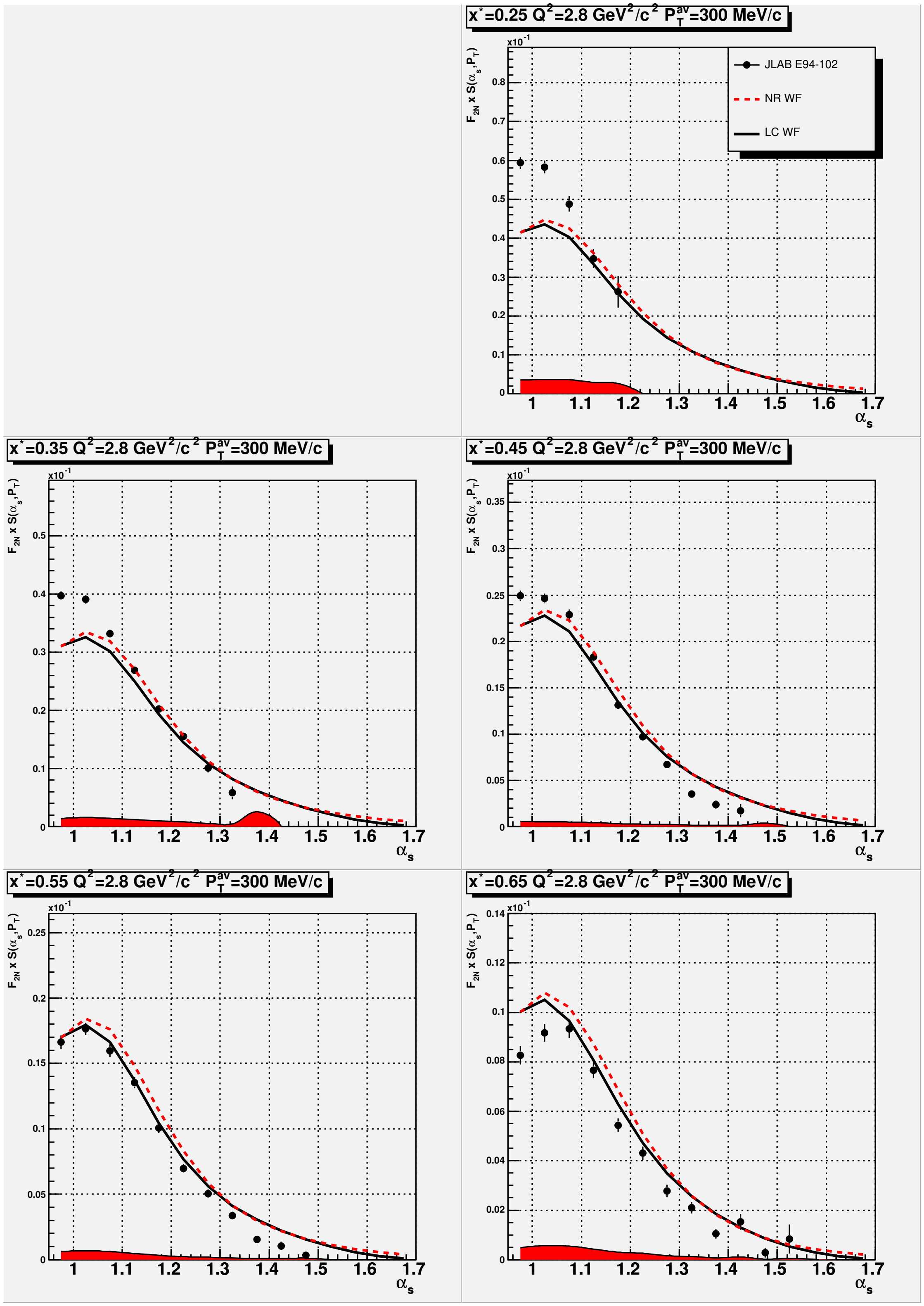

FIG. 150: The same as Fig. 149, but for the higher momentum transfer Q^2 bin ($2.1 - 5.0$ GeV^2/c^2).

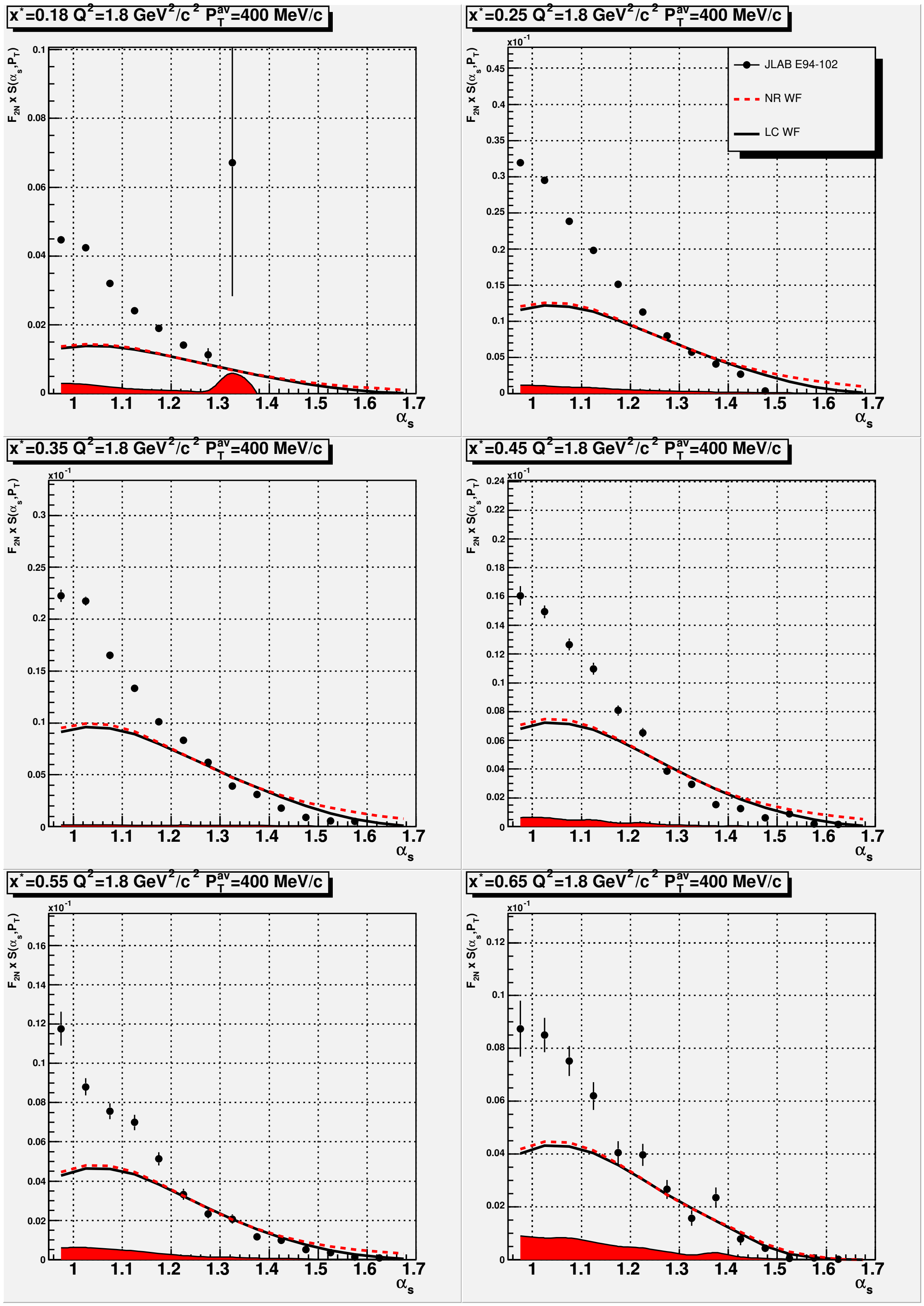

FIG. 151: The same as Fig. 147, but for the higher proton transverse momentum p_T bin $(350 - 450$ MeV/c).

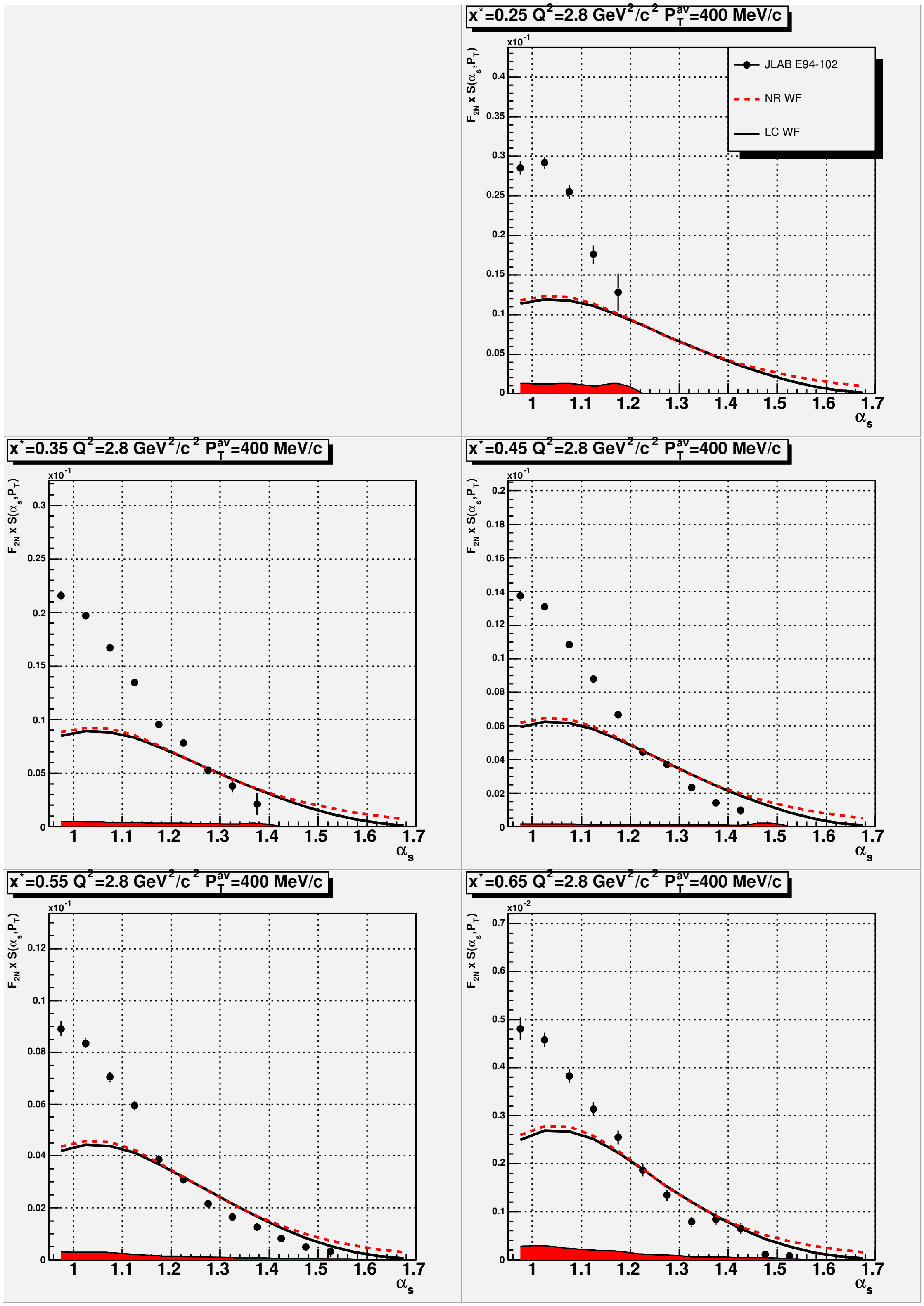

FIG. 152: The same as Fig. 151, but for the higher momentum transfer Q^2 bin $(2.1 - 5.0\ \mathrm{GeV}^2/\mathrm{c}^2)$.

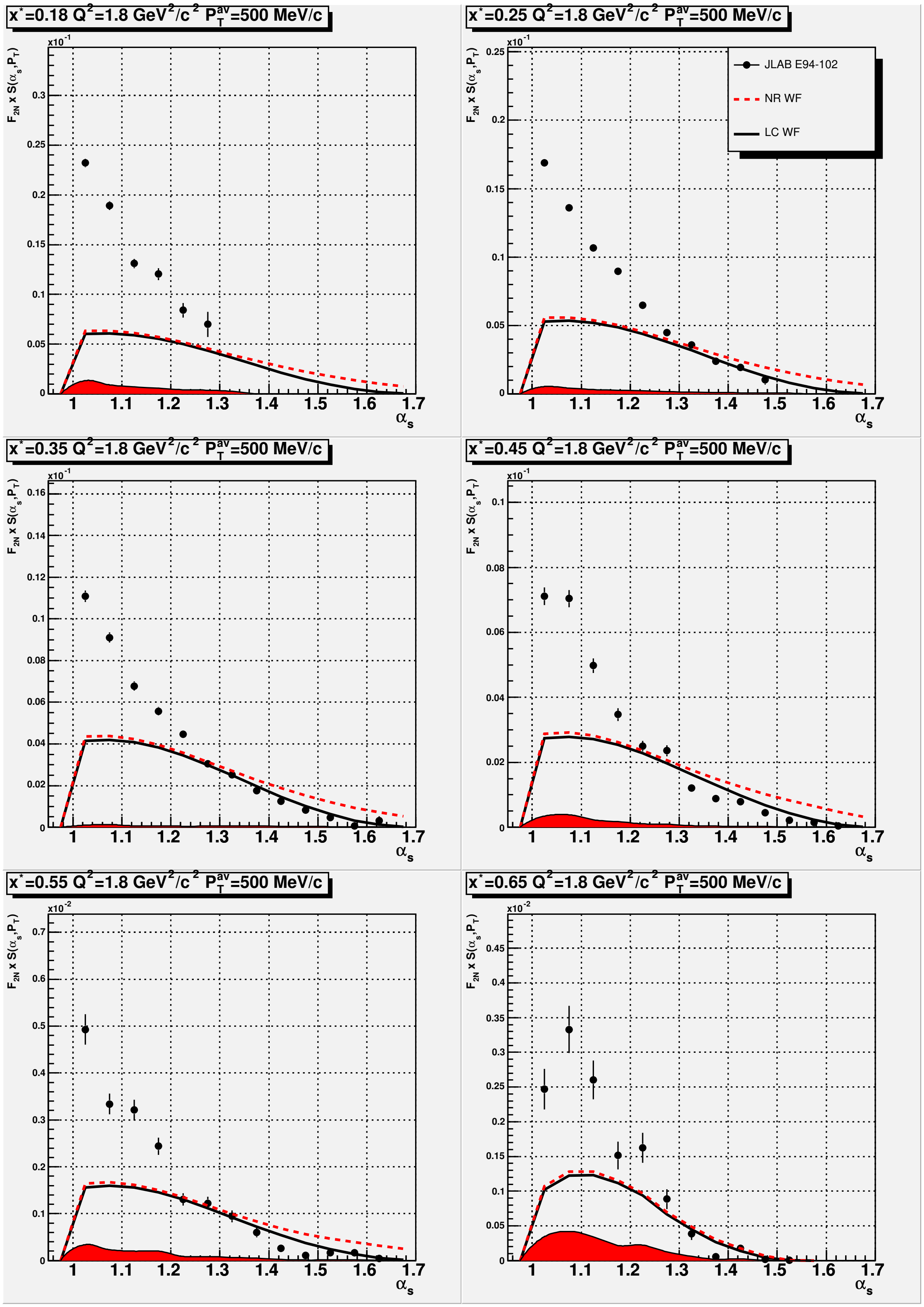

FIG. 153: The same as Fig. 147, but for the higher proton transverse momentum p_T bin $(450 - 550$ MeV/c).

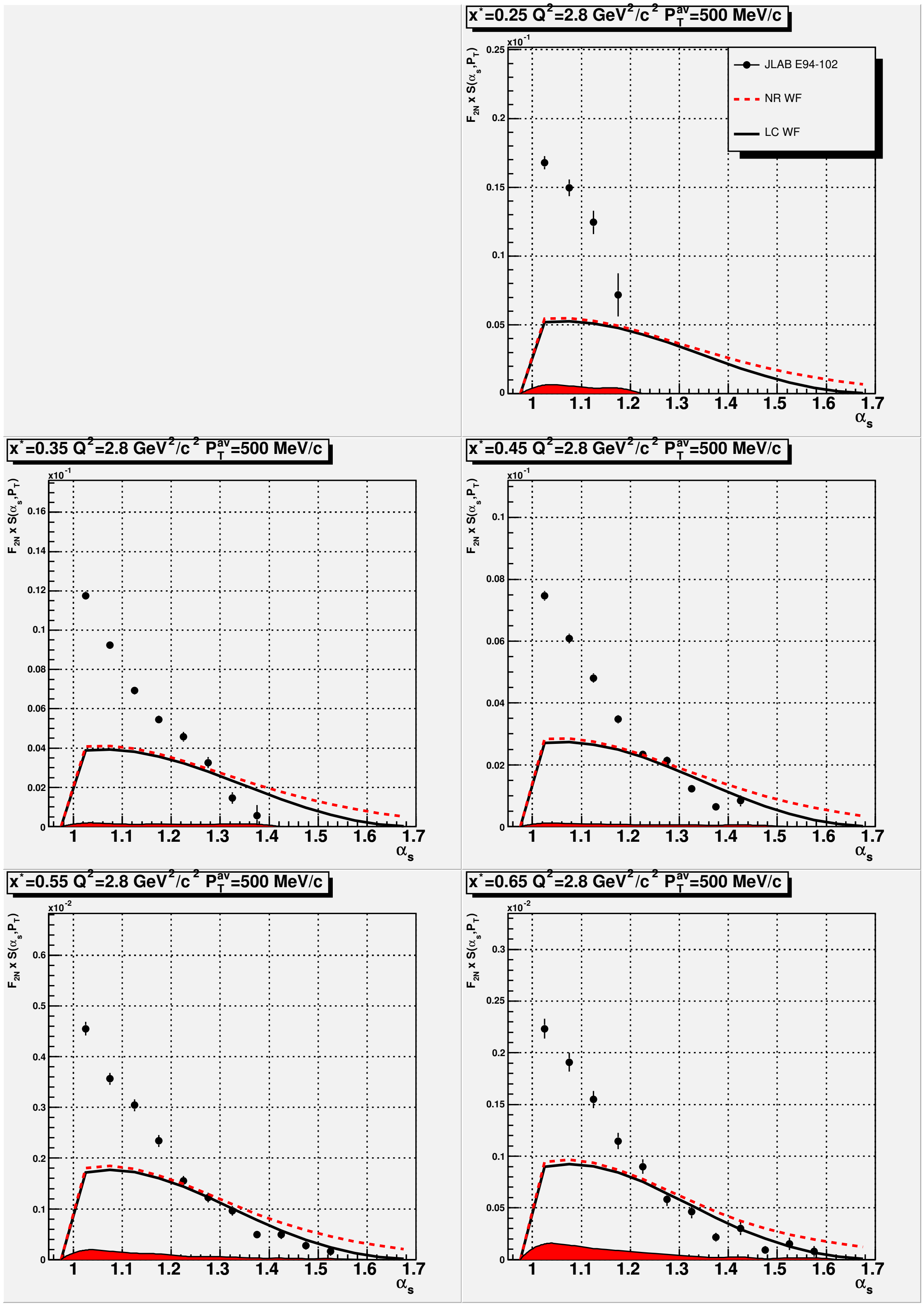

FIG. 154: The same as Fig. 153, but for the higher momentum transfer Q^2 bin $(2.1 - 5.0\ \mathrm{GeV}^2/\mathrm{c}^2)$.

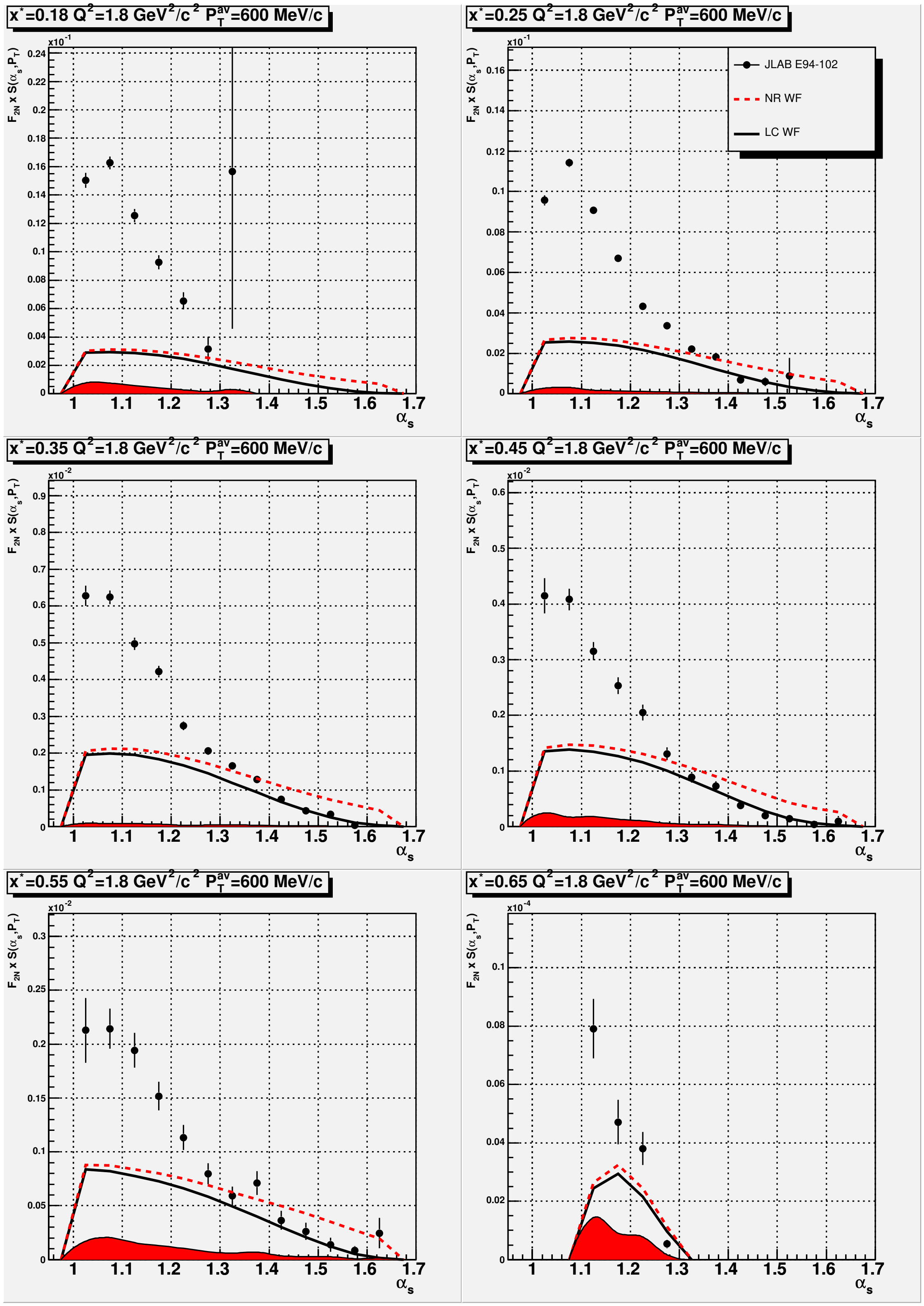

FIG. 155: The same as Fig. 147, but for the higher proton transverse momentum p_T bin ($550-650$ MeV/c).

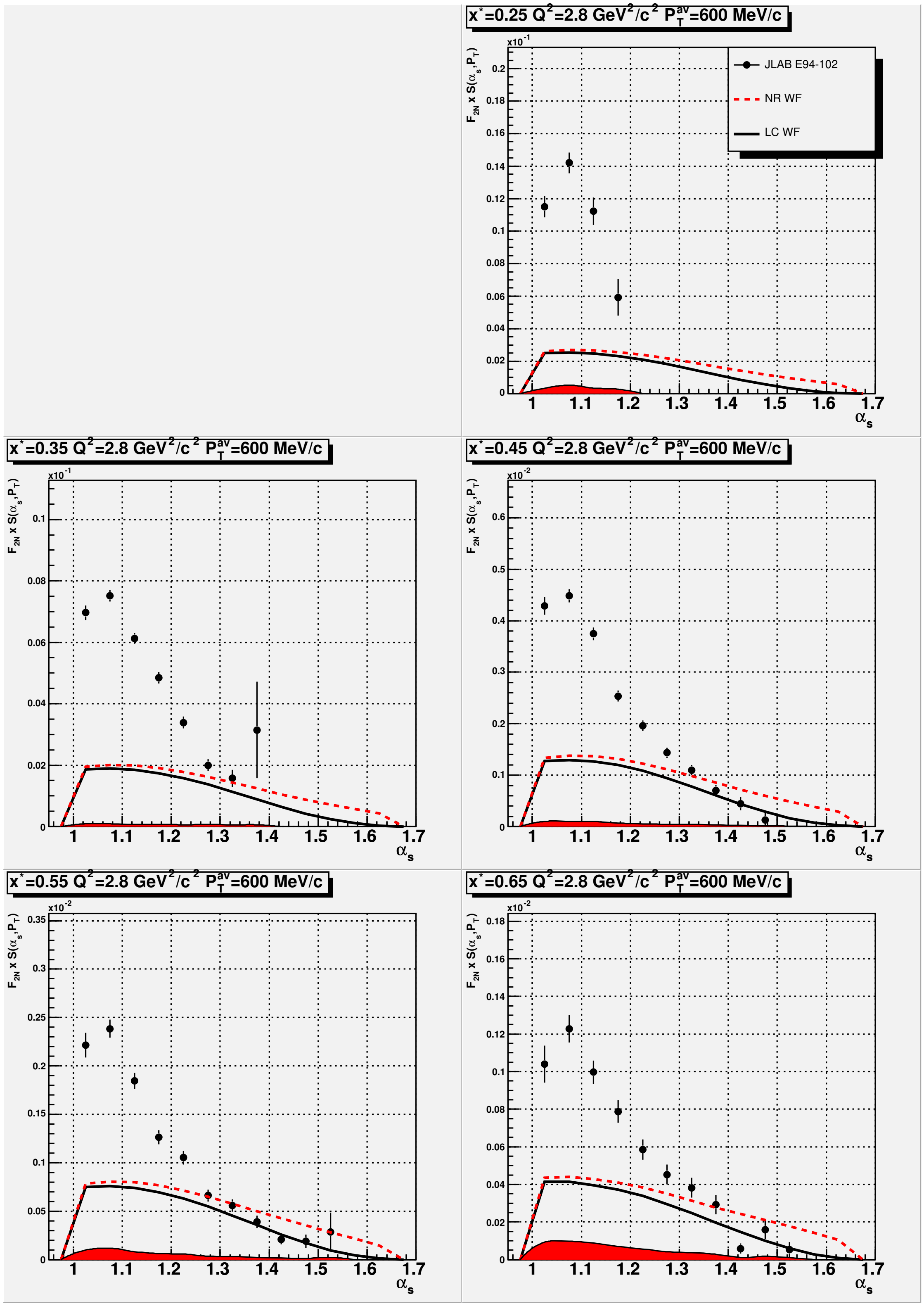

FIG. 156: The same as Fig. 155, but for the higher momentum transfer Q^2 bin $(2.1 - 5.0\ \mathrm{GeV}^2/\mathrm{c}^2)$.

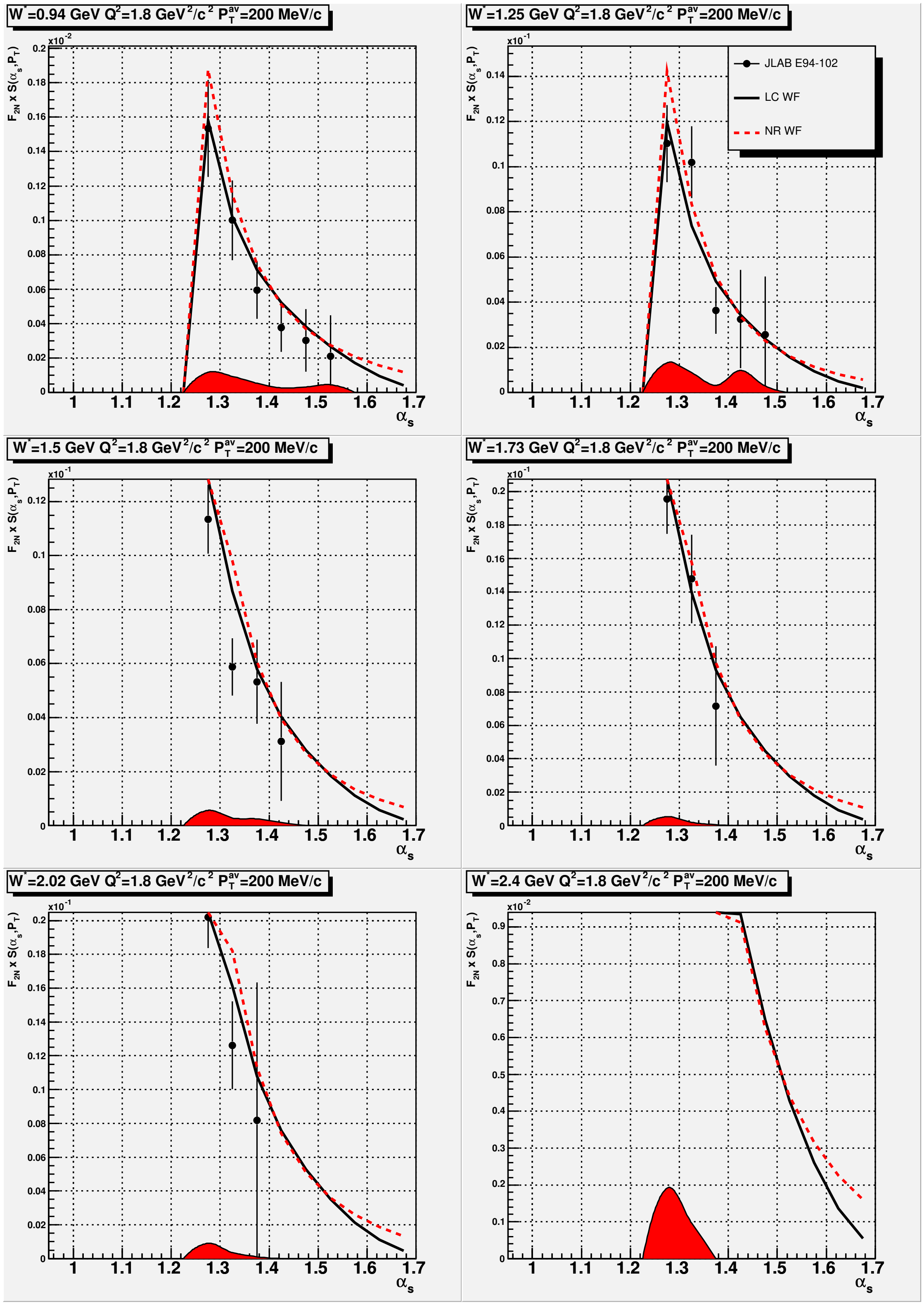

FIG. 157: $F_{2n}(W^*, Q^2)$ times $S(\alpha_s, p_T)$ versus α_s for different ranges of the invariant mass W^*, for lower Q^2 bin (1.2-2.1 GeV^2/c^2) and for the lowest proton transverse momentum bin $(150 - 250\ \text{MeV/c})$.

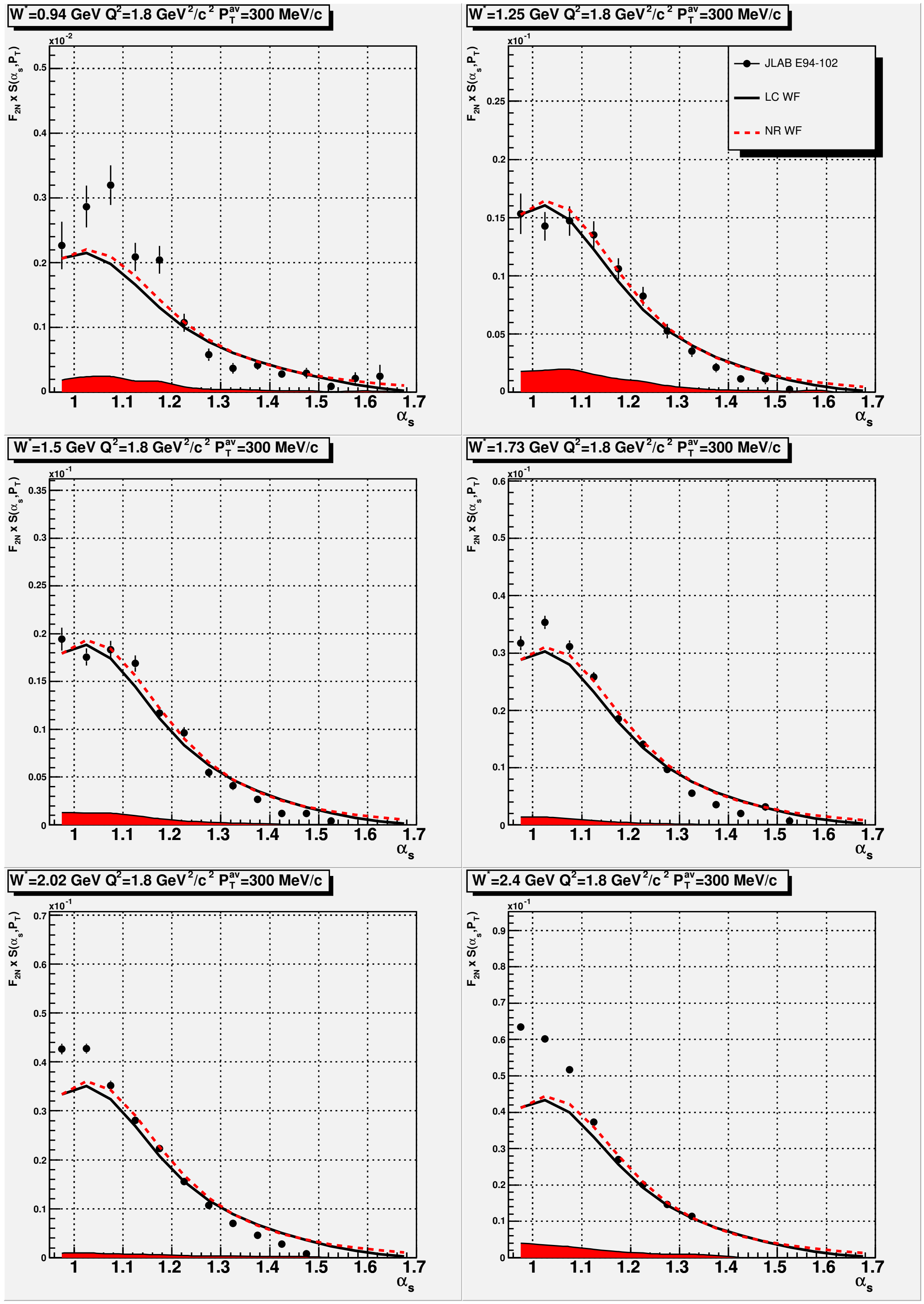

FIG. 158: The same as Fig. 157, but for the higher proton transverse momentum p_T bin $(250 - 350$ MeV/c).

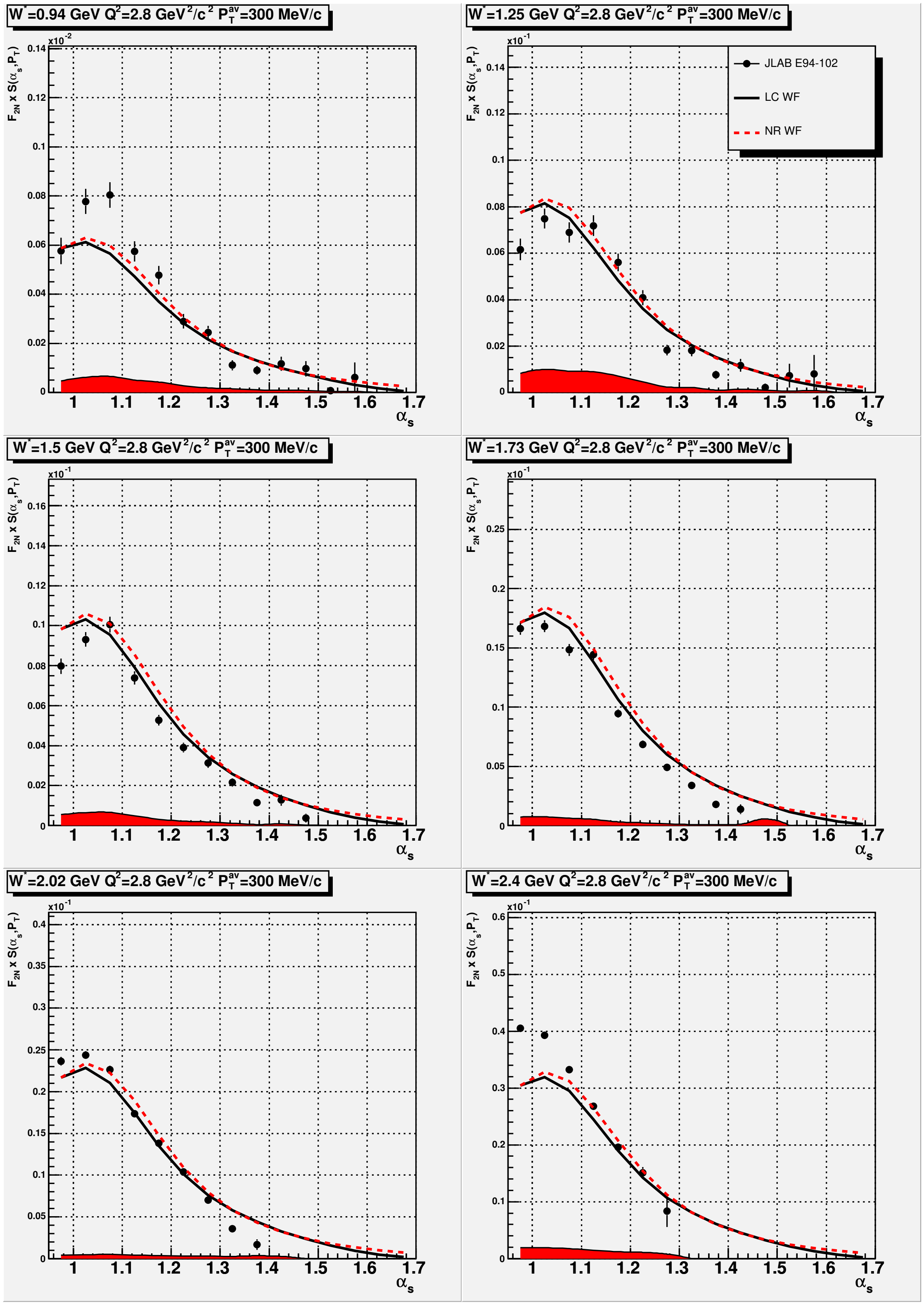

FIG. 159: The same as Fig. 158, but for the higher momentum transfer Q^2 bin $(2.1 - 5.0\ \mathrm{GeV}^2/\mathrm{c}^2)$.

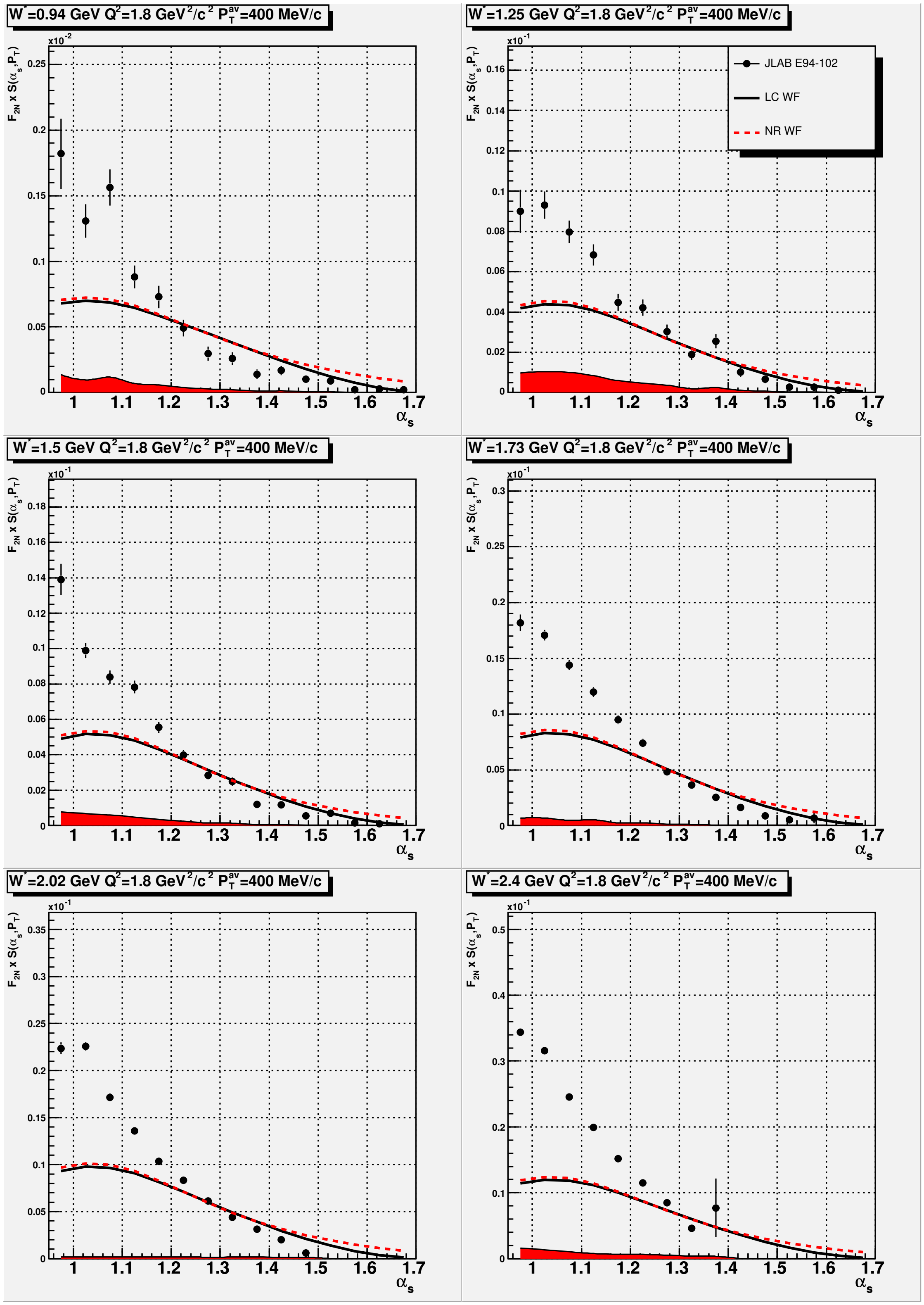

FIG. 160: The same as Fig. 157, but for the higher proton transverse momentum p_T bin $(350 - 450$ MeV/c).

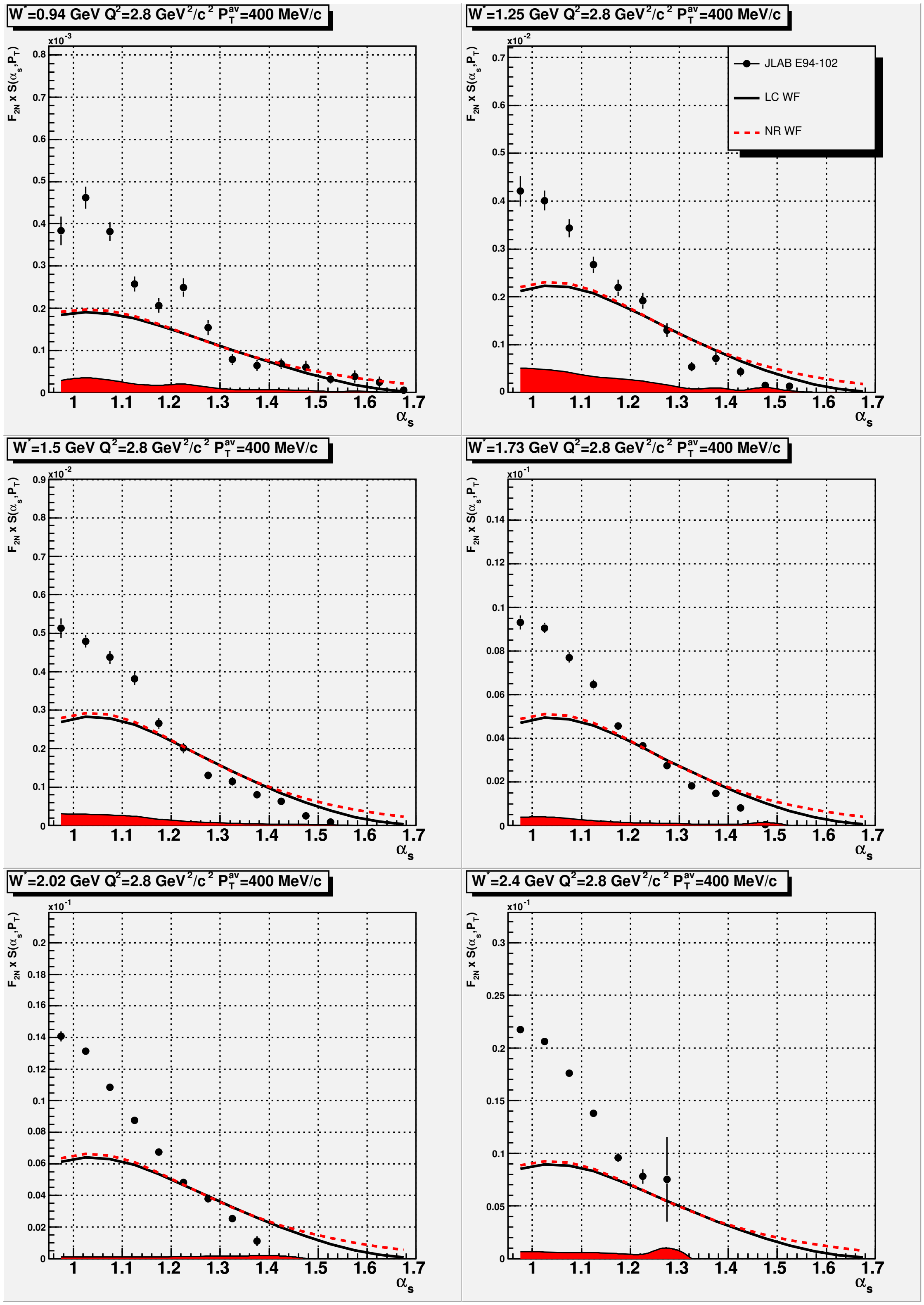

FIG. 161: The same as Fig. 160, but for the higher momentum transfer Q^2 bin $(2.1 - 5.0\ \mathrm{GeV}^2/\mathrm{c}^2)$.

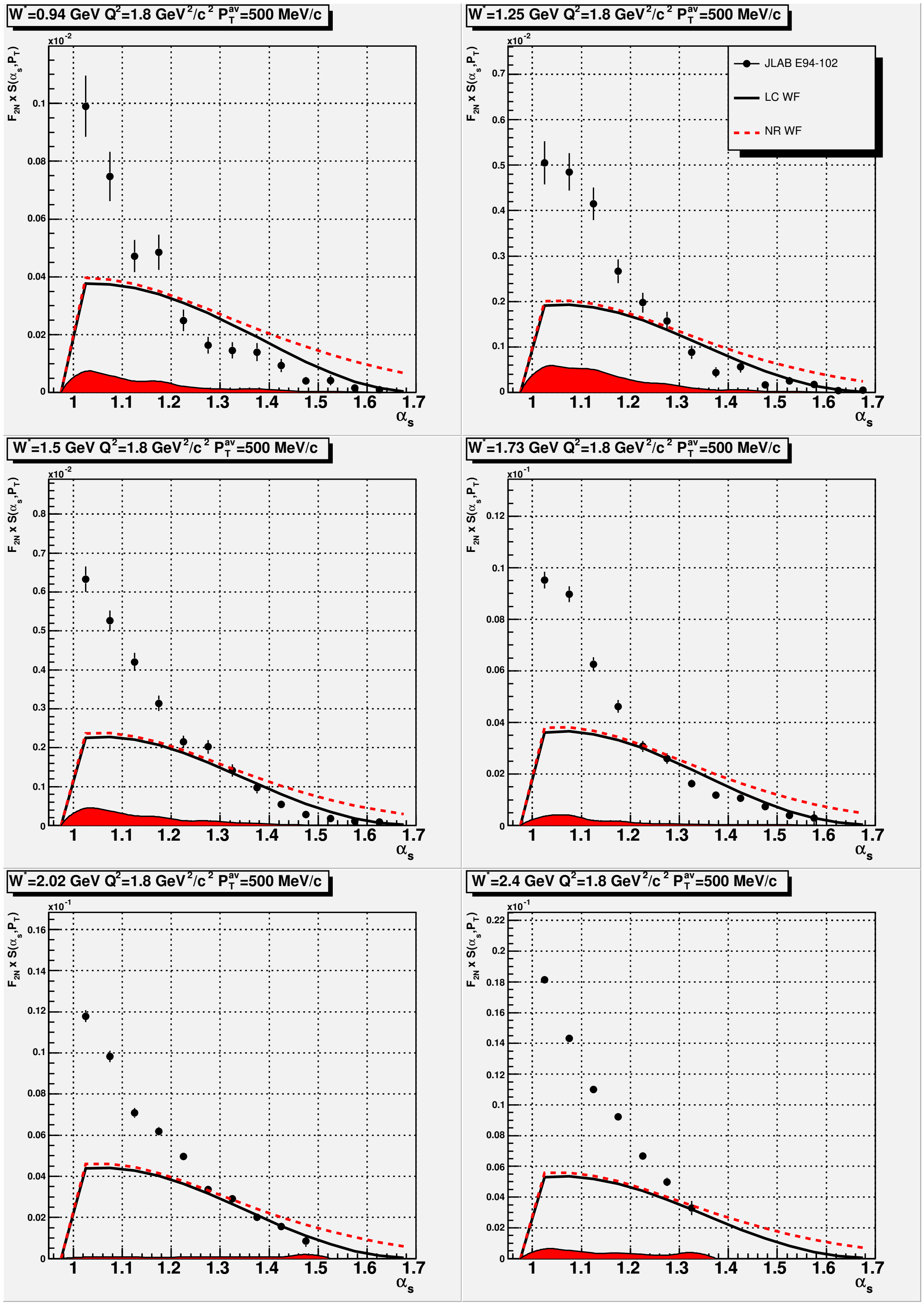

FIG. 162: The same as Fig. 157, but for the higher proton transverse momentum p_T bin $(450 - 550$ MeV/c).

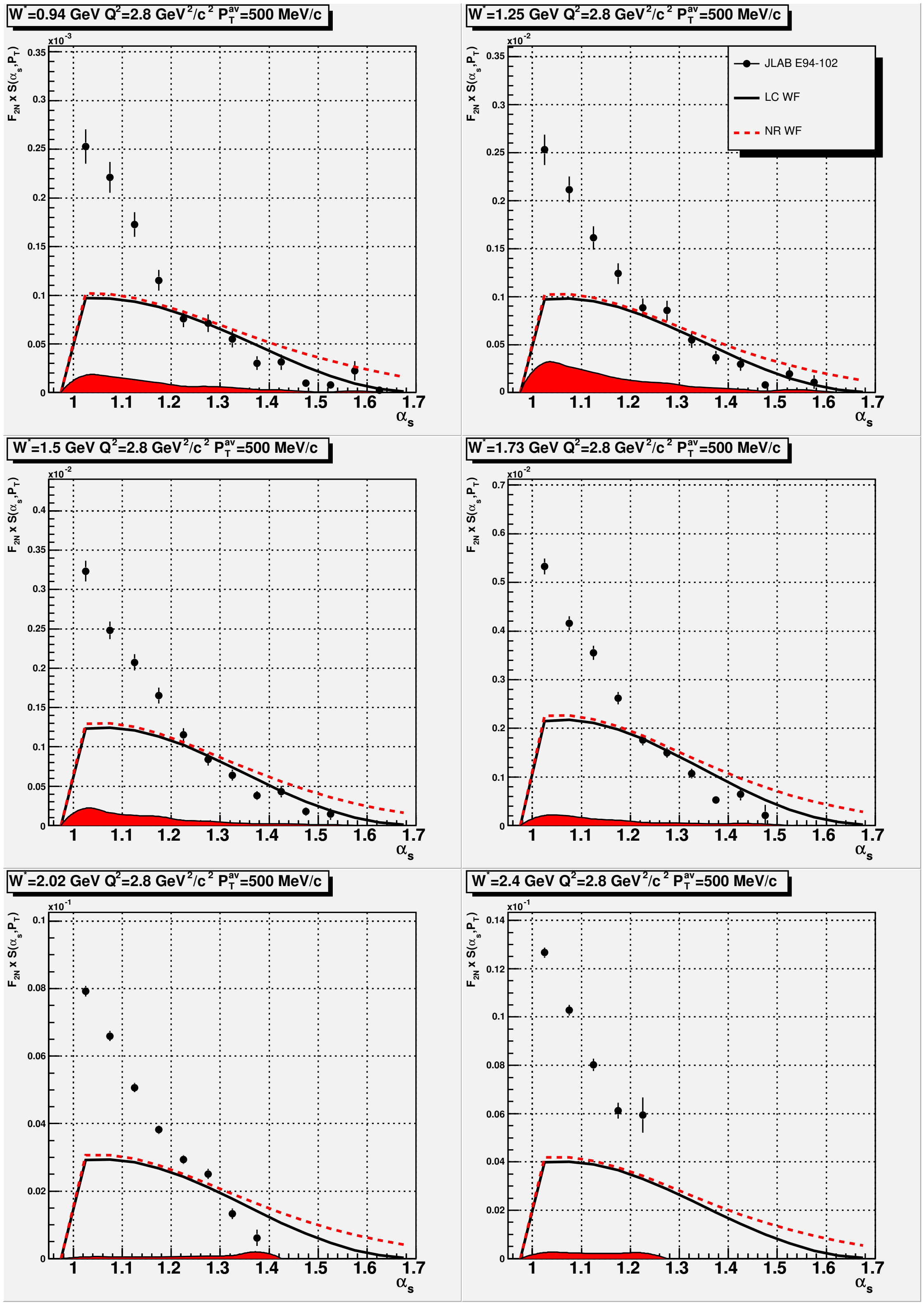

FIG. 163: The same as Fig. 162, but for the higher momentum transfer Q^2 bin $(2.1 - 5.0\ \mathrm{GeV}^2/c^2)$.

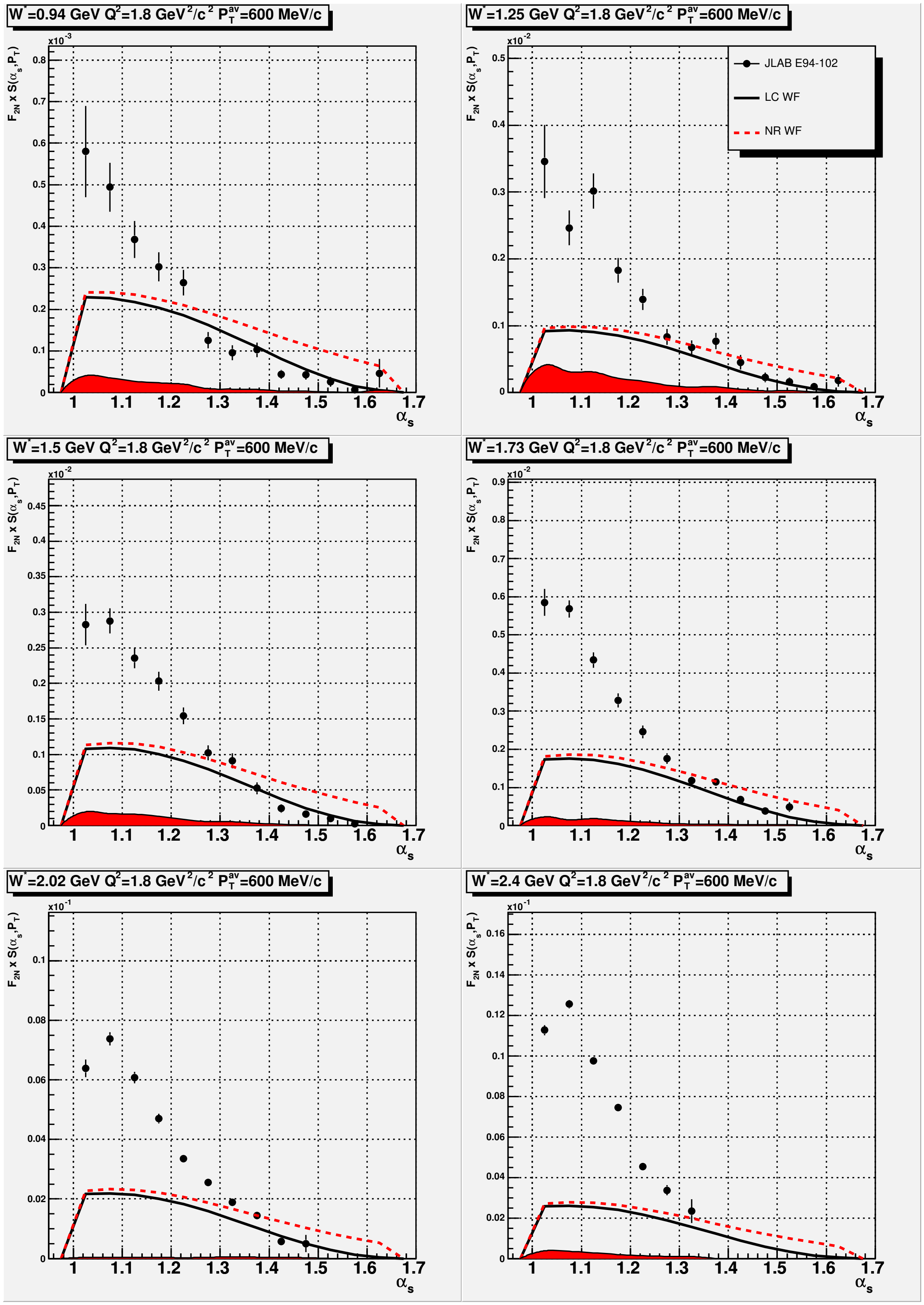

FIG. 164: The same as Fig. 157, but for the higher proton transverse momentum p_T bin $(550 - 650$ MeV/c).

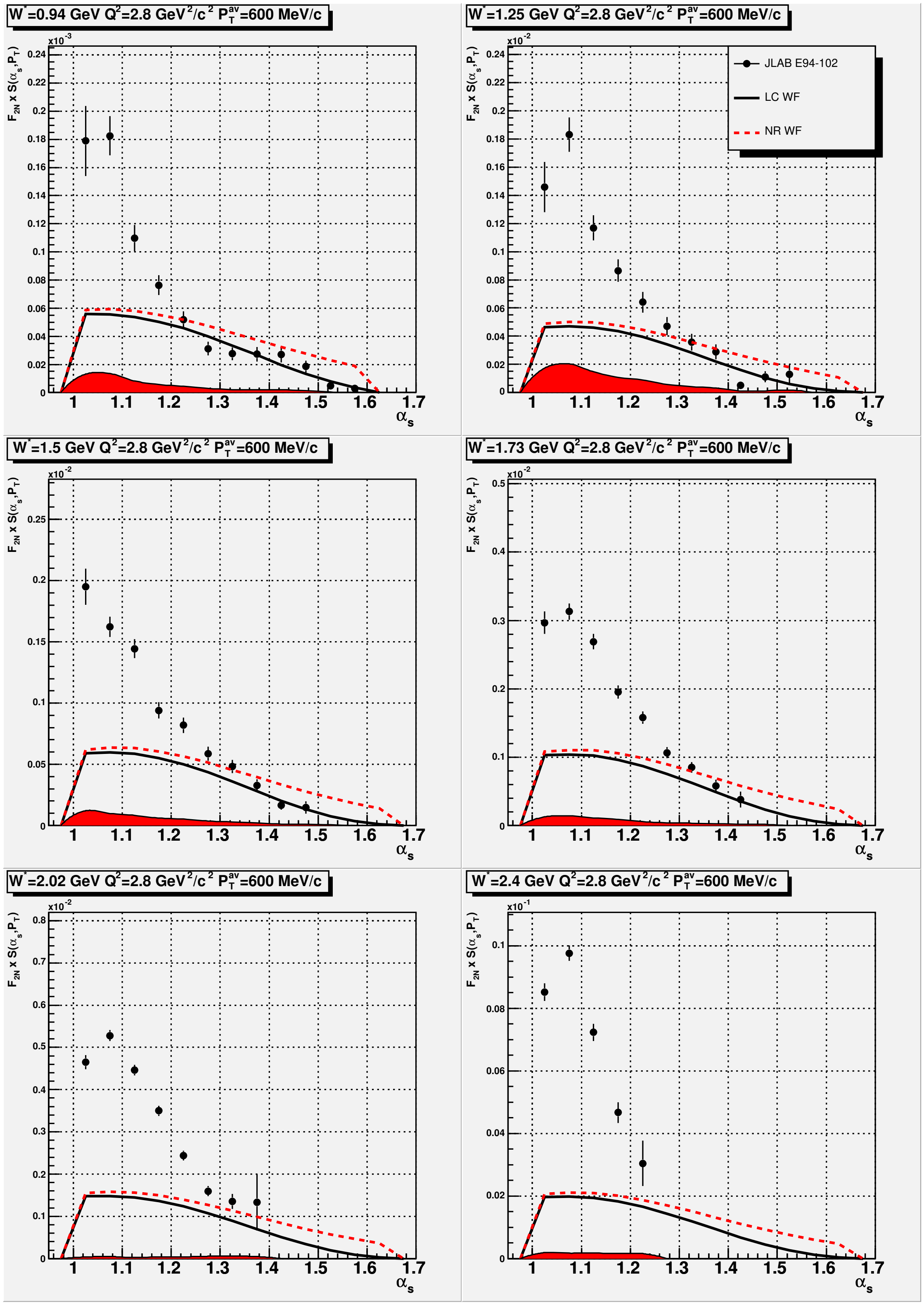

FIG. 165: The same as Fig. 164, but for the higher momentum transfer Q^2 bin $(2.1 - 5.0\ \mathrm{GeV}^2/\mathrm{c}^2)$.

VITA

Alexei V. Klimenko
Department of Physics
Old Dominion University
Norfolk, VA 23529

Alexei V. Klimenko has defended his "diploma" (equivalent of the Mater of Science degree) in Electrical Engineering at the Moscow Institute of Steel and Alloys (Moscow University of Technology) in June 1999. In August 1999 A.V. Klimenko was admitted to the Old Dominion University, Physics Department graduate school. By May 2001 he earned the degree of Master of Science in Physics. In Fall 2001 he became a term member of the Jefferson Lab Hall B (CLAS) Collaboration. In Spring 2002 Alexei has received a South-Eastern University Research Association graduate student fellowship. In Spring 2004 he also received the Graduate Assistant Excellence Reward from the ODU Office of Graduate Studies.

Typeset using LaTeX.